Detection of Acute Biomarkers to Optimize Target Engagement in Bioelectronic Medicine

by

Nishant Verma

A dissertation submitted in partial fulfillment of the requirements for the degree of

Doctor of Philosophy (Biomedical Engineering)

at the

University of Wisconsin – Madison 2022

Date of final oral examination: 22nd November 2022

The dissertation is approved by the following members of the Final Oral Committee:

Kip Ludwig, Associate Professor, Biomedical Engineering

Jill Barnes, Associate Professor, Kinesiology

Wally Block, Professor, Biomedical Engineering

Chris Brace, Associate Professor, Biomedical Engineering

LaTasha Crawford, Assistant Professor, Pathobiological Sciences

© Copyright by Nishant Verma 2022

All Rights Reserved

To those whose curiosity got the better of them.

Abstract

Bioelectronic medicine, or neuromodulation, is a class of medical therapies that act by delivering stimulation to directly manipulate neurobiological activity and address pathophysiology. While the therapeutic response can be highly effective, it is often limited to a subset of 'responders'. We show that bioelectronic therapies are critically limited by inconsistent engagement of on- and off-target neural substrates at the site of stimulation. The work presented here consists of four studies focusing on improving local neural target engagement in bioelectronic medicine.

In the first study, we develop a technique to directly measure on- and off-target neural activation that is minimally invasive and could be used clinically. A real-time measure is critical to guide stimulation electrode design and placement to optimize neural target engagement. We showed in large-animal experiments that a microneurography electrode, currently used in human research to measure spontaneous neural activity, can also be used to measure stimulation evoked neural activity relevant to bioelectronic medicine.

In the second study, we use cadaver-validated computational models to investigate the Injectrode, a minimally invasive stimulation electrode. We showed the Injectrode increased the target engagement profile of noninvasive transcutaneous electrical stimulation (TENS) based bioelectronic medicine therapies by over an order of magnitude.

In the third study, we apply the methods developed in the first two studies to improve the target engagement of an existing bioelectronic device: electronic bone growth stimulators (EBGSs). EBGS therapy has been used clinically for decades but shows sign of poor local target engagement. We used cadaver experiments and computational modeling to show that a miniscule fraction of the externally applied electric field (1,100 V/m) reaches the fracture site (21 V/m) during noninvasive EBGS therapy. We showed that Injectrode delivered at the fracture site could increase the electric field strength at the fracture site.

In the fourth study, we combine MRI-based biomarkers, reflecting physiological effect, with considerations of local neural target engagement to develop a novel bioelectronic medicine therapy to restore glymphatic function with applications to Alzheimer's disease. We showed that electrical stimulation increased cerebral blood flow and decreased flow pulsatility, reversing the trends established with disease progression. This fourth preliminary study lays the groundwork for future directions in my career.

This thesis contains a chapter, Chapter 6, written for the public audience to communicate the main findings and significance of the work.

Acknowledgements

Kip, thank you for being the best PhD advisor I could have imagined. You were just the right amount of hands-off. I remember many lessons, each of them practical, understanding, and highly effective. In addition, I would like to thank my thesis committee: Dr. Wally Block, Dr. LaTasha Crawford, Dr. Chris Brace, and Dr. Jill Barnes for their guidance and feedback. I would especially like to thank Wally for the many conceptual teachings on MRI and Jill for hands-on training on microneurography and transcranial doppler techniques.

I thank the undergraduate and post-baccalaureate researchers that worked with me over the last few years: Jonah Mudge, Maïsha Kasole, Lily Xistris, Aaron Skubal, Aaron Gholston, and Matthew Wroblewski amongst others. Your hard work, enthusiasm, and curiosity are found in every chapter of this thesis.

There are many members of the Wisconsin Institue of Translational Neuroengineering (WITNe) who have contributed to this work and my time in the lab. I would especially like to thank my peers and friends for coloring in the experiences of grad school: Ashlesha Deshmukh, Rex Chen, Jack Kegel, Andrea Brzeczkowski, and Bruce Knudsen. Thank you, Dr. James Trevathan for many an equally insightful and confusing technical discussion. Maria LaLuzerne, thank you for doing an excellent job managing our lab. Thank you, Dr. Justin Williams, Dr. Aaron Suminski, Dr. Megan Settell, Sarah Brodnick, Stephan Blanz, and Dr. Kevin Cheng, for your guiding input and collaboration over the years past and many more to come.

During my time in the lab, I have worked with a great group of collaborators. I would especially like to thank Bobby Graham from Dr. Scott Lempka's lab for his 'very real'

discussions. I also want to thank Jennifer Frank for her can do attitude and for inspiring confidence in my surgical training.

I have met incredible mentors and teachers in my career that have guided me on the path I am on. Thank you, Dr. Erika Ross, Dr. Albert Huang, Michael Pica, Ms Chee Hwai Mei, Mr Terrence Chiew, Mr Bernard Taylor, Mr Jason Chan, Ms Ni Ni Tun, Dr. Ann Saterbak, Dr. Jacob Robinson, Dr. Gary Woods, and Dr. Caleb Kemere. I would also like to thank the many industry researchers and engineers who took time off their day to speak with me – I thoroughly enjoy those conversations.

Sid, Linh, and Namita I am grateful for your friendship and companionship, especially in those early years of graduate school.

Lastly, thank you to my closest friends and family for your support, love, and curiosity in what I do. Jyoti Verma (Mama), Sanjiv Verma (Papa), Shikhar Verma (Bro), Leonardo Da Verma (Dog 2006-2022), Andrew Maust, Robyn Jingwen Kwok, and Carly Frieders.

Table of Contents

Abstract	ii
Acknowledgements	iv
Table of Contents	vi
List of Tables	x
List of Figures	xi
List of Key Acronyms	xiv
Chapter 1 Introduction and Background	1
1.1 The premise of bioelectronic medicine	3
1.2 Current bioelectronic medicine therapies	3
1.3 Biophysics of electrical stimulation	6
1.4 Vagus nerve stimulation	10
1.5 Target engagement in bioelectronic medicine therapies	12
1.6 Need for direct measures of target engagement	14
1.7 Computational models to study bioelectronic medicine	15
1.8 Contributions of this thesis	17
References	21
Chapter 2 Microneurography as a Minimally Invasive Method to Assess 1 During Neuromodulation	
Abstract	28
Introduction	30
Methods	34
Pre-registration	
Recording and stimulation electrodes	
Electrophysiology data analysis	
Results	49
Measuring ECAPs during invasive stimulation	50
Reference electrode on nerve versus in surrounding non-neural tissue	
Measuring asynchronous neural activity	
Artifacts in electrophysiology recordings	
Discussion	
Electrode choice by application	
Referencing strategy	
Mechanisms of neural recording	69

Recording spontaneous neural activity	69
Measuring ECAPs during non-invasive stimulation	
Sources of noise in electrophysiology recordings	
Correlation of VNS cardiac response and B-fiber ECAPs	
General limitations	
Conclusions	77
Acknowledgements	78
Conflicts of Interest	78
References	79
Supplementary Materials	86
Chapter 3 Augmented Transcutaneous Stimulation Using an Injectable Electrode: A	
Computational Study	108
Abstract	110
Introduction	111
Methods	115
Electroquasistatic FEM model	
Tissue conductivity and permittivity values	
Cadaver validation of FEM model	
Multi-compartment neuron model	
Simulating the neural response to the Injectrode system	
Results	
Transcutaneous coupling FEM model output and cadaver validation	
Mechanism of charge transfer to the nerve	
Validated transcutaneous coupling model to investigate Injectrode system parameters	
Validated transcutaneous coupling model to investigate patient-dependent parameters	
Effect of the Injectrode on vagal axon activation (biophysical model)	
Effect of the Injectrode system on on- and off-target neural recruitment (biophysical model)	
Effect of surface electrode size on relative activation of on-target vagal and off-target cutaneous a (biophysical model)	
Discussion	144
High-frequency carrier waveform	145
Waveform design for the Injectrode system	146
Geometry design of Injectrode system	147
Selection of tissue electrical properties for FEM model and their limitations	149
Effects of hydrogel	
Implications to TES modeling	
Implications of biophysical modeling of Injectrode system	
General limitations of study	
Conclusions	
Acknowledgements	158
Conflicts of Interest	158
References	159
Sunnlementary Material	165

by Weak Electric Fields Reaching Fracture	
Abstract	176
Introduction	176
Methods	179
Cadaver measurements	
Finite element method (FEM) model	
Injectrode Concept	
Statistical Analysis	190
Results	
First measurements of electric field at the fracture site during EBGS therapy	
Computational model of noninvasive EBGS therapy in humans	
Stage of healing and electric field at fracture site with conventional EBGSs	
Electric field at fracture site during EBGS therapy in sheep	
Computational models and cadaver experiments support use of Injectrode to augment EBGS therapy. Depth of fracture increased utility of Injectrode-augmented EBGS therapy	
Stage of healing and electric field at fracture site with Injectrode-augmented EBGS	
Discussion	
Conclusions	
Acknowledgements	209
Author Contributions	210
Competing Interests	210
Data Availability	210
References	211
Supplementary Material	214
Supplementary Material References	218
Chapter 5 Pilot Data for Future Directions: Trigeminal Nerve Stimulation to Restore	
Glymphatic Function	219
Abstract	221
Introduction	222
Results	225
Neural target engagement during stimulation	
Macrovasculature blood flow increases and flow pulsatility decreases during stimulation	
Evaluating CSF movement during stimulation	232
Evaluating CSF clearance from the brain using PET	
Effect of electrical stimulation and dobutamine on heart rate and blood pressure	236
Discussion	236
Methods	242
Acknowledgements	2/15

Conflicts of Interest	246
References	246
Chapter 6 Thesis Chapter for the Public	. 251
Purpose of this chapter	252
6.1 Analogy of the nervous system	253
6.2 Example of a bioelectronic medicine therapy	253
6.3 The problem of imprecise stimulation in bioelectronic medicine	254
6.4 Improving target engagement in bioelectronic medicine	254
6.5 How I used the Injectrode and microneurography electrode to improve electronic bone growstimulators	wth 256
6.6 What I am doing now	258
6.7 My journey to bioelectronic medicine	258
6.8 My future	259
Conclusions and Next Steps	. 260

List of Tables

Table 2.1: Recording electrode choice by application	65
Table 3.1: Material electrical properties used in the FEM model	119
Table 3.2: Energy transfer methods used in minimally invasive neuromodulation devices	166
Table 4.1: Summary of electric potentials reaching fracture site in humans	192
Table 4.2: Summary of electric potential at fracture site in sheep	197
Table 4.3: Human results of Injectrode-augmented EBGS	199
Table 4.4: Sheep results of Injectrode-augmented EBGS	200
Table 4.5: Conductivity of materials in human finite element method (FEM) model	215
Table 4.6: Conductivity of materials in sheep FEM model	215
Table 5.1: Subject anesthesia summary	227
Table 5.2: 4D-Flow data summary	229
Table 5.3: DWI data summary	233

List of Figures

Figure 1.1: Bioelectronic medicine stimulation electrodes	5
Figure 1.2: Nerves are composed of various fiber types.	6
Figure 1.3: Longitudinal versus transverse mode of neural activation	8
Figure 1.4: Activating function 1	LO
Figure 1.5: Noninvasive vagus nerve stimulation devices 1	L2
Figure 1.6: Auricular branch of vagus nerve anatomy1	L4
Figure 1.7: <i>In silico</i> modeling workflow used in bioelectronic medicine1	L6
Figure 2.1: Illustration of three types of recording electrodes, synchronous versus asynchronou neural activity, and effect of electrode-fiber distance on recorded signals	
Figure 2.2: Experimental setup and surgical preparation	39
Figure 2.3: Comparison of electrodes in recording ECAPs from larger myelinated fibers5	53
Figure 2.4: Nose floor of recording electrodes5	55
Figure 2.5: Comparison of electrodes in recording ECAPs from smaller myelinated fibers and correlation to evoked bradycardia5	57
Figure 2.6: Effect of referencing strategy on stimulation artifact and ECAP6	50
Figure 2.7: Comparison of electrodes in recording asynchronous sensory evoked neural activity	
Figure 2.8: Close up photograph of three recording electrodes characterized in this study 8	37
Figure 2.9: Representative histology of great auricular nerve cross sections (5 um) for four subjects	38
Figure 2.10: Surgical pocket to access great auricular nerve and surrounding anatomy 8	39
Figure 2.11: Subject 1 vagus micro 2 was a non-functional electrode classified by the high noise floor (green trace) compared to the blue and red traces (figure below) and no ECAP signal even at 5 mA of stimulation	I
Figure 2.12: Subject 4 vagus cuff 2 was a non-functional electrode classified by the high noise floor (green trace) compared to the blue and red traces (figure below) and noted as physically disconnected at the end of the recording	94
Figure 2.13: ECAPs from Subject 6 microelectrode recordings during the vagus dose-response amplitude sweep were contaminated by stimulation artifact	€
Figure 2.14: Microelectrode traces from subject 1 before (top) and after (bottom) filtering 9) 6
Figure 2.15: (top) An example of cardiac related artifact appearing in electrophysiology recordings, which may be mistaken for a neural signal	96

Figure 2.16: B-fiber ECAPs across recording electrodes.	97
Figure 2.17: A β ECAP at 1.5 mA of stimulation on cervical vagus nerve from all subjects	98
Figure 2.18: A β -fiber dose-response curves during vagus nerve stimulation from all subjects.	98
Figure 2.19: B-fiber dose-response curves during vagus nerve stimulation from all subjects	99
Figure 2.20: Stimulated evoked heart rate change dose-response curves during vagus nerve stimulation (VNS) from all subjects.	100
Figure 2.21: Tripolar vs. bipolar reference cuff recordings.	101
Figure 2.22: Spike count from sensory stroking evoked naturally occurring activity on all subjects.	102
Figure 2.23: Subject 1 cVN spontaneous activity recording.	103
Figure 2.24: Subject 2 cVN spontaneous activity recording.	104
Figure 2.25: Subject 3 cVN spontaneous activity recording.	104
Figure 2.26: Subject 4 cVN spontaneous activity recording.	105
Figure 2.27: Subject 5 cVN spontaneous activity recording	105
Figure 2.28: Subject 6 cVN spontaneous activity recording	106
Figure 2.29: Subject 6 cVN spontaneous activity recording presented as an integrated neurogram.	107
Figure 3.1: Injectrode placement and usage.	112
Figure 3.2: Model of the Injectrode system in COMSOL Multiphysics	117
Figure 3.3: NEURON biophysical study	125
Figure 3.4: Cadaver validation of finite element method (FEM) model	128
Figure 3.5: Finite element method (FEM) model results investigating Injectrode system parameters	135
Figure 3.6: Finite element method (FEM) model results investigating tissue parameters and TENS electrode placement error.	139
Figure 3.7: Biophysical model results showing Injectrode reduces activation threshold by an order of magnitude compared to traditional TENS.	143
Figure 3.8: Plot of voltage against time when a 20 mA current pulse was delivered to two TE hydrogel electrodes adhered to each other.	
Figure 3.9: Current-controlled waveform in swine cadaver	170
Figure 3.10: Domestic swine cadaver verification of FEM model with fitted skin properties	172
Figure 3.11: Main mechanism of transcutaneous charge transfer is ohmic	173

Figure 4.1: Direct electric field measurements at fracture site during noninvasive EBGS therapy18	
Figure 4.2: EBGS computational FEM modeling in humans and sheep18	7
Figure 4.3: Results of noninvasive EBGS FEM models in sheep investigating stimulation electrode configurations	6
Figure 4.4: Injectrode to augment electric field reaching the fracture site during noninvasive EBGS therapy	8
Figure 4.5: Injectrode increases electric field at fracture site when used with noninvasive EBGS therapy20	
Figure 4.6: Raw waveform from all human cadaver measurements	.7
Figure 5.1: Mouthguard stimulator concept and measurement of neural target engagement during stimulation22	4
Figure 5.2: Blood flow, velocity, and flow pulsatility measured in the cerebral vessels using 4D- Flow MRI23	
Figure 5.3: Diffusion weighted imaging (DWI) to measure cerebrospinal fluid (CSF) movement in the paravascular and subarachnoid spaces (PVS) of the anterior cerebral artery (ACA) 23	
Figure 6.1: Injectrode delivery to the target nerve25	5
Figure 6.2: Ottaviani and his colleagues inserted a very thin metal wire through the skin and into the target nerve25	6

List of Key Acronyms

ABVN Auricular branch of vagus nerve

ACA Anterior cerebral artery

aVNS Auricular vagus nerve stimulation

BAT baroreflex activation therapy

CC Capacitive coupling

CSF cerebrospinal fluid

cVN Cervical vagus nerve

DBS Deep brain stimulation

DCES Direct current electrical stimulation

DWI Diffusion weighted imaging

ECAP Evoked compound action potential

EBGS electronic bone growth stimulator

EES epidural electrical stimulation

FDA United States Food and Drug Administration

FEM Finite element method

IPG implantable pulse generator

LIFE Longitudinal intrafascicular electrode

LC locus coeruleus

MCA Middle cerebral artery

MRI Magnetic resonance imaging

ncVNS Noninvasive cervical vagus nerve stimulation

PCA Posterior cerebral artery

PVS Paravascular spaces

PET Positron emission tomography

ROI Region of interest

TENS transcutaneous electrical stimulation

VNS Vagus nerve stimulation

Chapter 1 Introduction and Background

Portions of this chapter were adapted from the following articles published in peer-reviewed journals:

Verma, N., Mudge, J. D., Kasole, M., Chen, R. C., Blanz, S. L., Trevathan, J. K., et al. (2021).

Auricular Vagus Neuromodulation—A Systematic Review on Quality of Evidence and Clinical

Effects. Front. Neurosci. 15, 664740. doi: 10.3389/fnins.2021.664740.

Verma, N., Graham, R. D., Mudge, J., Trevathan, J. K., Franke, M., Shoffstall, A. J., et al. (2021).

Augmented Transcutaneous Stimulation Using an Injectable Electrode: A Computational Study.

Front. Bioeng. Biotechnol. 9, 796042. doi: 10.3389/fbioe.2021.796042.

1.1 The premise of bioelectronic medicine

Neurons connect our peripheral organs to our brain. These neurons communicate information from our brain to the peripheral organ systems and from the peripheral organ systems to the brain. In doing so, they present a communication channel that may be 'hijacked' to manipulate organ function. The bidirectional communication between the brain and the periphery are encoded as action potentials, actively regenerating electrical signals that propagate down the axons of the neurons. Various forms of stimulation, including electricity, heat, and ultrasound pressure can be used to modulate neural activity. The field of bioelectronic medicine, or neuromodulation, has been around for several decades and has developed several United States Food and Drug Administration (FDA) approved medical devices.

1.2 Current bioelectronic medicine therapies

Examples of clinically adopted bioelectronic medicine therapies include cervical vagus nerve stimulation (VNS) for the treatment of epilepsy, epidural electrical stimulation (EES) of the spinal cord for the treatment of several types of chronic pain, deep brain stimulation (DBS) for the treatment of tremors, and baroreflex activation therapy (BAT) for the treatment of heart failure. These are just a subset of the invasive bioelectronic medicine therapies currently in clinical use. An implantable device that directly interfaces with the nerve can achieve on-target neural engagement of deep nerves in a specific manner (Aristovich et al., 2021). However, traditional implantable devices consisting of an implanted battery, electronics, leads, and stimulation electrodes are complex and costly (Kumar and Bishop, 2009; Udo et al., 2012). The complexity of the implanted device and the associated supply chain, in which manufacturing

procedures must be tightly controlled across several suppliers, contributes to the cost of the therapy and is prone to multiple points of failure (FDA, 1997; Carome, 2020). Once manufactured, a traditional implantable device requires invasive surgical placement, which adds to the cost of the therapy (Trevathan, 2019; Kumar and Bishop, 2009). Traditional implanted devices also use pre-formed, rigid neural interfacing electrodes that do not conform well to complex neural structures (He et al., 2020). These fully implanted devices are depicted in panel E and F of Figure 1.1.

There are numerous more clinically used therapies based on noninvasive transcutaneous electrical stimulation (TENS). For example, auricular vagus nerve stimulation (aVNS) commonly delivered at the cymba conchae in the ear with the intention of activating the cutaneous auricular branch of the vagus nerve (ABVN). aVNS is being investigated as a therapy for the treatment of epilepsy, chronic pain, rheumatoid arthritis, and atrial fibrillation, amongst others (Verma et al., 2021a). Because TENS based therapies are non-invasive, they are generally low-cost and low risk. While these completely non-invasive devices can engage deep nerves, they also activate more superficial neural structures, such as cutaneous receptors in the skin and off-target superficial nerves (Bucksot et al., 2020). Activation of superficial off-target neural structures leads to side effects, including noxious sensation and uncomfortable muscular contractions (Bucksot et al., 2020; Manson et al., 2020), which limit the stimulation dose from being increased to engage the deep on-target nerve. These noninvasive devices are depicted in panel A of Figure 1.1.

Minimally invasive bioelectronic medicine therapies are a growing category of devices.

They are designed to attain the spatial specificity and neural target engagement depth of an

implantable therapy while maintaining the accessibility and low-risk attributes of non-invasive TES. Examples of current minimally invasive technologies include the Freedom SCS System and the Nalu Neurostimulation System for the treatment of chronic pain. These minimally invasive systems generally consist of a small device implanted at the target neural structure and an external power source, which powers the implant (Loeb et al., 2006; Ilfeld et al., 2021). However, these devices are still complex and costly and use stiff neural interfacing electrodes that do not conform to the target neural structure to reduce tissue trauma and better isolate the target nerve (Loeb et al., 2006). These minimally invasive devices are depicted in panel C and D of Figure 1.1.

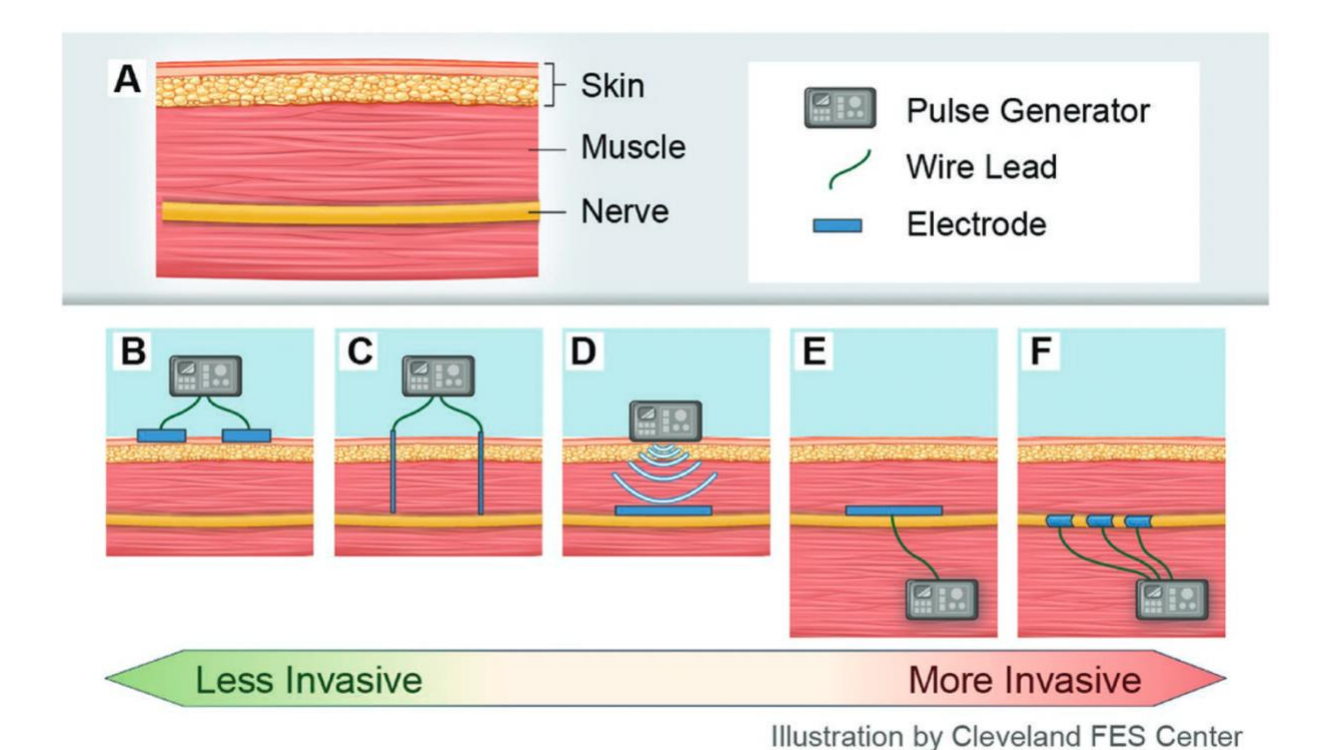


Figure 1.1: Bioelectronic medicine stimulation electrodes.

Noninvasive on the left (B), minimally invasive in the center (C, D) to fully implantable on the right (E, F). Figure from Trevathan et al. (2019).

1.3 Biophysics of electrical stimulation

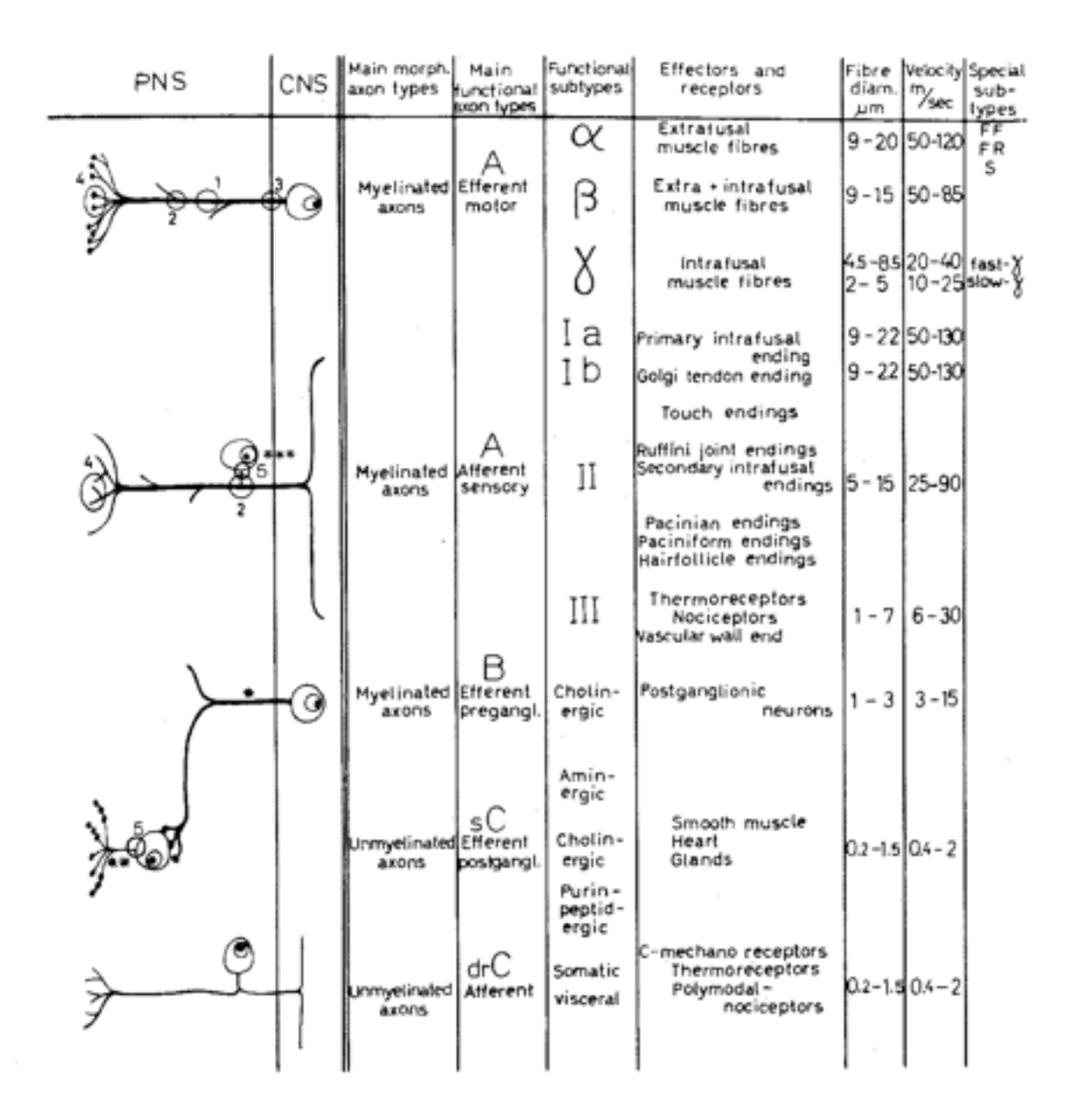


Figure 1.2: Nerves are composed of various fiber types.

Larger diameter fibers (top) are faster conducting and activate with lower levels of electrical stimulation, while smaller diameter fibers (bottom) are slower conducting and require higher levels of electrical stimulation to activate. Figure from Waxman (1978).

The biophysics of neural activation by electrical stimulation, the most common implementation of bioelectronic medicine therapy, dictates that large diameter neurons are activated before

smaller diameter neurons (Figure 1.2). In the case of VNS, recruitment of easier to activate large off-target motor neurons in or around the vagus produce intolerable neck muscle contractions and limits stimulation dosage (i.e., current) (Nicolai et al., 2020 & Yoo et al., 2013). Limited stimulation dosage may be insufficient for activating the putatively therapeutic smaller diameter sensory and parasympathetic neurons in the vagus (Nicolai et al., 2020).

The excitability, or its inverse, stimulation current threshold, of a neuron depends on several factors, including region of the neuron being targeted, neuron diameter and myelination thickness, voltage-gated ion channel type and density, and distance and orientation of the neuron relative to the stimulation electrode. In peripheral bioelectronic medicine, the cell axon is often targeted for activation as it is more excitable than the cell body (Rattay, 1999). Larger diameter neurons have larger intracellular spaces, thicker myelination, and greater distances between nodes of Ranvier (Waxman, 1980). The larger intracellular diameter of the axon results in less resistance to ion movement and increased excitability (Rattay, 1999). The thicker myelination translates to less charge leakage from the intracellular space, more effective coupling between nodes of Ranvier, and increased excitability (Ye and Ng, 2018; Resnick et al., 2019). Greater distances between nodes of Ranvier results in larger 'steps' and faster saltatory conduction. Sensory neurons generally have lower stimulation thresholds to activate than motor neurons of the same size due to differences in voltage-gated ion channel types and a higher persistent Na+ conductance (Gaines et al., 2018; Burke et al., 2017).

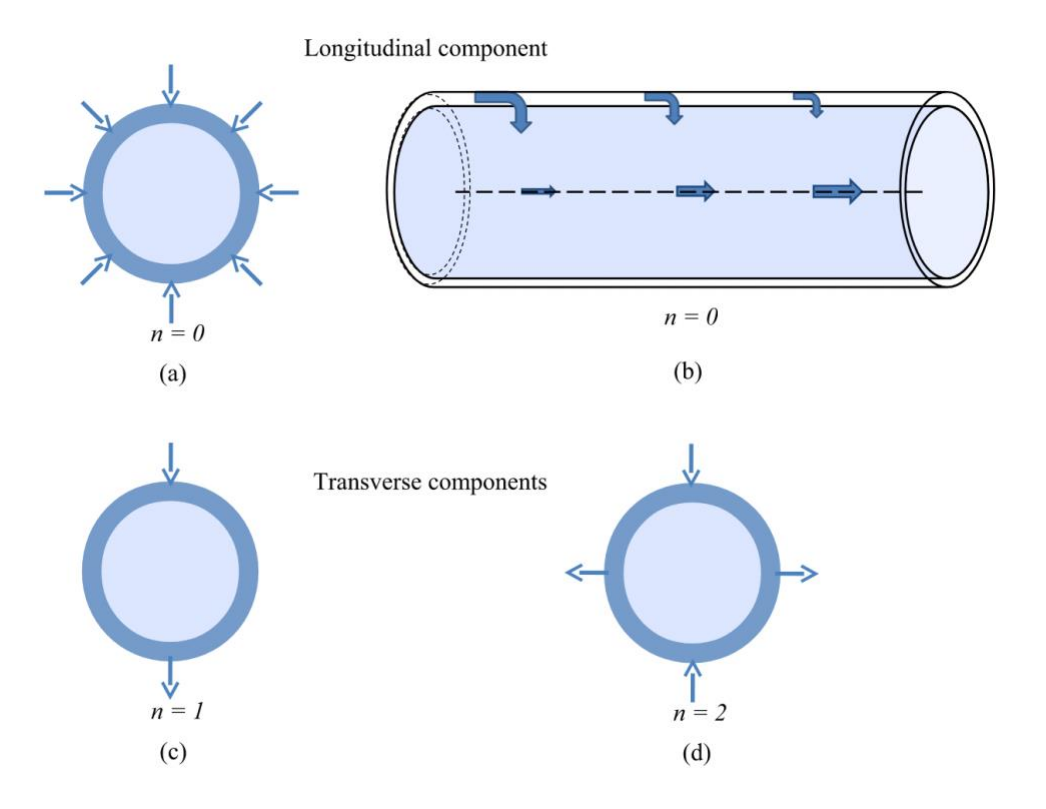


Figure 1.3: Longitudinal versus transverse mode of neural activation.

Top illustrates flow of current inside the neuron along its length and shows the longitudinal model of activation. Bottom illustrates flow of current transversely through the neuron and shows the transverse mode of activation. Figure from Meffin et al. (2012).

The closer the stimulation electrode is to the target neuron, the lower the stimulation current threshold is to activate that neuron. The electric potential falls off from a monopolar stimulation electrode is proportional to ~1/r and proportional to ~1/r² for a bipolar stimulation electrode (Plonsey and Barr, 1995), where r is the distance between the electrode pair and the target neuron. An external electric field activates neurons by triggering voltage-gated ion channels to initiate an action potential. The electric field can be applied along the length of the neuron (longitudinal) or across the diameter (transverse) of the neuron – both of which can initiate an action potential (Meffin et al., 2012; Ye and Ng, 2018) (Figure 1.3). The longitudinal mode of activation typically occurs at a lower stimulation threshold and is approximated by the

activating function. The activating function states that the stimulation threshold of a neuron is proportional to the second order spatial derivative of the electric potential along the length of the neuron (Rattay, 1999) and is illustrated in Figure 1.4 for a monopolar stimulation electrode. Following the activating function, large changes in electric field that occur along the length of the neuron are prime points of neural activation.

The activating function also illustrates the complexities of neural stimulation in the *in* vivo setting. In Figure 1.4 (bottom), for the case of a single neuron, the activating function shows a central point of activation, associated with cathodic stimulation, surrounded by a 'virtual' anode or an 'anulus ring' of inactivation (hyperpolarization). It is therefore possible that if too high a level of electrical stimulation is applied, the zone of inactivation may be strong enough to prevent propagation of an action potentials from the center cathodic activation point to outside the inactivation zone. Further complicating the matter, in a nerve, multiple neurons are present at slightly different spatial locations and experience different strengths of the applied electric field and activating function. The center 'activation' zone covers multiple neurons while the 'inactivation' zone also covers multiple neurons, including some of those covered by the 'activation' zone. Similarly, the anodic electrode, carrying return current, forms a central zone of inactivation surrounded by a virtual cathode zone of activation (Rattay, 1999). These varying stimulation electrode-neuron distances and virtual cathodes and anodes phenomena interact in the *in vivo* environment and careful consideration must be given to electrode design, which informs electric field spread and the activating function, and stimulus waveform design to attain the desired neural activation or inactivation results.

Cathodic (-)

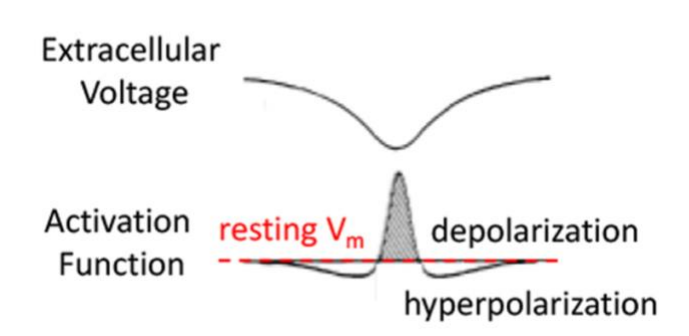


Figure 1.4: Activating function.

(top) Electric potential from a monopolar source is proportional to ~1/r (Plonsey and Barr, 1995). (bottom) Activating function calculated along the length of a neuron due to the monopolar stimulation source (Rattay, 1999). Figure adapted from Aplin and Fridman (2019).

1.4 Vagus nerve stimulation

The wandering path of the vagus nerve, the tenth cranial nerve, and its communication with several visceral organs and brain structures makes it an attractive target to address many diseases. The vagus nerve innervates several critical visceral organs including the heart, lungs, and upper gastrointestinal tract. VNS to treat epilepsy has been approved by the FDA since 1997 (Wellmark, 2018). VNS has also been approved for depression and is being studied for treatment of rheumatoid arthritis, irritable bowel syndrome, and heart failure. An implantable pulse generator (IPG) is implanted below the clavicle and delivers controlled doses of electrical stimulation through electrodes wrapped around the cervical vagus. Due to the safety versus efficacy profile of the therapy, implantable VNS is currently a last line therapy after patients have been shown refractory to at least two appropriately dosed anti-epileptic drugs (American Association of Neurological Surgeons, 2021). Implantable VNS for epilepsy is purported to work through vagal afferents terminating in the nucleus of the solitary tract (NTS). NTS in turn has

direct or indirect projections to the nuclei providing noradrenergic, endorphinergic, and serotonergic fibers to different parts of the brain (Kaniusas et al., 2019).

In a similar fashion, the auricular branch of the vagus also projects to the NTS, carrying somatosensory signals from the ear (Kaniusas et al., 2019). The superficial path of the nerve (Bermejo et al., 2017) in the ear means a low amplitude electrical stimulation applied at the surface of the skin can, in theory, generate electric field gradients at the depth of the nerve sufficient to alter its activity. Auricular vagus nerve stimulation (aVNS) delivered percutaneously or transcutaneously offers a method to modulate neural activity on the vagus nerve with the potential for a more favorable safety profile. However, the efficacy profile of aVNS may be different from VNS as the auricular VN contains only somatosensory neurons while the cervical VN contains autonomic and visceral sensory neurons, whose modulation may be more closely tied to organ function and pathophysiology. Figure 1.5 (A) shows a commercial device used to deliver aVNS. Figure 1.6 shows innervation of the auricle by four major nerve branches and overlapping regions of innervation in the auricle.

Given aVNS can be implemented with minimally invasive approaches and has the potential to modulate vagal activity, there have been many early-stage clinical trials investigating a diverse range of potential therapeutic indications, including heart failure, epilepsy, depression, pre-diabetes, Parkinson's, and rheumatoid arthritis. Several companies are already developing aVNS devices, such as Parasym (London, UK), Cerbomed (Erlangen, Germany), Spark Biomedical (Dallas, Texas, USA), SzeleSTIM (Vienna, Austria), Ducest Medical (Ducest, Mattersburg, Germany), Innovative Health Solutions (Versailles, IN, USA) and Hwato (Suzhou, Jiangsu Province, China). Despite the large number of aVNS clinical studies, clinical

evidence to support a specific therapeutic outcome is often mixed, with conflicting trial results for the same physiological outcome measure (Burger et al., 2020; Keute et al., 2020).

Lastly, noninvasive cervical vagus nerve stimulation (ncVNS) is used clinically to treat epilepsy and migraine. Figure 1.5 (B) shows a commercial device to deliver ncVNS. However, due to the depth of the cervical vagus nerve in humans, it is unclear if the device is directly activating the vagus nerve with electrical stimulation or activating another nerve instead for its therapeutic effects (Nonis et al., 2017; Nicolai et al., 2020; Verma et al., 2021b).

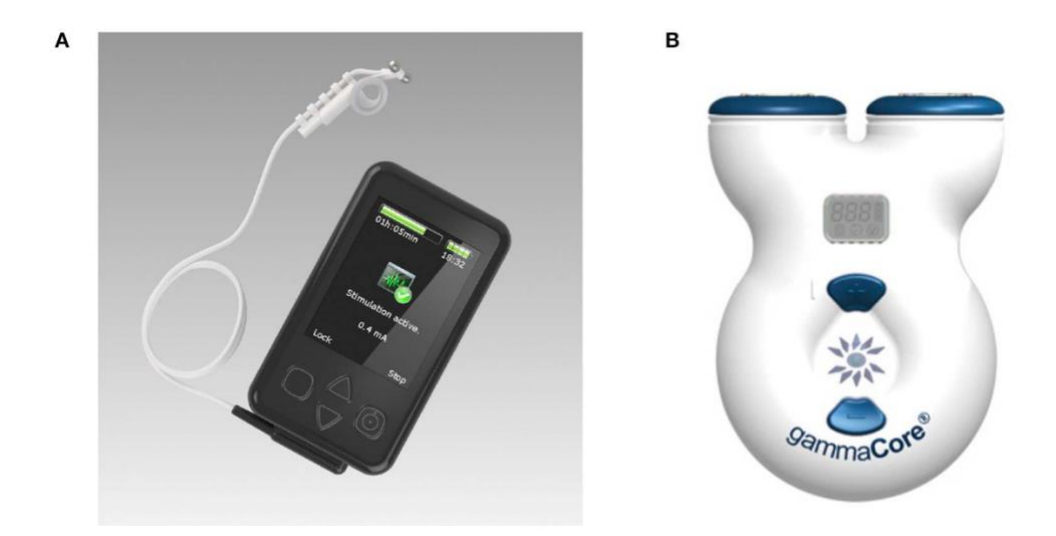


Figure 1.5: Noninvasive vagus nerve stimulation devices.Targeting the auricular branch of the vagus nerve (A) and the deep cervical vagus nerve (B). Figure adapted from Yap et al. (2020).

1.5 Target engagement in bioelectronic medicine therapies

Target engagement of neurons at the site of stimulation is not routinely measured in bioelectronic medicine therapies. In fact, off-target nerve activation critically limits the stimulation dose that can be delivered in many therapies and therefore the clinical efficacy. For example, De Ferrari and colleagues (2017) explained the failure of a clinical trial testing VNS for

heart failure to be due to poor target engagement in the clinical population. This was despite encouraging results in large animal studies. They derived heat maps from Holter recordings and showed that while almost every animal showed signs of target engagement during the delivery of VNS, only 12% of patients in the failed clinical trial did. As another example, Heusser and colleagues (2016) showed that BAT therapy to lower blood pressure was also critically limited by the stimulation does that could be delivered due to off-target nerve activation. They showed that when they stimulation dose was titrated to a chronically comfortable level for patients, with minimal side effects, the average decrease in systolic blood pressure was 6.3 mmHg. However, when the stimulation dose was acutely set to a higher level that was uncomfortable but tolerable, the average decrease in systolic blood pressure was 16.9 mmHg. The increased stimulation dose increased the efficacy of the therapy in lowering systolic blood pressure and converted several initial 'non responders' to responders.

Currently, therapies are often titrated by increasing the stimulation dose till an off-target effect is visible (e.g., unintended muscle contraction) or the patient reports discomfort. Then, the stimulation is turned down slightly to avoid that off-target effect and the patient is sent home. This assumption of successful on-target neural engagement based on titration to off-target effects is unfounded and is critically limiting bioelectronic medicine therapies (Heusser et al., 2016; De Ferrari et al., 2017; Verma et al., 2021a).

Furthermore, the lack of tools to directly study on- and off-target neural engagement clinically has led to a poor understanding of the neural substrates involved in the therapeutic and side effects of these therapies in human patients. Thereby hampering the study of mechanisms of action of these therapies in humans.

VNS and aVNS based therapies are especially limited by inconsistent local neural target engagement and poor isolation of on- and off-target neural substrates. The biophysics of electrical stimulation, described prior, exacerbates target engagement issues in VNS based therapies. Where, unfortunately, smaller diameter sensory neurons, which are more difficult to activate with electrical stimulation than larger diameter motor neurons, are purported for the therapeutics effects of VNS based therapies. In aVNS, the poor understanding of the neuroanatomy of the several nerves innervating the ear, overlap in their regions of innervation, (Figure 1.6) and the lack of tools to directly measure target engagement *in vivo* in patients makes it challenging to design and place the stimulation electrodes to achieve consistent neural target engagement across subjects.

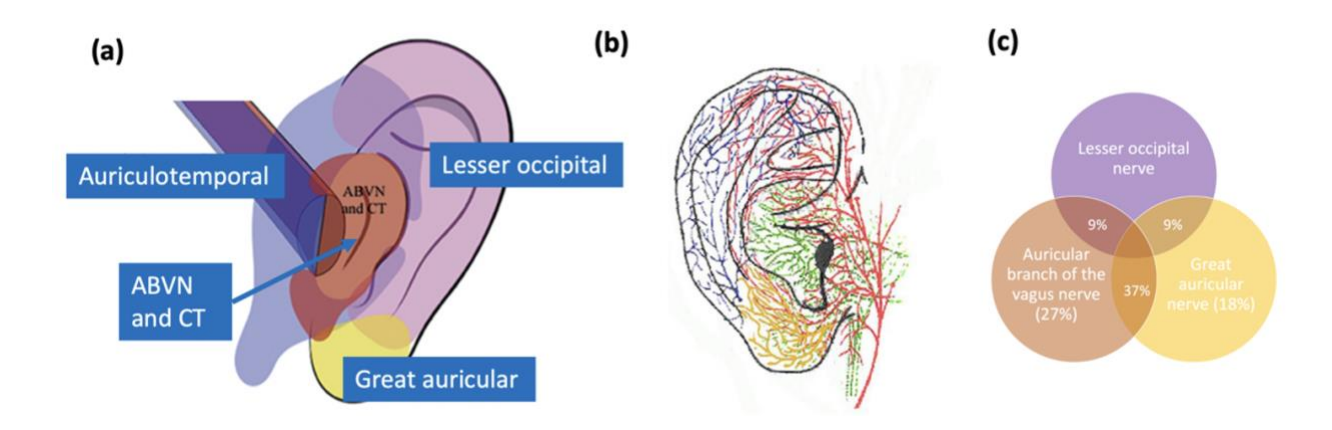


Figure 1.6: Auricular branch of vagus nerve anatomy.

Several nerves innervate the ear with substantial overlap in their innervation regions. The subject-to-subject variability in innervation is not well characterized. This makes it challenging to design and place aVNS stimulation electrodes to engage a specific nerve while avoiding potential off-target nerves. Figure adapted from Verma et al. (2021a).

1.6 Need for direct measures of target engagement

Target engagement is commonly measured using secondary surrogates such as fMRI, somatosensory evoked potentials (SSEPs), and cardiac measures. Secondary surrogates of

target engagement are often contaminated with physical and biological noise, leading to potential confounds. For example, Botvinik-Nezer et al. (2020) and Becq et al. (2020) showed that results of fMRI studies were highly dependent on data processing techniques applied. fMRI of the brainstem, where nucleus tractus solitarius (NTS) is located (termination location of afferent sensory vagal fibers in the brain), is further complicated (Napadow et al., 2019) as distance from the measurement coils increases, the effective resolution decreases (Gruber et al., 2018). Still further, novelty, such as being stimulated in the ear or being in an MRI scanner, activates the locus coeruleus (LC) (Wagatsuma, 2017), which has connections with NTS. This novelty mediated activation of LC may consequently activate NTS and confound the interpretation of potential VNS effects on NTS. Lastly, fMRI has nonstandard results between subjects requiring individual calibration and making subject to subject comparisons challenging. Additionally, SSEP recordings are sometimes contaminated and misinterpreted due to EMG leakage (Usami et al., 2013). The common measures of target engagement are secondary surrogates and prone to confounds – creating a need for direct measures of local target engagement.

1.7 Computational models to study bioelectronic medicine

In silico models in bioelectronic medicine employ the finite element method (FEM) to study volumetrically accurate spread of electric fields from stimulation electrodes. These FEM models are coupled to NEURON equivalent circuit models to predict neural activation (Hines and Carnevale, 1997). The modeling workflow is illustrated in Figure 1.7. Computational modeling is

used to iterate through the large design space of electrode design, placement, and stimulation parameters.

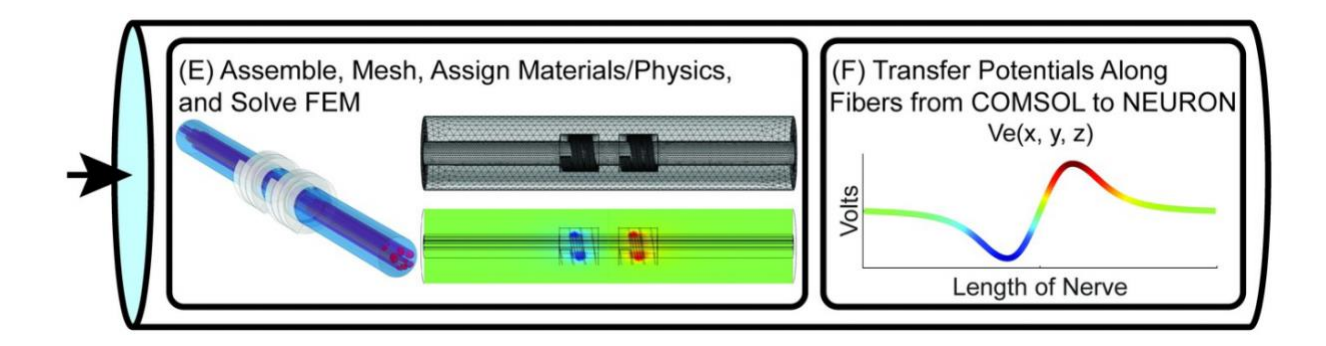


Figure 1.7: In silico modeling workflow used in bioelectronic medicine.

Finite element method (FEM) is used to calculate volumetrically realistic electric field spread from the stimulation electrode. The electric field solution is then used as an input to equivalent circuit NEURON models. Figure adapted from Musselman et al. (2021).

The accuracy of FEM models, especially for the low frequencies used in bioelectronic medicine stimulation waveforms, is critically limited by the accuracy of literature values of tissue conductivities. These measurements are challenging to make due to the quick changes in tissue properties following biopsy as well as the electrode-tissue effects prominent at low frequencies (Verma et al., 2021; Gabriel, 1996).

Further, the FEM models commonly neglect the contribution of dielectric effects of tissue. This assumption is valid at lower frequencies and with tissues with lower charge relaxation times (Zhu et al., 2017). At higher frequencies, and when considering tissues with longer dielectric charge relaxation times, such as skin, it may be important to consider dielectric effects.

1.8 Contributions of this thesis

The three primary projects of this thesis are shared in Chapters 2-4. The first project, in Chapter 2, is on the preclinical development of a minimally invasive technique that could be used to directly measure on- and off- target neural activation around the stimulation electrode in clinical patients. The second project shows how stimulation electrode design can be optimized to improve the local neural target engagement profile. Measurement of local neural target engagement, developed in the first project, is a critical first step to guide this optimization. In the third project, the local target engagement framework and the tools and techniques developed in the first two projects, are applied to show how they could improve an existing bioelectronic medicine therapy. An additional study, building on the primary projects of this thesis, and forming the basis for future works, is shared in Chapter 5. I have briefly noted the main contributions of this thesis, by chapter, below.

Chapter 2: Microneurography as a Minimally Invasive Method to Directly Assess Target Engagement

Peripheral neural signals recorded during neuromodulation therapies provide insights into local neural target engagement and serve as a sensitive biomarker of physiological effect. Although these applications make peripheral recordings important for furthering neuromodulation therapies, the invasive nature of conventional nerve cuffs and longitudinal intrafascicular electrodes (LIFEs) limit their clinical utility. Microneurography, a minimally invasive technique, is already used routinely in humans to record asynchronous neural activity in the periphery. However, the relative performance of microneurography microelectrodes compared to cuff and

LIFE electrodes in measuring neural signals relevant to neuromodulation therapies is not well understood. To address this gap, we recorded cervical vagus nerve electrically evoked compound action potentials (ECAPs) and spontaneous activity in a human-scaled large animal model – the pig. Additionally, we recorded sensory evoked activity and both invasively and non-invasively evoked CAPs from the great auricular nerve. In aggregate, this study assesses the potential of microneurography electrodes to measure neural activity during neuromodulation therapies with statistically powered and pre-registered outcomes (https://osf.io/y9k6j).

Main contributions:

- Showed minimally invasive microneurography electrode could be used to measure neural signals relevant to neuromodulation therapies.
- 2. Side by side comparison showing comparative performance of microneurography electrode to established cuff and LIFE electrodes used in the field.
- 3. Demonstrated pre-registration of preclinical study design to improve scientific rigor.

Chapter 3: Device design to improve target engagement with transcutaneous stimulationbased therapies

The previous chapter develops minimally invasive methods that could be applied clinically to directly measure neural target engagement. Those measures will be useful in guiding adjustment to the stimulation electrode and protocol to improve neural target engagement. In Chapter 3, we investigate optimization of device design to improve neural target engagement. Specifically, we use computational modeling to investigate the Injectrode and its ability to

augment standard transcutaneous electrical stimulation. The Injectrode is a needle-delivered electrode that is injected onto neural structures under image guidance. Power is then transcutaneously delivered to the Injectrode using surface electrodes. We show that the Injectrode serves as a low-impedance conduit to guide current to the deep on-target nerve, reducing activation thresholds by an order of magnitude compared to using only surface stimulation electrodes.

Main contributions:

- Showed minimally invasive injectable Injectrode could improve target engagement of non-invasive electrical stimulation
- Presented computational model considering dielectric properties of the tissue, often neglected in the field
- 3. Validated model outputs with large animal cadaver measurements

Chapter 4: Apply target engagement framework to improve existing bioelectronic medicine therapy

Noninvasive electronic bone growth stimulators (EBGS) have been in clinical use for decades. However, systematic reviews show inconsistent and limited clinical efficacy. Further, noninvasive EBGS studies in small animals, where the stimulation electrode is closer to the fracture site, have shown promising efficacy, which has not translated to large animals or humans. We propose that this is due to the weaker electric fields reaching the fracture site when scaling from small animals to large animals and humans. To address this gap, we

measured the electric field strength reaching the bone during noninvasive EBGS therapy in human and sheep cadaver legs and in validated finite element method (FEM) models of human and sheep legs. To augment the electric field strength reaching the fracture site during noninvasive EBGS therapy, we introduced the Injectrode, an injectable electrode that spans the distance between the bone and subcutaneous tissue.

Main contributions:

- Showed that a miniscule fraction of the externally applied electric field (1,100 V/m)
 reaches the fracture site (21 V/m) during noninvasive EBGS.
- 2. Showed substantially weaker electric fields reached the fracture site during the later stages of healing and at increased bone depths.
- Laid the groundwork for a future *in vivo* sheep study to investigate the efficacy of Injectrode-augmented noninvasive EBGSs by increasing the electric field strength reaching the fracture site.

Chapter 5: Preliminary works to apply target engagement framework and additional physiology-relevant acute biomarkers to develop novel bioelectronic medicine therapy

Direct measurements of neural target engagement at the stimulation site are critical to inform electrode design and placement and is thoroughly explored in the three primary projects of this thesis. This final project presents preliminary work on using the target engagement framework along with therapy-relevant acute biomarkers to guide the development of a novel bioelectronic medicine therapy. The therapy under development is targeting the glymphatic

system, which has been shown to be compromised during Alzheimer's disease (Li et al., 2022).

Acute biomarkers based on magnetic resonance imaging (MRI) were used to inform the development of the therapy. This preliminary work forms the basis for future directions in my career.

Main contributions:

- Developed surgical technique to measure ECAPs from the trigeminal nerve during stimulation of the V3 branch of the trigeminal.
- 2. Showed V3 branch of trigeminal nerve can be engaged with minimal off-target muscle activation.
- Developed and implemented MRI techniques to assess cerebral hemodynamics and cerebrospinal fluid (CSF) flow in large animals.
- 4. Showed, for the first time in a large animal, that dobutamine increases CSF movement in the paravascular spaces (PVS) of large pial arteries.

References

- American Association of Neurological Surgeons. (2021). Vagus Nerve Stimulation. https://www.aans.org/Patients/Neurosurgical-Conditions-and-Treatments/Vagus-Nerve-Stimulation [accessed January 12, 2021].
- Aplin, F. P., and Fridman, G. Y. (2019). Implantable Direct Current Neural Modulation: Theory, Feasibility, and Efficacy. *Front. Neurosci.* 13, 379. doi: 10.3389/fnins.2019.00379.
- Aristovich, K., Donega, M., Fjordbakk, C., Tarotin, I., Chapman, C. A. R., Viscasillas, J., et al. (2021). Model-based geometrical optimisation and in vivo validation of a spatially selective multielectrode cuff array for vagus nerve neuromodulation. *Journal of Neuroscience Methods* 352, 109079. doi: 10.1016/j.jneumeth.2021.109079.

- Becq, G. J.-P. C., Barbier, E. L., and Achard, S. (2020). Brain networks of rats under anesthesia using resting-state fMRI: comparison with dead rats, random noise and generative models of networks. *J. Neural Eng.* 17, 045012. doi: 10.1088/1741-2552/ab9fec.
- Bermejo, P., López, M., Larraya, I., Chamorro, J., Cobo, J. L., Ordóñez, S., et al. (2017). Innervation of the Human Cavum Conchae and Auditory Canal: Anatomical Basis for Transcutaneous Auricular Nerve Stimulation. *BioMed Research International* 2017, 1–10. doi: 10.1155/2017/7830919.
- Botvinik-Nezer, R. Variability in the analysis of a single neuroimaging dataset by many teams. 26.
- Bucksot, J. E., Morales Castelan, K., Skipton, S. K., and Hays, S. A. (2020). Parametric characterization of the rat Hering-Breuer reflex evoked with implanted and non-invasive vagus nerve stimulation. *Experimental Neurology* 327, 113220. doi: 10.1016/j.expneurol.2020.113220.
- Burger, A. M., D'Agostini, M., Verkuil, B., and Van Diest, I. (2020). Moving beyond belief: A narrative review of potential biomarkers for transcutaneous vagus nerve stimulation. *Psychophysiology* 57. doi: 10.1111/psyp.13571.
- Burke, D., Howells, J., and Kiernan, M. C. (2017). Sensory and motor axons are different: implications for neurological disease. *Ann Clin Neurophysiol* 19, 3. doi: 10.14253/acn.2017.19.1.3.
- Carome, M. A. (2020). Implanted Spinal Cord Stimulators for Pain Relief. *Public Citizen*. doi: https://www.citizen.org/wp-content/uploads/2526_200610_Spinal-Cord-Stimulator-Report_FINAL.pdf?eType=EmailBlastContent&eld=765162c2-baeb-41db-a6ae-0694813ad96c
- De Ferrari, G. M., Stolen, C., Tuinenburg, A. E., Wright, D. J., Brugada, J., Butter, C., et al. (2017). Long-term vagal stimulation for heart failure: Eighteen month results from the NEural Cardiac TherApy for Heart Failure (NECTAR-HF) trial. *International Journal of Cardiology* 244, 229–234. doi: 10.1016/j.ijcard.2017.06.036.
- FDA. (1997). Design Control Guidance for Medical Device Manufacturers.
- Gabriel, S., Lau, R. W., and Gabriel, C. (1996). The dielectric properties of biological tissues: II. Measurements in the frequency range 10 Hz to 20 GHz. *Phys. Med. Biol.* 41, 2251–2269. doi: 10.1088/0031-9155/41/11/002.
- Gaines, J. L., Finn, K. E., Slopsema, J. P., Heyboer, L. A., and Polasek, K. H. (2018). A model of motor and sensory axon activation in the median nerve using surface electrical stimulation. *J Comput Neurosci* 45, 29–43. doi: 10.1007/s10827-018-0689-5.
- He, F., Lycke, R., Ganji, M., Xie, C., and Luan, L. (2020). Ultraflexible Neural Electrodes for Long-Lasting Intracortical Recording. *iScience* 23, 101387. doi: 10.1016/j.isci.2020.101387.
- Heusser, K., Tank, J., Brinkmann, J., Menne, J., Kaufeld, J., Linnenweber-Held, S., et al. (2016). Acute Response to Unilateral Unipolar Electrical Carotid Sinus Stimulation in Patients With Resistant Arterial Hypertension. *Hypertension* 67, 585–591. doi: 10.1161/HYPERTENSIONAHA.115.06486.

- Hines, M. L., and Carnevale, N. T. (1997). The NEURON Simulation Environment. *Neural Computation* 9, 1179–1209. doi: 10.1162/neco.1997.9.6.1179.
- Ilfeld, B. M., Plunkett, A., Vijjeswarapu, A. M., Hackworth, R., Dhanjal, S., Turan, A., et al. (2021). Percutaneous Peripheral Nerve Stimulation (Neuromodulation) for Postoperative Pain: A Randomized, Sham-controlled Pilot Study. *Anesthesiology*, 10.1097/ALN.000000000003776. doi: 10.1097/ALN.00000000000003776.
- Kaniusas, E., Kampusch, S., Tittgemeyer, M., Panetsos, F., Gines, R. F., Papa, M., et al. (2019). Current Directions in the Auricular Vagus Nerve Stimulation I A Physiological Perspective. *Front. Neurosci.* 13, 854. doi: 10.3389/fnins.2019.00854.
- Keute, M., Machetanz, K., Berelidze, L., Guggenberger, R., and Gharabaghi, A. (2021). Neuro-cardiac coupling predicts transcutaneous auricular Vagus Nerve Stimulation effects. *Brain Stimulation*, S1935861X21000024. doi: 10.1016/j.brs.2021.01.001.
- Kumar, K., and Bishop, S. (2009). Financial impact of spinal cord stimulation on the healthcare budget: a comparative analysis of costs in Canada and the United States: Clinical article. *SPI* 10, 564–573. doi: 10.3171/2009.2.SPINE0865.
- Li, L., Ding, G., Zhang, L., Davoodi-Bojd, E., Chopp, M., Li, Q., et al. (2022). Aging-Related Alterations of Glymphatic Transport in Rat: In vivo Magnetic Resonance Imaging and Kinetic Study. *Front. Aging Neurosci.* 14, 841798. doi: 10.3389/fnagi.2022.841798.
- Loeb, G. E. (2006). The BION devices: injectable interfaces with peripheral nerves and muscles. *Neurosurg. Focus* 20, 9.
- Manson, G. A., Calvert, J. S., Ling, J., Tychhon, B., Ali, A., and Sayenko, D. G. (2020). The relationship between maximum tolerance and motor activation during transcutaneous spinal stimulation is unaffected by the carrier frequency or vibration. *Physiol Rep* 8. doi: 10.14814/phy2.14397.
- Meffin, H., Tahayori, B., Grayden, D. B., and Burkitt, A. N. (2012). Modeling extracellular electrical stimulation: I. Derivation and interpretation of neurite equations. *J. Neural Eng.* 9, 065005. doi: 10.1088/1741-2560/9/6/065005.
- Musselman, E. D., Cariello, J. E., Grill, W. M., and Pelot, N. A. (2021). ASCENT (Automated Simulations to Characterize Electrical Nerve Thresholds): A pipeline for sample-specific computational modeling of electrical stimulation of peripheral nerves. *PLoS Comput Biol* 17, e1009285. doi: 10.1371/journal.pcbi.1009285.
- Napadow, V., Sclocco, R., and Henderson, L. A. (2019). Brainstem neuroimaging of nociception and pain circuitries: *PAIN Reports* 4, e745. doi: 10.1097/PR9.0000000000000745.
- Nicolai, E. N., Settell, M. L., Knudsen, B. E., McConico, A. L., Gosink, B. A., Trevathan, J. K., et al. (2020). Sources of off-target effects of vagus nerve stimulation using the helical clinical lead in domestic pigs. *J. Neural Eng.* 17, 046017. doi: 10.1088/1741-2552/ab9db8.

- Nonis, R., D'Ostilio, K., Schoenen, J., and Magis, D. (2017). Evidence of activation of vagal afferents by non-invasive vagus nerve stimulation: An electrophysiological study in healthy volunteers. *Cephalalgia* 37, 1285–1293. doi: 10.1177/0333102417717470.
- Plonsey, R., and Barr, R. C. (1995). Electric field stimulation of excitable tissue. *IEEE Trans. Biomed. Eng.* 42, 329–336. doi: 10.1109/10.376126.
- Rattay, F. (1999). The basic mechanism for the electrical stimulation of the nervous system. *Neuroscience* 89, 335–346. doi: 10.1016/S0306-4522(98)00330-3.
- Resnick, J. M., O'Brien, G. E., and Rubinstein, J. T. (2018). Simulated auditory nerve axon demyelination alters sensitivity and response timing to extracellular stimulation. *Hearing Research* 361, 121–137. doi: 10.1016/j.heares.2018.01.014.
- Trevathan, J. K., Baumgart, I. W., Nicolai, E. N., Gosink, B. A., Asp, A. J., Settell, M. L., et al. (2019). An Injectable Neural Stimulation Electrode Made from an In-Body Curing Polymer/Metal Composite. *Adv. Healthcare Mater.* 8, 1900892. doi: 10.1002/adhm.201900892.
- Udo, E. O., Zuithoff, N. P. A., van Hemel, N. M., de Cock, C. C., Hendriks, T., Doevendans, P. A., et al. (2012). Incidence and predictors of short- and long-term complications in pacemaker therapy: The FOLLOWPACE study. *Heart Rhythm* 9, 728–735. doi: 10.1016/j.hrthm.2011.12.014.
- Usami, K., Kawai, K., Sonoo, M., and Saito, N. (2013). Scalp-Recorded Evoked Potentials as a Marker for Afferent Nerve Impulse in Clinical Vagus Nerve Stimulation. *Brain Stimulation* 6, 615–623. doi: 10.1016/j.brs.2012.09.007.
- Verma, N., Graham, R. D., Mudge, J., Trevathan, J. K., Franke, M., Shoffstall, A. J., et al. (2021a). Augmented Transcutaneous Stimulation Using an Injectable Electrode: A Computational Study. *Front. Bioeng. Biotechnol.* 9, 796042. doi: 10.3389/fbioe.2021.796042.
- Verma, N., Mudge, J. D., Kasole, M., Chen, R. C., Blanz, S. L., Trevathan, J. K., et al. (2021b). Auricular Vagus Neuromodulation—A Systematic Review on Quality of Evidence and Clinical Effects. *Front. Neurosci.* 15, 664740. doi: 10.3389/fnins.2021.664740.
- Wagatsuma, A., Okuyama, T., Sun, C., Smith, L. M., Abe, K., and Tonegawa, S. (2018). Locus coeruleus input to hippocampal CA3 drives single-trial learning of a novel context. *Proc Natl Acad Sci USA* 115, E310–E316. doi: 10.1073/pnas.1714082115.
- Waxman, S.G. (Ed.), 1978. Physiology and pathobiology of axons. Raven Press, New York.
- Waxman, S. G. (1980). Determinants of conduction velocity in myelinated nerve fibers. *Muscle Nerve* 3, 141–150. doi: <u>10.1002/mus.880030207</u>.
- Wellmark. (2018). Vagus Nerve Stimulation (VNS) and Vagal Blocking Therapy. https://www.wellmark.com/Provider/MedpoliciesAndAuthorizations/MedicalPolicies/policies/

- <u>Vagus_Nerve_Stimulation.aspx?fbclid=IwAR0Bq8iogosvLVR7p3xBW7J5flziGxbyQk-2MnRRKADoQcJ0gJFotbOk_dM [accessed November 26, 2020].</u>
- Yap, J. Y. Y., Keatch, C., Lambert, E., Woods, W., Stoddart, P. R., and Kameneva, T. (2020). Critical Review of Transcutaneous Vagus Nerve Stimulation: Challenges for Translation to Clinical Practice. *Front. Neurosci.* 14, 284. doi: 10.3389/fnins.2020.00284.
- Ye, H., and Ng, J. (2018). Shielding effects of myelin sheath on axolemma depolarization under transverse electric field stimulation. *PeerJ* 6, e6020. doi: 10.7717/peerj.6020.
- Yoo, P. B., Lubock, N. B., Hincapie, J. G., Ruble, S. B., Hamann, J. J., and Grill, W. M. (2013). High-resolution measurement of electrically-evoked vagus nerve activity in the anesthetized dog. *J. Neural Eng.* 10, 026003. doi: 10.1088/1741-2560/10/2/026003.
- Zhu, K., Li, L., Wei, X., and Sui, X. (2017). A 3D Computational Model of Transcutaneous Electrical Nerve Stimulation for Estimating Aβ Tactile Nerve Fiber Excitability. *Front. Neurosci.* 11, 250. doi: 10.3389/fnins.2017.00250.

Chapter 2 Microneurography as a Minimally Invasive Method to Assess Target Engagement During Neuromodulation

This chapter was adapted from the following article under review in a peer-reviewed journal:

Verma, N., Knudsen, B., Gholston, A., Skubal, A., Blanz, S., Settell, M., et al. (2022).

Microneurography as a Minimally Invasive Method to Assess Target Engagement During

Neuromodulation. *Under review at Journal of Neural Engineering*. Pre-print doi:

10.1101/2022.08.19.504592.

Abstract

Objective. Peripheral neural signals recorded during neuromodulation therapies provide insights into local neural target engagement and serve as a sensitive biomarker of physiological effect. Although these applications make peripheral recordings important for furthering neuromodulation therapies, the invasive nature of conventional nerve cuffs and longitudinal intrafascicular electrodes (LIFEs) limit their clinical utility. Furthermore, cuff electrodes typically record clear asynchronous neural activity in small animal models but not in large animal models. Microneurography, a minimally invasive technique, is already used routinely in humans to record asynchronous neural activity in the periphery. However, the relative performance of microneurography microelectrodes compared to cuff and LIFE electrodes in measuring neural signals relevant to neuromodulation therapies is not well understood.

Approach. To address this gap, we recorded cervical vagus nerve (cVN) electrically evoked compound action potentials (ECAPs) and spontaneous activity in a human-scaled large animal model – the pig. Additionally, we recorded sensory evoked activity and both invasively and non-invasively evoked CAPs from the great auricular nerve (GAN). In aggregate, this study assesses the potential of microneurography electrodes to measure neural activity during neuromodulation therapies with statistically powered and pre-registered outcomes (https://osf.io/y9k6j).

Main results. The cuff recorded the largest ECAP signal (p<0.01) and had the lowest noise floor amongst the evaluated electrodes. Despite the lower signal to noise ratio, microneurography electrodes were able to detect the threshold for neural activation with similar sensitivity to cuff and LIFE electrodes once a dose-response curve was constructed.

Furthermore, the microneurography electrode was the only electrode to record distinct sensory evoked neural activity (p<0.01).

Significance. The results show that microneurography electrodes can measure neural signals relevant to neuromodulation therapies. Microneurography could further neuromodulation therapies by providing a real-time biomarker to guide electrode placement and stimulation parameter selection to optimize local neural fiber engagement and study mechanisms of action.

Introduction

Inconsistent local neural target engagement and poor isolation of on- and off-target neural substrates is critically limiting neuromodulation therapies (Heusser et al., 2016; De Ferrari et al., 2017; Verma et al., 2021a). Direct measurements of neural activity during the acute deployment of neuromodulation therapies could 1) guide electrode design and placement to chronically improve consistency of local target engagement and 2) prove critical for understanding on- and off-target neural substrates and therapeutic mechanisms of action (Verma et al., 2021a).

Although these applications make it pertinent to record neural activity from the peripheral nervous system acutely, the invasiveness of conventional cuff electrodes and longitudinal intrafascicular electrodes (LIFEs) limit their clinical utility. In contrast, clinical microneurography electrodes are minimally invasive, as they can be placed percutaneously into a nerve guided by ultrasound or palpation without a surgical window. Microneurography microelectrodes are often made of tungsten and have a smaller recording tip compared to cuff and LIFE electrodes. They are already used in humans to perform acute recordings for diagnostic and research purposes (Macefield, 2020), but have yet to be evaluated for informing neuromodulation therapies. The relative performance of microneurography electrodes, compared to conventional cuffs and LIFE electrodes, in measuring neural signals relevant to neuromodulation therapies is also not well understood.

To understand the relative performance of microneurography electrodes, compared to conventional cuff and LIFE electrodes, we performed a side-by-side comparison of recording electrodes in the peripheral nervous system of pigs, a large animal model (Fig. 2.1A). We

compared each electrode's ability to measure both synchronous electrically evoked compound action potentials (ECAPs) (Fig. 2.1B, top) and asynchronous activity that was either sensory evoked or spontaneously occurring (Fig. 2.1B, bottom). ECAPs represent the recruitment of neurons around the stimulation electrode and are a direct measurement of local on- and off-target neural engagement. Spontaneously occurring activity is a real-time and sensitive measure of changes induced by neurostimulation, sometimes even before physiological changes become evident (Gonzalez-Gonzalez et al., 2021; Chao et al., 2021). Growing interest in modulating spontaneously occurring neural activity outside the period of stimulation (e.g., burst stimulation for chronic pain therapy) will make spontaneously occurring activity a key biomarker in neuromodulation therapies.

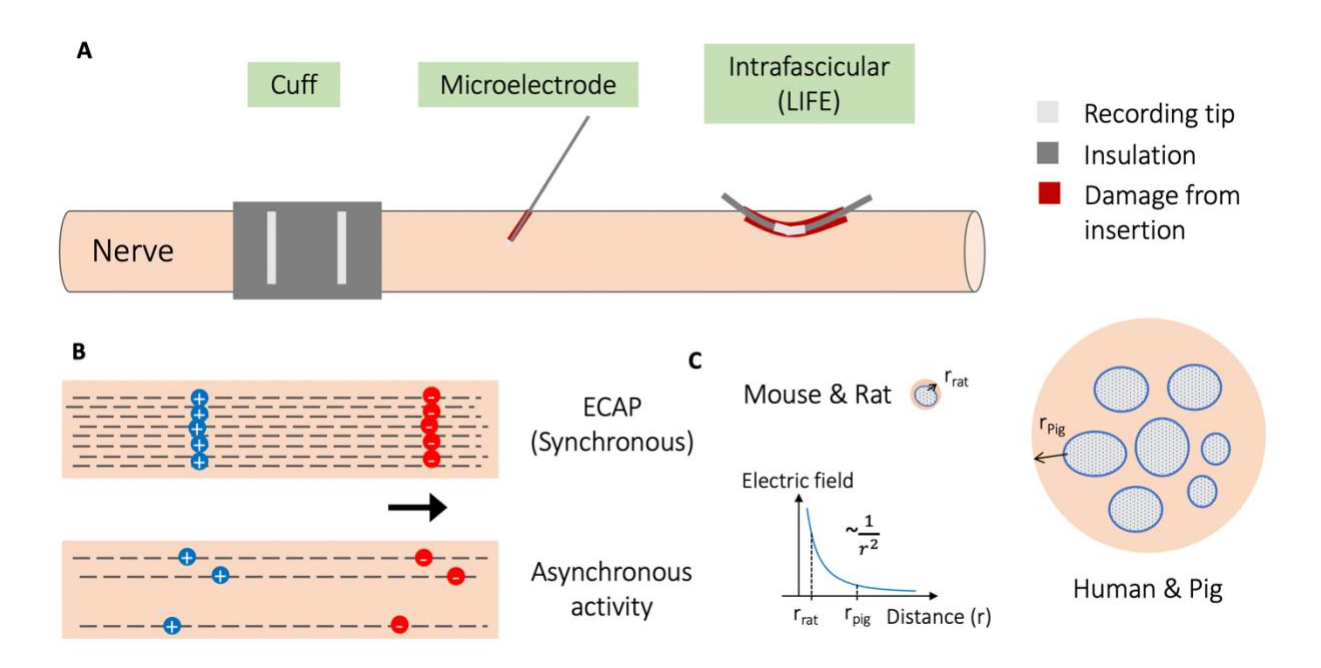


Figure 2.1: Illustration of three types of recording electrodes, synchronous versus asynchronous neural activity, and effect of electrode-fiber distance on recorded signals.

(A) Illustration showing the three different types of recording electrodes characterized for their performance in measuring neural signals from the peripheral nervous system. The longitudinal

- intrafascicular electrode (LIFE) has a larger area of exposed metal for recording than the microneurography microelectrode, and the LIFE causes more damage to tissue upon insertion, indicated by the red blood track.
- **(B)** Synchronous electrically evoked compound action potential (ECAP) vs. asynchronous neural activity illustrated by number of fibers activated and synchrony of neural activity. Both illustrate a neural signal as a moving dipole with a finite length. This dipole length increases with conduction velocity and fiber size.
- **(C)** Cartoon illustrating the relevance of scale in interpreting neural recording electrode performance. For example, in the cervical vagus nerve (cVN) for smaller mammals, there is 1) less distance between the neural fiber and the surface of the nerve, where a recording electrode is placed, and hence less falloff in electric field, and 2) there is a thinner layer of perineurium insulation (Pelot et al., 2020), and hence less falloff in electric field. Electric field falloff from the neural source, approximated as a monopole, is proportional to $\sim 1/r^2$, where r is the distance from the neural source to the recording electrode (Plonsey and Barr, 1995).

We performed the experiments in pigs, a human-scaled model, which is critical for the translatability of the findings (Koh et al., 2022). Studies in animal models with smaller peripheral nerves, such as rodents, have shown recordings of spontaneously occurring neural activity made with non-penetrating hook and cuff electrodes (Moncrief and Kaufman, 2006; Silverman et al., 2018; Stumpp et al., 2020). However, this might not be possible in human-scaled nerves (Koh et al., 2022). The cervical vagus nerves (cVNs) in mice and rats are 200-300 μ m in diameter with a single fascicle while the cVNs in humans and pigs are 2-3 mm in diameter with many fascicles (Settell et al., 2020; Pelot et al., 2020). The larger diameter of the nerve and thicker low electrical conductivity perineurium and epineurium increase the distance between the firing neuron and the recording electrode (electrode-fiber distance), thereby reducing the recorded signal amplitude (Yoo et al., 2013) (Fig. 2.1C). As an example, Yoo and colleagues (2013) reported that they had to de-sheath the epineurium of cVN in dogs, thereby reducing electrode-fiber distance, to clearly record C-fiber ECAP components. The larger electrode-fiber

distances of nerves in human-scaled models might make it challenging to record asynchronous neural activity with non-penetrating electrodes.

Here, we evaluated microneurography electrodes against cuff and LIFE electrodes in their ability to measure invasively and non-invasively evoked CAPs, sensory evoked neural activity, and spontaneously occurring activity in the peripheral nerves of swine, a large animal model representative of the human peripheral nervous system (Settell et al., 2020). The cVN, a major autonomic nerve of great interest as a neuromodulation therapy target (Johnson and Wilson, 2018), was used as the first model nerve. In addition, the great auricular nerve (GAN), a sensory nerve innervating the ear and implicated in auricular vagus nerve stimulation (aVNS) (Verma at el., 2021a), was used as the second model nerve to evaluate sensory evoked potential and non-invasively evoked CAP recordings. We examined the effects of reference electrode placement on neural signal fidelity and artifacts. We noted common non-neural artifacts in electrophysiology recordings, and we discuss appropriate controls to verify neural recording authenticity. Based on the findings, we summarize considerations and recommend minimally invasive microneurography as a technique that can be used acutely during the deployment of neuromodulation therapies to inform electrode placement, electrode design, and selection of stimulation parameters to optimize local neural target engagement. Understanding on- and off- target neural fibers engaged is a critical step in investigating therapeutic mechanisms of action and could deepen our understanding of both peripheral and central mechanisms of neuromodulation therapies.

Methods

In this study, we characterized the ability of three electrodes to measure neural activity in the peripheral nervous system. We characterized 1) cuff electrodes, 2) LIFE electrodes, an intrafascicular electrode used in pre-clinical studies (Yoshida and Stein, 1999; Nicolai et al., 2020), and 3) microneurography electrodes, a clinical microelectrode used routinely in humans (Macefield, 2021). The cVN, a major autonomic nerve innervating organs in the thorax and abdomen as well as muscles in the throat, and the great auricular nerve (GAN), a sensory nerve innervating the ear and periauricular region, were used as model nerves due to their relevance in existing peripheral neuromodulation therapies. The cVN is targeted during invasive vagus nerve stimulation (VNS) for epilepsy and depression (Johnson and Wilson, 2018) and the GAN is involved in non-invasive aVNS (Cakmak et al., 2017; Verma et al., 2021a).

Pre-registration

Pilot experiments (n=10) were conducted to refine the surgery and establish the study protocol. The study was then pre-registered (https://osf.io/y9k6i) with sequentially defined primary, secondary, and exploratory outcomes, statistical comparisons, analysis parameters, and sample size (n=6). The confirmatory experiments were conducted after pre-registration with no exclusion of subjects.

Recording and stimulation electrodes

Photographs of the recording electrodes are in Supplementary Material 1.

The microneurography electrodes were fabricated of tungsten with epoxylite insulation. They had an impedance of 0.8-1.2 M Ω at 1 kHz, shaft diameter of 250 μ m, and rounded tip diameter of ~5 μ m (part #UNA40GCT, FHC Inc., ME, USA).

The GAN recording cuffs were identical to the GAN stimulation cuffs and were fabricated in-house with two platinum wires 127 μ m (0.005") in diameter, separated by ~1 mm, glued (using a silicone-based glue) into a split silicone tube of 0.75 mm inner diameter with a total length of 3 mm (Fig. 2.2B).

The cVN recording cuff was fabricated of platinum and silicone with three cylindrical contacts 1 mm in width, 3 mm apart edge-to-edge, and 2 mm from the edge of the silicone. Each of the three cylindrical contacts was split into seven contacts (1 x 1 mm² size), 0.5 mm apart edge-to-edge, with all seven contacts electrically connected to improve mechanical flexibility. The cVN recording cuff had an inner diameter of 3 mm (Ardiem Medical Inc., PA, USA).

The cVN stimulation cuff was fabricated of platinum-iridium and silicone. It was a six-contact cuff with each contact 2 mm in diameter (Blanz et al., 2022). Contacts 2 and 5 were used as the bipolar pair for stimulation (Fig. 2.2A).

The LIFE electrodes were fabricated in-house of platinum-iridium wire, 102 μ m (0.004") diameter with insulation, 51 μ m (0.002") without insulation, and an exposed window length of ~2 mm (Nicolai et al., 2020; Blanz et al., 2022). A curved insertion needle was used to 'sew' the LIFE electrode into the nerve. The impedance of the LIFE electrodes was 1-10 k Ω at 1 kHz.

Acute swine experiments

We used n=6 (3M/3F) domestic swine, 50-60 kg, ~3 months old in the confirmatory experiments. All animal care and procedures were approved by the University of Wisconsin-Madison Institutional Animal Care and Use Committee (IACUC).

Anesthesia

An intramuscular injection of Telazol (6 mg/kg) and xylazine (2 mg/kg) was used to induce anesthesia. The animals were intubated and mechanically ventilated, and the surgical anesthetic plane was maintained with inhaled isoflurane (1-2%) and intravenous fentanyl (12-30 μ g/kg/hr), administered with lactated Ringer's solution (LRS), for analgesia.

Several hours into the experiment, an onset of tremors was observed in the animals. Pigs are known to be especially prone to tremor during anesthesia (Ringer et al., 2016). The tremors were observed despite confirmation of the surgical anesthetic plane by means of nasal septum pinch, jaw slackness, unresponsiveness to corneal reflex, and verification of other physiologic parameters such as temperature, blood glucose, and blood pH. The tremors persisted despite increased dosing of isoflurane and fentanyl. We found either intramuscular injection of Telazol (4-6 mg/kg) or intravenous ketamine (10 mg/kg/hr) eliminated the tremors. The effects of Telazol lasted for ~2 hours while ketamine effects on tremor washed in and out in ~15 minutes.

A muscle paralytic, vecuronium, was administered intravenously during cVN recordings to avoid EMG artifacts in the neural recordings from electrically evoked muscle movement (Yoo et al., 2013; Nicolai et al., 2020; Blanz et al., 2022) or ongoing tremors – without cardiac

blunting effects. We delivered vecuronium as a 0.1 mg/kg bolus over 1 minute followed by 1-1.5 mg/kg/hr constant rate infusion.

Physiological recordings and data analysis

We recorded heart rate from a pulse transducer (AD Instruments, Sydney, Australia) and EKG (AD Instruments, Sydney, Australia), blood pressure from a femoral artery catheter (Millar, Houston, TX, USA), temperature from a rectal probe (Physitemp, Clifton, NJ, USA), and SpO2 from a pulse oximeter (Nonin, Plymouth, MN, USA) applied on the tongue. The signals were recorded with a PowerLabs 8/35 (AD Instruments, Sydney, Australia). Stimulation timings were synced with the physiological recordings, using a TTL signal line from the stimulator to the PowerLabs, for further analysis of stimulation-evoked physiological changes.

Stimulation-evoked heart rate changes were calculated as the difference between the mean heart rate 1-3 s before stimulation and the maximum change in heart rate during stimulation (Blanz et al., 2022).

Cervical vagus nerve preparation and electrophysiology

ECAPs from invasive stimulation and spontaneous activity were measured from the cVN (Fig. 2.2A, C). With the subject in supine position, a midline approach was used to access the left carotid sheath. The carotid artery was mobilized and carefully retracted to minimize obstruction to blood flow. The cVN was exposed for a length of 9-12 cm and instrumented with a bipolar stimulation electrode caudal to the superior laryngeal branching off the nodose ganglion (Settell et al., 2020). Three LIFE electrodes, three microneurography electrodes, and a

cuff electrode with three recording contacts were instrumented on the nerve caudal to the stimulation electrode. A separation of >4 cm was kept between the stimulation electrode and the closest recording electrode. The order of the recording electrodes (cuff, LIFE, and microneurography) were randomized, without replacement, per subject to reduce bias arising from distance between the stimulation and recording electrode, which is known to affect the ECAP (Parker et al., 2020). A reference electrode, similar in design to the recording LIFE electrodes, inserted in superficial fat was used to reference the cuff and LIFE electrodes while a microneurography electrode inserted in superficial fat was used to reference the microneurography electrodes. Superficial fat was selected for its similarity in composition to the fatty tissue of nerves, thereby best matching the mechanical and electrochemical environment of the recording electrodes (Ludwig et al., 2008). An off-nerve reference also allowed for post-hoc virtual re-referencing between all recording electrode pairs in each reference group. The reference electrode site was selected at a distance approximately equidistant from the stimulation electrode to the recording electrodes to best match, and 'subtract', the representation of the stimulation artifact. In addition, several recordings were collected with on-nerve 'bipolar' and 'tripolar' referencing to compare the three referencing methods.

A Tucker-Davis Technologies (TDT) electrophysiology system was used for stimulation and recording. The analog front-end and digitizer were on the battery-powered Subject Interface Module (SIM, TDT Inc., FL, USA). Data were digitized at 25 kHz with a 28-bit Sigma-Delta analog to digital converter (ADC) (45%/11.25 kHz low-pass anti-aliasing filter) without amplification. High impedance (microneurography electrodes) and low impedance (LIFEs and

cuff) were recorded into two separate recording cards with an active (ZC32, TDT Inc., FL, USA) and passive (S-Box, TDT Inc., FL, USA) head stage, respectively. Stimulation was delivered in bipolar mode with two floating current sources.

ECAPs were recorded during delivery of 750 symmetric biphasic stimulation pulses with a 200 μ s pulse width at 25 Hz. These stimulation pulse trains, 30 seconds each, with amplitudes between 0 and 10 mA were presented in a randomized order with 60 seconds between subsequent trains. Spontaneous activity recordings were made before electrical stimulation was delivered.

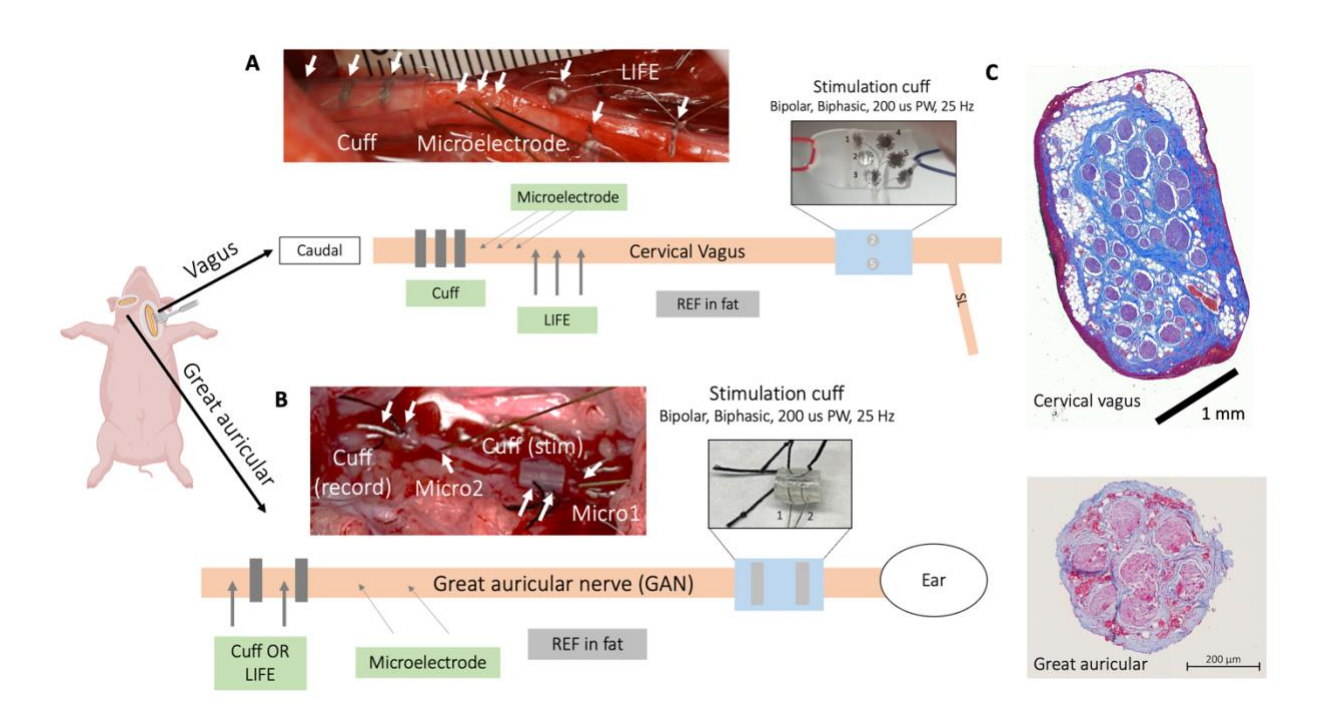


Figure 2.2: Experimental setup and surgical preparation.

(A) Cervical vagus nerve (cVN) instrumented with bipolar stimulation cuff (contact 2 and 5) and, at least 4 cm caudal, three replicates each of three different recording electrodes: three longitudinal intrafascicular electrodes (LIFEs), three microneurography electrodes, and a three-contact cuff. All recording electrodes were referenced to fat (off-nerve local tissue reference).

(B) Great auricular nerve (GAN) instrumented with bipolar stimulation cuff and two replicates each of two different recording electrodes: two microneurography electrodes, and either a

two-contact cuff or two LIFE electrodes (alternated by subject). All recording electrodes were referenced to fat (off-nerve local tissue reference).

(C) Histology of the cVN and the GAN under the stimulation cuff illustrating the relative difference in size and fascicular organization. The cVN is approximately 5x larger than the GAN and contains a greater number of fascicles. GAN histology from additional subjects is shown in Supplementary Material 2.

Great auricular nerve preparation and electrophysiology

The GAN innervates the auricle and is implicated as an off-target nerve in some aVNS therapies. The GAN is also purported to be part of the therapeutic effect pathway for auricular stimulation-based therapies to treat Parkinson's disease (Cakmak et al., 2017) and pain (Kaniusas et al., 2019). Therefore, measuring neural activity directly from the GAN could be used to assess both on- and off-target neural engagement during auricular stimulation therapies to inform stimulation electrode location and parameters. The GAN (Fig. 2.2C, bottom) is morphologically distinct from the cVN (Fig. 2.2C, top), which is larger and contains a greater number of fascicles – influencing the spread of electric fields generated by firing neurons and consequent neural recordings. Characterizing recording electrode performance in both these nerves improves the applicability of our findings. The GAN was also selected because it was more surgically accessible than the primary on-target nerve for aVNS therapies, the auricular branch of the vagus (ABVN), and potentially amenable to percutaneous microneurography under ultrasound, which may be problematic for the ABVN due to its anatomical course.

ECAPs from invasive stimulation and non-invasive stimulation and sensory evoked neural activity in response to sensory stroking were measured from the GAN. The GAN was accessed by the approach described in the following paragraph, which to our knowledge, offers

the first surgical description of a procedure specifically accessing and identifying the GAN in swine.

We created a larger than necessary surgical pocket, as our approach was to find the pathway of the sensory GAN and identify the association it had with the auricular motor components of the facial nerve (facial auricular nerves). In the surgical pocket (photograph in Supplementary Material 3), we located and traced either of two landmarks to locate the GAN. We followed the facial auricular nerves dorsally in search of the GAN traveling in association. Alternatively, we followed the lateral auricular vein ventrally, to where the nerves (sensory and motor) and vein course together. The skin and subcutaneous fat were incised from the medial posterior margin of the ramus. A small notch was palpated at this point and indicated the approximate level of the stylomastoid foramen. Here, the facial nerve exited and divided into its various branches (Getty, 1975) (more details on facial nerve anatomy are provided in the Supplementary Material 4). The incision continued dorsally following a line posterior to the temporomandibular articulation and up to the medial base of the ear just inferior to the medial crus of the helix. This allowed us to follow the lateral vein through the base of the ear as a landmark for finding the sensory input for the exterior skin of the auricle (the GAN). This incision exposed the superficial musculoaponeurotic system (SMAS), a superficial fibromuscular layer that integrated with the superficial temporal fascia dorsally and platysma ventrally. The SMAS layer was divided along the posterior margin of the ramus and posterior margin of the temporomandibular articulation/zygomatic process to expose the subfascial level adipose tissue. This underlying adipose tissue along the posterior margin of the temporomandibular articulation was the location where we were able to isolate the GAN (more details on GAN

anatomy are provided in the Supplementary Material 5) and branches of the facial nerve (Getty, 1975; Lefkowitz et al., 2013; Yang et al., 2015; Sharma et al., 2017). Running in conjunction with these nerves were the lateral/caudal auricular artery and vein, matching the description of Duisit et al. (2017).

To determine which of the exposed nerves were motor or sensory in origin we electrically stimulated each of the nerve branches to evoke a motor response – indicative of a motor pathway (200 μ s pulse width symmetric biphasic pulses, 0.02-1 mA, 1 Hz). This is similar to the procedure used to localize a microneurography electrode into the desired fascicle (Macefield, 2021). When the sensory branch of the posterior auricular nerve was identified by no motor response, it was instrumented with a stimulation cuff (Fig. 2.2B) and recording electrodes (two microneurography electrodes and a two-contact cuff or two LIFE electrodes). The total length of the exposed GAN was ~5 cm. The identification of the sensory GAN was verified by recording sensory evoked responses during stroking of the skin at the base of the auricle. Reference electrodes were placed similarly as described above in the cVN preparation and the same electrophysiology recording setup was used.

Sensory evoked neural activity was recorded by lightly stroking the region, close to the base of the ear, innervated by the GAN ('on-target') with a toothbrush (Fig. 2.7A, green). Each trial lasted 90 seconds: 30 seconds of no stroking, 30 seconds of 'on-target' stroking, and 30 seconds of 'off-target' stroking (closer to tip of ear, Fig. 2.7A red) where the GAN is not expected to innervate. The 'off-target' stroking served as a control to ensure that the light stroking applied to the ear did not transfer to the recording electrodes as motion artifacts.

Transcutaneous electrical nerve stimulation (TENS) electrodes cut to 2 x 2 cm² in size were applied to the 'on-target' region and at the base of the ear through which the main trunk of the GAN courses. Non-invasively evoked CAPs were recorded during application of stimulation waveforms with parameters identical to those used to stimulate the cVN.

Invasively evoked CAPs were recorded during application of stimulation waveforms with parameters identical to those used to stimulate the cVN, except with stimulation amplitudes between 0 and 3-10 mA (determined based on each subject's motor response threshold).

Sensory evoked recordings were performed first, followed by invasively evoked CAP recordings, and lastly non-invasively evoked CAP recordings.

Electrophysiology data analysis

A custom-built and publicly available Python package, PyeCAP (https://github.com/ludwig-lab/pyeCAP), was used for offline analysis of electrophysiology and physiology data.

Filtering

ECAP electrophysiology data was filtered with a high pass 1st order Butterworth filter with a corner frequency at 100 Hz and a low pass Gaussian filter with a corner frequency at 3 kHz. The low pass gaussian filter negates the possibility of introducing filter 'ringing' artifact, which may be introduced by a Butterworth filter that has an 'overshoot' to an impulse response (Bovik and Acton, 2005). The stimulation artifact approximates an impulse, and an overshoot following a stimulation artifact – caused by inappropriate filter selection – could be mistaken for an ECAP. An additional 60 Hz band stop finite impulse response (FIR) filter constructed with a Hamming

window was used on the sensory evoked and spontaneously occurring neural activity electrophysiology data. All filtering was performed on the time series data in both the forward and backward direction to eliminate group delays caused by filtering (Scipy, 2022).

Non-functional recording electrodes

As per the pre-registration (https://osf.io/y9k6i), non-functional recording electrodes were identified by a high noise floor, high 60 Hz noise, or a flat ECAP dose-response behavior in comparison to other contacts of the same electrode type. Electrodes deemed non-functional by these criteria were noted (Supplementary Material 6) and removed from analysis.

Spike detection

Spike detection for spontaneously occurring activity and sensory evoked recordings was done using a voltage thresholding method. The threshold voltage was set per electrode at six times the standard deviation (SD) from time=1-6 seconds of the time series trace recorded by that electrode added to the mean calculated from the same time window (time=1-6 seconds) to account for baseline offsets. No sensory evoked activity was initiated during time=1-6 seconds, although spontaneously occurring activity was not accounted for. This may have inflated the threshold for spike detection slightly.

Detecting authentic ECAPs

ECAPs were plotted by averaging (point-by-point median) the stimulation evoked response across 750 pulses in a particular stimulation train. Averaging multiple stimulation evoked

responses reduces uncorrelated noise by a factor of \sqrt{n} , where n is the number of traces averaged (Metcalfe et al., 2018). The averaged ECAP traces were split into time windows by neural fiber type according to the distances between recording and stimulation electrode and published conduction velocities (Erlanger and Gasser, 1937; Manzano et al., 2008).

ECAP authenticity was confirmed by several methods. First, signal propagation delay across recording electrodes (Gaunt et al., 2009) was verified to be in the expected nerve fiber conduction velocity range (Erlanger and Gasser, 1937; Manzano et al., 2008). An artifact (e.g., EMG, motion) could occur at a similar time point as an ECAP but would not show up with a signal propagation delay across spatially separated recording electrodes (Gaunt et al., 2009). Second, a muscle paralytic, vecuronium, was used to abate EMG artifact, which could be mistaken for an ECAP, in the cVN ECAP recordings. Third, transection of the nerve caudal and cranial to the recording electrodes and subsequent recordings were used to confirm the disappearance of the ECAP signal, which is no longer able to propagate along the transected neural pathway from stimulation to recording electrode (Nicolai et al., 2020).

Detrending neural signal from stimulation artifact

A small subset of ECAP recordings were contaminated with stimulation artifacts; the neural signal of interest was riding 'on top' of a stimulation artifact decay. The ECAP signal had to be separated from the baseline offset of the stimulation artifact to quantify its RMS magnitude accurately. Neural signal was detrended from stimulation artifact using an exponential based 'fit and subtract' approach (Harding, 1991; Chakravarthy et al., 2022; Drebitz et al., 2020). A simple method was used as only ECAPs from Subject 6 microneurography electrode recordings

during the cVN dose-response experiment were contaminated by stimulation artifacts. A single exponential decay of the form:

$$y = Ae^{-b(x+c)}$$

with free parameters A, b, and c were used for a least-squares fit of ECAP data points between 2.2-2.4 ms and 5.8-6.0 ms. This time range excluded ECAPs from fiber types of interest so that only data points from the decay of the stimulation artifact, and not the neural signal, were fitted. A representative fit is shown in Supplementary Material 7. The fit was subtracted from the raw ECAP trace to produce a detrended ECAP trace, which was used for further quantification of ECAP magnitude.

Quantifying ECAP magnitude

 $A\beta$ - and B-fiber ECAPs were quantified to investigate their magnitude as recorded by the microneurography, cuff, and LIFE electrodes. $A\beta$ -fibers were selected as a measure of faster-conducting myelinated fibers and B-fibers were selected as a measure of slower-conducting myelinated fibers.

Time windows corresponding to A β - and B-fiber ECAPs were calculated for each electrode based on distance from the closest edge of that recording electrode to the center of the stimulation electrode and published values of conduction velocity: 30-70 m/s for A β -fibers and 3-15 m/s for B-fibers (Erlanger and Gasser, 1937; Manzano et al., 2008). A tolerance up to 20% was allowed on the conduction velocity if the ECAP was truncated by the initially calculated time window. Then, the fiber-type time windows were further narrowed to be of equal duration across recording electrodes – without removing any portion of the ECAP signal

of interest. Equalizing the analysis time window was critical to avoid bias that would arise with increasing distance of the recording electrode from the stimulation electrode. This increased distance translates to a longer computed time window over which the ECAP magnitude calculation is performed – possibly leading to a skewed ECAP magnitude measurement due to the inclusion of additional noise into the measurement. Root mean square (RMS) was calculated on the narrowed fixed-duration window as a measure of ECAP magnitude. RMS was selected over alternative methods (e.g., integral or area under the curve) as it indicates the equivalent steady state energy value of an oscillating signal and represents the noise floor of the recording electrode (Rawlins, 2000). The noise floor is a useful measure, even when no ECAP signal is present at subthreshold stimulation currents. Further, the measure of peak-to-peak voltage is more susceptible to noise and amplitude is more susceptible both to noise and baseline offsets (Mitra et al., 2018).

Cohort-based statistics

For ECAP magnitudes and spike counts, the mean value was taken for the replicates of each type of electrode per subject. These mean ECAP magnitudes and spike counts measured on each electrode were normalized to the mean value measured on the cuff contacts and microneurography electrodes, respectively. We performed this normalization for each subject to facilitate comparison across subjects. Log10 was applied to the normalized values to redistribute to normality (Chen, 1994). The Shapiro-Wilk test was used to verify the normality assumption of the student t-tests. One-sided t-tests were used to test the four primary outcomes:

- 1) The Aeta-fiber ECAP magnitude recorded on the cuff is greater than that recorded on the microneurography electrode
- 2) The A β -fiber ECAP magnitude recorded on the cuff is greater than that recorded on the LIFE electrode
- The sensory evoked spike count from the microneurography electrode recording is greater than that from the LIFE electrode recording
- 4) The sensory evoked spike count from the microneurography electrode recording is greater than that from the cuff electrode recording.

Following the pre-registration, $\alpha=0.05$ was used in a sequential analysis and propagated down the four primary outcomes listed above and then the secondary outcomes until a null result was hit. Confidence intervals (CI) were calculated using the 95% bounds of the t-distribution. Mean is denoted as μ and standard error is denoted as (SE).

ECAP Dose-response curves

Dose-response plots for cVN ECAPs were generated by plotting ECAP magnitude against stimulation current. The $A\beta$ -fiber dose-response curve for each recording electrode was normalized to the ECAP magnitude at 5 mA of stimulation current for that recording electrode, as it was the highest common stimulation current applied across all subjects. Logistic growth functions (sigmoidal shape) were used to fit the dose-response curves following the method of least squares (Castoro et al., 2011). After subtracting the initial offset from the fitted logistic growth functions, EC10 points were calculated for each of the three electrodes for all n=6 subjects. The EC10 point is the stimulation current at 10% of the saturation ECAP magnitude

and is a measure of the stimulation level at which the ECAP is first detectable. A repeated measures ANOVA was used to detect if the EC10 point, and hence sensitivity to ECAP detection, was different across the three recording electrodes.

Results

In this study, we characterized the ability of three commonly used electrodes (i.e., recording cuff, microneurography electrode, and LIFE electrode) to record neural activity from the peripheral nervous system. We investigated both synchronous electrically evoked CAPs and asynchronous spontaneously occurring and sensory evoked neural activity. These results provide the first side-by-side comparison in a human-scaled, large animal model of the recording magnitude, sensitivity, and noise floors of the three recording electrodes in the peripheral nervous system. Further, we compare several referencing strategies and comment on their appropriate use. Lastly, we highlight several artifacts in our recordings that initially appeared to be neural signals but were later classified as artifacts as informed by appropriate control tests. We intend the results of this study to guide the development of neural recording techniques that can be used in the development and deployment of neuromodulation therapies. Direct measures of on- and off-target neural recruitment around the stimulation electrode could advance understanding of therapeutic mechanisms and guide adjustments to electrode design and placement so as to optimize stimulation specificity. Neural activity recordings may also enable continuous closed-loop titration and operation of neuromodulation therapies.

Data associated with this study were shared as part of the Stimulating Peripheral Activity to Relieve Conditions (SPARC) project and are available through the SPARC Data Portal (https://doi.org/10.26275/vm1h-k4kq) under a CC-BY-4.0 license.

Measuring ECAPs during invasive stimulation

Poor local neural target engagement is critically limiting in some neuromodulation therapies (Heusser et al., 2016; De Ferrari et al., 2017). In these therapies, our ability to directly measure neural activation around the stimulation site and understand fiber types activated could be essential for guiding electrode placement to create more efficacious therapies and better understand those therapies' mechanisms of action (Verma et al., 2021a). Measurements of local neural target engagement could be done either acutely in the doctor's office during device placement and therapy titration or chronically by the implanted therapy device. For the acute scenario, a microneurography electrode – already used in clinical research – could be percutaneously introduced to the nerves of interest (Ottaviani et al., 2020). For the chronic scenario, when the treatment is already an invasive device, an additional recording cuff could be implanted on the nerve of interest during the surgery to place the stimulation electrode.

Here, we compared the abilities of these two clinically viable electrodes (microneurography electrode and invasive recording cuff) to record ECAPs in the cVN of the domestic swine. Alongside these two devices, we also compared a commonly used pre-clinical electrode, the LIFE electrode (Yoshida and Stein, 1999; Nicolai et al., 2020). Each electrode's recordings were compared to characterize their ECAP recording magnitudes, sensitivities, and noise floors.

Magnitude of ECAP recorded

We characterized the magnitude of the ECAP recorded on each electrode. In general, a larger magnitude signal requires less demanding electronic design to record than a smaller magnitude signal. A representative trace from each electrode is shown in Fig. 2.3A. ECAPs were recorded concurrently on all three types of recording electrodes (3 contacts each, for a total of 9 recording contacts per subject) at 1.5 mA of stimulation. The stimulation current was selected because it was close to the saturation point of $A\beta$ fibers and provided a stable point of comparison across subjects (n=6).

Fig. 2.3B shows the magnitude of ECAP recorded by each of the recording electrodes during cervical vagus nerve stimulation (VNS). The magnitude of the ECAP recorded by the cuff was significantly larger than the magnitude of the ECAP recorded by the microneurography electrode (normalized to cuff $\mu=0.208$ SE=0.088 $\mu V_{rms}/\mu V_{rms}$) (p=0.002, $\alpha=0.05$, CI=[0.052,0.343]). Similarly, the magnitude of the ECAP recorded by the cuff was significantly larger than the magnitude of the ECAP recorded by the LIFE electrode (normalized to cuff $\mu=0.335$ SE=0.077 $\mu V_{rms}/\mu V_{rms}$) (p=0.003, $\alpha=0.05$, CI=[0.147,0.541]).

Sensitivity of recording electrodes

The sensitivity of a recording electrode is critical when the electrode is used to detect the threshold of neural activation, which is a plausible use case in closed-loop control designed to avoid activation of an off-target nerve. The sensitivities of the three recording electrodes were quantified by constructing dose-response curves using 16-18 stimulation current doses between 0-10 mA. The dose-response curves were fitted with logistic growth functions, and the

stimulation current at 10% of the maximal ECAP magnitude (EC10) was extracted as a measure of when an ECAP is first detectable (Fig. 2.3C).

Fig. 2.3D summarizes the EC10 point of each recording electrode across all subjects (n=6). The microneurography electrode had the lowest mean EC10 stimulation current, suggesting it was the most sensitive recording electrode. However, variability was large and the individual data plots showed that the microneurography electrodes were not consistently the most sensitive electrode in every subject. A repeated measures ANOVA test concluded non-significant differences in EC10 currents across recording electrode type ($p=0.26, \alpha=0.05$). Repeating the analysis using the EC50 point confirmed a similar trend also with non-significant difference findings (data not shown). Due to this non-significant result, type II error was entirely lost at this secondary outcome and further conclusions in the sequential analysis (see preregistration) are exploratory, indicated by ($\alpha=0$) where applicable. Note that the study was powered for the primary outcomes (as reported in the pre-registration) and not this secondary outcome on sensitivity.

Since sensitivity was evaluated by fitting to multiple points in the dose-response curve, it was a measure of the electrodes 'denoised' performance and not reflective of the electrodes' ability to detect the threshold of neural activation from a single level of stimulation current, which depends more critically on the signal-to-noise ratio (SNR).

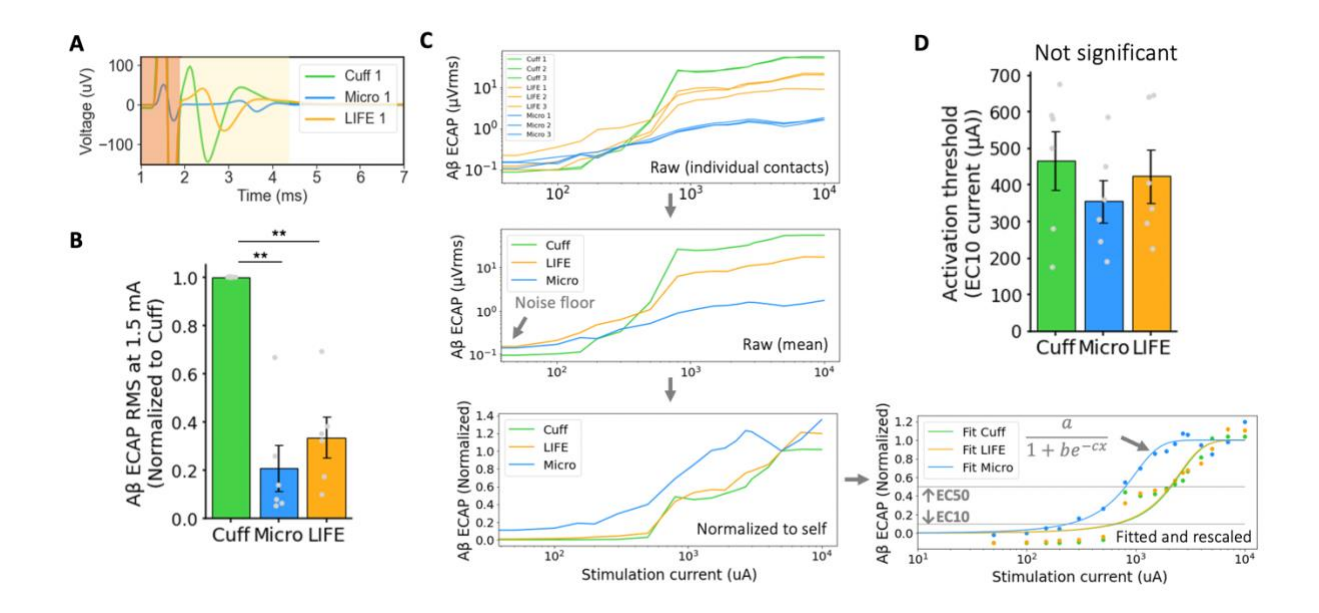


Figure 2.3: Comparison of electrodes in recording ECAPs from larger myelinated fibers.

- (A) Representative ECAP traces from concurrent cuff, microneurography electrode, and longitudinal intrafascicular electrode (LIFE) recordings at 1.5 mA of stimulation on the cervical vagus nerve (cVN). Contact one of three was selected for each electrode type. Stimulation artifact shaded in orange and $A\beta$ -fiber ECAP shaded in yellow.
- **(B)** Bar plot summarizing magnitude of A β -fiber ECAP recorded with three different electrodes on cVN showing significantly larger recording on cuff compared to both the microneurography electrode and LIFE electrode.
- (C) (top left) Dose-response curves of A β -fiber ECAPs for three replicates each of the three recording electrode types characterized. From top left, in an anti-clockwise direction, shows the steps of fitting dose-response curves with logistic growth functions: 1) averaging of replicate contacts, 2) normalization to ECAP amplitude at 5 mA of stimulation, and 3) fitting to logistic growth functions and rescaling y-range to be from zero to one.
- **(D)** Bar plot summarizing sensitivity of the three recording electrodes across subjects. Sensitivity was measured as EC10 stimulation currents extracted from the dose-response curve logistic growth function fits in **(C)**.

Noise floor of recording electrodes

The electrode's practical performance in detecting the threshold of neural activation from a single stimulation pulse is determined by the ECAP magnitude and sensitivity of the recording electrode, along with the noise floor of the electrode. The noise floor of each electrode was characterized by calculating the RMS signal across 5 seconds of time series (un-averaged)

electrophysiology data both before (Fig. 2.4A) and after (Fig. 2.4B) filtering. The noise floor of ECAP traces (Fig. 2.4C) was characterized by reporting the RMS signal in the A β window range at 0 mA of stimulation (no stimulation delivered).

Fig. 2.4 shows the noise floor of all three recording electrodes before and after filtering in time series and after filtering in averaged (n=750) ECAP traces. As expected, the noise floor is higher in the time series and lower in the averaged ECAP traces (2.53 μV_{rms} vs. 0.11 μV_{rms} taking the recording cuff as an example). In the time series electrophysiology data, the noise is higher before filtering than after (15.85 μV_{rms} vs. 2.53 μV_{rms} taking the recording cuff as an example), largely due to the contribution of low frequency noise (Supplementary Material 8). The microneurography electrode has the highest noise floor across all three electrodes (0.26 μV_{rms} for the microneurography electrode vs. 0.11 μV_{rms} for the cuff and LIFE, taking the filtered ECAP traces as an example). In subject 5 and 6, an active head stage was used on the microneurography electrode, which pre-amplified the signal at the electrode, theoretically reducing SNR loss due to noise pick up on the wire from the electrode to the main amplifier. However, in using the active head stage, additional electronic noise was introduced by the preamplifier and is observed in the two higher noise data points in Fig. 2.4B (mean of 3.51 μV_{rms} for subjects 1-4 vs. 8.77 μV_{rms} for subjects 5-6, taking the filtered time series as an example). We summarize and compare the sources of noise (i.e., environmental, biological, electrochemical, and electronics) between the recording electrodes in the Discussion section.

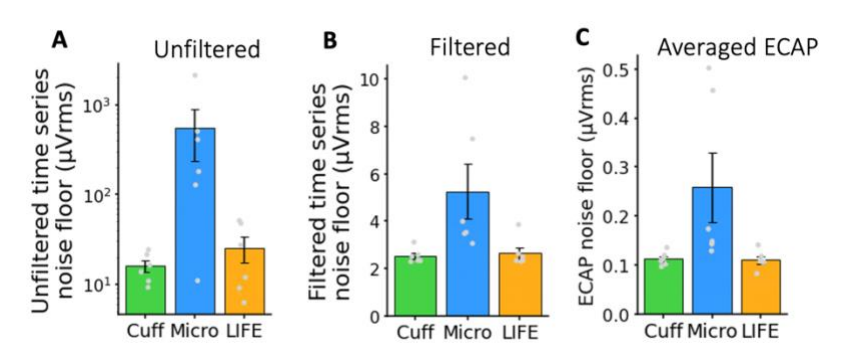


Figure 2.4: Nose floor of recording electrodes.

Noise measurements in electrophysiology recordings showing largest noise levels on the microneurography electrode. Note the different y-axis scales in the three plots as the noise level after filtering and averaging is reduced by orders of magnitude.

- (A) Unfiltered time series electrophysiology.
- **(B)** Filtered time series electrophysiology.
- **(C)** Filtered averaged ECAPs (median of n=750).

B-fiber recordings on recording electrodes

Smaller diameter myelinated fibers are hypothesized to be responsible for the therapeutic effects of several neuromodulation therapies. For example, B-fibers are putatively responsible for the therapeutic effects in the heart failure application of VNS (Sabbah et al., 2011). B-fibers are more challenging to record from due to the smaller fiber size and signal magnitude (Yoo et al., 2013; Nicolai et al., 2020). We compared the three recording electrodes in their ability to record B-fiber ECAPs from the cVN. Vecuronium was administered at a sufficient dose in subjects 4-6 to blunt muscle activity and prevent EMG artifact from contaminating the neural recordings. However, due to a protocol restriction, insufficient vecuronium was administered in subjects 1-3 to fully prevent EMG artifact from contaminating the neural recordings. B-fibers were differentiated from EMG artifact by verifying signal propagation delay across the replicate contacts of each electrode type (Fig. 2.5A, inset). It was not possible to conclude that we were quantifying only B-fibers because of the overlap of B-fibers and A δ -fibers in the conduction

velocity ranges (Erlanger and Gasser, 1937; Manzano et al., 2008). However, the purpose of this analysis was only to contrast slower-conducting myelinated fibers (B/A δ) with the previous, faster-conducting myelinated fibers (A β). Analyzing results from two distinct fiber types allowed us to investigate any differences in ECAP magnitude across the recording electrodes by fiber type and hence widen applicability of the results.

B-fiber ECAPs were most consistently recorded on the cuff, only evident in certain subjects with the LIFE electrode, and not evident with the microneurography electrode. Fig. 2.5A shows B-fiber ECAPs confirmed by signal propagation delay across two cuff contacts. Similar plots to Fig. 5A for the other electrodes show authentic B-fiber ECAPs recorded on the LIFE electrode but not the microneurography electrode (Supplementary Material 9). Fig. 2.5B and 2.5C show dose-response curves for B-fiber ECAPs and stimulation-evoked bradycardia, respectively. B-fibers are putatively responsible for decreases in heart rate during VNS (Qing et al., 2018). The bradycardia dose-response curve best tracks the cuff B-fiber recordings up to ~2 mA. After that, afferent pathways may be recruited counteracting the efferent B-fiber mediated effects (Ardell et al., 2017). The cuff B-fiber ECAP recordings correlate best with stimulation-evoked bradycardia in this subject (R_cuff = 0.70 and R_LIFE = 0.39). Data from remaining subjects are shown in Supplementary Material 10.

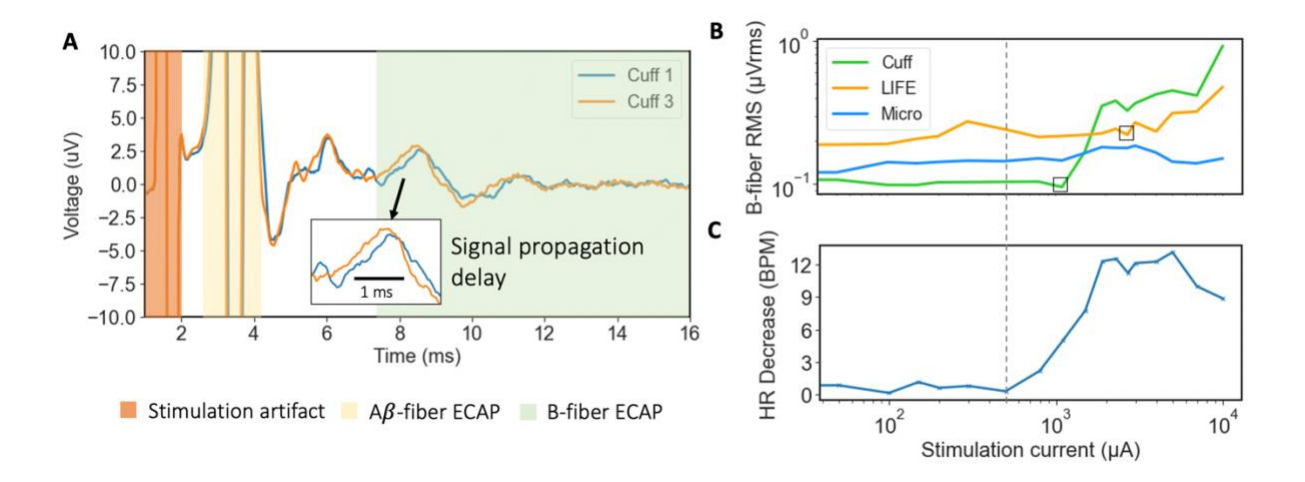


Figure 2.5: Comparison of electrodes in recording ECAPs from smaller myelinated fibers and correlation to evoked bradycardia.

- (A) Authenticity of B-fiber recordings was confirmed by signal propagation delay across recording electrodes in the range of 3-15 m/s (Erlanger and Gasser, 1937; Manzano et al., 2008). An artifact (e.g., EMG, motion) could occur in a similar time window but would not show up with a signal propagation delay across spatially separated recording electrodes. Stimulation artifact shaded in orange, $A\beta$ -fiber ECAP shaded in yellow, and B-fiber ECAP shaded in green. Stimulation was delivered at 10 mA. A similar plot is shown for the LIFE and microneurography electrodes in Supplementary Material 9.
- **(B)** B-fiber dose-response curves for all three recording electrodes on a single subject showing the largest ECAP magnitude recorded with the cuff electrode. The cuff electrode also recorded ECAPs at the lowest stimulation current. The ECAP detection threshold for each electrode is boxed; a clear threshold was not apparent on the microneurography electrode. The dash line from **(C)** indicates the bradycardia onset threshold.
- **(C)** Evoked heart rate decrease (bradycardia) dose-response curve in the same subject as **(B)**. The bradycardia stimulation current threshold is lower than the B-fiber ECAP detection thresholds in **(B)**.

Reference electrode on nerve versus in surrounding non-neural tissue

Judicious choice of reference electrode placement can optimize neural signal fidelity and minimize artifacts (Sabetian et al., 2017). Neural recordings can be referenced to a location on the active nerve itself or in local non-neural tissue. Conventionally, cuff electrodes have been referenced on the nerve (e.g., bipolar or tripolar), while in microneurography, the reference is placed in local non-neural tissue (Macefield, 2021). We conducted ECAP recordings with

different referencing strategies and systematically compared 'on-nerve' references with 'local tissue' references.

Fig. 2.6A shows that local tissue referenced recordings have a much larger stimulation artifact than on-nerve referenced recordings, but also a ~2.5x larger peak-to-peak ECAP magnitude. The smaller magnitude ECAP recorded with on-nerve references may be explained by 'subtraction' of neural signal between the recording and reference electrode due to the 2-3 cm wavelength of the A β -fibers that appears common to both electrodes (Andreasen and Struijk, 2002). The ECAP can be visualized as a moving electric dipole with the negative depolarizing charge leading the positive repolarizing charge (Fig. 2.1B). The distance between the poles is the 'wavelength' of the ECAP and positively relates to fiber diameter. For smaller fibers, with wavelengths less than the distance between the recording and reference contacts on the nerve, this subtraction effect should not be evident. Thus, on-nerve references may be superior to local tissue references when recording smaller diameter fibers, as ECAP magnitude may be preserved while common mode artifact is reduced.

Tripolar versus bipolar on-nerve referencing strategies with recording cuff

An on-nerve reference close to the active recording electrode can efficiently reduce common-mode artifacts external to the electrodes, such as spillover electric fields from muscle activity and stimulation artifact (Sabetian et al., 2017). Cuff recording electrodes lend themselves to on-nerve reference strategies and are typically employed in a bipolar or tripolar configuration. Past studies have shown several key differences between tripolar (contact 1 and 3 tied together to reference, contact 2 used for recording) and bipolar referenced cuff recordings (Sabetian et al.,

2017). Namely, tripolar referencing reduced the representation of common mode artifacts (Sabetian et al., 2017), which is pertinent because these artifacts can appear at similar time points as neural fiber signals (Nicolai et al., 2020). However, bipolar cuffs, compared to tripolar cuffs, can detect neural signal propagation direction (afferent vs. efferent). Meanwhile, the magnitude of neural signal recorded by the bipolar vs. tripolar cuff depends on the geometry of the cuff. In particular, the ECAP magnitude recorded depends on the electrode length (EL) and electrode edge length (EEL) of the insulation, which are further explored in computational work by Sabetian and colleagues (2017).

We collected both tripolar and bipolar referenced recordings using the same cuff. Fig. 2.6A shows representative bipolar and tripolar traces at 2.3 mA of stimulation. The stimulation artifact magnitude is smaller with the tripolar compared to the bipolar reference. The peak-to-peak ECAP magnitude is also smaller with the tripolar reference by a factor of ~2.2x compared to the bipolar reference. Data from other subjects are shown in Supplementary Material 10 and support the conclusions reported here. Our experimental results support the computational results reported by Sabetian and colleagues (2017), which predicted a ~1.4x larger peak-to-peak neural signal on the bipolar compared to the tripolar referenced recordings (EL = 9 mm and EEL = 2 mm).

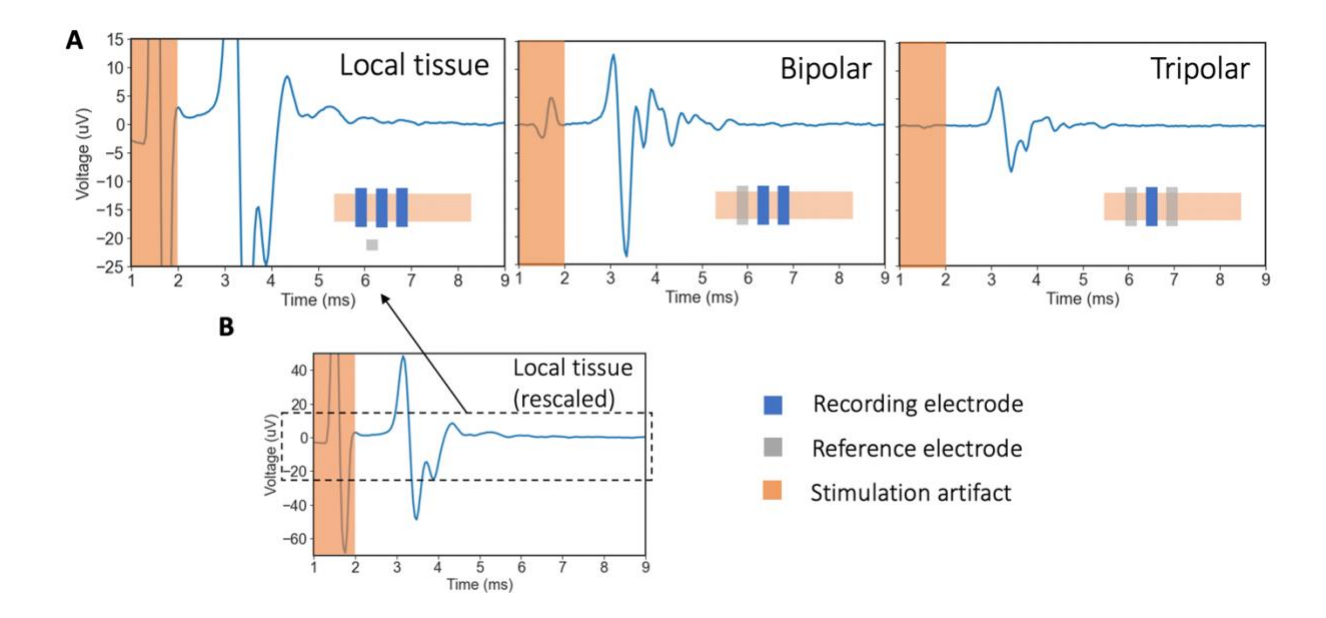


Figure 2.6: Effect of referencing strategy on stimulation artifact and ECAP.

(A) Representative data showing ECAP traces with three different referencing strategies at 2.3 mA of stimulation: (left) reference in 'local tissue', (center) bipolar 'on-nerve' reference, and (right) tripolar on-nerve reference. Orange highlights overlap the stimulation artifact, an example of common mode noise, which is substantially reduced in the on-nerve referencing strategies. The A β -fiber ECAP (~3-4 ms) is also smaller in the on-nerve referencing strategies. In the illustration of the recording setup in each plot, recording electrodes are in blue and reference electrodes are in gray.

(B) Zoomed out plot of local tissue referenced recording from **(A)** to show larger y-axis range.

Measuring asynchronous neural activity

Changes in spontaneously occurring neural activity could be a sensitive and real-time marker for neuromodulation therapies (Gonzalez-Gonzalez et al., 2021; Chao et al., 2021). Measuring spontaneous activity may be especially important in cases when there is an afferent-efferent pathway with one or more synaptic connections, which introduces variable conduction latency and desynchronizes the timing of the neural signal, thereby preventing a clear ECAP from appearing in the later efferent pathway. Instead, changes in spontaneously occurring neural activity of the later efferent pathways can be a sensitive measure of therapy effect and can be used for therapy titration. Recording spontaneous activity may also be important for non-

traditional waveforms such as burst, pink noise, high frequency block, or direct current (DC) block wherein the timing of initiation of an action potential may be variable or moot, and the intended effect is to change spontaneous activity in between stimulus trains. Consequently, we compared the three recording electrodes in their ability to measure sensory evoked neural activity, an asynchronous neural signal, from the great auricular nerve (GAN), which is implicated as an on- or off-target nerve in various auricular stimulation-based therapies.

Fig. 2.7B shows representative data of sensory evoked neural activity recordings from a cuff electrode, microneurography electrode, and LIFE electrode during a 30 second quiescent period, 30 seconds of on-target stroking at a region of the auricle innervated by the GAN, and 30 seconds of off-target stroking at a region of the auricle not innervated by the GAN (Fig. 2.7A). The representative recording from the cuff electrode showed spike-like activity throughout the 90 second recording period. The shape of the spike (Fig. 2.7C, bottom panel) and the synchronization of the timing with the ventilator indicated that the spike activity on the cuff electrode was due to motion artifacts from the ventilator. Transection of the GAN was also attempted as a control to further verify the authenticity of the neural recordings. However, due to the webbed nature of the nerve at the insertion point to the ear, we were unable to completely transect it in every subject to eliminate the sensory evoked neural activity.

The bar plot in Fig. 2.7D summarizes the spike count on each recording electrode (normalized to the microneurography electrode in that subject) during on-target sensory stroking of the region of the auricle innervated by the GAN. The microneurography electrode recording spike count was significantly larger than the cuff recording spike count (normalized to microneurography $\mu = 4.38 \times 10^{-3}$ $SE = 2.43 \times 10^{-3}$) (p = 0.01, $\alpha = 0.05$, CI = 0.05)

 $[5.22 \times 10^{-5}, 6.34 \times 10^{-2}]$). Similarly, the microneurography electrode recording spike count was significantly larger than the LIFE electrode recording spike count (normalized to microneurography $\mu=1.95 \times 10^{-2}$ $SE=2.7 \times 10^{-3}$) ($p=0.001, \alpha=0.05, CI=[9.38 \times 10^{-3}, 3.76 \times 10^{-2}]$).

Spontaneous activity recordings collected from the cVN did not show authentic neural spikes with any of the recording electrodes (Supplementary Material 11). Signals that initially appeared neural were likely motion artifacts as they persisted more than 20 minutes after the nerve was double transected cranial and caudal to the recording electrodes. Further, the artifacts were more pronounced in subjects 1-3, where the subjects experienced more tremor compared to subjects 4-6.

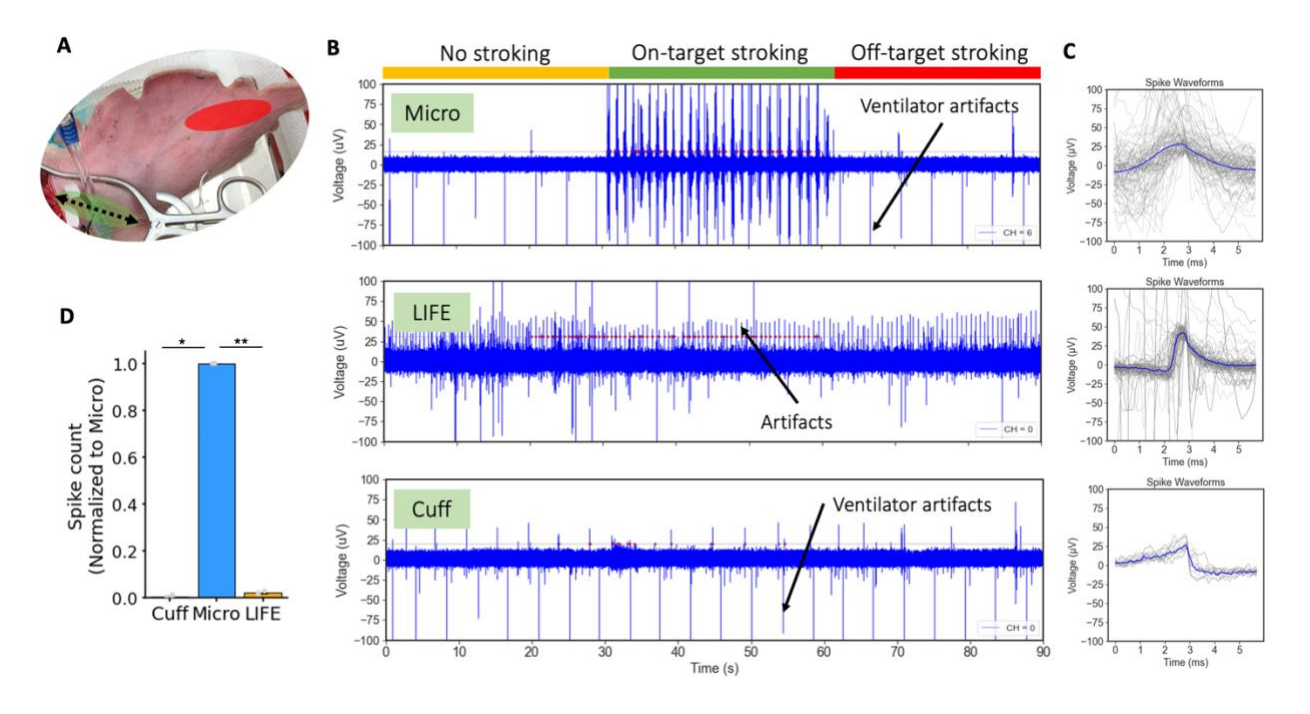


Figure 2.7: Comparison of electrodes in recording asynchronous sensory evoked neural activity.

(A) Using a toothbrush to gently stroke the ear at off-target (red, not innervated by GAN) and on-target (green, innervated by GAN) areas corresponding to green and red color coding in (B).

- (B) Representative electrophysiology recordings: first 30 seconds with no stroking, middle 30 seconds with on-target stroking, and last 30 seconds with off-target stroking to control for motion artifacts from stroking. Only the microneurography electrode showed a robust response specific to on-target stroking. LIFE and cuff recordings were selected to illustrate artifacts, which appeared neural, but were not authenticated by appropriate controls. The gray line in each plot is the spike detection voltage threshold and the red dots indicate detected 'spikes'.

 (C) Spike shapes for electrophysiology recordings in (B) indicating multi-unit hash recordings on the microneurography electrode, tremor or cardiac motion artifact on the LIFE electrode, and ventilator artifact on the cuff electrode.
- **(D)** Bar plot summarizing spike count recorded by the three electrodes across all subjects showing the microneurography electrode records significantly more spikes than both the cuff and LIFE electrodes.

Artifacts in electrophysiology recordings

We applied several controls to differentiate artifacts from bona-fide neural signals. These included: administration of a muscle paralytic, nerve transections, verifying signal propagation delay across recording contacts, concurrent monitoring of heart rate and respiration to investigate synced 'neural' activity, inspection of waveform shapes, and controls for induced motion. With these controls, we classified several signals that initially appeared neural as non-neural artifacts. Specifically, in time series (non-averaged) recordings we identified artifacts due to respiration, cardiac, and tremor effects.

Firstly, respiration related artifacts are captured in Fig. 2.7B (cuff recording) occurring at a rate of once every ~4s (15 times/minute) in sync with the respiration rate set on the ventilator. The artifact was still present after nerve transections and had a unique non-natural spike shape (Fig. 2.7C, bottom panel versus sensory evoked activity in top panel). The ventilator-induced artifacts likely occurred due to motion of the animal with respiration.

Secondly, tremor-related effects are observed in Fig. 2.7B (LIFE recording). Subject tremor is described in the Methods. These motion related artifacts from tremors disappeared with the

administration of a muscle paralytic, vecuronium, or the anesthetics Telazol or Ketamine, all of which stopped the tremors. Lastly, cardiac related artifacts were recorded (shown in Supplementary Material 8), which were removed with high pass filtering at 100 Hz. Cardiac artifacts can be directly from electrocardiogram (EKG) electrical activity or from cardioballistic effects due to the beating motion of arteries adjacent to the nerve (Ulrich et al., 2016), which causes motion in the nerve and the recording electrode. The cardioballistic effect was visible to us in several instances and was synced with heart rate. Direct EKG may be a more likely source of the artifact if the recording and reference electrode pair are across the heart or generally separated by a larger distance. The susceptibility of all three recording electrodes to motion induced artifacts suggests that one needs to be careful in interpreting spontaneous neural activity recordings in response to physiological events that also create motion, such as respiration, cardiac activity, etc.

Discussion

In the Discussion, we first summarize the strengths and weaknesses of different recording electrodes and discuss suitable electrode type and referencing strategy for each application.

Second, we outline potential mechanisms of neural recording to explain the results. Third, we discuss challenges in recording spontaneously occurring activity and TENS evoked CAPs. Fourth, we discuss sources of noise in electrophysiology recordings. Finally, we discuss correlation of ECAP magnitudes recorded on the three electrodes with evoked cardiac responses.

Electrode choice by application

In the context of neuromodulation therapies, ECAPs can be used as a real-time and precise measure of neural target engagement around the stimulation electrode (Verma et al., 2021a). Several neuromodulation therapies are critically limited by off-target nerve activation (Heusser et al., 2016; De Ferrari et al., 2017), which may be addressed by electrode design and stimulation parameters. Electrode design and stimulation waveforms are often translated directly from animal models and not adjusted for human use due to lack of real-time measures to guide development. We believe ECAPs represent a readily available method to guide development and deployment of neuromodulation therapies to improve on-target neural engagement and consequently therapeutic efficacy. Table 2.1 summarizes the performance and utility of the different recording electrodes based on the outcomes of the experiments performed in this study.

Table 2.1: Recording electrode choice by application

	Large	Small	Asynchronous	Chronic	Minimally	Noise
	diameter	diameter	neural	recording	invasive	floor
	fiber ECAPs	fiber ECAPs	activity	interface	introduction	
Microneurography						
Recording cuff						
LIFE electrode						

^{*}Green indicates good performance while orange indicates poor performance

Use of microneurography electrodes to develop and deploy minimally invasive neuromodulation therapies

Our data showed that recordings made using microneurography electrodes consistently measured A β -fiber ECAPs. In fact, once full ECAP dose-response curves were constructed and fitted to overcome the SNR limitations of the microneurography electrodes, they showed the highest sensitivity in detecting an ECAP amongst the three recording electrodes tested. We also showed that recordings made using microneurography electrodes most consistently measured sensory evoked neural activity compared to recordings made using cuff and LIFE electrodes.

The microneurography electrode tested is already used in humans to record muscle sympathetic nerve activity (MSNA) from the common peroneal nerve (Macefield, 2021) and median nerve (Macefield, 2021) and, most recently, to record neural activity from the cVN (Ottaviani et al., 2020). Similar to this existing human use, a microneurography electrode may be inserted percutaneously during clinical trials and at the deployment of neuromodulation therapies to map sensory innervation (Meier et al., 2018) and inform non-invasive stimulation electrode placement. The temporarily inserted microelectrode can also measure stimulation evoked on- and off-target neural activation, and that data can be used in real-time to adjust stimulation electrode position, design, and stimulation parameters (Verma et al., 2021a).

To aid in the translation of the microneurography technique to routine clinical use, the technique needs to be easy to perform and deployable within minutes. Currently, the technique requires a skilled microneurography practitioner, and even then, it can be time consuming for that practitioner to target specific fascicles in a nerve. To overcome these obstacles, automation, such as insertion based on force or electrical impedance

(Kodandaramaiah et al., 2012; Park et al., 2018), can be used to guide the microneurography electrode into the nerve and specific fascicle, where necessary. The epineurium and perineurium have vastly different mechanical properties and may be ideal for differentiating between fascicles (Koppaka et al., 2022).

Use of cuff electrodes to provide high-fidelity chronic recordings

Our data showed that the cuff electrode recorded ECAPs with the highest SNR. The cuff was also the only electrode to consistently record smaller diameter myelinated fiber (e.g., B-fiber) ECAPs. An implanted recording cuff would be a suitable option in applications where a chronic recording interface is necessary and smaller fiber types are of interest.

The high SNR of the cuff ECAP recordings will be advantageous in closed-loop strategies that rely on detecting first activation of a particular fiber type, and where time for averaging is limited. A potential application could be a waveform block strategy attempting to block larger diameter fibers while activating smaller diameter fibers. In this application, sensitive and real-time monitoring of the large diameter fiber activity will be required to ensure that the nerve block is sustained. If any large diameter fiber activity is detected, the stimulation parameters must be quickly adjusted to restore the nerve block. The recording cuff provides the highest SNR ECAP recording from a single stimulation pulse, without the time delay of averaging, required by such applications.

Referencing strategy

The results show that referencing strategies (i.e., on-nerve bipolar vs. on-nerve tripolar vs. local non-neural tissue) have a profound effect on recorded ECAP and artifact magnitude (Fig. 2.6). On-nerve references reject common mode noise more effectively but also abate the recorded ECAP magnitude. The microneurography technique lends itself to the local tissue reference (Macefield, 2021), resulting in larger magnitude ECAPs recorded, which compensates for the lower ECAP magnitudes otherwise observed with the microneurography electrode. To minimize common mode noise, the microneurography electrode should be inserted approximately equidistant from the stimulation site as the recording electrode and in fat. The reference electrode tip should also be of similar material and design to the recording electrode to match the representation of common mode artifact (Ludwig et al., 2008). The cuff electrode lends itself to on-nerve referencing strategies, which reduces the magnitude of the ECAPs recorded (Fig. 2.6A), due to 'subtraction' of the neural signal when it appears common on both the recording and on-nerve reference electrode. See Results section for a discussion on how the 'subtraction' effect is less prominent for smaller fiber types (with shorter wavelengths) and with larger spacing between the cuff recording and reference contacts. We observed that the cuff otherwise recorded the largest magnitude ECAPs, thereby balancing out this 'subtraction' effect due to on-nerve referencing. The on-nerve reference strategies performed better at rejecting common mode artifacts, which is critical in out-of-clinic ambulatory settings where a chronically implanted cuff would likely be required regardless. Therefore, we conclude that local tissue reference, which is conveniently implemented in microneurography recordings, and on-nerve

reference, which is conveniently implemented in cuff recordings, are appropriate for use as such.

Mechanisms of neural recording

Surprisingly, although recordings made with the microneurography electrode showed the most distinct sensory evoked neural activity (Fig. 2.7B), they measured A β -fiber ECAPs with the smallest magnitude (Fig. 2.3A-B). In contrast, the recordings made with the cuff did not show distinctive sensory evoked neural activity but measured ECAPs with the largest magnitude. The sensitivity of the penetrating microneurography electrode may be explained by its proximity to the firing neural source. The larger ECAP magnitude on the recording cuff may be explained by the cuff more linearly summing the electric potentials from all neurons firing within it (Humphrey and Schmidt, 1990). On the other hand, the microneurography electrode sums up potentials with a greater weight from neurons firing adjacent to the recording tip and a substantially reduced weight from neurons at a distance from the recording tip (Buzsáki, 2004; Khodagholy et al., 2015). In this manner, the microneurography electrode records a large signal from an adjacent neural source and a small signal from a further neural source, while the cuff records and sums moderate signals from throughout the nerve it is applied on.

Recording spontaneous neural activity

None of the recordings from the cVN showed clear and repeatable spontaneously occurring neural activity (Supplementary Material 11). This contrasted with the clear recordings of sensory evoked activity from the GAN recorded by the microneurography electrode. This also

contrasted with past microneurography work, which showed spontaneous activity recordings from the cVN of humans (Ottaviani et al., 2020). Compared to the human recordings, which were done percutaneously, we had an open surgical preparation. This may have led to additional trauma during electrode insertion with less mechanical stability provided by surrounding tissue. Further, the largest spontaneous signals from the cVN are expected to come from $A\beta$ muscle afferents under muscle tone. The manipulation of these muscles and the application of the muscle paralytic, vecuronium, in our experiments may have substantially reduced neural signaling from these muscles compared to clinical recordings in awake subjects. Similarly, the sensory evoked neural activity on the GAN is expected from $A\beta$ fibers, which are a large fiber type and produce larger extracellular signals than the smaller B and C fibers, which may be the only source of spontaneous activity remaining on the cVN under the mentioned surgical and anesthetic conditions.

Given our results, it is surprising that experiments in rodents have shown recordings of spontaneous activity from the cVN with simple hook electrodes (similar to cuff but without insulation) (Silverman et al., 2018; Stumpp et al., 2020). The difference in nerve size and perineurium thickness between rodents and pigs or humans may explain these results (Koh et al., 2022). As illustrated in Fig. 2.1C, the neurons in a rodent are much closer to the recording cuff than in a pig or human. The shorter electrode-fiber distances in rodents results in a stronger extracellular signal at the point of the recording cuff and larger amplitude neural activity recordings (Koh et al., 2022).

While clear sensory evoked neural activity was not evident on the macroelectrode (cuff and LIFE electrode) recordings on the GAN, it is possible that the neural signals were masked by the low SNR of the recordings. Metcalfe and colleagues (2018) have shown that velocity selective addition of neural signals from multiple spatially separated channels, can be used to improve the SNR and detect spontaneous neural activity in macroelectrode recordings of human-scaled peripheral nerves. Such strategies may be considered if the conduction velocity of the fiber of interest is known and computational resources to implement the algorithms are not limited by the intended clinical application. The absence of spontaneous activity in recordings collected using macroelectrodes compared to microelectrodes is also seen in the central nervous system and in humans (Winestone et al., 2012).

Measuring ECAPs during non-invasive stimulation

Numerous non-invasive stimulation devices have hit the market in recent years. Several claim to stimulate nerves deep below the surface of the skin without activating superficial off-target nerves (Nonis et al., 2017; Verma et al., 2021b). Microneurography-based studies (Ottaviani et al., 2020) that attempt to record non-invasive ECAPs from the intended on-target nerve and expected off-target nerves during delivery of the non-invasive stimulation could clarify the actual nerves responsible for effect and side effect in an already efficacious therapy. Then, in future deployment of the therapy, the same microneurography techniques can be used to customize electrode position to account for inter-subject variability in anatomy. Customizing electrode position to the individual's anatomy will ensure that the same on-target nerve is recruited in each patient – possibly increasing responder rates. Direct and real-time measures

of local neural target engagement are critical, as surrogate or indirect measures can be confounded by muscle activity (Feucht and Ward, 2021), poor temporal resolution, and other factors (Verma et al., 2021a).

We used TENS electrodes (2 x 2 cm²) to stimulate 1) the region of the ear innervated by the GAN and 2) the base of the ear through which the trunk of the GAN courses. Using up to 10 mA of stimulation current, we did not detect ECAPs with any of the three recording electrodes (data not shown). While this current density was comparable to the lower end of current densities used in aVNS clinical trials (Verma et al., 2021a), and should have been sufficient for perception, it may have been insufficient to create enough synchronous recruitment of neurons to record clear ECAPs. The larger surface area of the TENS electrodes translates to temporally synchronous activation of fibers but at spatially distinct locations across the span of the TENS electrode. As the neural signals propagate, they remain asynchronous and do not form a clear large magnitude ECAP at the recording electrode. Janko and Trontelj (1980) reported on microneurography recordings from the median, radial, and ulnar nerve during non-invasive stimulation of the finger. They used a smaller surface area stimulation electrode, which would have lent to more synchronized recruitment of neurons and a clearer ECAP. These findings may have implications towards stimulation electrode design for non-invasive neuromodulation therapies – especially if the mechanism of action is reliant on synchronous or coordinated recruitment of neurons.

Sources of noise in electrophysiology recordings

Fig. 2.4 summarizes the noise floor of each recording electrode before and after filtering and with averaging for ECAP presentation. Several key sources of noise in neural recordings are listed here in order from the external environment, the *in vivo* environment, the electrode, and finally the electronics:

- External noise capacitively and/or inductively coupled, conducted, or radiated (in the case of higher frequency electromagnetic field), into the recording, including mains 50/60 Hz noise (Yasar, 2021).
- Biological noise consisting of background neural and other electrical activity in the body (Yang et al., 2009).
- Noise due to motion of the electrode relative to tissue (Simakov and Webster, 2010).
- Thermal noise, generated by thermal motion of charge carriers and dependent on electrode impedance (Yang et al., 2009).
- Electrochemical noise reflecting corrosion on the metal electrode and interaction of charged ions with the solution (Obot et al., 2019).
- Electronic noise in the recording equipment including flicker noise, thermal noise, digitization noise, etc. (Molecular Devices, 2006).

We found that electronic noise dominated in the 0.1-3 kHz filtered time series relevant to peripheral ECAP and spiking activity. We measured the electronic noise of the TDT SIM head stage to be $1.95~\mu V_{rms}$. The measurement was made by shorting the input to reference while the setup was in a Faraday's cage (to reduce pick up of external noise). The recorded time

series trace was then filtered, and RMS noise was calculated as it was for *in vivo* recordings (Fig. 2.4). Our measurement of the input referred noise floor was verified by the TDT SIM head stage datasheet values after adjustment for the appropriate bandwidth (TDT, 2022). *In vivo* measurements of noise from the recording cuff filtered time series trace was 2.53 μV_{rms} on average (Fig. 2.4B), which suggests that ~77% of RMS noise is from the recording equipment electronics front end and digitization. This noise is highly uncorrelated: averaging over 750 pulses, to construct ECAP trace presentations, reduces noise on the recording cuff to 0.11 μV_{rms} compared to a theoretical reduction by $\sqrt{750}$ to 0.09 μV_{rms} if the noise was entirely uncorrelated (Metcalfe et al., 2018). Since most of the noise in this recording frequency band is coming from electronics front-end and digitization, application specific front-end and analog to digital converter (ADC) architecture and design can be exploited to reduce noise. Further tightening the recording bandwidth will also reduce RMS noise. Note that electronic noise may not be the dominant noise source in other recording frequency bands, such as local field potential (LFP) recordings.

For the higher impedance microneurography electrode, we see additional noise contributions for a total noise floor of 3.51 μV_{rms} in the microneurography electrode filtered time series trace versus 2.53 μV_{rms} in the lower impedance recording cuff trace. This difference of 0.98 μV_{rms} is likely attributable to increased electrode thermal noise, increased biological noise from background neural activity, and/or increased external noise pickup due to the higher impedance of the microneurography electrode. Note that although the impedance of the microneurography electrode was specified as 1 MOhm at 1 kHz, 1 MOhm would not be used as the resistance (R) to calculate thermal noise in the equation (Molecular Devices, 2006):

$$V_{rms} = \sqrt{4k_B T R \Delta f}$$

This is because the 1 MOhm includes both real and imaginary impedances. Only real impedance (resistance, R) is used to calculate thermal noise. An ideal capacitor, despite having an imaginary impedance, does not generate thermal noise (Lundberg, 2002). The true thermal noise of the electrode is the noise calculated with the real impedance and filtered by the equivalent circuit capacitance of the electrode (Lundberg, 2002). The true thermal noise of the microneurography electrode would be much lower than the 6.9 μV_{rms} calculated incorrectly using R=1 MOhm. This is supported by the experimental results where there was only an additional 0.98 μV_{rms} noise on the much higher impedance (~1 MOhm) microneurography electrode compared to the lower impedance (~1 kOhm) cuff electrode.

Our results also showed that all three recording electrodes were susceptible to motion induced artifacts from respiration, cardiac activity (e.g., motion of vessels adjacent to recording electrode), tremoring, etc. In this animal study, we were able to use controls such as nerve transections and administration of a muscle paralytic, vecuronium, to differentiate neural signals from motion artifacts. However, use of these controls may not be feasible in human studies. Therefore, practitioners need to be careful in interpreting clinical microneurography recordings that are expected to correlate to physiological events that also create motion, such as respiration, cardiac activity, etc. Inspection of neural spike shapes and control recordings from close-by, non-neural tissue can help differentiate between neural signals and artifacts. High pass filtering to remove lower frequency artifacts and placement of the reference electrode close to the recording electrode to lower common mode artifacts can further reduce motion induced artifacts in the recordings.

Correlation of VNS cardiac response and B-fiber ECAPs

A previous publication from our group showed strong tracking between A α -fiber ECAP recordings and EMG activity recorded from the laryngeal muscles, implicated as off-target activation in clinical VNS for epilepsy (Blanz et al., 2022). However, the publication did not investigate tracking between stimulation-evoked bradycardia and B-fiber ECAPs, which are putatively responsible for bradycardia during VNS (Qing et al., 2018).

In Fig. 2.5, we show correlation between stimulation-evoked bradycardia and B-fiber ECAPs magnitude from a select subject. The correlation was strong with cuff ECAP recordings (R_cuff = 0.70) but poor with LIFE recordings (R_LIFE = 0.39), which were the electrodes used exclusively in the previous study by our group (Blanz et al., 2022). Interestingly, shown in Fig. 2.5C, we saw an increasing bradycardia response up to a VNS amplitude of ~2 mA, and then a flat and subsequently a decreased bradycardia response. We hypothesize that at higher stimulation currents, additional fiber types, which have a tachycardia effect, are activated, partially counteracting the bradycardia effect.

General limitations

A general limitation of our side-by-side characterization of recording electrode types for the peripheral nervous system is the varying degree of surgical trauma caused by the application of each electrode. The LIFE electrode insertion likely created the most trauma due to the large diameter insertion needle used to guide the electrode into the nerve, followed by the microneurography electrode, and lastly the cuff recording electrode, which created minimal additional trauma. Further, the open surgical preparation was not reflective of the minimally

invasive clinical insertion typical with the microneurography electrode or the chronic healed-in recording state of an implanted cuff electrode. Another general limitation is that we did not fully optimize the design of each recording electrode type. However, many studies have already used computational and *in vivo* methods to optimize the design of each recording electrode type (Yoshida and Stein, 1999; Boretius et al., 2010; Sabetian et al., 2017; Jiman et al., 2020; Ottaviani et al., 2020; Blanz et al., 2022). We drew from these studies and prior experience to inform the electrode design for each electrode type tested. Despite these limitations, we believe the strong effect sizes of the primary outcomes give validity to the study's conclusions.

Conclusions

This publication is the first to report on a side-by-side comparison of electrodes for recording electrically evoked compound action potentials (ECAPs) and sensory evoked neural activity from the peripheral nervous system of a human-scaled large animal model. We characterized a recording cuff, microneurography electrodes, and longitudinal intrafascicular electrodes (LIFEs). We found that while the cuff records a significantly larger ECAP magnitude and has a lower noise floor than the microneurography electrode, the microneurography electrode may be the most sensitive recording electrode due to its proximity to the neural source. Further, the microneurography electrode consistently recorded $A\beta$ ECAPs and was the only electrode to consistently record sensory evoked neural activity. We concluded that minimally invasive microneurography electrodes, already in routine human use, could be an important tool in the development and deployment of neuromodulation therapies to improve local on-target neural engagement.

Acknowledgements

Dr. Jill Barnes for assistance with the microneurography technique and electrode selection. Dr. Rick Chappell for insights and input on statistical design and analysis. Maria LaLuzerne for swine study scheduling and animal care. Jonah Mudge for fabricating electrodes used in the pilot experiments. Carly Frieders, Ashlesha Deshmukh, Dr. Nicole Pelot, and Rex Chen for reviewing drafts of this manuscript. Members of the Wisconsin Institute for Translational Neuroengineering (WITNe) for feedback during group meetings. University of Wisconsin Translational Research Initiatives in Pathology laboratory (TRIP), supported by the UW Department of Pathology and Laboratory Medicine, UWCCC (P30 CA014520) and the Office of The Director-NIH (S10 OD023526) for use of its facilities and services to prepare the histology images.

This work was funded by the United States National Institute of Health (NIH) SPARC Program OT2OD025340.

Conflicts of Interest

NV was an employee of Abbott Neuromodulation and BioCircuit Technologies during the completion of this work. KAL is a scientific board member and has stock interests in NeuroOne Medical Inc. KAL is also a paid member of the scientific advisory board of Cala Health, Blackfynn, Abbott Neuromodulation, Presidio Medical, and Battelle. KAL also is a paid consultant for CVRx, Galvani, and the Alfred Mann Foundation. KAL is a co-founder of NeuronOff Inc and NeuraWorx.

The remaining authors declare that the research was conducted in the absence of any commercial or financial relationships that could be construed as a potential conflict of interest.

References

- Ackerley, R., and Watkins, R. H. (2018). Microneurography as a tool to study the function of individual C-fiber afferents in humans: responses from nociceptors, thermoreceptors, and mechanoreceptors. *Journal of Neurophysiology* 120, 2834–2846. doi: 10.1152/jn.00109.2018.
- Andreasen, L. N. S., and Struijk, J. J. (2002). Signal strength versus cuff length in nerve cuff electrode recordings. *IEEE Trans. Biomed. Eng.* 49, 1045–1050. doi: 10.1109/TBME.2002.800785.
- Ardell, J. L., Nier, H., Hammer, M., Southerland, E. M., Ardell, C. L., Beaumont, E., et al. (2017). Defining the neural fulcrum for chronic vagus nerve stimulation: implications for integrated cardiac control: Vagus nerve stimulation neural fulcrum for cardiac control. *J Physiol* 595, 6887–6903. doi: 10.1113/JP274678.
- Barry, J. M. (2015). Axonal activity in vivo: technical considerations and implications for the exploration of neural circuits in freely moving animals. *Front. Neurosci.* 9. doi: 10.3389/fnins.2015.00153.
- Blanz, S. L., Musselman, E. D., Settell, M. L., Knudsen, B. E., Nicolai, E. N., Trevathan, J. K., et al. (2022). Spatially selective stimulation of the pig vagus nerve to modulate target effect versus side effect. Bioengineering doi: 10.1101/2022.05.19.492726.
- Boretius, T., Badia, J., Pascual-Font, A., Schuettler, M., Navarro, X., Yoshida, K., et al. (2010). A transverse intrafascicular multichannel electrode (TIME) to interface with the peripheral nerve. *Biosensors and Bioelectronics* 26, 62–69. doi: 10.1016/j.bios.2010.05.010.
- Bovik, A. C., Acton, S. T. (2005). Handbook of Image and Video Processing (Second Edition). Academic Press, 99-108, ISBN 9780121197926. doi: 10.1016/B978-012119792-6/50070-X.
- Buzsáki, G. (2004). Large-scale recording of neuronal ensembles. *Nat Neurosci* 7, 446–451. doi: 10.1038/nn1233.
- Cakmak, Y. O., Apaydin, H., Kiziltan, G., Gündüz, A., Ozsoy, B., Olcer, S., et al. (2017). Rapid Alleviation of Parkinson's Disease Symptoms via Electrostimulation of Intrinsic Auricular Muscle Zones. *Front. Hum. Neurosci.* 11, 338. doi: 10.3389/fnhum.2017.00338.
- Castoro, M. A. (2011). Excitation properties of the right cervical vagus nerve in adult dogs. *Experimental Neurology*, 7.

- Chakravarthy, K., Bink, H., and Dinsmoor, D. (2020). Sensing Evoked Compound Action Potentials from the Spinal Cord: Novel Preclinical and Clinical Considerations for the Pain Management Researcher and Clinician. *JPR* Volume 13, 3269–3279. doi: 10.2147/JPR.S289098.
- Chakravarthy, K., FitzGerald, J., Will, A., Trutnau, K., Corey, R., Dinsmoor, D., et al. (2022). A Clinical Feasibility Study of Spinal Evoked Compound Action Potential Estimation Methods.

 Neuromodulation: Technology at the Neural Interface 25, 75–84. doi: 10.1111/ner.13510.
- Chao, D., Mecca, C. M., Yu, G., Segel, I., Gold, M. S., Hogan, Q. H., et al. (2021). Dorsal root ganglion stimulation of injured sensory neurons in rats rapidly eliminates their spontaneous activity and relieves spontaneous pain. *Pain* 162, 2917–2932. doi: 10.1097/j.pain.000000000002284.
- Chen, H. (1994). Comparisons of Lognormal Population Means. *Proceedings of the American Mathematical Society* 121, 915. doi: 10.2307/2160293.
- De Ferrari, G. M., Stolen, C., Tuinenburg, A. E., Wright, D. J., Brugada, J., Butter, C., et al. (2017). Long-term vagal stimulation for heart failure: Eighteen month results from the NEural Cardiac TherApy foR Heart Failure (NECTAR-HF) trial. *International Journal of Cardiology* 244, 229–234. doi: 10.1016/j.ijcard.2017.06.036.
- Donaldson, N., Rieger, R., Schuettler, M., and Taylor, J. (2008). Noise and selectivity of velocity-selective multi-electrode nerve cuffs. *Med Biol Eng Comput* 46, 1005–1018. doi: 10.1007/s11517-008-0365-4.
- Drebitz, E. (2020). A novel approach for removing micro-stimulation artifacts and reconstruction of broad-band neuronal signals. *Journal of Neuroscience Methods*, 11.
- Duisit, J., Debluts, D., Behets, C., Gerdom, A., Vlassenbroek, A., Coche, E., et al. (2017). Porcine ear: A new model in large animals for the study of facial subunit allotransplantation. *JPRAS Open* 12, 47–58. doi: 10.1016/j.jpra.2017.01.004.
- Erlanger, J., and Gasser, H. (1937). Electrical Signs of Nervous Activity (London: University of Pennsylvania Press)
- Feucht, M., Ward, M. (2021). Non-invasive, Spatiotemporal Characterization of Muscle Activation Patterns from Vagus Nerve Stimulation in Human Subjects. *Proceedings of IMPRS* 4. doi: 10.18060/25920
- Gaunt, R. A., Hokanson, J. A., and Weber, D. J. (2009). Microstimulation of primary afferent neurons in the L7 dorsal root ganglia using multielectrode arrays in anesthetized cats: thresholds and recruitment properties. *J. Neural Eng.* 6, 055009. doi: 10.1088/1741-2560/6/5/055009.
- Getty, R., and Grossman, J. D. (1975). The Anatomy of the Domestic Animals, Vol. 2. *W B Saunders Co.* ISBN: 0721641075.

- Gonzalez-Gonzalez, M. A., Bendale, G. S., Wang, K., Wallace, G. G., and Romero-Ortega, M. (2021). Platinized graphene fiber electrodes uncover direct spleen-vagus communication. *Commun Biol* 4, 1097. doi: 10.1038/s42003-021-02628-7.
- Harding, G. W. (1991). A method for eliminating the stimulus artifact from digital recordings of the direct cortical response. *Computers and Biomedical Research* 24, 183–195. doi: 10.1016/0010-4809(91)90029-V.
- He, S., Teagle, H. F. B., and Buchman, C. A. (2017). The Electrically Evoked Compound Action Potential: From Laboratory to Clinic. *Front. Neurosci.* 11, 339. doi: 10.3389/fnins.2017.00339.
- Heusser, K., Tank, J., Brinkmann, J., Menne, J., Kaufeld, J., Linnenweber-Held, S., et al. (2016). Acute Response to Unilateral Unipolar Electrical Carotid Sinus Stimulation in Patients With Resistant Arterial Hypertension. *Hypertension* 67, 585–591. doi: 10.1161/HYPERTENSIONAHA.115.06486.
- Humphrey, D., and Schmidt, E. (1990). Neurophysiological Techniques Applications to Neural Systems Neuromethods 15. *Humana Totowa*, ISBN: 978-1-4899-4117-6, doi: 10.1385/0896031853
- Janko, M., and Trontelj, J. V. (1980). Transcutaneous Electrical Nerve Stimulation: A Microneurographic and Perceptual Study. *Pain* 9, 219–230. doi: 10.1016/0304-3959(80)90009-3
- Jiman, A. A., Ratze, D. C., Welle, E. J., Patel, P. R., Richie, J. M., Bottorff, E. C., et al. (2020). Multichannel intraneural vagus nerve recordings with a novel high-density carbon fiber microelectrode array. *Sci Rep* 10, 15501. doi: 10.1038/s41598-020-72512-7.
- Johnson, R. L., and Wilson, C. G. (2018). A review of vagus nerve stimulation as a therapeutic intervention. *JIR* Volume 11, 203–213. doi: 10.2147/JIR.S163248.
- Kaniusas, E., Kampusch, S., Tittgemeyer, M., Panetsos, F., Gines, R. F., Papa, M., et al. (2019). Current Directions in the Auricular Vagus Nerve Stimulation I A Physiological Perspective. *Front. Neurosci.* 13, 854. doi: 10.3389/fnins.2019.00854.
- Khodagholy, D., Gelinas, J. N., Thesen, T., Doyle, W., Devinsky, O., Malliaras, G. G., et al. (2015). NeuroGrid: recording action potentials from the surface of the brain. *Nat Neurosci* 18, 310–315. doi: 10.1038/nn.3905.
- Kodandaramaiah, S. B., Franzesi, G. T., Chow, B. Y., Boyden, E. S., and Forest, C. R. (2012). Automated whole-cell patch-clamp electrophysiology of neurons in vivo. *Nat Methods* 9, 585–587. doi: 10.1038/nmeth.1993.
- Koh, R. G. L., Zariffa, J., Jabban, L., Yen, S.-C., Donaldson, N., and Metcalfe, B. W. (2022). Tutorial: A guide to techniques for analysing recordings from the peripheral nervous system. *J. Neural Eng.* doi: 10.1088/1741-2552/ac7d74.

- Koppaka, S., Hess-Dunning, A., and Tyler, D. J. (2022). Biomechanical characterization of isolated epineurial and perineurial membranes of rabbit sciatic nerve. *Journal of Biomechanics* 136, 111058. doi: 10.1016/j.jbiomech.2022.111058.
- Lefkowitz, T., Hazani, R., Chowdhry, S., Elston, J., Yaremchuk, M. J., and Wilhelmi, B. J. (2013). Anatomical Landmarks to Avoid Injury to the Great Auricular Nerve During Rhytidectomy. *Aesthetic Surgery Journal* 33, 19–23. doi: 10.1177/1090820X12469625.
- Lundberg, K. H. (2002). Noise Sources in Bulk CMOS. *MIT web* accessed at https://web.mit.edu/klund/www/papers/UNP noise.pdf
- Macefield, V. G. (2021). Recording and quantifying sympathetic outflow to muscle and skin in humans: methods, caveats and challenges. *Clin Auton Res* 31, 59–75. doi: 10.1007/s10286-020-00700-6.
- Manzano, G. M., Giuliano, L. M. P., and Nóbrega, J. A. M. (2008). A brief historical note on the classification of nerve fibers. *Arq. Neuro-Psiquiatr.* 66, 117–119. doi: 10.1590/S0004-282X2008000100033.
- Meier, K., Qerama, E., Ettrup, K. S., Glud, A. N., Alstrup, A. K. O., and Sørensen, J. C. H. (2018). Segmental innervation of the Göttingen minipig hind body. An electrophysiological study. *J. Anat.* 233, 411–420. doi: 10.1111/joa.12865.
- Mekhail, N., Levy, R. M., Deer, T. R., Kapural, L., Li, S., Amirdelfan, K., et al. (2022). Durability of Clinical and Quality-of-Life Outcomes of Closed-Loop Spinal Cord Stimulation for Chronic Back and Leg Pain: A Secondary Analysis of the Evoke Randomized Clinical Trial. *JAMA Neurol* 79, 251. doi: 10.1001/jamaneurol.2021.4998.
- Metcalfe, B. W., Nielsen, T. N., Donaldson, N. de N., Hunter, A. J., and Taylor, J. T. (2018). First demonstration of velocity selective recording from the pig vagus using a nerve cuff shows respiration afferents. *Biomed. Eng. Lett.* 8, 127–136. doi: 10.1007/s13534-017-0054-z.
- Mitra, S., Mitra, M., and Halder, B. (2018). Automatic feature extraction of ECG signal based on adaptive window dependent differential histogram approach and validation with CSE database. *IJCSYSE* 4, 146. doi: 10.1504/IJCSYSE.2018.10012644.
- Molecular Devices. (2006). The Axon CNS Guide. 235-263, Part Number 2500-102 Rev B 200
- Moncrief, K., and Kaufman, S. (2006). Splenic baroreceptors control splenic afferent nerve activity. *American Journal of Physiology-Regulatory, Integrative and Comparative Physiology* 290, R352–R356. doi: 10.1152/ajpregu.00489.2005.
- Nicolai, E. N., Settell, M. L., Knudsen, B. E., McConico, A. L., Gosink, B. A., Trevathan, J. K., et al. (2020). Sources of off-target effects of vagus nerve stimulation using the helical clinical lead in domestic pigs. *J. Neural Eng.* 17, 046017. doi: 10.1088/1741-2552/ab9db8.

- Nonis, R., D'Ostilio, K., Schoenen, J., and Magis, D. (2017). Evidence of activation of vagal afferents by non-invasive vagus nerve stimulation: An electrophysiological study in healthy volunteers. *Cephalalgia* 37, 1285–1293. doi: 10.1177/0333102417717470.
- Obot, I. B., Onyeachu, I. B., Zeino, A., and Umoren, S. A. (2019). Electrochemical noise (EN) technique: review of recent practical applications to corrosion electrochemistry research. *Journal of Adhesion Science and Technology* 33, 1453–1496. doi: 10.1080/01694243.2019.1587224.
- Ottaviani, M. M., Wright, L., Dawood, T., and Macefield, V. G. (2020). In vivo recordings from the human vagus nerve using ultrasound-guided microneurography. *J Physiol*, JP280077. doi: 10.1113/JP280077.
- Park, J., Choi, W.-M., Kim, K., Jeong, W.-I., Seo, J.-B., and Park, I. (2018). Biopsy Needle Integrated with Electrical Impedance Sensing Microelectrode Array towards Real-time Needle Guidance and Tissue Discrimination. *Sci Rep* 8, 264. doi: 10.1038/s41598-017-18360-4.
- Parker, J. L., Karantonis, D. M., Single, P. S., Obradovic, M., and Cousins, M. J. (2012). Compound action potentials recorded in the human spinal cord during neurostimulation for pain relief. *Pain* 153, 593–601. doi: 10.1016/j.pain.2011.11.023.
- Parker, J. L., Obradovic, M., Hesam Shariati, N., Gorman, R. B., Karantonis, D. M., Single, P. S., et al. (2020). Evoked Compound Action Potentials Reveal Spinal Cord Dorsal Column Neuroanatomy. *Neuromodulation: Technology at the Neural Interface* 23, 82–95. doi: 10.1111/ner.12968.
- Pelot, N. A., Behrend, C. E., and Grill, W. M. (2019). On the parameters used in finite element modeling of compound peripheral nerves. *J. Neural Eng.* 16, 016007. doi: 10.1088/1741-2552/aaeb0c.
- Pelot, N. A., Goldhagen, G. B., Cariello, J. E., Musselman, E. D., Clissold, K. A., Ezzell, J. A., et al. (2020). Quantified Morphology of the Cervical and Subdiaphragmatic Vagus Nerves of Human, Pig, and Rat. *Front. Neurosci.* 14, 601479. doi: 10.3389/fnins.2020.601479.
- Plonsey, R., and Barr, R. C. (1995). Electric field stimulation of excitable tissue. *IEEE Trans. Biomed. Eng.* 42, 329–336. doi: 10.1109/10.376126.
- Qing, K. Y., Wasilczuk, K. M., Ward, M. P., Phillips, E. H., Vlachos, P. P., Goergen, C. J., et al. (2018). B fibers are the best predictors of cardiac activity during Vagus nerve stimulation: Qing, vagal B fiber activation and cardiac effects. *Bioelectron Med* 4, 5. doi: 10.1186/s42234-018-0005-8.
- Rawlins, J. C. (2000). "AC and the Sine Wave," in *Basic AC Circuits* (Elsevier), 29–63. doi: 10.1016/B978-075067173-6/50003-1.
- Ringer, S. K., Spielmann, N., Weiss, M., and Mauch, J. Y. (2016). Fentanyl bolus induces muscle tremors in sevoflurane-anaesthetized piglets. *Lab Anim* 50, 312–314. doi: 10.1177/0023677215623896.

- Robinson, D. A. (1968). The electrical properties of metal microelectrodes. *Proc. IEEE* 56, 1065–1071. doi: 10.1109/PROC.1968.6458.
- Sabbah, H. N., Ilsar, I., Zaretsky, A., Rastogi, S., Wang, M., and Gupta, R. C. (2011). Vagus nerve stimulation in experimental heart failure. *Heart Fail Rev* 16, 171–178. doi: 10.1007/s10741-010-9209-z.
- Sabetian, P., Popovic, M. R., and Yoo, P. B. (2017). Optimizing the design of bipolar nerve cuff electrodes for improved recording of peripheral nerve activity. *J. Neural Eng.* 14, 036015. doi: 10.1088/1741-2552/aa6407.
- Scipy. (2022). scipy.signal.filtfilt. *Scipy v1.9.1 Manual* accessed at https://docs.scipy.org/doc/scipy/reference/generated/scipy.signal.filtfilt.html
- Settell, M. L., Pelot, N. A., Knudsen, B. E., Dingle, A. M., McConico, A. L., Nicolai, E. N., et al. (2020). Functional vagotopy in the cervical vagus nerve of the domestic pig: implications for the study of vagus nerve stimulation. *J. Neural Eng.* 17, 026022. doi: 10.1088/1741-2552/ab7ad4.
- Sharma, V. S., Stephens, R. E., Wright, B. W., and Surek, C. C. (2017). What Is the Lobular Branch of the Great Auricular Nerve? Anatomical Description and Significance in Rhytidectomy: *Plastic and Reconstructive Surgery* 139, 371e–378e. doi: 10.1097/PRS.000000000002980.
- Silverman, H. A., Stiegler, A., Tsaava, T., Newman, J., Steinberg, B. E., Masi, E. B., et al. (2018). Standardization of methods to record Vagus nerve activity in mice. *Bioelectron Med* 4, 3. doi: 10.1186/s42234-018-0002-y.
- Simakov, A. B., and Webster, J. G. (2010). Motion Artifact From Electrodes and Cables. *Iranian Journal of Electrical and Computer Engineering* 9, 139-143.
- Stumpp, L., Smets, H., Vespa, S., Cury, J., Doguet, P., Delbeke, J., et al. (2020). Recording of spontaneous vagus nerve activity during Pentylenetetrazol-induced seizures in rats. *Journal of Neuroscience Methods* 343, 108832. doi: 10.1016/j.jneumeth.2020.108832.
- Tucker-Davis Technologies, Inc. (TDT). (2022). SIM Subject Interface Module Hardware Reference, Page 23
- Ulrich, G., Schlosser, W., and Juckel, G. (2016). The impact of Arterial Pulse Impedance Artifact (APIA) on test-retest reliability of quantitative EEG. *Neuropsychiatr Electrophysiol* 2, 5. doi: 10.1186/s40810-016-0019-y.
- Verma, N., Graham, R. D., Mudge, J., Trevathan, J. K., Franke, M., Shoffstall, A. J., et al. (2021a). Augmented Transcutaneous Stimulation Using an Injectable Electrode: A Computational Study. *Front. Bioeng. Biotechnol.* 9, 796042. doi: 10.3389/fbioe.2021.796042.

- Verma, N., Mudge, J. D., Kasole, M., Chen, R. C., Blanz, S. L., Trevathan, J. K., et al. (2021b). Auricular Vagus Neuromodulation—A Systematic Review on Quality of Evidence and Clinical Effects. *Front. Neurosci.* 15, 664740. doi: 10.3389/fnins.2021.664740.
- Winestone, J. S., Zaidel, A., Bergman, H., and Israel, Z. (2012). The use of macroelectrodes in recording cellular spiking activity. *Journal of Neuroscience Methods* 206, 34–39. doi: 10.1016/j.jneumeth.2012.02.002.
- Yang, H.-M., Kim, H.-J., and Hu, K.-S. (2015). Anatomic and histological study of great auricular nerve and its clinical implication. *Journal of Plastic, Reconstructive & Aesthetic Surgery* 68, 230–236. doi: 10.1016/j.bjps.2014.10.030.
- Yang, Z., Zhao, Q., Keefer, E., and Liu, W. (2009). Noise Characterization, Modeling, and Reduction for In Vivo Neural Recording. *NIPS Advances in Neural Information Processing Systems* 22. ISBN: 9781615679119
- Yasar, N. (2021). Causes of noise in electrophysiological recordings. *Plexon blog* accessed at https://plexon.com/blog-post/causes-of-noise-in-electrophysiological-recordings/
- Yoo, P. B., Lubock, N. B., Hincapie, J. G., Ruble, S. B., Hamann, J. J., and Grill, W. M. (2013). High-resolution measurement of electrically-evoked vagus nerve activity in the anesthetized dog. *J. Neural Eng.* 10, 026003. doi: 10.1088/1741-2560/10/2/026003.
- Yoshida, K., and Stein, R. B. (1999). Characterization of signals and noise rejection with bipolar longitudinal intrafascicular electrodes. *IEEE Trans. Biomed. Eng.* 46, 226–234. doi: 10.1109/10.740885.

Supplementary Materials

Supplementary Material 1 – Close-up photographs of recording electrodes

Supplementary Material 2 – Histology of great auricular nerve

Supplementary Material 3 – Great auricular nerve surgical pocket

Supplementary Material 4 – Facial nerve anatomy

Supplementary Material 5 – Great auricular nerve anatomy

Supplementary Material 6 – Non-functional electrodes

Supplementary Material 7 – Detrending of ECAPs from stimulation artifact

Supplementary Material 8 – Primary noise contribution in time series from low-frequency

noise (e.g., cardiac related artifacts)

Supplementary Material 9 – Verifying authenticity of B-fiber recordings using signal

propagation delay

Supplementary Material 10 – Data from all subjects

Supplementary Material 11 – Spontaneous activity recordings from cervical vagus nerve (cVN)

Supplementary Material 1 – Close-up photographs of recording electrodes

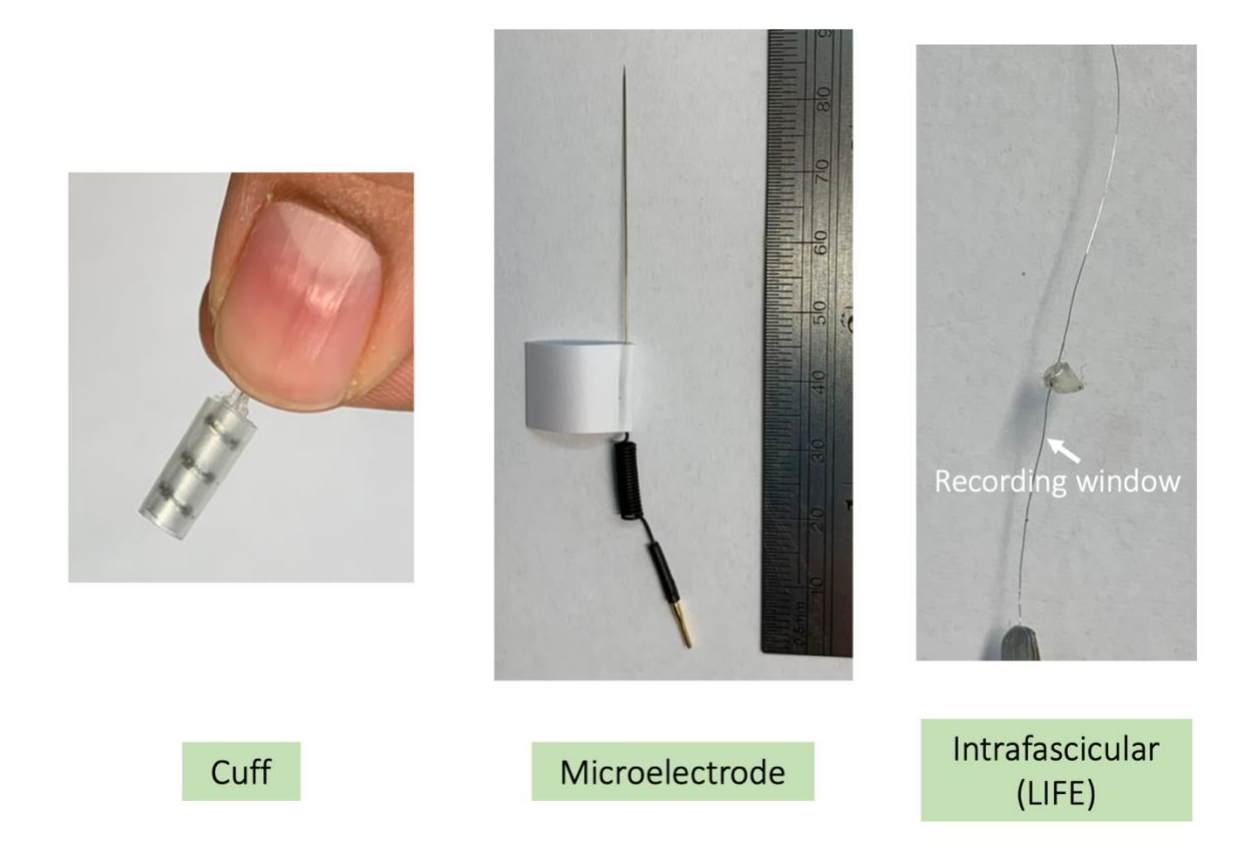


Figure 2.8: Close up photograph of three recording electrodes characterized in this study.

Supplementary Material 2 – Histology of great auricular nerve

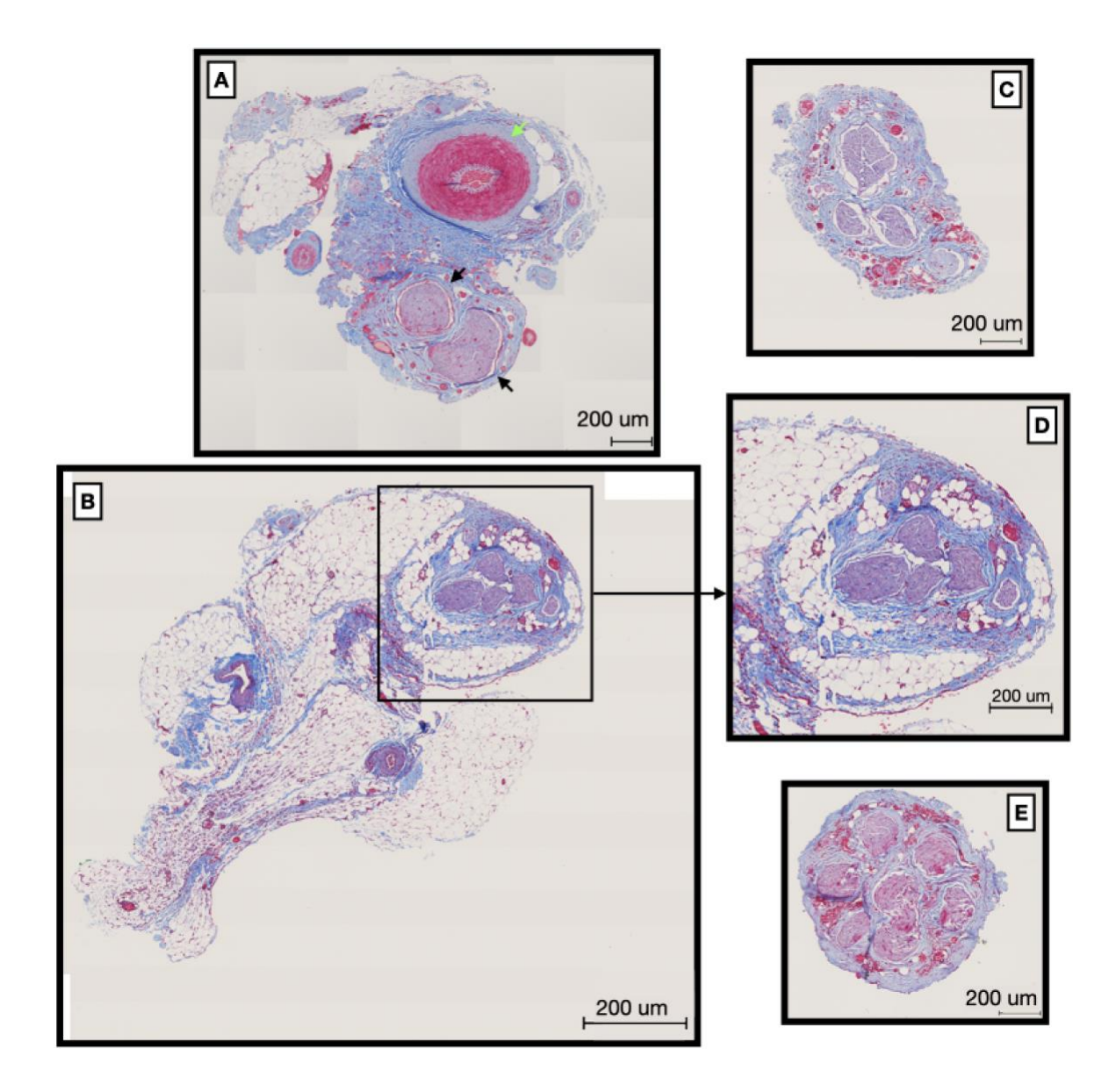


Figure 2.9: Representative histology of great auricular nerve cross sections (5 um) for four subjects.

(A) Contains both the fascicles of the great auricular nerve (black arrow heads) and the associated artery (green arrowhead) (D) Zoomed region of (B), showing fascicles of the great auricular nerve.

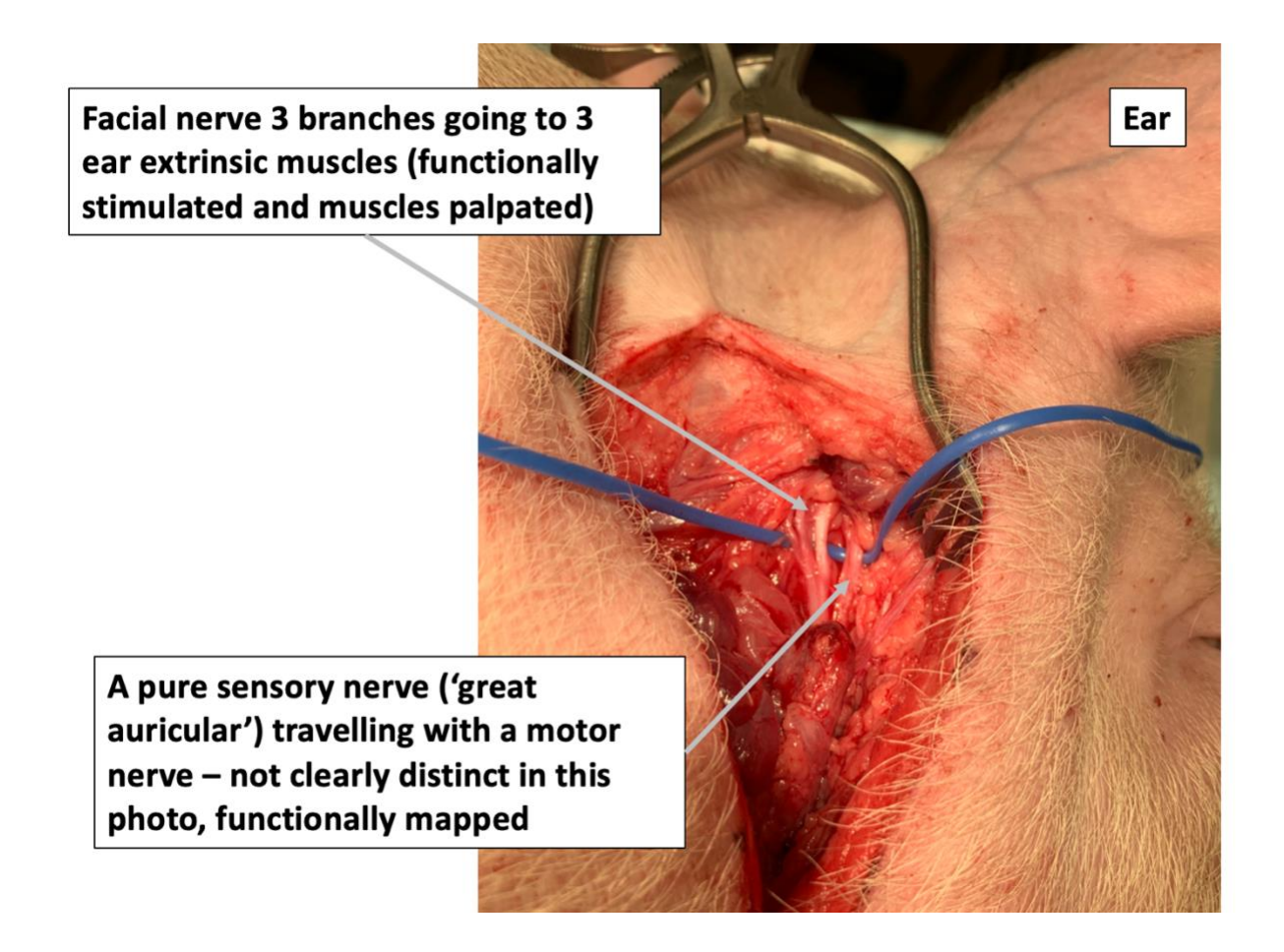


Figure 2.10: Surgical pocket to access great auricular nerve and surrounding anatomy. Functional mapping allowed differentiation between motor nerves (facial) and the sensory nerve (great auricular)

Supplementary Material 4 – Facial nerve anatomy

Facial nerve (pig):

- 1 caudal auricular nerve
- 2 internal auricular nerve
- 3 auriculopalpebral nerve
- 4 dorsal buccal branch
- 5 ventral buccal branch
- 6 stylohyoid branch
- 7 cervical branch

Note in human literature, 'anterior' and 'posterior' are used while in animal literature 'rostral' and 'caudal' are used respectively.

Caudal/posterior auricular nerve:

Initiates near stylomastoid foramen courses dorsal bifurcating into caudal and rostral branches.

Both caudal and rostral branches course in association with caudal auricular artery and internal auricular nerve. Caudal branch is smaller of the two and innervates cervicoauricularis profundus muscle, with smaller branches innervating transverse and oblique auricular muscles as well as parotidoauricularis muscle. Innervates both intrinsic and extrinsic muscles of the outer ear.

Rostral/anterior auricular branch:

Continues a dorsal course and passes between retroauricular fat pad and ventral surface of the cervicoauricularis profundus muscle. In this area the rostral branch gives off smaller branches

to styloauricularis muscle. These branches penetrate the auricular cartilage at helicine fissure and innervate the helicine muscle, terminating in the styloauricularis m.

Internal auricular branch:

Originates from dorsal margin of facial nerve and courses dorsal.

Divides into two to three branches before entering auricular cartilage and ramifying the skin of the inner surface of the auricular cartilage.

Auriculopalpebral nerve:

Courses dorsal communicating with auriculotemporal nerve then dividing into rostral auricular branches which innervate the auriculares rostrales muscles and a zygomatic branch to the frontoscutularis, levator angulioculi medialis and orbicularis oculi muscles.

*Sisson and Grossman's "The Anatomy of the Domestic Animals", 1975.

Supplementary Material 5 – Great auricular nerve anatomy

The great auricular nerve (GAN) courses dorsally after emerging from the sternomastoid muscle. Traveling below the platysma muscle and coursing in association with the external jugular vein to the parotid margin. At this point the GAN begins to divide into its terminal branches. The GAN bifurcates into two primary branches with each of the primary branches dividing further.

The first division is the anterior branch. This branch courses rostrally over the parotid gland bifurcating into superficial and deep branches. The superficial branch innervates the skin over the parotid gland on the face. The deep branch penetrates the SMAS and parotid fascia and communicates with the facial nerve within the parotid gland (Yang et.al JPRAS 2015).

The posterior branch continues dorsal towards the posterior base of the ear and in association with the lateral auricular vein. It continues coursing around the posterior margin of the ear branching out to innervate the skin over the mastoid process. Another branch enters the cartilage at the base of the ear and supplies the anterior lower third of the ear. In humans this branch has been identified and referred to as the lobular branch (Sharma et al 2016). In pigs the lobular or lower third of the ear does not have a fatty lobule, the lobular equivalent of the pig would include the exterior skin around the tragus, antitragus, and intertragic notch areas of the ear. The posterior branch then continues along the posterior/caudal margin of the ear to innervate the posterior surface/skin of the auricle.

Some studies have suggested that this "lobular" branch be identified as a separate branch that supplies sensory innervation to the lower third of the ear. There are several studies that suggest that the GAN branches have four to five main configurations, we however did not

dissect the entire configuration from each pig but did note that locations for the nerve configurations varied between animals (Sharma et al ASPS 2016; Lefkowitz et al., Aesthetic Surgery Journal, 2013; Yang et al. JPRAS 2015).

We found very little information on peripheral nerve anatomy or function in the pig model. Furthermore, the information can be misleading and inconsistent compared with surgical observations. We did not conduct a complete anatomical study for our purposes. However, future studies are warranted if the GAN in pig is to become a standard model.

Supplementary Material 6 – Non-functional electrodes

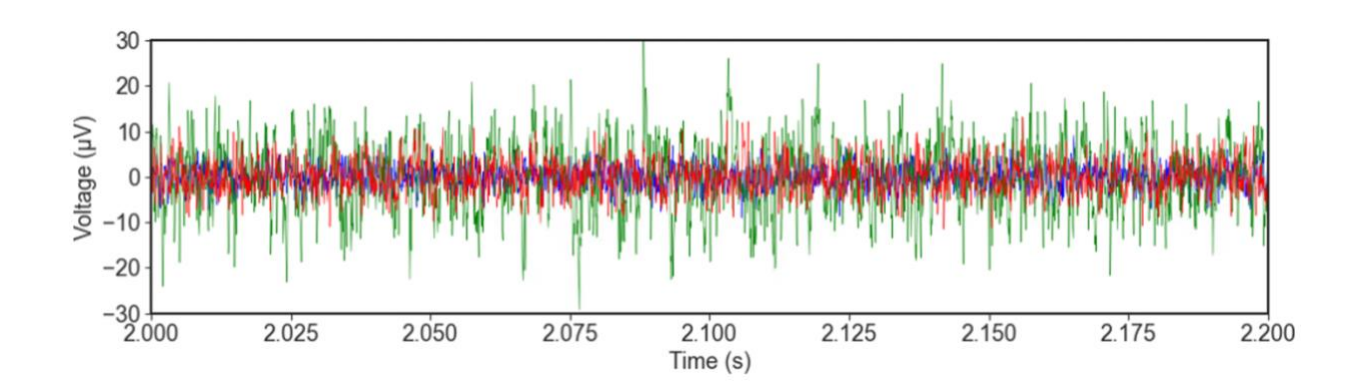


Figure 2.11: Subject 1 vagus micro 2 was a non-functional electrode classified by the high noise floor (green trace) compared to the blue and red traces (figure below) and no ECAP signal even at 5 mA of stimulation

Subject 1 great auricular micro 2 was a non-functional electrode classified by the high noise floor (figure in Supplementary Material 10 – Data from all subjects).

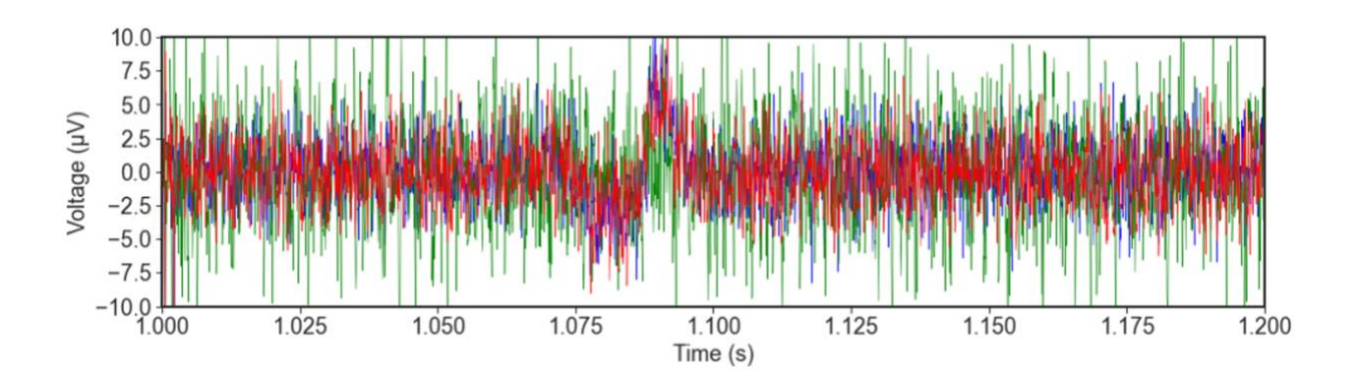


Figure 2.12: Subject 4 vagus cuff 2 was a non-functional electrode classified by the high noise floor (green trace) compared to the blue and red traces (figure below) and noted as physically disconnected at the end of the recording.

Supplementary Material 7 – Detrending of ECAPs from stimulation artifact

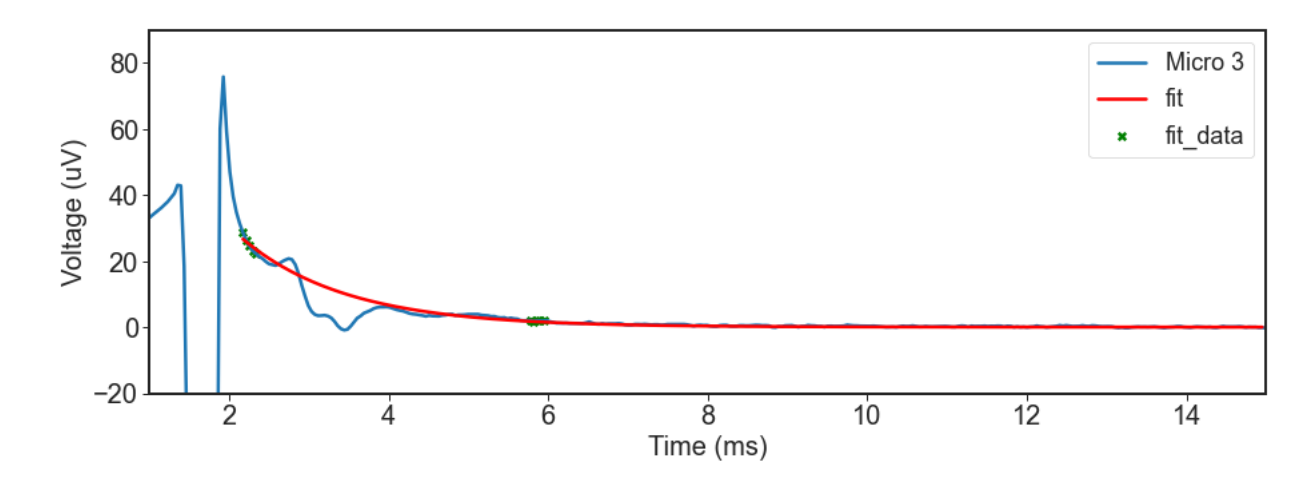


Figure 2.13: ECAPs from Subject 6 microelectrode recordings during the vagus dose-response amplitude sweep were contaminated by stimulation artifact.

This is a representative fit of an exponential decay to the stimulation artifact in the ECAP trace.

Supplementary Material 8 – Primary noise contribution in time series from low-frequency noise (e.g., cardiac related artifacts)

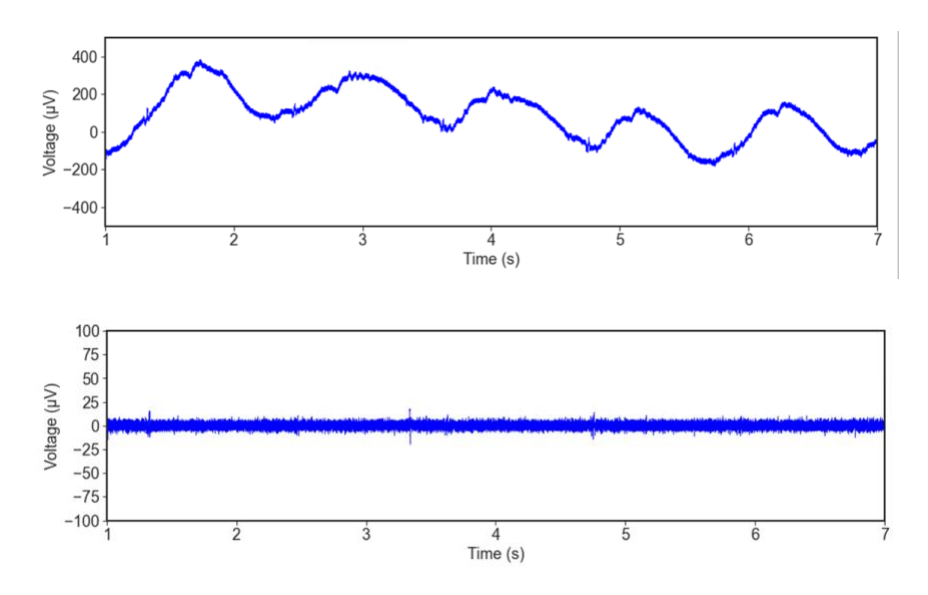


Figure 2.14: Microelectrode traces from subject 1 before (top) and after (bottom) filtering. High RMS noise in unfiltered microelectrode time series is coming largely from low frequencies.

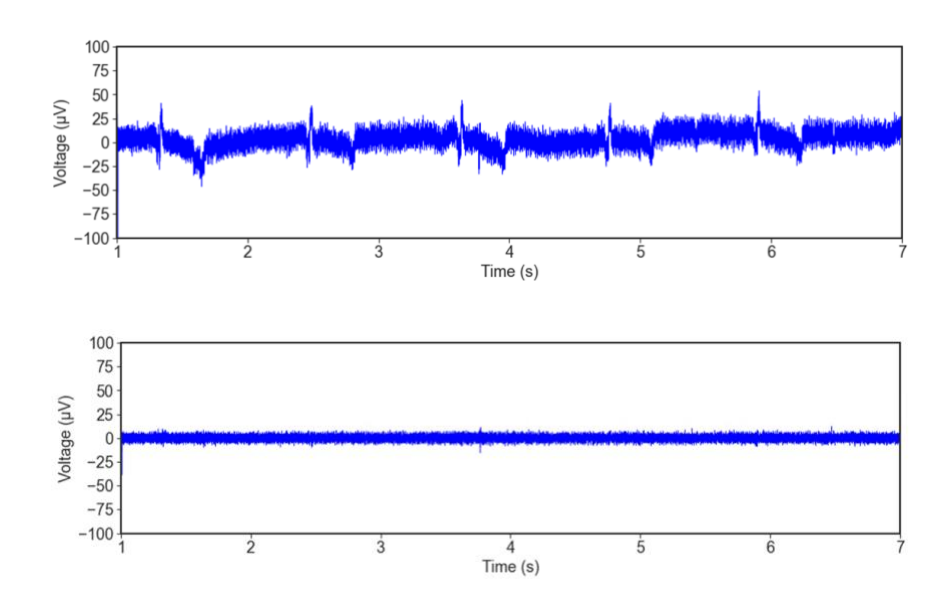


Figure 2.15: (top) An example of cardiac related artifact appearing in electrophysiology recordings, which may be mistaken for a neural signal.

The cardiac related effect could be cardioballistic in nature or from the electrical activity of the heart, depending on the setup of the reference and recording electrode. (bottom) Removed by high pass filtering (fc = 100 Hz). See Fig. 2.5B in main paper for additional artifact examples. Cuff traces from subject 1.

Supplementary Material 9 – Verifying authenticity of B-fiber recordings using signal

propagation delay

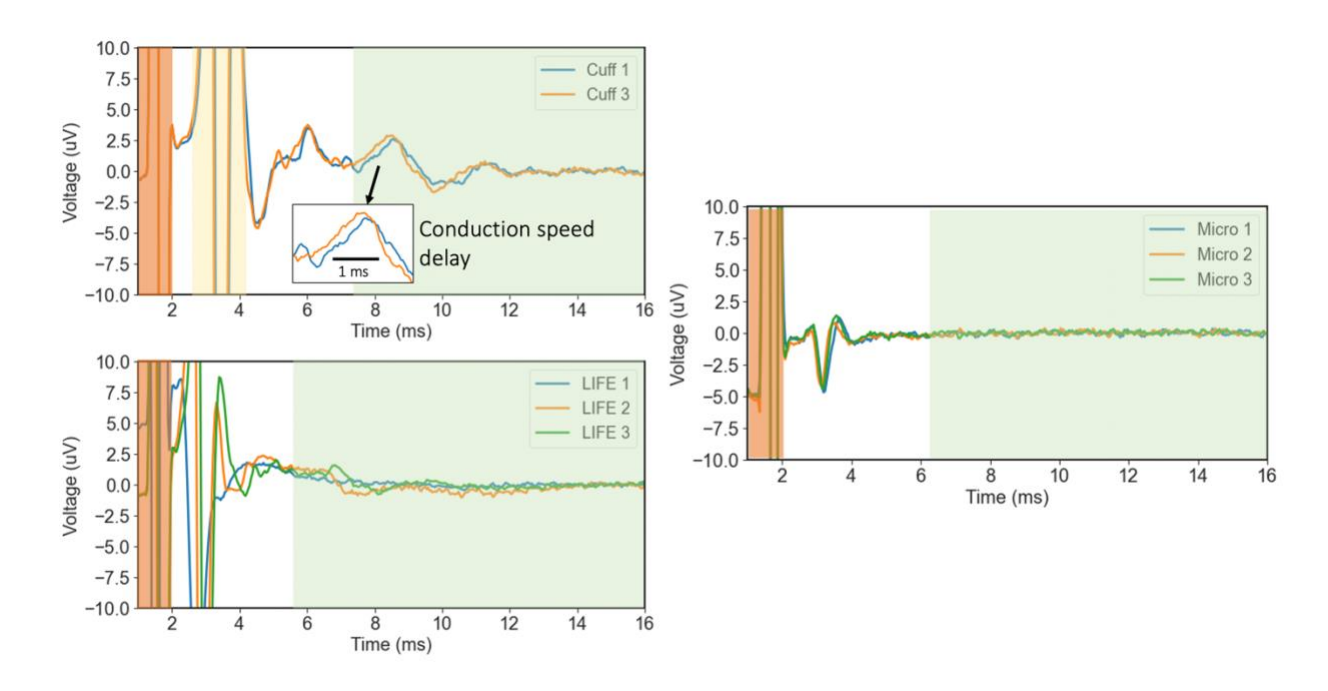


Figure 2.16: B-fiber ECAPs across recording electrodes.

ECAP during 10 mA of stimulation on the vagus nerve in subject 4. (top left) with recording cuff (bottom left) with intrafascicular electrodes and (right) with microneurography microelectrode. Stimulation artifact shaded in orange, $A\beta$ -fiber ECAP shaded in yellow, and B-fiber ECAP region shaded in green. Authenticity of B-fiber ECAP is suggested by signal propagation delay in cuff and intrafascicular electrode recording but not in microneurography microelectrode recording.

Supplementary Material 10 – Data from all subjects

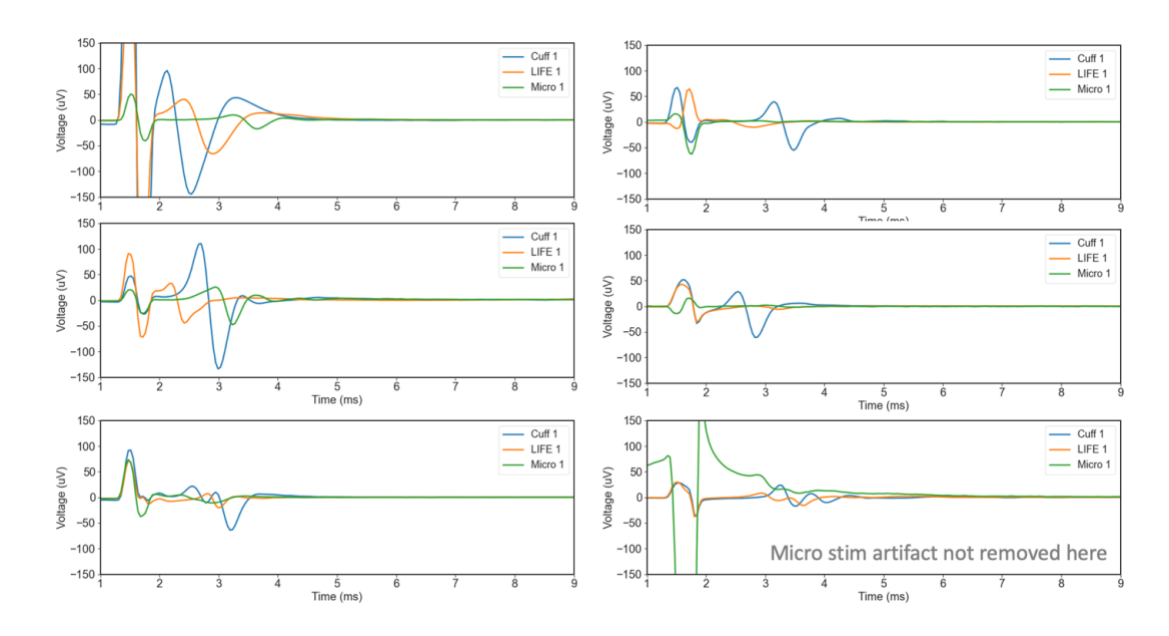


Figure 2.17: $A\beta$ ECAP at 1.5 mA of stimulation on cervical vagus nerve from all subjects. (top-left) subject 1 to (bottom-left) subject 3 and (top-right) subject 4 to (bottom-right) subject 6. Cuff consistently records the largest ECAP. Apparent triphasic morphology in subject 1 cuff may be due to stimulation artifact recovery.

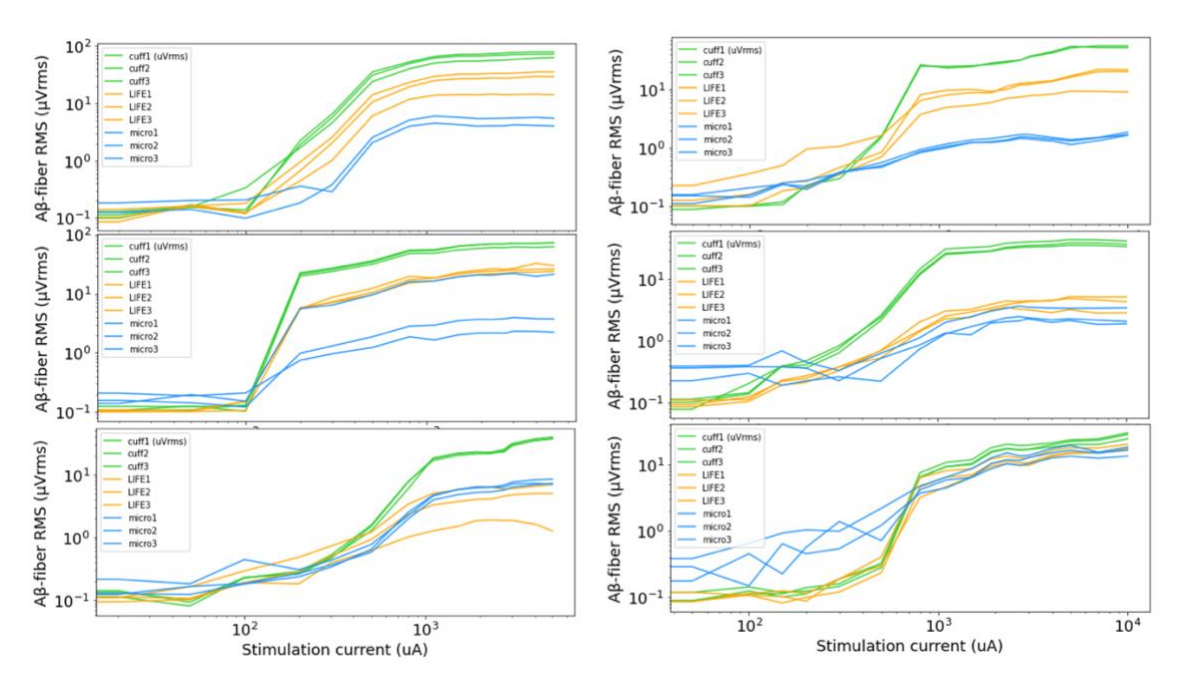


Figure 2.18: A β -fiber dose-response curves during vagus nerve stimulation from all subjects. (top-left) subject 1 to (bottom-left) subject 3 and (top-right) subject 4 to (bottom-right) subject 6.

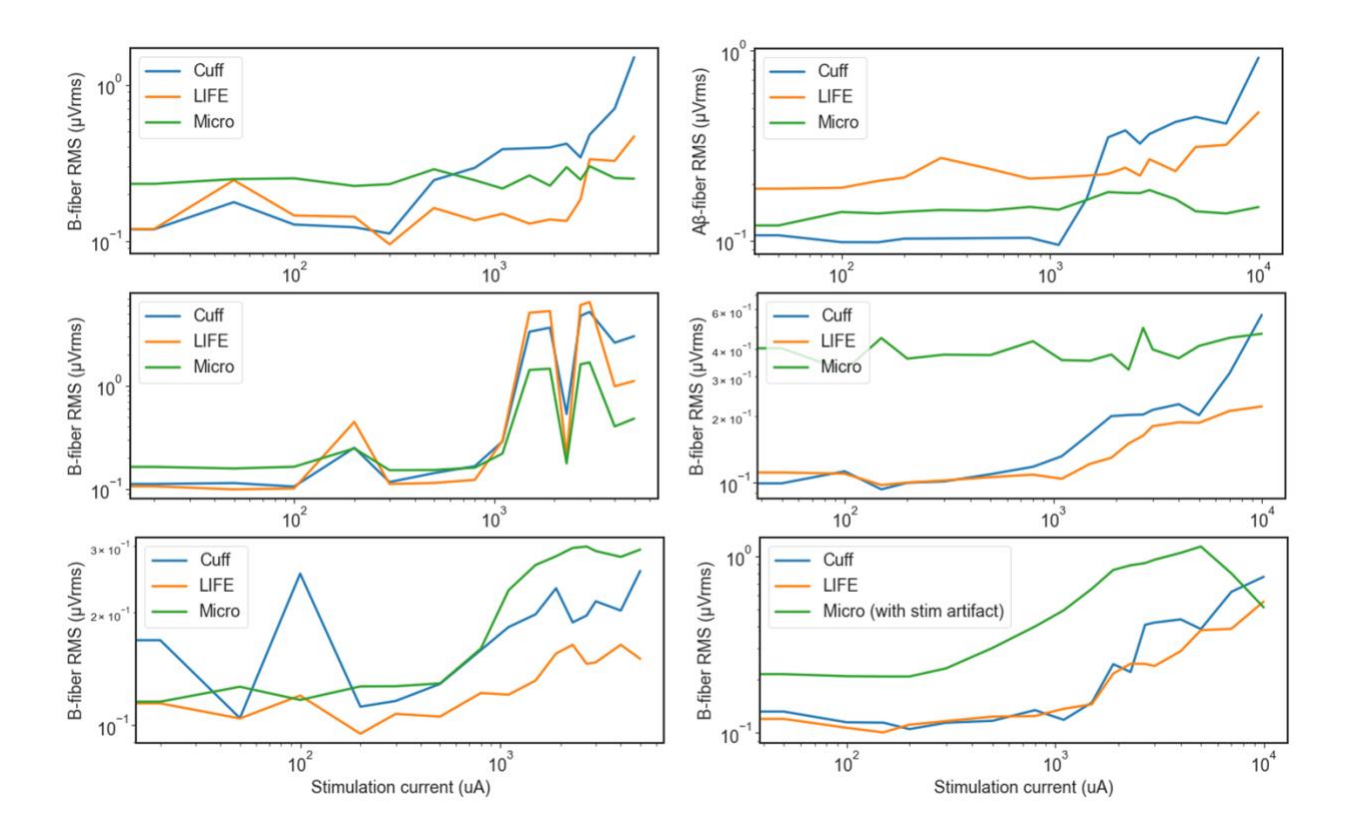


Figure 2.19: B-fiber dose-response curves during vagus nerve stimulation from all subjects. (top-left) subject 1 to (bottom-left) subject 3 and (top-right) subject 4 to (bottom-right) subject 6. An insufficient dose of Vecuronium (muscle blocker) was used in subjects 1-3 so EMG contamination of the B-fiber dose-response curves is likely. Not subject 6 microneurography microelectrode recordings are contaminated by stimulation artifact.

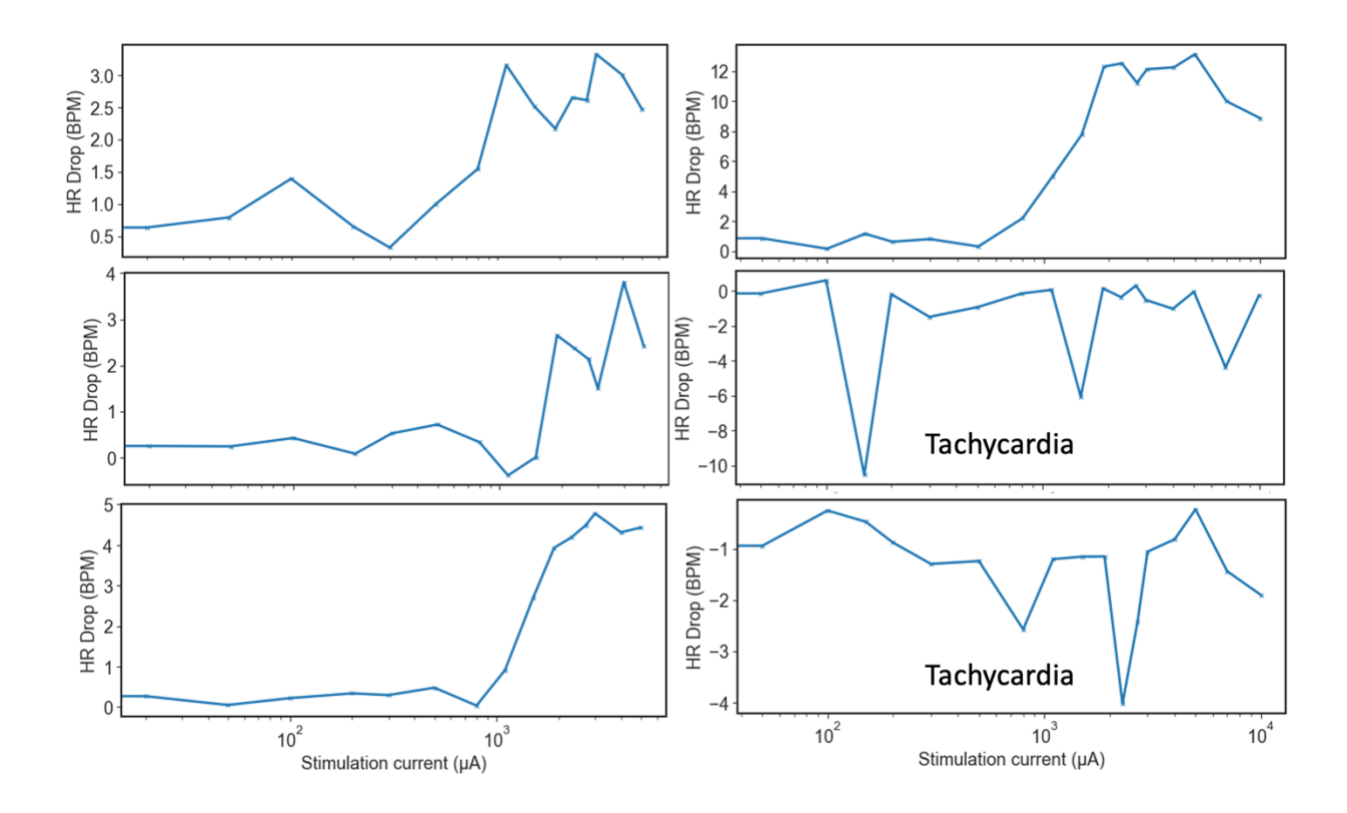


Figure 2.20: Stimulated evoked heart rate change dose-response curves during vagus nerve stimulation (VNS) from all subjects.

(top-left) subject 1 to (bottom-left) subject 3 and (top-right) subject 4 to (bottom-right) subject 6. Subjects 5 and 6 are showing a tachycardia response instead of the canonical bradycardia response to VNS. Note that subjects 1-3 had the vagus experiment performed in the afternoon and were under greater doses of anesthesia compared to subjects 4-6 that had the vagus experiment performed in the morning and were under lower doses of anesthesia.

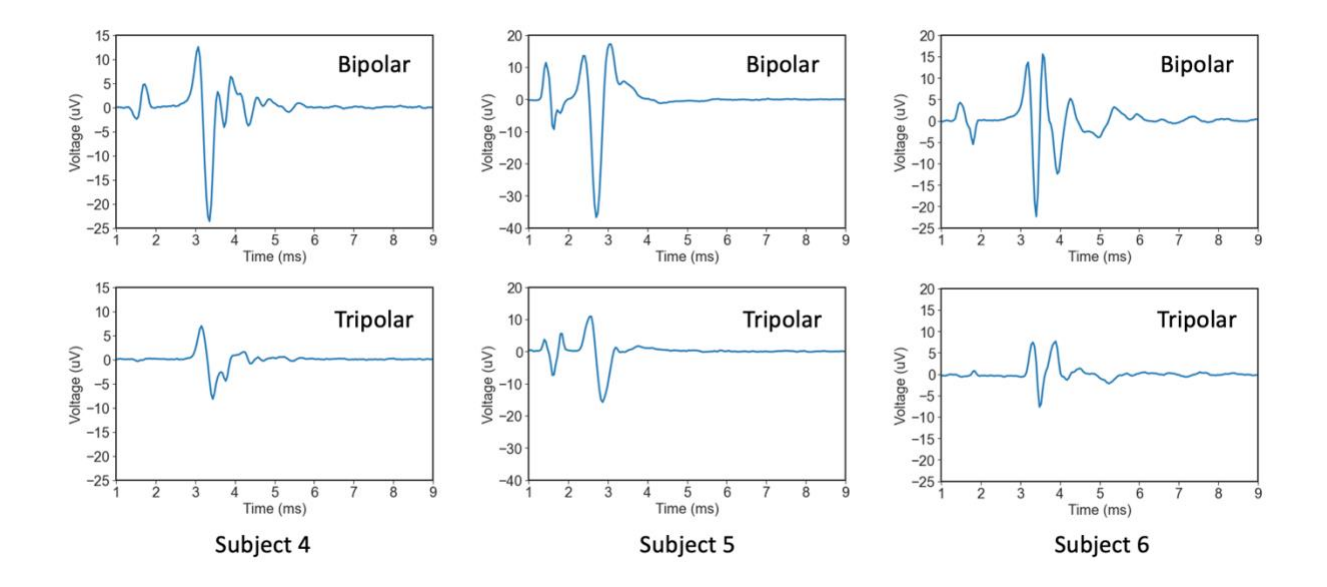


Figure 2.21: Tripolar vs. bipolar reference cuff recordings.Subject 4 (left), 5 (center), and 6 (right). Stimulation artifact is consistently smaller in tripolar. ECAP magnitude is consistently smaller in tripolar by factor of ~2.2x compared to bipolar reference.

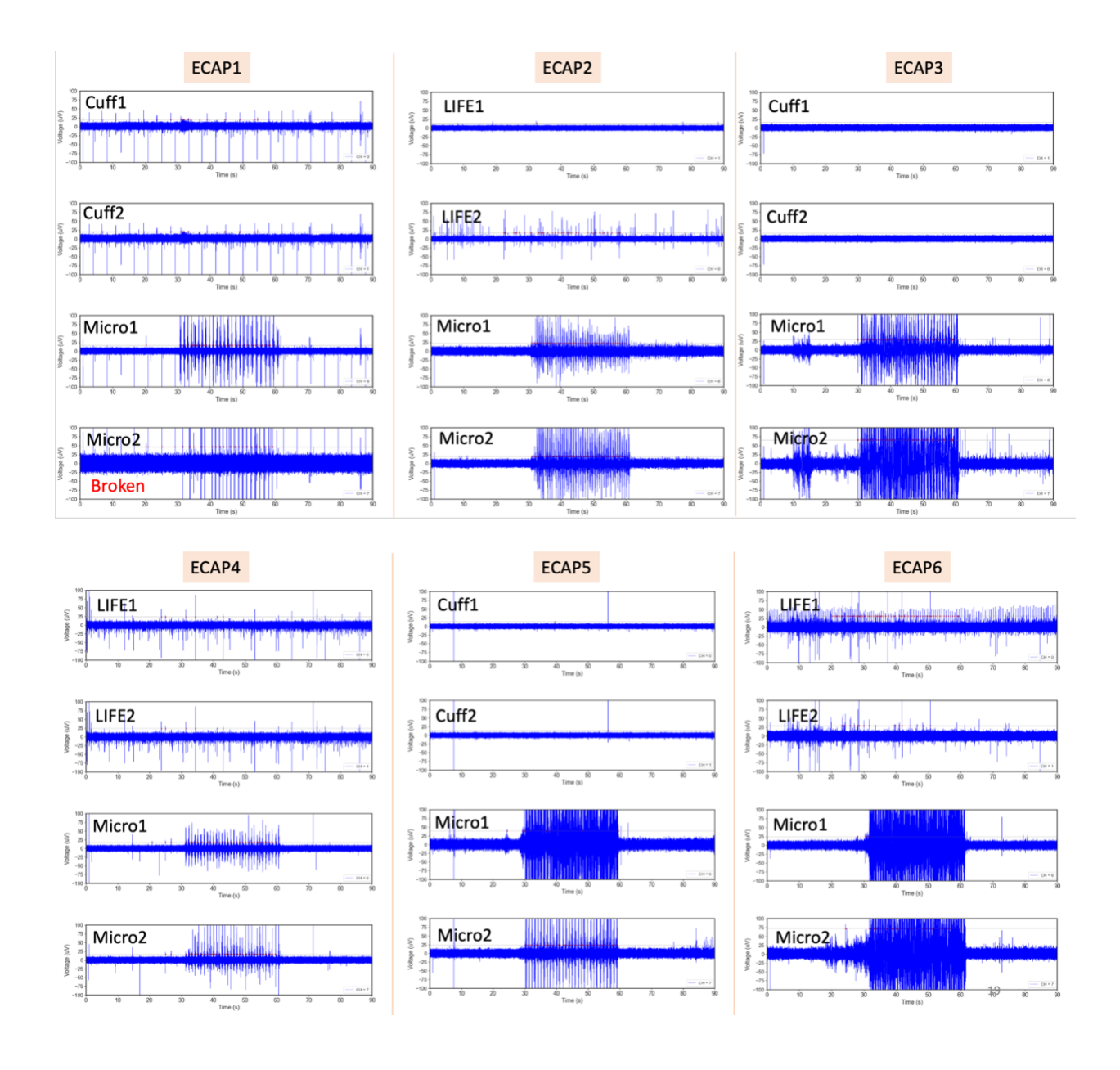


Figure 2.22: Spike count from sensory stroking evoked naturally occurring activity on all subjects.

(top-left) subject 1 to (bottom-right) subject 6. 90 seconds of recording shown: first 30 seconds are quiescent with no stroking, 30-60s are on-target stroking at the region of the auricle innervated by the great auricular nerve, and 60-90s are off-target stroking at a region of the auricle not innervated by the great auricular nerve.

Supplementary Material 11 – Spontaneous activity recordings from cervical vagus nerve (cVN)

None of the electrode recordings showed clear and repeatable spontaneously occurring neural activity in the cVN. Signals that initially appeared neural were likely motion artifacts as they persisted more than 20 minutes after the nerve was transected cranial and caudal to the recording electrodes. Further, the artifacts were more pronounced in subjects 1-3, where the subjects experienced more tremor as insufficient muscle paralytic, vecuronium, was administered, compared to subjects 4-6.

Representative recordings from 1 cuff contact (channel 0), 1 LIFE electrode (channel 5), and 1 microneurography electrode (channel 8) per subject:

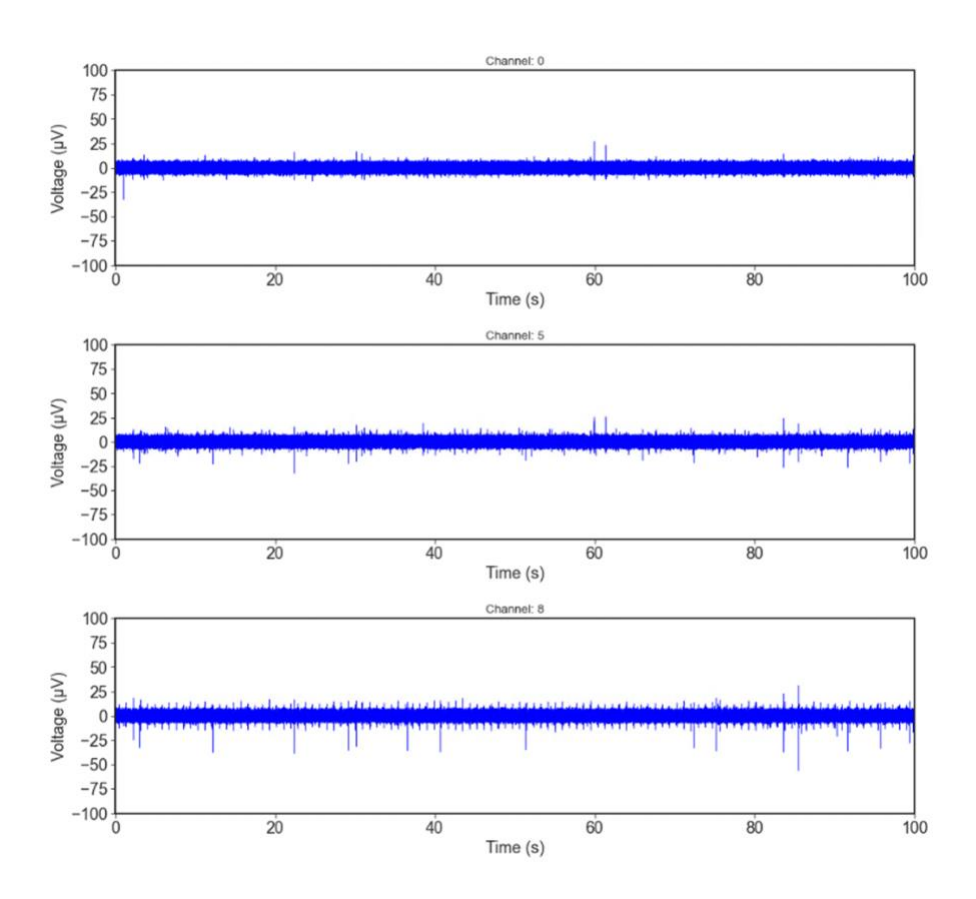


Figure 2.23: Subject 1 cVN spontaneous activity recording.

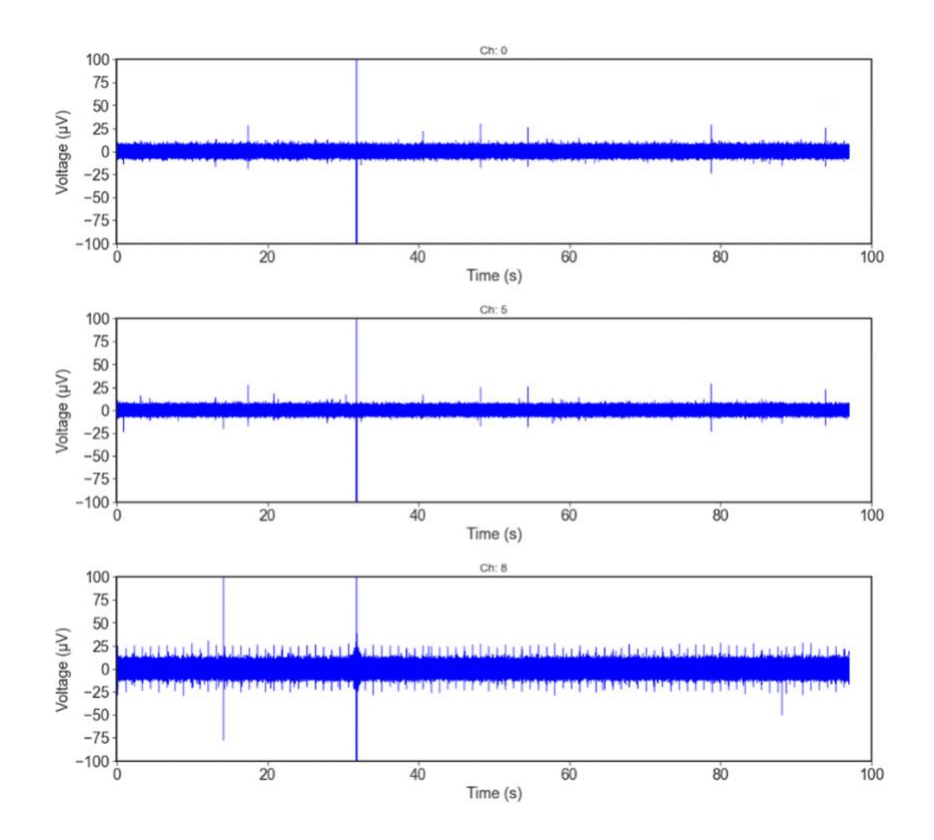


Figure 2.24: Subject 2 cVN spontaneous activity recording.

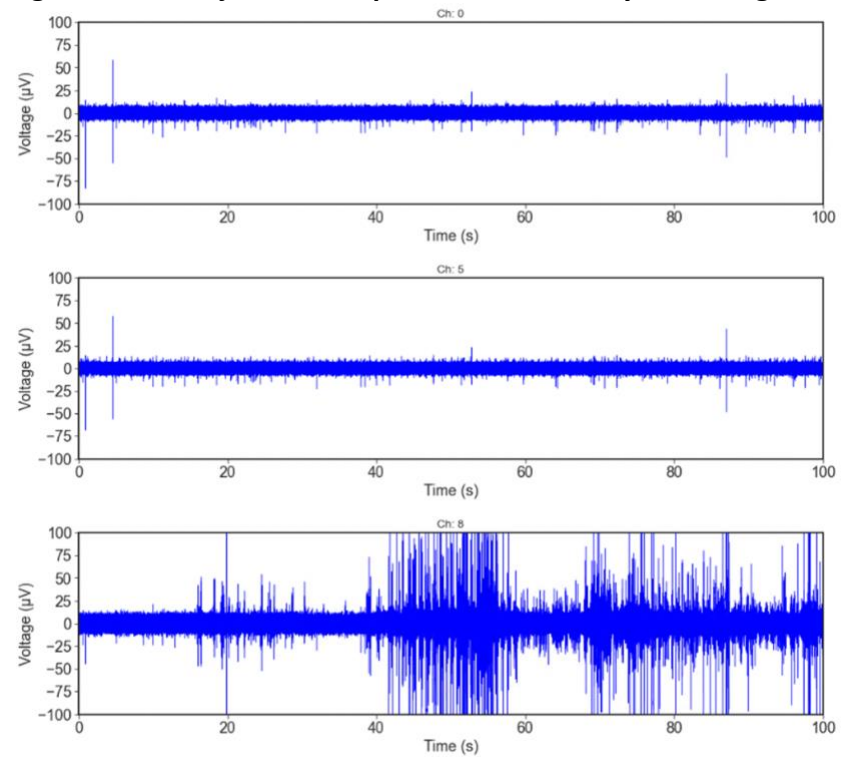


Figure 2.25: Subject 3 cVN spontaneous activity recording.

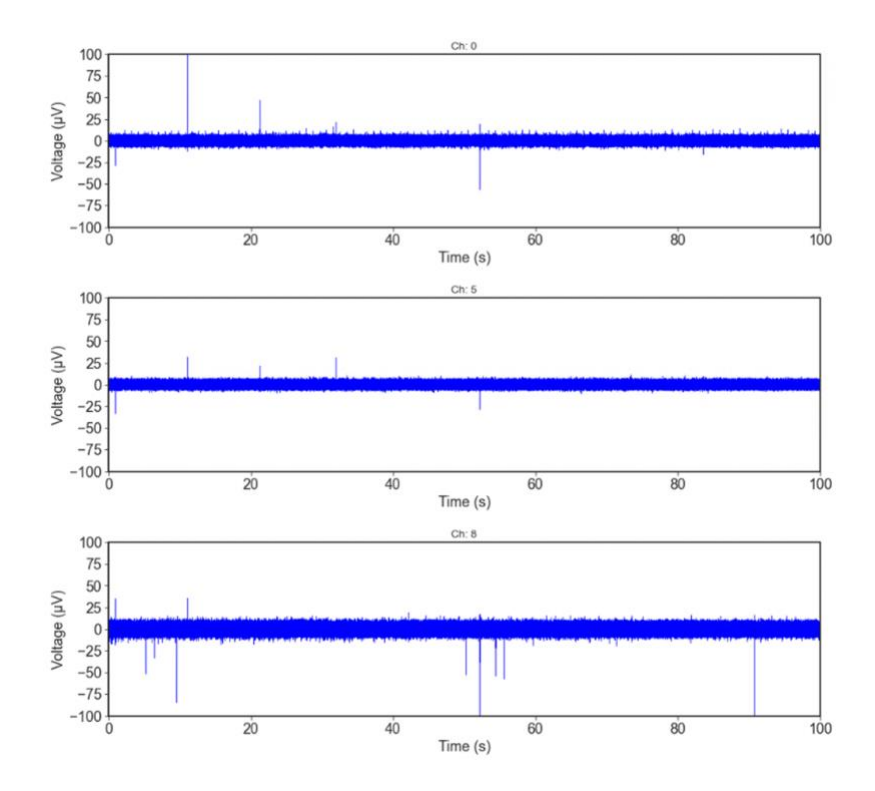


Figure 2.26: Subject 4 cVN spontaneous activity recording.

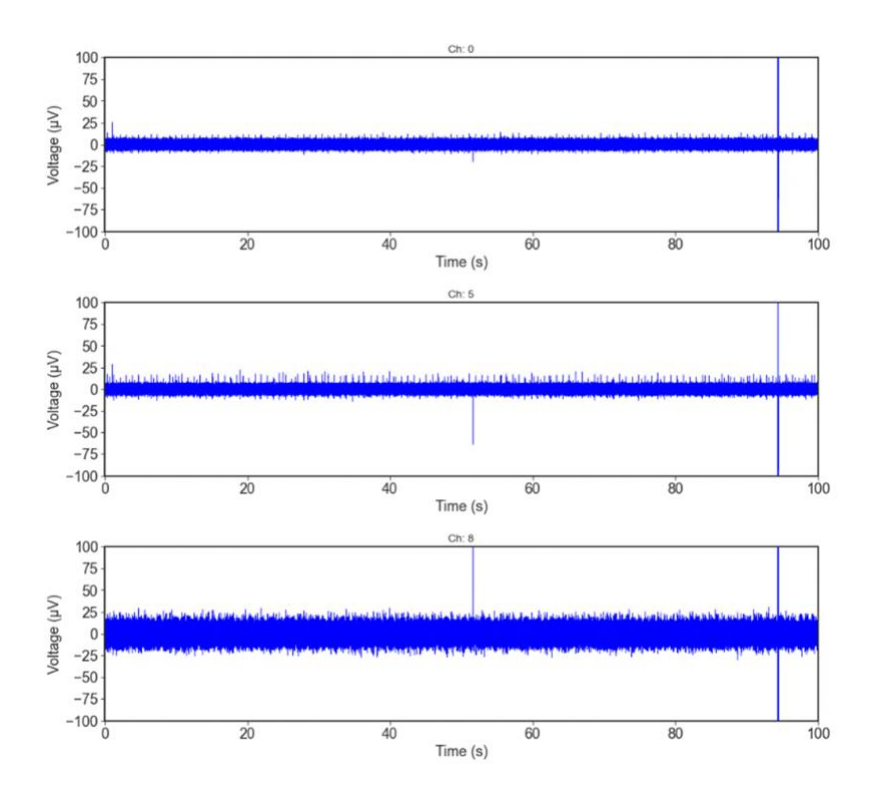


Figure 2.27: Subject 5 cVN spontaneous activity recording.

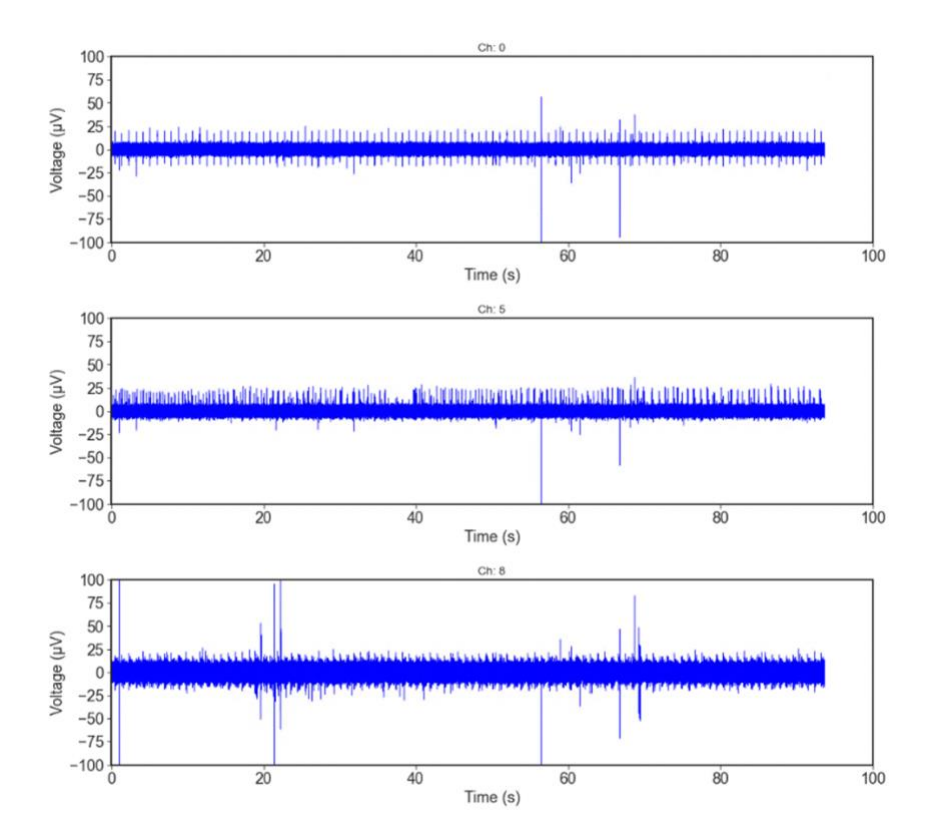


Figure 2.28: Subject 6 cVN spontaneous activity recording.

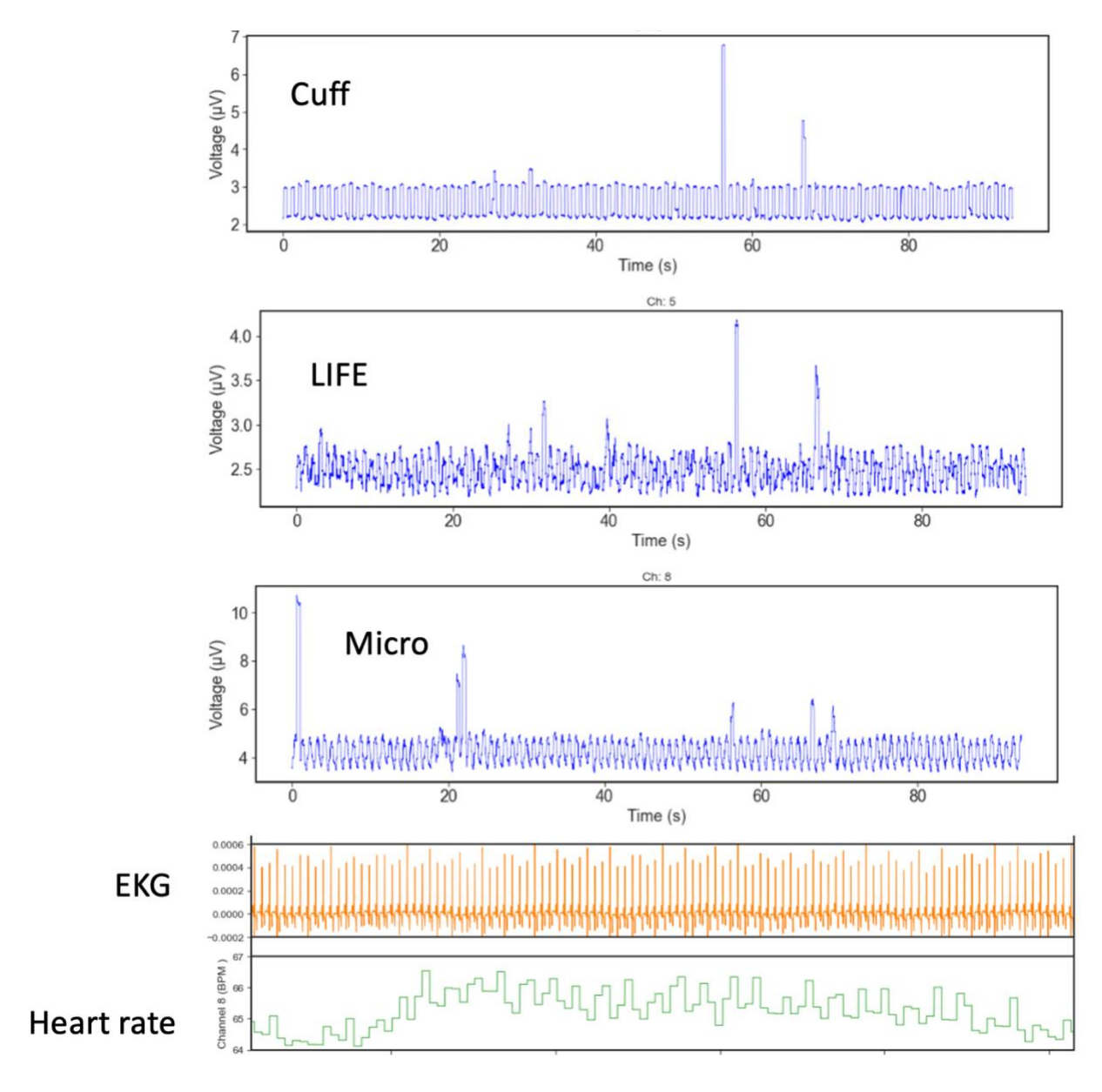


Figure 2.29: Subject 6 cVN spontaneous activity recording presented as an integrated neurogram.

(top) Neurogram constructed of moving average (400 ms window) root mean square (RMS) signal. (bottom) EKG and HR calculated from EKG for corresponding time window.

Chapter 3 Augmented Transcutaneous Stimulation Using an Injectable Electrode: A Computational Study This chapter was adapted from the following article published in a peer-reviewed journal:

Verma, N., Graham, R. D., Mudge, J., Trevathan, J. K., Franke, M., Shoffstall, A. J., et al. (2021).

Augmented Transcutaneous Stimulation Using an Injectable Electrode: A Computational Study.

Front. Bioeng. Biotechnol. 9, 796042. doi: 10.3389/fbioe.2021.796042.

Abstract

Minimally invasive neuromodulation technologies seek to marry the neural selectivity of implantable devices with the low-cost and non-invasive nature of transcutaneous electrical stimulation (TES). The Injectrode® is a needle-delivered electrode that is injected onto neural structures under image guidance. Power is then transcutaneously delivered to the Injectrode using surface electrodes. The Injectrode serves as a low-impedance conduit to guide current to the deep on-target nerve, reducing activation thresholds by an order of magnitude compared to using only surface stimulation electrodes. To minimize off-target recruitment of cutaneous fibers, the energy transfer efficiency from the surface electrodes to the Injectrode must be optimized.

TES energy is transferred to the Injectrode through both capacitive and resistive mechanisms. Electrostatic finite element models generally used in TES research consider only the resistive means of energy transfer by defining tissue conductivities. Here, we present an electroquasistatic model, taking into consideration both the conductivity and permittivity of tissue, to understand transcutaneous power delivery to the Injectrode. The model was validated with measurements taken from (n=4) swine cadavers. We used the validated model to investigate system and anatomic parameters that influence the coupling efficiency of the Injectrode energy delivery system. Our work suggests the relevance of electroquasistatic models to account for capacitive charge transfer mechanisms when studying TES, particularly when high-frequency voltage components are present, such as those used for voltage-controlled pulses and sinusoidal nerve blocks.

Introduction

The Injectrode is a minimally invasive neuromodulation electrode technology designed to provide the selectivity of an implanted electrode with a more favorable risk profile (Trevathan et al., 2019; Dalrymple et al., 2021). It can be injected using a syringe and forms in-body onto the neural structure to better isolate the target nerve, even with individual anatomical differences. Prior work showed the Injectrode's ability to undergo large reversible deformations, and therefore keep up with the natural stretch of peripheral nerves during body motion, and its stiffness (Young's modulus) to be only slightly higher than that of nerve tissue (Trevathan et al., 2019). The flexibility of the Injectrode allows it to conform around complex neural structures, including nerve plexi found close to target end-organs, which is difficult with conventional pre-formed neurostimulation electrodes. Therefore, the Injectrode may extend the range of nerves that can be targeted with neurostimulation and improve end-organ targeting specificity. Additional Injectrode material is extruded as part of the injection to form a conductive conduit connecting the deep nerve target to just under the surface of the skin. Finally, more Injectrode is injected just under the skin to create a disc shaped 'collector'. This collector couples with external non-invasive TES electrodes to transfer charge delivered from a non-invasive TES unit and route it to the deep target nerve. Fig. 3.1 (a) illustrates the delivery procedure of the Injectrode system.

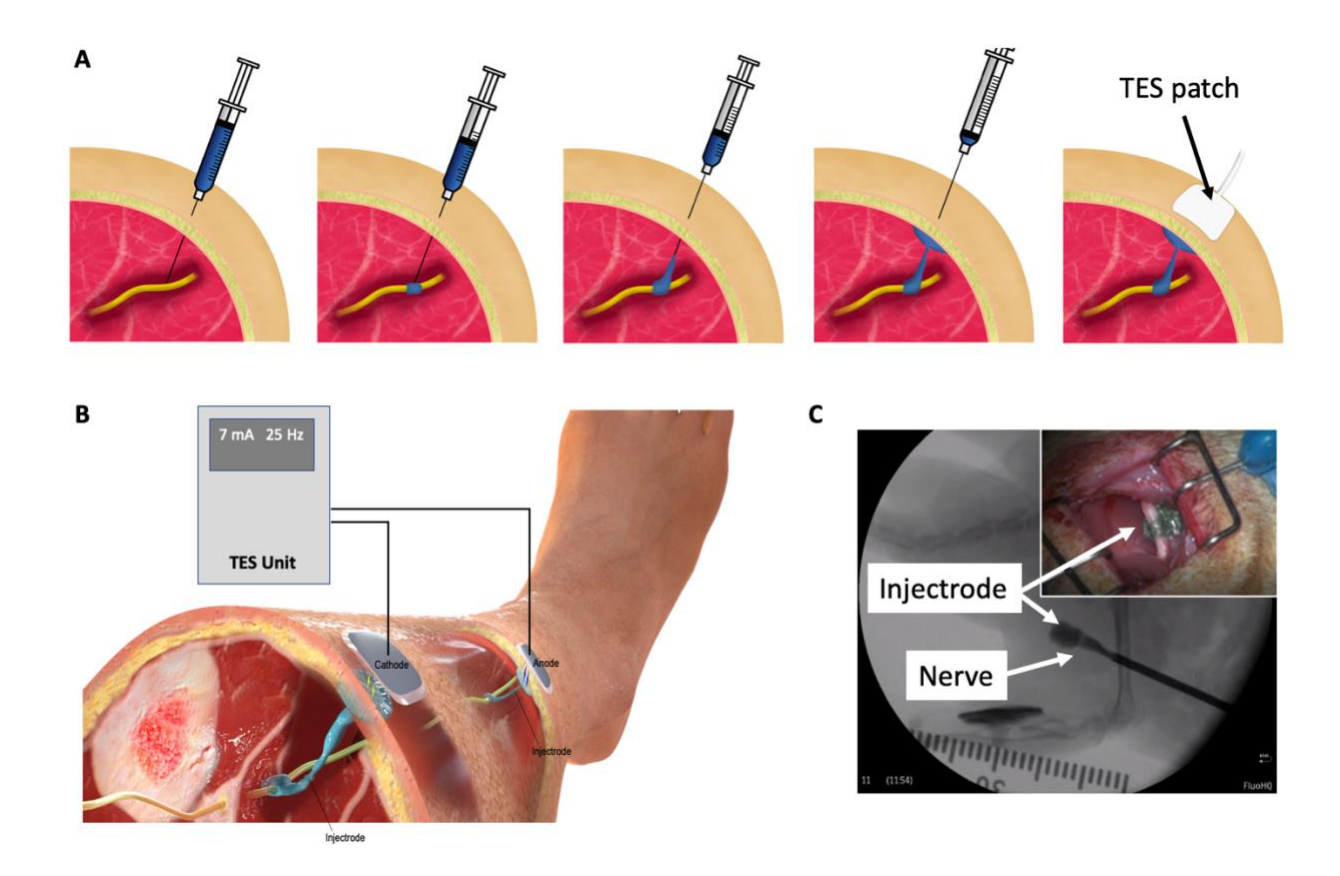


Figure 3.1: Injectrode placement and usage.

(a) Delivery procedure of the Injectrode system. The Injectrode is injected onto a neural structure. A syringe containing the Injectrode is deployed to the target nerve under image guidance. The Injectrode is deployed to form an interface with the nerve. The syringe is then drawn back while injecting the Injectrode – to form a conductive path from the deep nerve to skin. More Injectrode material is then injected under the skin to form a 'collector'. An externally placed TES patch electrode non-invasively delivers charge to the Injectrode. (b) Injectrode system in bipolar configuration after deployment. A TES unit is used to deliver energy non-invasively to the Injectrode collectors. The Injectrode sets up a low-impedance conduit to guide current to the deep target nerve. (c) Injectrode delivery onto a neural structure under image guidance. Opacity in the figure corresponds to the Injectrode's thickness with a portion going around the nerve showing lightest opacity. (Inset top right) Injectrode conforming to neural structure.

Energy is delivered to the Injectrode by external surface electrodes using low-frequency electric fields through both capacitive and resistive mechanisms. Capacitively, the external surface electrode and the in-body subcutaneous collector act like two plates of a capacitor with skin as the dielectric. High-frequency components of the electric field are transferred

preferentially through this capacitive route. Simultaneously, current is also transferred through a resistive route. The surface electrodes set up an electric potential gradient in tissue, visualized in Fig. 3.2 (d). The Injectrode collector is placed subcutaneously, close to the surface electrodes, and provides a low-impedance conduit for current to flow from one collector, down the Injectrode lead, through the nerve and other tissue, and back up the other Injectrode lead and collector. If the path formed by the Injectrode is of lower impedance than a direct path between the two collectors through tissue, current preferentially travels through the Injectrode path, stimulating the deep on-target nerve in the process. The concept of power transfer across the skin from surface electrodes to implanted electrodes using low-frequency electric fields has been previously presented (Gan and Prochazka, 2007; Gan and Prochazka, 2010; Gaunt and Prochazka, 2009), with the Injectrode system now providing a minimally invasive injectable implementation of the concept.

The Injectrode system is a platform technology that could be applied to various neuromodulation indications. To minimize off-target recruitment of cutaneous and superficial fibers by the surface electrodes, energy transfer efficiency from the surface electrodes to the Injectrode must be optimized. Investigating power transfer across the skin to the Injectrode collector requires consideration of charge transfer due to both resistive and capacitive means. Finite element analysis in the TES field traditionally considers charge transfer only due to resistive means using an electrostatic analysis (Kuhn et al., 2009). An electrostatic, or direct-current (DC), analysis ignores the capacitive displacement current that accompanies oscillating electric fields, which is essential to understand the transcutaneous capacitive charge coupling behavior of the Injectrode. Previous work has established the importance of dielectric

properties of tissue and capacitive charge transfer even when studying TES therapies (Medina and Grill, 2014; Poulsen et al., 2020; Kuhn et al., 2009). The skin acts as a dielectric and allows direct coupling of higher-frequency components in the TES waveform from surface electrodes to the underlying tissue. The placement of subcutaneous Injectrode collectors increases this capacitive coupling and resultant capacitive charge transfer.

Here, we use the finite element method (FEM) to develop an electroguasistatic model for the Injectrode system to study power transfer from the surface electrodes to the Injectrode collector by both capacitive and resistive means. We selected model dimensions considering the neck region in humans. The desired on-target effect was recruitment of the vagus nerve and undesired off-target effect was activation of cutaneous and superficial fibers responsible for paresthesia or lip curl (likely due to activation of the cervical branch of the facial nerve innervating the platysma muscle, as seen in use of the gammaCore non-invasive vagus nerve stimulation (nVNS) device (Nonis et al., 2017)). We validated the model output in swine cadavers and then used the validated model to investigate Injectrode system and anatomic parameters (e.g., tissue thickness and conductivity) that influence the coupling efficiency of charge delivery to the Injectrode collector. Finally, we performed biophysical modeling to investigate how the Injectrode alters recruitment of on- and off-target neural structures in comparison to traditional TES. These results provide insights into waveform design and system parameters for the optimization of the Injectrode system to achieve on-target activation of deep neural structures while minimizing off-target activation of superficial neural fibers.

Methods

Electroquasistatic FEM model

COMSOL Multiphysics version 5.5 software (COMSOL, Burlington, MA) was used to create and solve the FEM model for electric field and currents. A three-dimensional model was set up using the Electric Currents physics interface under the AC/DC module. The Electric Currents physics interface computes both ohmic (resistive) and displacement (capacitive) currents by considering tissue conductivity and permittivity, respectively, while ignoring inductive effects (Bossetti et al., 2008). A three-layer tissue model consisting of skin, fat, and muscle was set-up as shown in Fig. 3.2 (a). The Injectrode system was constructed using two square surface electrodes and two subcutaneous circular collector electrodes. To isolate and investigate the effects of system parameters on transcutaneous coupling between the surface electrodes and collectors, we used a defined electrical load between the two collectors (Fig. 3.2 (b)) implemented in the Electric Circuit physics interface in COMSOL. The electrical load was defined as a 1 k Ω resistor, based on electrical impedance spectroscopy (EIS) measurements from Trevathan et al. (2019), to model the impedance of the Injectrode connection from the collector down to the nerve, the Injectrode-nerve interface, the nerve impedance, and the leakage between the two Injectrode conduction paths (Fig. 3.2 (c)). Boundary conditions for the external tissue surfaces were set to zero normal current and an initial condition of 0 V. In the monopolar configuration, shown in Fig. 3.2 (e), ground was set as the five surfaces (left, right, bottom, front, and back) of the muscle layer and an end of the 1 $k\Omega$ resistor was set to the 0 V ground potential. The other external tissue surfaces in the monopolar model were set to the same boundary conditions as in the bipolar model. The model was run with stationary (DC),

time-dependent (transient), and frequency-domain studies. The frequency-domain study used a complex analysis denoting ohmic currents as real and displacement currents as imaginary. All currents and voltages reported are absolute values.

In the simplified three-layer transcutaneous coupling efficiency model, internal current (Gan and Prochazka, 2010), or nerve current, was measured as the current flowing through the 1 k Ω resistor and denoted as I_{Nerve} (mA). External current or TES current was measured as the current delivered by the external TES electrode and denoted as I_{TES} (mA), with the corresponding voltage to drive the TES current denoted as V_{TES} (V). The simplified three-layer model allowed study of the transcutaneous coupling behavior of the surface electrodes with the subcutaneous Injectrode collectors. A capture ratio (Gan and Prochazka, 2010) of I_{Nerve}/I_{TES} was calculated to estimate the efficiency of the transcutaneous current delivery to current arriving at the modeled deep nerve and reported as 'efficiency' (%). Lastly, surface electrode current density was used as a proxy for off-target cutaneous fiber activation (Slopsema et al., 2018) and I_{Nerve} was used as a proxy for on-target neural fiber activation.

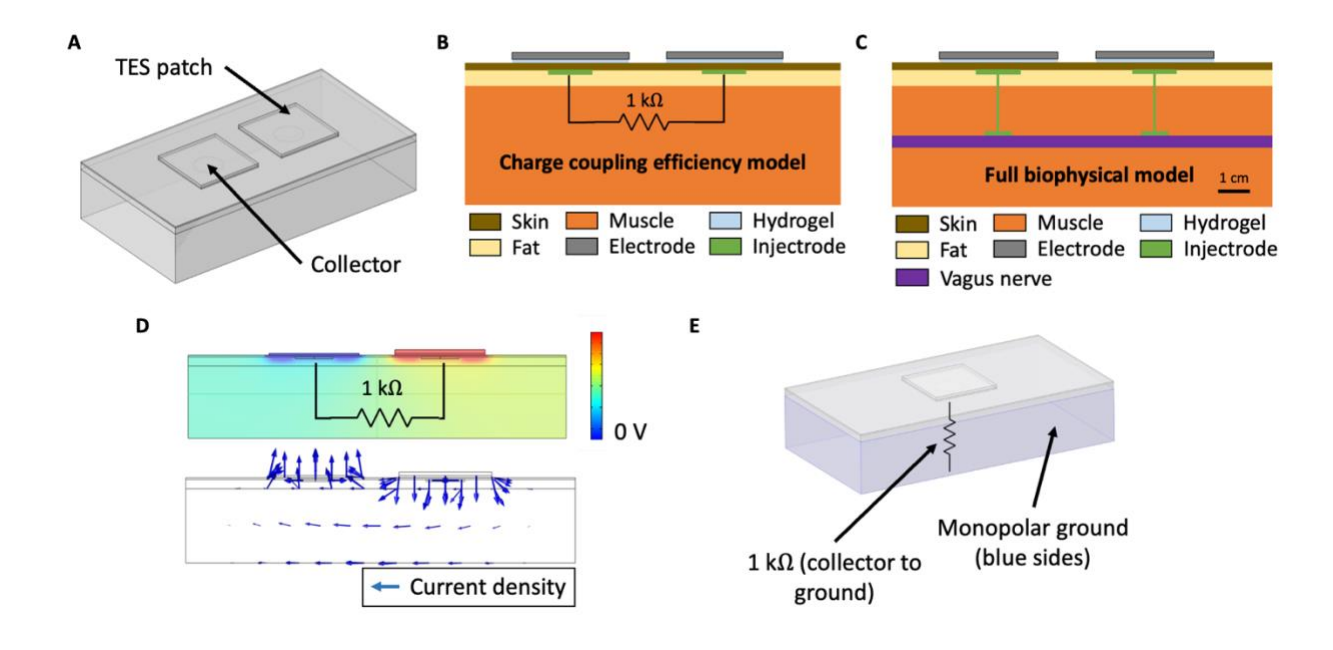


Figure 3.2: Model of the Injectrode system in COMSOL Multiphysics

(a) Three-layer tissue model of the Injectrode system in COMSOL Multiphysics to study transcutaneous charge transfer from the surface electrodes to the subcutaneous collectors. (b) Schematic of the Injectrode system simplified FEM model. The charge coupling efficiency model was used to study the transcutaneous charge transfer from the surface electrodes to the subcutaneous collectors. The 1 k Ω resistor was used to represent the impedance of the Injectrode connection to the deep nerve, the Injectrode-nerve interface, the nerve, and the leakage between the two Injectrode conduction paths. (c) Schematic of the Injectrode system full FEM model. The full biophysical model was used to study on- and off-target neural recruitment with the Injectrode system. (d) (Top) Electric potential solution for the standard model configuration at 10 kHz. Electric potential difference between the two subcutaneous collectors causes current to flow through the 1 k Ω resistor connecting the two collectors. (Bottom) Arrows representing current density flow (1 k Ω resistor not shown). (e) Monopolar configuration of the Injectrode system to study the transcutaneous power transfer from the surface electrode to the subcutaneous Injectrode collector. Here, the 1 k Ω resistor is connected from the single collector to a 0 V ground potential.

Model geometry was set to replicate the parameters of a 50-60 kg domestic swine's lower abdomen, on which the model was validated, and is in the range of human tissue thicknesses at the neck. The human neck represents a possible target to access the vagus nerve for an Injectrode deployment. Tissue thickness was set as 1 mm for skin – typical of the

measurements made in the swine model at the abdomen (mean=1.01 mm; standard deviation (SD)=0.31 mm; n=16 measurements). However, the skin at the neck is thicker in swine. The selected model skin thickness of 1 mm is also in the range of human skin thickness at the neck (mean=1.3 mm; SD=0.2 mm) (Hoffmann et al., 1994). Fat and muscle thickness were set at 5 mm and 40 mm, respectively, to represent the measured values in swine. These values are representative of the human neck region (Störchle et al., 2018). A FEM model area of 21 cm by 11 cm was studied, leaving a minimum border of 2 cm between the surface electrodes and model edges to reduce interference from edge effects. The model size was varied to ensure that a larger area would not results in a difference of more than 1% in nerve current (I_{Nerve}) (Poulsen et al., 2020).

Several steps were taken to ensure proper selection of mesh size and time steps for the FEM analysis. 'Physics' settings in the COMSOL software were used to efficiently define the mesh properties and time steps, allowing for shorter intervals in regions of greater parameter gradients. Mesh density was progressively made coarser to decrease computation time while nerve current (I_{Nerve}) remained within 1% of the finest mesh size (Kuhn et al., 2009; Poulsen et al., 2020). The direct solver was used to solve the stiffness matrix. Computations were run locally on a Windows 10 desktop with a 3.00 GHz Intel i7 processor and 32 GB of RAM.

Tissue conductivity and permittivity values

The selection of appropriate skin, fat, and muscle conductivity and permittivity values is important to construct an accurate model. We used values from the well-established Gabriel et al. (1996b) database – summarized in Table 3.1. Where available, values were drawn from the

same database to prevent bias that may arise when selecting values from multiple sources. Several formulations of the Injectrode exist and they are all highly conductive either because they are made of thin metal wires (gold or platinum) or because they exceed the percolation threshold of the material mixtures (Deepalekshmi et al., 2018; Trevathan et al., 2019). The Injectrode was modelled as a conductive metal, which is several orders of magnitude more conductive than tissues, and hence its exact value was not a sensitive parameter. In COMSOL, the "contact impedance" was set to $6.9 \times 10^{\text{A}} - 2 \Omega \cdot \text{m}^2$, based on empirical measurements detailed in Supplementary Material 2, to define all Injectrode-tissue electrochemical interfaces.

Table 3.1: Material electrical properties used in the FEM model

Tissue	Conductivity	Relative	Source
	(S/m)	permittivity	
Skin	1.80 x 10^-4	1.17 x 10^3	Human, 37 °C, 1 kHz, dry (Gabriel et al.,
			1996b)
Fat	2.46 x 10^-2	2.08 x 10^4	Bovine, 37 °C, 1 kHz, non-infiltrated fat
			(Gabriel et al., 1996b)
Muscle	5.23 x 10^-1	1.24 x 10^6	Ovine, 37 °C, 1 kHz, parallel muscle fibers
			(Gabriel et al., 1996b)
Epineurium	1.59 x 10^-1	NA	Pelot et al., 2019
Hydrogel	1.6 x 10^-2	1.4 x 10^6	Measured, see Supplementary Material 2
Injectrode	3.774 x 10^7	1	COMSOL in-built value for a conductive
			metal

Dispersive properties, or frequency-dependent conductivity and permittivity, were not considered in the current model. Literature values (Gabriel et al., 1996b) show that skin, fat, and muscle conductivity do not change substantially within the 10 Hz – 25 kHz frequency range, which is the range relevant to this study. Fat and muscle permittivity (but not skin permittivity) are a function of frequency in this range but were considered a second-order effect in this simplified model. Frequency-dependent conductivity and permittivity may be added to the model – improving its accuracy by <10 percentage points, but in exchange for increased mathematical complexity and computation time (Zander et al., 2020).

Cadaver validation of FEM model

To validate the FEM model, measurements were taken from the abdominal region of domestic swine within two hours of death. Tissue has been reported to preserve its electrical properties for a few minutes to hours after death (Foster and Schwan, 1989). Skin at the abdominal region of the pig is similar in thickness to human skin at the neck (Hoffmann et al., 1994). The domestic swine is a good model for human skin, with similar histological and biochemical properties, such as epidermal turnover time, subdermal adipose tissue, vasculature, and collagen structure, and arrangement in the dermis (Avci et al., 2013). Although domestic swine do not possess eccrine sweat glands, they have apocrine glands distributed throughout their skin surface (Avci et al., 2013). The protocol described below was developed through (n=5) preliminary cadaver experiments (data not shown). Once the final protocol was established, confirmatory measurements were taken from both sides of (n=4) swine cadavers and are presented here.

An approximately 2 cm incision was made in the skin using a scalpel. Forceps were used to bluntly dissect a space between the skin and fat layer, creating a pocket for the collector to be inserted. The creation of the incision a distance from the surface electrodes prevented current from routing through a break in the skin. Similar to Gan and colleagues (Gan and Prochazka, 2010), a stainless-steel disk (2.1 cm diameter) was used as a consistent representation of an Injectrode collector for comparison to FEM model outputs, because an Injectrode collector varies from deployment to deployment due to local tissue consistency and conformance. Fig. 3.4 (a) shows the similar size and shape between a stainless-steel disc and the cured Injectrode collector. This similar size and shape ensures similar results for V_{TES} , I_{TES} , and I_{Nerve} . A second 2 cm incision was made to insert the second collector. A 1 k Ω resistor was connected externally between the two collectors (between the two red wires running out of the incision on the left side of Fig. 3.4 (a)), which allowed us to precisely compare cadaver data to the paired FEM model. Surface electrodes 5 x 5 cm in size (TENSpros, Saint Louis, MO) were applied with an edge-to-edge separation of 2 cm. Prior to taking measurements, 5 minutes were allowed for the surface electrodes to equilibrate with skin.

After equilibration, stability of the electrode-skin interface was verified by delivering ten $300~\mu s$ current-controlled pulses at 19 mA and measuring the voltage across the TES electrodes. Next, our test stimulation waveforms were delivered at the surface TES electrodes using an AM 4100 isolated high-power stimulator (AM Systems, Sequim, WA). Stimulus was delivered at 19 mA for current-controlled and 28 V for voltage-controlled waveforms, below the voltage at which electroporation occurred. Electroporation, marked by a sudden decrease in electrode-skin impedance, was observed during preliminary testing at the swine neck when a stimulus

over 90 V was applied during a 300 μ s pulse. Several waveforms, including monophasic pulses of varying rise times, were tested. Waveform test order was randomized. The initial 300 μ s current-controlled pulse at 19 mA was delivered again at the end of testing to check for degradation over time in the cadaver model. All measurements were made within 20 minutes of incision to reduce fluid buildup in the surgical pockets. No appreciable degradation was measured during any confirmatory experiment. The procedure was then repeated on the contralateral side of the abdomen.

Nerve current (I_{Nerve}), i.e., internal current (Gan and Prochazka, 2010), was calculated from voltage measurements taken across the 1 k Ω resistor connected between the two collectors using a TMDP0200 high-voltage differential probe (Tektronix, Beaverton, OR). V_{TES} , the voltage across the TES electrodes, was measured using an identical differential probe. Both differential probes were connected to a DPO2004B oscilloscope (Tektronix, Beaverton, OR) with an external probe power supply. A Keithley DAQ 6510 (Tektronix, Beaverton, OR) measured the current to the TES electrode (I_{TES}). It was crucial to use a setup that was well isolated from ground for the appropriate frequency range under measurement. The AM 4100 isolated stimulator was not well isolated from ground at higher-frequency voltages; therefore, in confirmatory experiments, differential probes were used to achieve electrical isolation. After waveform testing, the skin between the surface electrode and collector was cut with a scalpel and its thickness was measured using a Vernier caliper to be (mean=1.01 mm; SD=0.31 mm; n=16 measurements).

Multi-compartment neuron model

To study on-target (i.e., vagus) and off-target (i.e., cutaneous) neuronal activation, we modified the validated FEM model used to study transcutaneous charge coupling (Fig. 3.3 (a)) and implemented multi-compartment cable models of cutaneous and vagal axons using the NEURON simulation environment (v7.7) (Hines et al., 1997). In the full biophysical FEM model, the vagus nerve was modelled as a 3 mm diameter (Hammer et al., 2018; Stakenborg et al., 2020) cylinder with the conductivity of epineurium (Pelot et al., 2019). Vagus nerve stimulation for epilepsy is believed to activate sensory fibers for its therapeutic benefits (Krahl, 2012). AB fibers are the lowest activation threshold sensory fibers in the cervical vagus and may feasibly be recruited during clinical stimulation (Nicolai et al. 2020; Krahl, 2012). We implemented previously described axon models of an A β -low-threshold mechanoreceptor (LTMR) in both the vagus and cutaneous regions (canonically responsible for paresthesia), and an A δ -highthreshold mechanoreceptor (HTMR) in the cutaneous region (canonically responsible for noxious sensations). Briefly, we modeled each axon morphology using the double-cable McIntyre-Richardson-Grill (MRG) model of a myelinated mammalian peripheral axon (McIntyre et al., 2002). We represented each nodal, paranodal, and juxtaparanodal section with a single compartment, and divided each internodal region into six compartments of equal length. The MRG axon model is parametrized for discrete axonal diameters. Therefore, we modeled a 10.0 μm diameter A β -axon and a 2.0 μm diameter A δ -axon to approximate the axonal diameters used in previous modeling studies of TES (McIntyre et al., 2004; Tigerholm et al., 2019). We modeled the membrane dynamics of each axon using previously described ion channel properties of A β -LTMRs (Graham et al., 2019) and A δ -HTMRs (Graham et al., 2020), which

reproduced experimental data describing action potential characteristics and conduction velocities found in sensory neurons.

We then distributed each axon type throughout the bipolar Injectrode FEM model. A modified FEM model was used for the biophysical study, additionally incorporating the vagus nerve, Injectrode leads down to the vagus nerve, and Injectrode interfaces with the vagus nerve (Fig. 3.3 (a)) all of which were previously modeled as a 1 k Ω resistor between the two collectors (Fig. 3.2 (b)). The previous simplified FEM model allowed direct interpretation of the results as being caused by changes in the transcutaneous charge coupling efficiency between the surface electrodes and collectors. For the biophysical investigation, we created two populations of axon trajectories: a population of axons in the vagus nerve, and a population of cutaneous afferents that terminated below the active TES patch electrode (Fig. 3.3 (b)). To generate the vagus axon population, we created a two-dimensional regular grid parallel to the face of the vagus nerve with 100 μ m spacings in all directions. Each point on the grid acted as a seed point for a vagus axon, which then traveled in a straight line to the other end of the nerve.

We also modeled A β - and A δ -cutaneous axons, morphologically and anatomically similar to the cutaneous afferent models developed by Tigerholm and colleagues (Tigerholm et al., 2019). The cutaneous axon population was constructed using a two-dimensional regular grid parallel to the active TES patch with 1.5 mm spacings in all directions, 900 μ m beneath the surface of the skin. This grid extended 5 mm beyond the edge of the TES patch. Each point on the grid acted as a terminal point for an A β -cutaneous axon, responsible for transmitting mechanosensations, which may result in paresthesias (Tigerholm et al., 2019). Cutaneous A δ -axons terminate more superficially than A β -axons and are responsible for transmitting noxious

sensations (Tigerholm et al., 2019; Mørch et al., 2011). Therefore, we generated a separate two-dimensional regular grid parallel to the active TES patch, 500 μ m beneath the surface of the skin to serve as terminal points for cutaneous A δ -axons. Each cutaneous axon traveled parallel to the vagus nerve 4 mm under the surface of the skin in the subcutaneous fat layer of the FEM model, before branching up towards the skin (Tigerholm et al., 2019). Cutaneous A β -axons terminated in a passive (i.e., containing no active membrane currents – only a membrane capacitance and leak conductance) node of Ranvier, while cutaneous A δ -axons terminated in an unmyelinated passive branching structure using a previously described morphology, which reproduces nerve fiber densities found in human skin (Tigerholm et al., 2019).

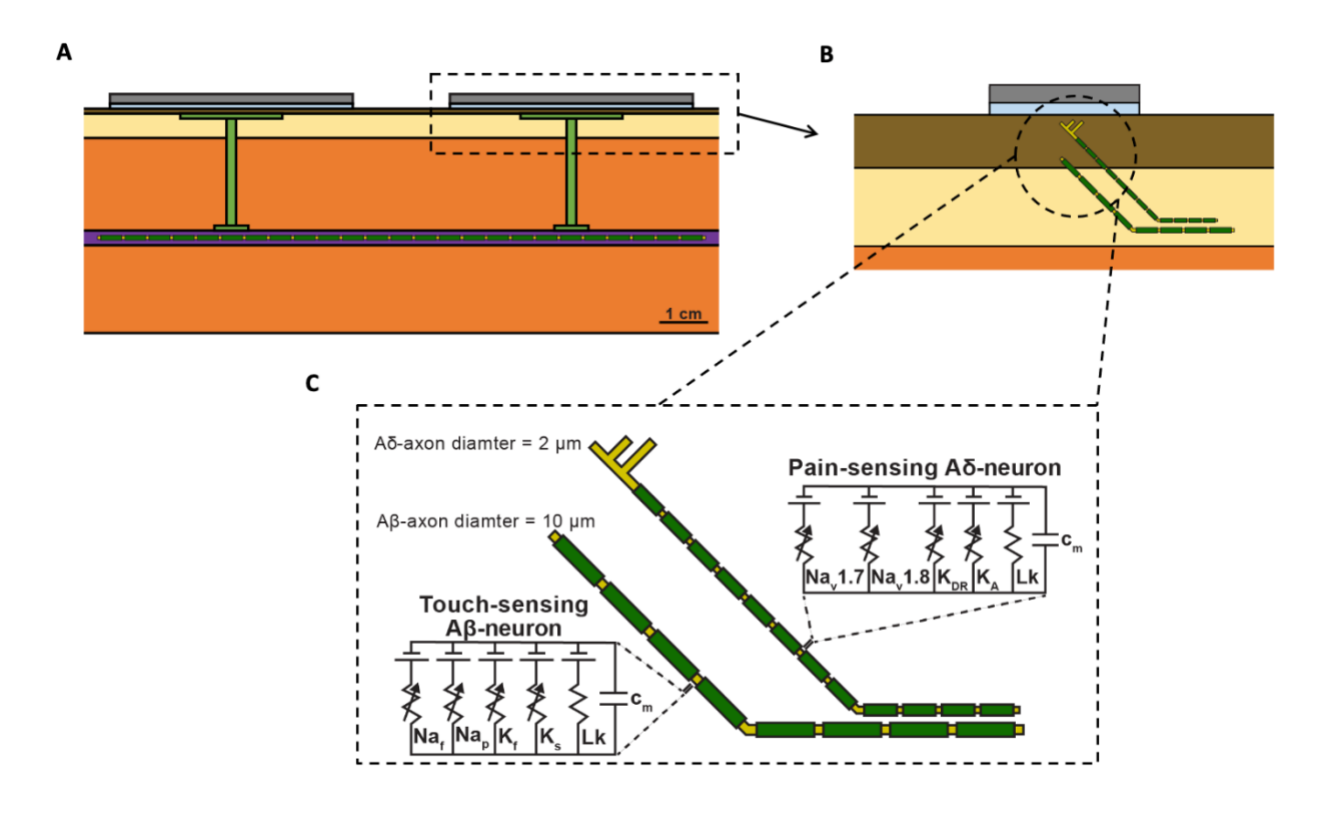


Figure 3.3: NEURON biophysical study

(a) Full FEM model used in the biophysical study. The 1 k Ω resistor between the two collectors in the simplified FEM model was replaced with the vagus nerve, Injectrode connections down to the vagus nerve, and Injectrode interfaces with the vagus nerve. The vagus nerve was

populated with axons. **(b)** Zoomed view of dotted box in (a) showing the skin populated with cutaneous fibers. **(c)** Biophysical equivalent circuit model of cutaneous $A\beta$ and $A\delta$ neural fibers.

Simulating the neural response to the Injectrode system

We interpolated the extracellular potentials calculated by the FEM model onto the middle of each neural compartment and used NEURON's extracellular mechanism within the Python programming environment to simulate the axonal response to the Injectrode system (Hines et al., 2009). We used a backward Euler implicit integration method with a time step of 5 μ s to calculate each compartment's time-varying transmembrane voltage in response to Injectrode-TES stimulation (Graham et al., 2019). Our goal was to investigate how the Injectrode system affects the activation of on- and off-target axons. Therefore, we calculated each axon's activation threshold, i.e., the minimum current amplitude needed to induce a propagating action potential, using a binary search algorithm with a resolution of 1 μ A. For all biophysical simulations, we used an idealized square-wave current-controlled stimulus pulse of 300 μ s pulse width.

Results

This work establishes a FEM model of the Injectrode system to study transcutaneous charge coupling using low-frequency electric fields. An electroquasistatic model was set up in COMSOL, solving for both ohmic (resistive) and displacement (capacitive) current to study transcutaneous charge coupling in the Injectrode system. The transcutaneous coupling FEM model was a simplified model used to isolate changes due to coupling behavior between the surface electrodes and the collector. The transcutaneous coupling FEM model was validated with

measurements of several waveforms on both the left and right side of recently dead swine (n=4). The validated model was used to investigate the Injectrode system and patient-dependent parameters (e.g., surface electrode placement, tissue thickness, skin preparation, tissue electrical properties) most sensitive to coupling efficiency (ratio between nerve current and externally applied surface electrode current). Maximizing the efficiency ratio minimizes surface electrode current, which activates off-target cutaneous and superficial nerves, while maximizing the current available at the deep on-target nerve. Finally, a full biophysical model was used to investigate on- versus off-target neural recruitment.

Transcutaneous coupling FEM model output and cadaver validation

Fig. 3.4 (b-c) show simulation results (solid line) compared to cadaver measurements (shaded area representing \pm 1 SD of n=8 measurements) used to validate the FEM model. Seen in Fig. 3.4 (b), the current drawn at the TES electrode patch (blue) with a symmetric trapezoidal voltage pulse (red) mimics the current seen at the deep nerve (green). As the TES-tissue interface is substantially capacitive, the current generated is more sensitive to the change in voltage applied dV_{TES}/dt than absolute voltage (V_{TES}) as seen in Fig. 3.4 (b-c). Supplementary Material 3 shows a similar figure for a current-controlled stimulation pulse.

A controlled rise time in surface electrode voltage could be used to exploit the additional displacement current provided by capacitive coupling without increasing the absolute voltage applied across the surface electrodes. The displacement current through a capacitor is proportional to the rate of change of voltage across it (dV/dt). Several rise times corresponding to dV_{TES}/dt of 0.6, 0.2, and 0.1 V/μ s were investigated in the FEM model and

cadaver. Faster rise times corresponded to greater surface electrode current and nerve current as shown in Fig. 3.4 (b-c). In this manner, controlled rise times on voltage-controlled waveforms can be used to add additional displacement current to the ohmic nerve current.

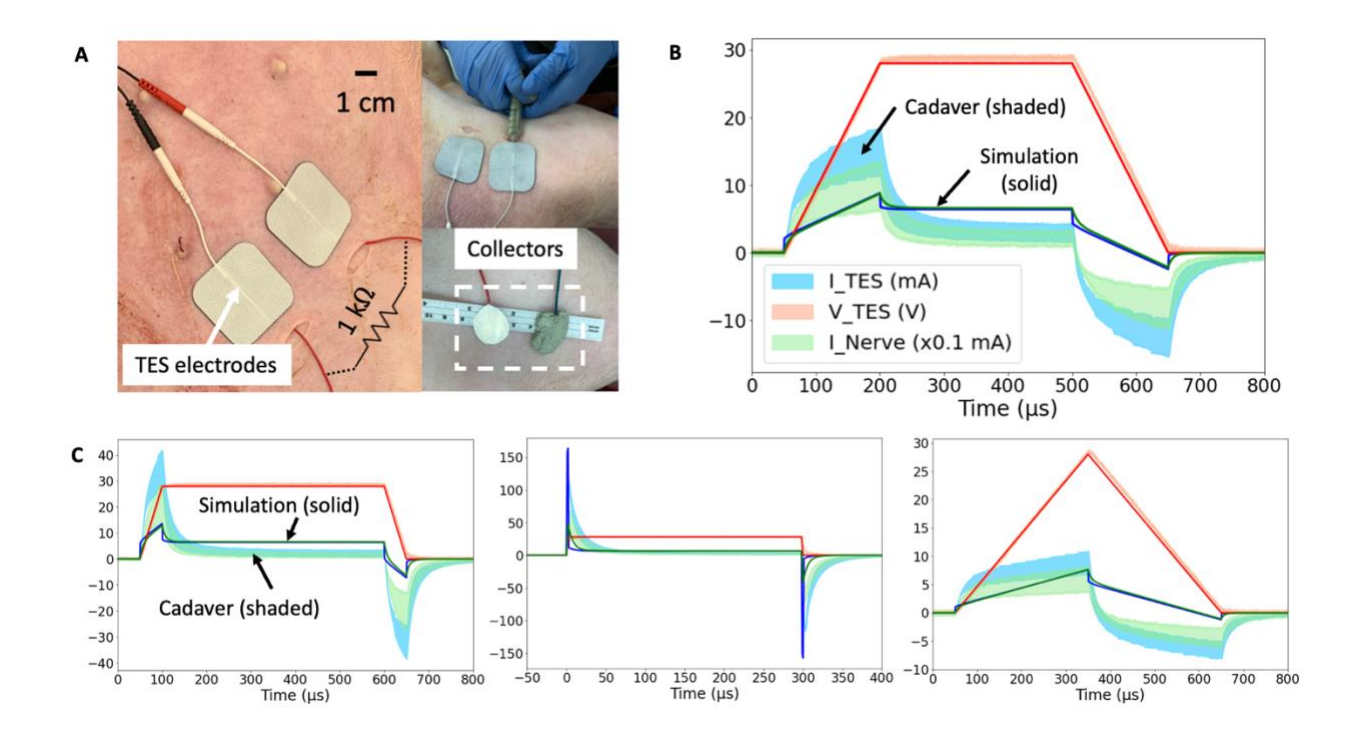


Figure 3.4: Cadaver validation of finite element method (FEM) model.

(a) Domestic swine cadaver verification of the FEM model using stainless-steel discs. (b) 28 V voltage-controlled 600 μ s pulses with 150 μ s rise and fall times. Three solid lines are simulation results, and three shaded areas are cadaver measurements \pm 1 SD (n=8 measurements from both sides of n=4 cadavers). Red solid line (simulation) and shaded area (cadaver validation measurements) represent voltage of applied stimulation waveform, blue represents current through surface electrodes, and green represents nerve current (scaled by x0.1 mA for visualization). A darker green color is seen at regions where the blue and green shaded areas overlap. (c) 28 V voltage-controlled pulses of 600 μ s duration with 50 μ s rise and fall times (left), 300 μ s duration with fastest (~2 μ s) rise and fall time (center), 600 μ s duration with 300 μ s rise and fall times (right). Note: 50 μ s rise time (left) is n=7 measurements due to the incorrect application of waveform amplitude in one sample. These cadaver data, overlayed with adjusted tissue values more representative of swine skin are shown in Supplementary Material 4.

General waveform shapes were well captured by the FEM model. For example, in Fig. 3.4 (c, left), the TES Voltage (V_{TES}) represents the applied voltage-controlled waveform with a 50 μ s rise and fall time. During the rise and fall, the exponential charging shape of TES Current (I_{TES}) means the TES electrodes are capacitively coupling with tissue and the collectors, and displacement current dominates. The identical shapes of I_{TES} and the nerve current (I_{Nerve}) means that once current enters tissue, ohmic current transfer dominates.

Differences in absolute values between the model and cadaver measurements can be explained by differences in the conductivity and permittivity values of human skin (on which the FEM model was based – solid line) compared to pig skin (on which validation measurements were made – shaded area representing \pm 1 SD of n=8 measurements). Pig skin at the abdomen lacks hair follicles and therefore sweat glands. This lowers the conductivity when compared to human skin, which has sweat glands even in regions without hair follicles (Avci et al., 2013), and explains the lower DC components of the waveforms measured in pig cadavers compared to simulation. Skin permittivity is highly dependent on the outermost stratum corneum layer. The pig skin had a higher permittivity than the FEM model, and therefore more distinct capacitive components to the waveform. Supplementary Material 4 shows the same waveforms when the model skin conductivity was adjusted to be lower and permittivity values were adjusted to be higher to reflect the properties of pig skin and a good fit was attained. The human literature skin conductivity and permittivity values were used for the rest of this study. Furthermore, while the model predicts a 10% efficiency (at DC portions of V_{TES}) in current transfer from I_{TES} to I_{Nerve}, the measurements show a value closer to 7%. This discrepancy in the capture ratio may be explained by highly conductive edema in the surgical

pocket and interfacing of the collectors with subcutaneous fat (inseparable from skin), instead of lying flush with lower conductivity skin, as in the model.

Mechanism of charge transfer to the nerve

Despite the exponential capacitive waveforms in Fig. 3.4 (b-c), the main mechanism of charge transfer to the nerve is ohmic. The TES-tissue interface is highly capacitive, but once charge enters tissue, ohmic charge transfer dominates. This trend was investigated by setting the skin conductivity to 0 S/m while leaving the permittivity unchanged (human literature value) in the transcutaneous coupling FEM model. A transient simulation was run, and charge transferred to the nerve was calculated as area under the rectified I_{Nerve} curve. In the Fig. 3.4 (c) waveform with the fastest rise time, 29% of the charge transferred to the nerve was maintained when the conductivity of skin was set to 0 S/m and the only way for charge to cross the skin layer was as displacement current. Data are shown in Supplementary Material 5.

Validated transcutaneous coupling model to investigate Injectrode system parameters

The validated FEM model, Fig. 3.2 (b), using the original literature conductivity and permittivity values representing human skin, was then used to further explore how waveform and geometric parameters affected system performance. Given the agreement in general shape but discrepancies between the absolute values in the model and swine cadaver measurements, expected differences in a live chronic experiment where scarring and healing occurs, and expected differences between swine and humans, the modeling results should be interpreted in terms of trends instead of absolute values.

Effect of collector size on charge transfer efficiency

After validating the FEM model with cadaver measurements, the model was used to further explore the parameter space of the Injectrode system on coupling efficiency. One key parameter explored was the ratio of the TES patch size to the collector size. Collector diameter was varied between 0.5 and 7 cm while holding the distance between the centers of the two collectors constant. Efficiency, or capture ratio (Gan and Prochazka, 2010), defined as I_{Nerve}/I_{TES}, was plotted in Fig 5. (a). The modeling suggests that efficiency increases with collector size until the collector diameter approaches the TES side length, after which efficiency decreases. This increase in efficiency as a function of collector diameter is expected as voltage directly under the TES electrode is roughly constant and increased collector area translates to a lower impedance interface with tissue and more current captured by the collector. However, when collector diameter exceeds TES electrode side length, it enters an area of tissue where the electric potential quickly drops off. The collector is a metallic conductor and hence forms an equipotential surface, where the collector voltage is defined by the lowest potential the collector contacts. Therefore, as collector diameter exceeds TES side length, the collector shunts current from under the TES electrodes to the edges of the collector where the electric potential of tissue is lower, and efficiency decreases. The trend in coupling efficiency with collector diameter was also demonstrated in the monopolar configuration. Collector size can be increased approximately up to the size of the surface electrode to increase current delivered to the deep target nerve.

Effect of high-frequency waveform on charge transfer efficiency

High-frequency waveforms are sometimes used in non-invasive neurostimulation devices with the hypothesis that they improve penetration depth of the delivered current (Nonis et al., 2017; Medina and Grill, 2014). Our model shows that charge transfer efficiency is lower when using a high-frequency (10 kHz) stimulation waveform when compared to a low-frequency stimulation waveform (orange and blue traces, respectively, in Fig. 5). Tissue impedance appears lower at 10 kHz due to the addition of capacitive charge transfer, which makes the path to the deep target nerve through the Injectrode collectors becomes less preferential for current compared to travelling in tissue – lowering coupling efficiency.

Effect of collector depth on charge transfer efficiency

A second key parameter that could impact the efficiency of charge transfer to the deep target nerve is the depth of the collector under the skin. To understand the sensitivity of transcutaneous charge transfer efficiency to collector depth, collector depth was varied from 0.5 to 5 mm – corresponding to the center of the 1 mm thick skin layer to the fat-muscle layer boundary. Fig. 3.5 (b) shows efficiency decreased with increased collector depth – most rapidly in the skin layer (14.5% to 10.3% over 0.5 mm) and then more gradually in the fat layer (10.3% to 9.9% over the first 0.5 mm). The decrease in efficiency was more rapid in the skin layer because skin is two orders of magnitude less conductive than fat and the electric potential drops off quickly in the skin layer with distance from the surface electrodes. The current through the 1 k Ω resistor connected between the two collectors, representing the deep nerve, is proportional to the voltage difference between the two collectors. As distance from the

surface electrode increases, the voltage difference between the two collectors decreases.

These data would suggest the collectors must be placed at the shallowest depth for highest efficiency. However, device extrusion (Zakhar et al., 2020; Uppal et al., 2021) and the position of sensory receptors in the skin (Crawford and Caterina, 2020) must also be considered to ensure that the collectors do not cause excessive pain.

Effect of surface electrode size on charge transfer efficiency

A critical parameter potentially impacting the ratio of on-versus off-target neural recruitment is the size of the TES electrodes. To investigate the effects of TES electrode size, edge-to-edge distance between the two surface electrodes was kept constant at 2 cm while the side length of the square surface electrodes was varied from 1 to 7 cm in the FEM model. The ratio of nerve current to surface electrode current density was plotted as a proxy for on-target nerve recruitment to off-target cutaneous fiber recruitment (Slopsema et al., 2018) in Fig. 3.5 (c), with the hypothesis that lower surface current densities generated by larger TES patches would reduce off-target cutaneous activation. Increasing the square surface electrode side length was found to improve the ratio of deep nerve current to surface electrode current density by ~8x when the TES side length was increased from 1 cm to 7 cm, suggesting a more favorable ontarget deep nerve recruitment to off-target cutaneous fiber recruitment ratio at larger TES electrode sizes. Spatial accuracy of the deep nerve stimulation is maintained by the constant Injectrode-nerve interface. Two effects are at play that make larger surface electrode sizes more suitable for preferential recruitment of on-target fibers. Firstly, larger surface electrode sizes result in lower TES-skin interface charge density for the same charge injected into tissue.

Secondly, both collectors were centered under their respective surface electrode and the collector-to-collector separation increased with increased surface electrode size. The impedance of the path current must travel through tissue between the two collectors increased and the alternative path provided through the collectors and 1 k Ω resistor became more favorable, with more current directed to the deep target nerve. The model suggests that larger surface electrode sizes results in increased deep target nerve activation while decreasing paresthesia or pain caused by recruitment of off-target cutaneous fibers.

Effect of bipolar surface electrode separation on charge transfer efficiency

Lastly, a parameter impacting efficiency of charge transfer from the surface electrodes to the deep target nerve, but not as sensitively as the previous three parameters presented, is the separation between the two TES electrodes. The edge-to-edge separation between the two surface electrodes was varied from 0 to 6 cm and results are shown in Fig. 3.5 (d). Both collectors were kept centered under their respective surface electrodes. A minimum separation of 0.1 cm (smallest separation investigated) is required to prevent the surface electrodes from 'shorting' and shunting current superficially. Under more realistic conditions, such as sweating and the presence of blood vessels in skin (Khadka and Bikson, 2020), where skin impedance is drastically lowered, it is possible that shunting of current superficially between the two surface electrodes will be prominent at separations much larger than 0.1 cm. However, this was not investigated. After that minimum separation, increased TES separation led to slightly increased efficiency (10% at 1 cm separation to 11% at 5 cm separation) as the path for current to flow through tissue between the two collectors increased in impedance. The current preferentially

routed through the comparatively lower impedance pathway of the collectors and 1 k Ω resistor and more current was directed through the deep target nerve. These data suggest that surface electrode separation should be increased for minor gains in efficiency. However, this increased electrode separation would require a longer wire to be tunneled from the deep target nerve, where the Injectrode interfaces with the nerve, to the subcutaneous collectors – increasing injection complexity and volume of injected material.

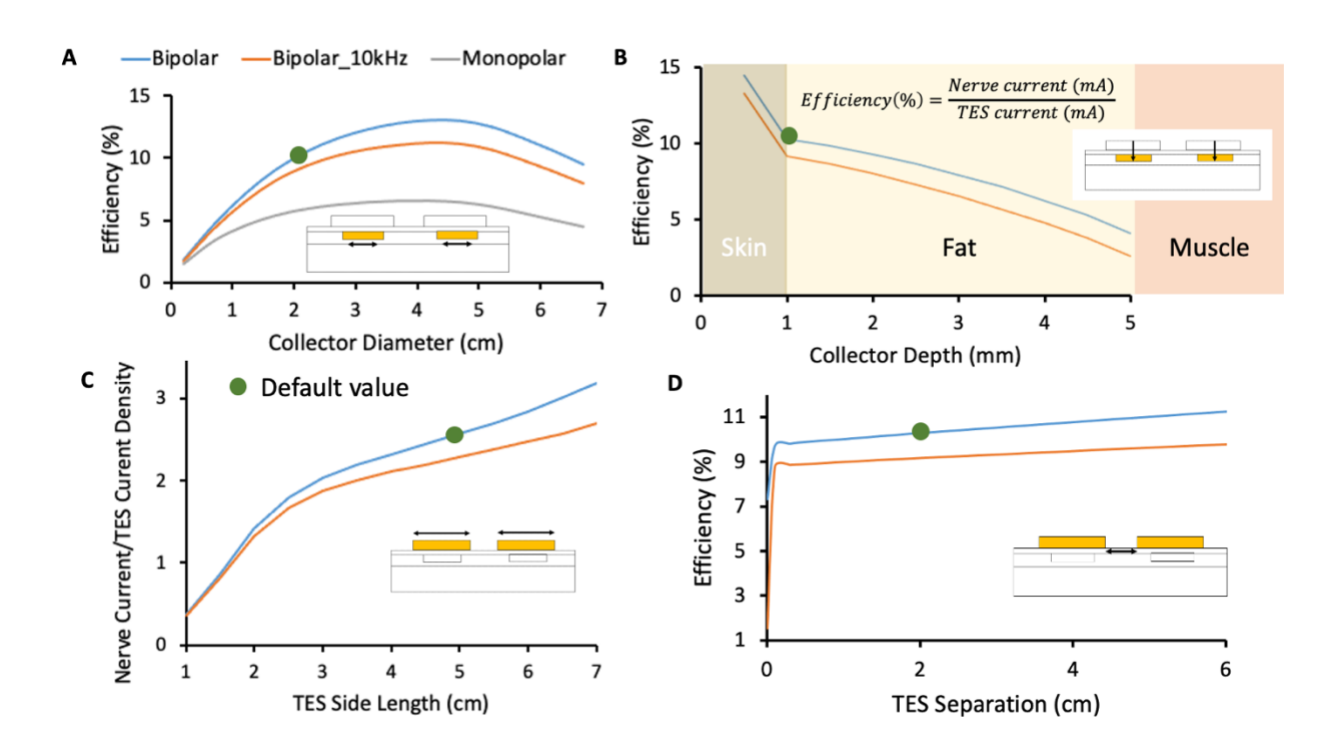


Figure 3.5: Finite element method (FEM) model results investigating Injectrode system parameters.

In this figure, blue and orange traces represent the Injectrode system in bipolar configuration with stimulation at DC and 10 kHz, respectively. The grey traces represent the Injectrode system in monopolar configuration with stimulation at DC. Green dots denote the default parameters used in the FEM model. (a) Change in efficiency with collector diameter. Optimal efficiency was achieved when the collector diameter approximately matched the surface electrode length. Tissue impedance is lower at higher frequency (orange trace at 10 kHz), which caused current to spread more and decreased capture efficiency. The current was more

volumetrically contained with a bipolar setup (blue trace compared to monopolar grey trace). **(b)** Efficiency was highest closest to the surface electrodes and dropped quickest in the least conductive skin layer. **(c)** The ratio of I_{Nerve} to TES current density increased for larger surface electrode sizes. I_{Nerve} is a proxy for on-target recruitment of the deep nerve and surface current density is a proxy for recruitment of cutaneous off-target neural fibers. **(d)** Increasing separation between bipolar surface electrodes increased efficiency marginally by increasing the impedance of the leakage path from collector to collector compared to the low-impedance conduit formed by the Injectrode to the nerve. At small separations (<0.1 cm in this idealized model of dry skin) between the TES electrodes, current shunts superficially between the two electrodes and is not delivered deeper into tissue.

Validated transcutaneous coupling model to investigate patient-dependent parameters

A critical limitation of current TES therapies is that they are applied at home by an untrained user, without consideration of local anatomy, which affects current flow and neural activation (Zander et al., 2020). A goal of the Injectrode system is to reduce the sensitivity of existing TES therapies to patch placement by an untrained user and other expected intra- and inter-subject differences. Furthermore, an implanted neurostimulation device typically assures extent of neural recruitment by precisely controlling the current or voltage delivered to the nerve at the electrode-nerve interface. In the case of the Injectrode system, power delivered at the surface electrode-skin interface is regulated while the energy delivered at the Injectrode-nerve interface is not as precisely regulated. With increased transcutaneous coupling efficiency, the same surface electrode current would result in more current at the deep on-target nerve. The subject's ability to 'feel' increased activation of the deep nerve via superficial sensation is minimized. Increased recruitment of an on-target autonomic nerve, for example, may not result in a sensation noticeable to the subject, yet still affect a physiological function unbeknownst to the patient. It is therefore crucial to understand the effect of variations in relevant parameters on coupling efficiency from the surface electrode to the deep target nerve. The FEM model was

used to investigate coupling efficiency of the Injectrode system to expected inter- and intrasubject variations: placement of surface electrode relative to injected collector, skin thickness, and tissue conductivities and permittivities. Both current- and voltage-controlled waveforms were investigated and plotted in Fig. 3.6.

Effect of collector and surface electrode offset on charge transfer efficiency

Fig. 3.6 (a) shows the stability in nerve current when a surface electrode is offset relative to its collector. Shaded in grey is the area where the collector remains entirely under the surface electrode, and the nerve current is stable. Nerve current drops rapidly when the surface electrode no longer overlaps the collector completely. Larger surface electrodes would be more tolerant to expected variations in reapplication, especially when done at home, along with the previously observed advantage in preferential on-target neural activation. Permanent markings on the skin or an automated electro impedance tomography (EIT) based system (Ansory et al., 2018) could also be used to guide at-home placement of the surface electrodes.

Effect of skin thickness and tissue electrical properties on charge transfer efficiency

In Fig 6. (b-d), the FEM model shows that current-controlled stimulation is stable to variations
in skin thickness, conductivity, and permittivity, while voltage-controlled stimulation is highly
susceptible to these variations. Skin thickness is expected to vary widely based on body location
(Sandy-Møller et al., 2003) and age (Hoffmann et al., 1994; Neerken et al., 2004). Skin
conductivity is also expected to vary widely based on sweating, weather, and skin preparation
(Tronstad et al., 2010). Particularly, skin permittivity is based largely on the outermost thin

stratum corneum layer and is expected to vary based on skin preparation (Tronstad et al., 2010). Skin preparation should be standardized and noted during clinical trials and replicated appropriately in clinical practice. On the other hand, nerve current during voltage-controlled stimulation was slightly more stable with variation in fat conductivity (Fig. 3.6 (e)). However, due to the reasons noted, it is expected that inter- and intra-subject variations in skin will be greater than fat. Given the critical safety and efficacy concerns surrounding a stable stimulation current delivered at the nerve (discussed earlier), and the larger expected variation in skin properties compared to fat properties, a current-controlled surface electrode stimulation may be preferred.

The analysis presented in this section creates an understanding of variations in the deep target nerve stimulation current with expected changes in patient-dependent parameters (e.g., surface electrode placement, tissue thickness, skin preparation, tissue electrical properties) during use of the Injectrode system. These analyses create a foundation for the Injectrode system to be designed to be more stable to expected patient-dependent changes, and thus improve device safety and efficacy for a wider patient population.

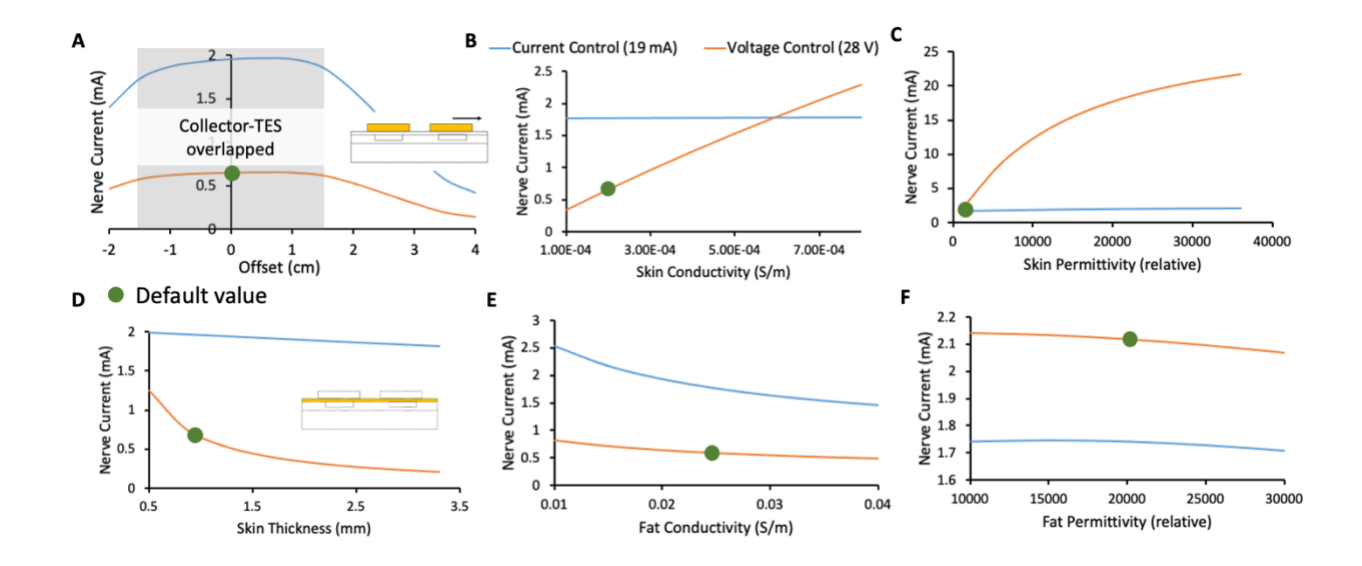


Figure 3.6: Finite element method (FEM) model results investigating tissue parameters and TENS electrode placement error.

In this figure, orange and blue traces represent the deep target nerve current in response to voltage-controlled and current-controlled stimulation, respectively. Green dots denote the default parameters used in the FEM model. (a) Deep target nerve current is stable while the surface electrode completely overlaps the collector. (b) Deep target nerve current is more stable to variations in skin conductivity under current-controlled stimulation relative to voltage-controlled stimulation. (c) Deep target nerve current is more stable to variations in skin permittivity under current-controlled stimulation relative to voltage-controlled stimulation. (d) Deep target nerve current is more stable to variations in skin thickness under current-controlled stimulation relative to voltage-controlled stimulation. (e) Deep target nerve current is somewhat more stable to variations in fat conductivity under voltage-controlled stimulation relative to current-controlled stimulation. (f) Deep target nerve current is not sensitive to variations in fat permittivity.

Effect of the Injectrode on vagal axon activation (biophysical model)

The goal of the Injectrode is to facilitate the activation of deep neural targets using TES. To investigate if the Injectrode system can achieve this goal, we examined how including the Injectrode system components (i.e., the subcutaneous collector, Injectrode lead, and Injectrode nerve interface) affected the activation thresholds of target $A\beta$ -axons in the vagus nerve compared to TES alone. Including the Injectrode system components lowered on-target vagus

Aβ-axon activation thresholds by one to two orders of magnitude, regardless of patch size (Fig. 3.7 (b)). When using a 2x2 cm TES patch with the Injectrode system, the median vagus Aβ-axon activation threshold was 2.76 mA, compared to 57.69 mA with TES alone. This estimate of ~57 mA of stimulation current to activate Aβ-axons in the human cervical vagus is in line with a recent *in vivo* study showing ~34 mA was required to non-invasively activate A-fibers in a rat, where the cervical vagus is at a more superficial depth (Bucksot et al., 2020). When using a 3x3 cm TES patch with the Injectrode system, the median vagus Aβ-axon activation threshold was 4.12 mA, compared to 72.53 mA with TES alone. When using a 5x5 cm TES patch, the median vagus Aβ-axon activation threshold was 8.58 mA when using the Injectrode system, compared to 117.38 mA with TES alone. Vagus Aβ-axon thresholds were always lower when using the Injectrode system compared to TES alone.

Effect of the Injectrode system on on- and off-target neural recruitment (biophysical model)

It is possible that the Injectrode system could produce undesired activation of cutaneous afferents when using stimulation amplitudes necessary to activate target axons in deeper nerve structures. Therefore, we compared the activation thresholds of target A β -axons in the vagus nerve to the activation thresholds of off-target A β - and A δ -cutaneous axons when using a 5x5 cm TES patch (Fig. 3.7 (c)). The median vagus A β -axon activation threshold was 8.58 mA. The median cutaneous A β -axon activation threshold was 0.73 mA. The median cutaneous A δ -axon activation threshold was 39.41 mA. Generally, the distributions of target vagus A β -axons thresholds and cutaneous A β -axon thresholds overlapped more than the distributions of target

vagus A β -axons thresholds and cutaneous A δ -axon thresholds when using the Injectrode system. Using only 5x5 cm TES patches (without the Injectrode system), the median vagus A β -axon activation threshold was 117.38 mA – much higher than the median activation threshold of cutaneous A β - and A δ -axons.

Effect of surface electrode size on relative activation of on-target vagal and off-target cutaneous axons (biophysical model)

Results from the simplified transcutaneous coupling FEM model showed that increased TES patch sizes increased the ratio of current in the deep target nerve to current density at the surface electrodes (Fig. 3.5 (c)), which suggests an improved ratio of on-target neural activation in the deep nerve to off-target cutaneous activation. We used the field-cable model to verify whether increasing TES patch size increases the ratio of neural activation in the vagus Aβ-axons compared to cutaneous Aβ-axons. We were particularly interested in how changing TES patch size may lead to paresthetic percepts resulting from TES while achieving neural activation in the vagus nerve. Therefore, we examined how increasing TES patch size affected the ratio of the median activation thresholds of the ten most excitable vagus axons and the ten most excitable cutaneous axons (i.e., the axons with the lowest activation thresholds). Though we are only presenting threshold ratios for the ten axons with the lowest thresholds, this trend held for the same analysis when considering more than 50 of the most excitable axons (data not shown). However, it is currently unknown how many axons must generate action potentials to produce a percept in a human subject or how many axons must be recruited for the therapeutic effects of vagus nerve stimulation for epilepsy. Preliminary studies indicate that single-axon

stimulation may be sufficient to produce percepts for some perceptual modalities (Macefield et al., 1990) while other modalities may require activity of many axons to induce a percept (Macefield 2021).

When using a TES electrode side length of 2 cm, the ratio of vagus-to-cutaneous median A β thresholds was 15.97 when using an Injectrode, compared to 460.66 when using TES alone. Increasing the TES electrode side length to 3 cm lowered the vagus-to-cutaneous median A β threshold ratio to 11.87 when using an Injectrode, compared to 281.03 when using TES alone. Further increasing the TES side length to 5 cm produced vagus-to-cutaneous A β threshold ratios of 9.14 and 180.37 when using an Injectrode and TES alone respectively. Overall, increasing TES side length reduced the median threshold ratio of A β axons in the vagus nerve compared to cutaneous afferents, suggesting that larger TES side lengths improve the engagement of ontarget vagal axons while reducing off-target cutaneous axon activation. These results support the findings of the simplified transcutaneous coupling FEM model investigation. Additionally, the Injectrode reduced threshold ratios by greater than an order of magnitude compared to using only surface electrodes, further underscoring the utility of the Injectrode system in activating deep nerves during TES.

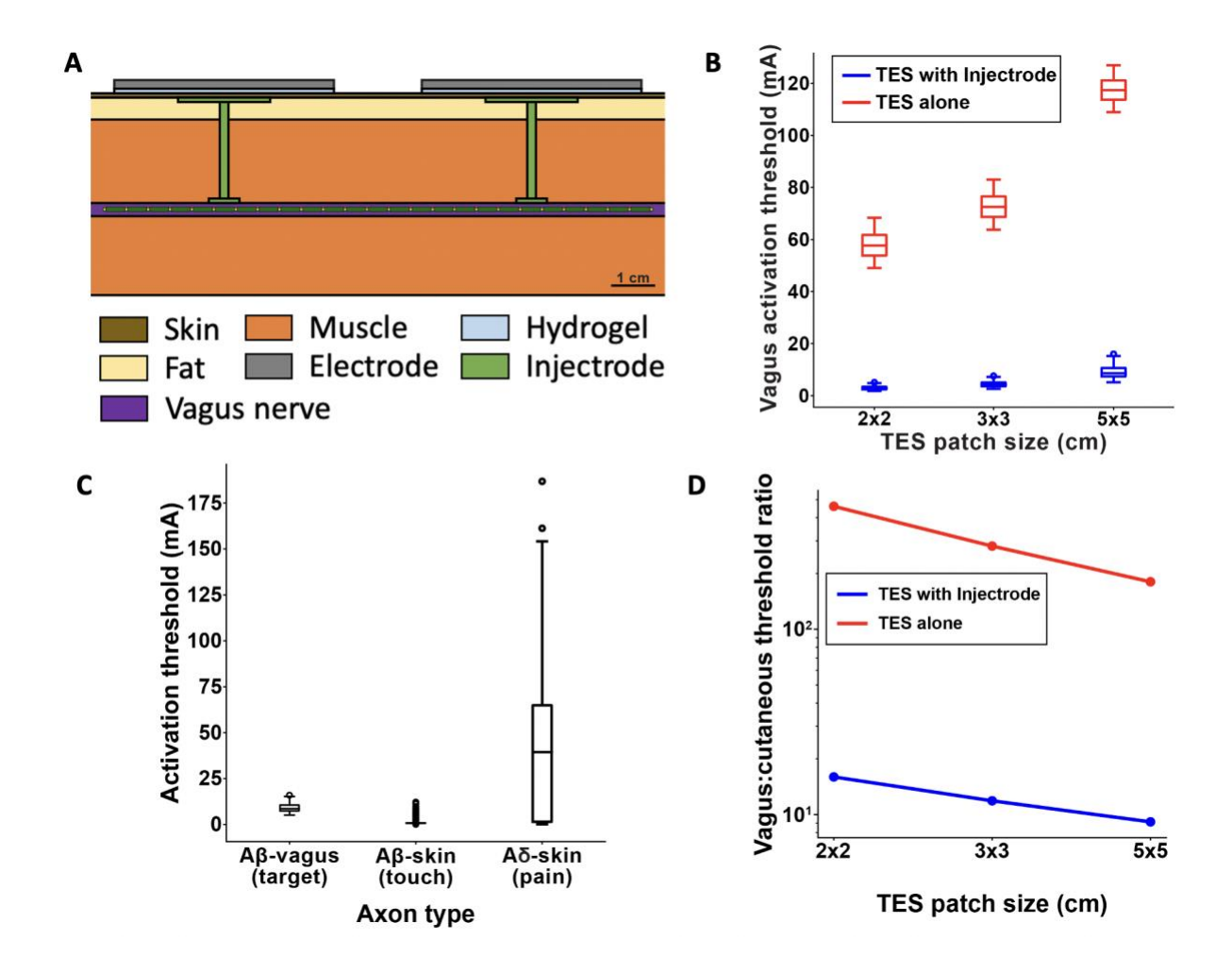


Figure 3.7: Biophysical model results showing Injectrode reduces activation threshold by an order of magnitude compared to traditional TENS.

(a) Full FEM model used in the biophysical study. The $1~\rm k\Omega$ resistor between the two collectors in the simplified transcutaneous coupling FEM model was replaced with the vagus nerve, Injectrode connections down to the vagus nerve, and Injectrode interfaces with the vagus nerve. This subfigure is reproduced from Fig. 3.2 (c). (b) Box plot of all axons showing that the Injectrode system reduced the current required to activate $A\beta$ vagal fibers by more than an order of magnitude compared to using only surface electrodes. This large difference was seen across TES patches of different sizes. (c) Box plot of activation thresholds of all on-target $A\beta$ vagal fibers compared to all off-target $A\beta$ cutanoues fibers responsible for paresthesia and off-target $A\delta$ cutaneous fibers responsible for noxious sensations. (d) Investigating the effect of TES patch side length on cutaneous and vagus $A\beta$ - fiber activation. Increasing the TES patch side length increased median thresholds, and this effect was less pronounced in vagal $A\beta$ fibers, improving the ratio of $A\beta$ vagal activation to $A\beta$ cutaneous activation. The Injectrode system achieved preferential on-target activation one to two orders of magnitude better than using surface stimulation electrodes alone.

Discussion

The goal of this study was to set up and use a validated FEM model to understand the transcutaneous energy delivery from surface electrodes to Injectrode collectors using low-frequency electric fields. The model was used to study waveform design and system parameters as well as sensitivity of the Injectrode system to expected inter- and intra-subject variations. Regarding expected variability in the deployment of the Injectrode and at-home application of the external TES electrodes, we found:

- <u>Collector depth</u> to be a sensitive parameter affecting transcutaneous charge coupling efficiency
- Optimal <u>collector size</u> to be approximately equal to the external TES electrode size and a sensitive parameter affecting transcutaneous charge coupling efficiency
- Increasing <u>external TES electrode size</u> to improve preferential recruitment of on-target deep neurons
- <u>Bipolar TES separation</u> to be an insensitive parameter on transcutaneous charge coupling efficiency, while greater than a minimum separation of 0.1 cm (in idealized model of dry skin)
- <u>Placement of external TES electrodes</u> to be an insensitive parameter on transcutaneous charge coupling efficiency, while the Injectrode collector is completely overlapped by the TES electrode
- Skin thickness, conductivity, and permittivity to be insensitive parameters on transcutaneous charge coupling efficiency under current-controlled stimulation, but sensitive under voltage-controlled stimulation

High-frequency carrier waveform

High-frequency waveforms have been proposed to transfer additional charge to the nerve while keeping the absolute amplitude of voltage applied across the surface electrodes constant. A sinusoidal 10 kHz carrier waveform was considered here as a method to get more current from surface electrodes to deep target nerves. Previous works showed that a high-frequency voltage-controlled waveform resulted in more current to deeper neural structures (Medina and Grill, 2014; Bucksot et al., 2020), although these studies concluded that the biophysics of neural activation would not necessarily lead to increased neural recruitment due to a filtering effect of the neural membrane on the high-frequency waveform (Medina and Grill, 2014; Medina and Grill, 2016). Results with the Injectrode system in Fig. 3.5 suggest that a high-frequency carrier would lead to less efficient coupling. For the same current delivered at the surface electrodes, less current was captured by the collectors and routed to the deep target nerve. This trend occurs because the effective tissue impedance decreases at high frequencies and provides a lower-impedance path for current to travel between the two collectors as opposed to the desired Injectrode route from the collector through the deep target nerve.

In both the TES only and TES with Injectrode situation, a higher frequency waveform would deliver additional current at the same voltage (Medina and Grill, 2014); however, the increased current would mean that off-target activation of cutaneous fibers would also increase (Fig. 3.5 (c)). This finding was also observed in Bucksot et al. (2020), where they showed that high-frequency sinusoidal waveforms required larger voltage amplitudes to non-invasively stimulate the vagus nerve in rats and that the ratio of on-target to off-target neural recruitment did not change with frequency (Bucksot et al., 2020). It is possible that high-frequency

waveforms may act to suppress neural activation close to the electrode akin to a high-frequency nerve block (Mirzakhalili et al., 2020); however, this is speculative and evidence to the contrary exists (Medina and Grill 2014; Mirzakhalili et al., 2020).

Waveform design for the Injectrode system

The waveform used in the Injectrode system may be optimized to increase on-target neural recruitment and minimize off-target neural activation, knowing the dual mechanisms of ohmic and capacitive charge transfer, utility of high-frequency carrier waveforms, underlying tissue composition, and expected inter- and intra-subject variabilities. Given the large dependence of nerve current on skin thickness, conductivity, and permittivity, a current-controlled waveform should be selected. This trend occurs because a current-controlled waveform delivers more energy when resistance is high and less energy when resistance is low, keeping the spread of energy more consistent despite variations in tissue impedance. If larger variations in the subdermal fat conductivity are expected, then a voltage-controlled waveform may be considered (Fig. 3.6 (e)). Overall, the current-controlled waveforms were found to more consistently regulate the current delivered to the nerve given expected variability in tissue thicknesses and electrical properties.

In general, a high-frequency carrier waveform is unlikely to be useful as outlined in the discussion above. In some situations, where skin resistance is extremely high and ohmic charge transfer across the skin is challenging, high-frequency waveform components may still be useful to transfer charge by displacement current instead. A voltage-controlled waveform delivering pulses with controlled rise times, as in Fig. 3.4 (b-c), could be used for this purpose. The ability

to deliver additional current using displacement current (Fig. 3.4 (b-c)) should also be kept in mind when selecting therapeutic targets for the Injectrode system. For example, the high-frequency sinusoidal waveforms characteristic of certain nerve blocks would lend naturally to the high dV_{TES}/dt that generates displacement currents.

Geometry design of Injectrode system

Similarly, the geometry of the Injectrode systems, such as the size of the collector and surface electrodes and collector to collector separation, may be optimized to achieve on-target deep fiber activation while minimizing off-target superficial fiber activation. Maximizing surface electrode size was shown to improve on-target vs. off-target neural fiber recruitment (Fig. 3.5 (c) and Fig. 3.7 (d)). Increased surface electrode size also increased the tolerance of the nerve current to differences in placement of the surface electrode relative to the collector (Fig. 3.6 (a)).

Our results form a conceptual basis for and complement earlier experimental work by Gan and Prochazka (Gan and Prochazka, 2007; Gan and Prochazka, 2010). They implemented TES surface electrodes, subcutaneous stainless-steel discs as collectors, and insulated wires running to a nerve cuff interfacing at the common peroneal nerve in rabbits to investigate parameters such as capture ratio (i.e., efficiency) and threshold current for a motor response from the animals. Their experimental trends match the theoretical findings presented here. They report higher capture ratios of up to ~0.4 (i.e., 40% efficiency). The higher efficiency of their system may be due to the lower impedance of the conductive path to the nerve and the tissue geometry of the rabbit compared to the pig.

In clinical deployment of the Injectrode, ultrasound and electrical impedance tomography (EIT) data may be used to develop subject-specific models of activation. The therapy could be personalized using ultrasound data gathered in the doctor's office — which may already be used to guide the injection of Injectrode at the on-target nerve — and extracting tissue thickness data to tailor the geometry and waveform parameters. EIT measurements may also be collected to select an appropriate waveform. Continuous EIT monitoring may be done using a multi-contact surface electrode design to understand the electrical properties of the underlying tissue and Injectrode as they change on the chronic time scale (Cooper et al., 2011) as well as with body position (Kim et al., 2013). Motion artifact on the EIT recordings from stimulation-evoked muscle activation may also provide data to the presence of on- and off-target effects.

In this study, we focused our investigation on the transcutaneous charge coupling efficiency and did not investigate parameters of the Injectrode-nerve interface, such as 'cuff' length and nerve interface position relative to TES surface patches, which affect local neural fiber excitation (Roointan et al., 2020). Recent work investigated the localized 'virtual bipole' created when a metal cuff is in contact with neural tissue (Roointan et al., 2020). The work by Roointan and colleagues suggests that a longer length of Injectrode on the nerve, higher Injectrode conductivity, and a slight offset of the Injectrode-nerve interface from the center of the surface stimulation electrodes will minimize the current threshold required to activate ontarget neural fibers.

Selection of tissue electrical properties for FEM model and their limitations

Measuring the electrical properties of tissue is challenging, and the results are sensitive to the measurement methods and tissue preparation. Consequently, widely varying values of tissue conductivity and permittivity are reported in the literature. Measurements at low frequencies (used in this study) are even more challenging. The values in this low-frequency range, taken from the Gabriel et al. (1996b) database, are inaccurate up to 25%, as quoted by the authors (Gabriel et al., 1996a), due to the two-electrode method used to make the measurements. The two-electrode method at low frequencies results in a high impedance across the electrodetissue interface and the addition of a substantial electrochemical potential drop to the recording. The study attempted to compensate with calibrations in saline solutions. In general, the values of fat and muscle conductivity are more reliable and consistent across studies compared to skin conductivity and permittivity values, which vary widely between studies.

Large variances in published values of skin electrical properties are due to the skin being composed of several layers. The outer most is the ~30 μ m thin stratum corneum (Mørch et al., 2011), a layer of dead skin with low conductivity and high permittivity (Tronstad et al., 2010). Depending on tissue preparation and handling, this outer layer can become fractured or peel off. Furthermore, the frequency of the waveform used for measurements dictates the effective depth at which the measurement is being taken (Tronstad et al., 2010). This issue is especially pertinent at low frequencies, where the effective depth is shallow, and sampling is prominent in the outermost stratum corneum layer (Tronstad et al., 2010).

Furthermore, the electrical properties of skin change under the application of surface electrodes (Tronstad et al., 2010; Vargas Luna et al., 2015) and the delivery of electrical

stimulation (Chizmadzhev et al., 1998). Gel used in the application of surface electrodes enters pores in the skin, lowering skin impedance (Tronstad et al., 2010; Vargas Luna et al., 2015). A similar effect is observed due to sweating under the surface electrodes after prolonged use (Tronstad et al., 2010; Vargas Luna et al., 2015). The delivery of an electric current during TES sets up an electric field across the skin, possibly resulting in electroporation of the skin (Chizmadzhev et al., 1998). Application of >30 V across the skin causes breakdown of the skin layers and creation of additional pathways of conduction through the skin, resulting in lower impedance (Chizmadzhev et al., 1998). Electroporation lasts for minutes to hours and may be irreversible if too high of a voltage is applied (Chizmadzhev et al., 1998). Skin impedance is also a function of the voltage applied even before electroporation occurs (Chizmadzhev et al., 1998).

Effects of hydrogel

Hydrogel applied at the skin-TES electrode boundary plays an important role in limiting the coupling current from the surface electrodes. The resistive hydrogel layer increases the RC time constant of charging and decreases current spikes in I_{TES} (data not shown). Furthermore, the hydrogel distributes the current density across the surface electrode-skin interface and ensures it is not concentrated along the edges of the surface electrodes (Khadka and Bikson, 2020). High current density at the edges would result in earlier cutaneous fiber activation. Conductivity of hydrogels as well as other surface electrode material, including more reusable options, should be further studied to optimize the Injectrode system.

Implications to TES modeling

Our FEM analysis suggests that it may be important to consider tissue permittivity in standard TES modeling – even without the Injectrode collectors. Tissue permittivity is particularly important when high-frequency TES voltage components are present, such as in voltagecontrolled pulses and high-frequency waveforms (e.g., in the gammaCore device (Nonis et al., 2017)). Charge relaxation time is often used to justify that the bulk RC time constants of tissues under consideration are too short for displacement current to be considered a significant factor (Zhu et al., 2017). However, sometimes charge relaxation times are only calculated for the nerve cell membrane, with the implication that the cell membrane will act as an RC filter to the neurons within, preventing high-frequency components from depolarizing the nerve and initiating action potentials. On the other hand, calculations of charge relaxation time for skin, fat, and muscle provide an imperative to consider permittivity (Gabriel et al., 1996b). Given that there are many types of sodium channels with different dynamics and that non-neural glial cells also modulate neural activity (Abdo et al., 2019), there is a possibility that charge due to displacement current may modulate neural function. Furthermore, high frequencies may not be filtered at the sensory receptors themselves, which are located at neuron endings and are more superficial and closer to the surface stimulation electrodes, experiencing higher potentials. The sensory receptor-to-neuron transitions and rapidly changing conductivity across skin layers also creates a unique set of boundaries for changing the activation function (i.e., second-order spatial derivative of the extracellular potentials) and thereby inducing neural activation. Therefore, permittivity may be important to consider for standard TES modeling, especially in high-frequency voltage-controlled waveforms.

Pertinently, TES modeling studies sometimes consider only the deep on-target nerve (Mourdoukoutas et al., 2018) and ignore the superficial and cutaneous neural structures that lie between the surface stimulation electrodes and the deep target nerve. Our results suggest that these more superficial off-target neural structures experience higher potentials from the stimulation electrodes and can have lower activation thresholds than the deep target nerve (Fig. 3.7 (c)). Recruitment of these superficial off-target structures can cause painful sides effects and limit the stimulation dose to sub-therapeutic levels. Our work supports the observation that off-target effects of the gammaCore device (visible as lip curl) are likely due to activation of the superficial cervical branch of the facial nerve, which runs in the neck under the stimulation electrodes and innervates the platysma muscle (Nonis et al., 2017).

Our results also suggest that the use of a voltage-controlled high-frequency carrier waveform, implemented in the gammaCore device (Nonis et al., 2017), does increase the current that reaches deeper tissue. However, it also increases overall current spread and decreases the portion of charge delivered to the on-target neural tissue (Fig. 3.5 (c)). Therefore, use of the high-frequency waveform may simultaneously increase off-target neural activation, as demonstrated in rat experiments (Bucksot et al., 2020).

Implications of biophysical modeling of Injectrode system

We used a field-cable modeling approach to investigate how the Injectrode system affects the activation of on-target axons in deep nerve structures compared to off-target axons in the skin. First, we examined whether the presence of the Injectrode components lowered activation thresholds of on-target vagal neurons compared to TES alone. The median vagus axon

activation thresholds were more than ten times lower when using the Injectrode system compared to TES without Injectrode components (Fig. 3.7 (b)). This trend suggests that the Injectrode system can dramatically reduce the activation threshold of axons in deep nerves and underlines the potential utility of the Injectrode as a minimally invasive clinical strategy to stimulate deep neural targets. However, there still are potential off-target effects of the Injectrode system, such as activation of nociceptive cutaneous afferents, which must be mitigated to ensure patient comfort.

Next, we investigated potential on- and off-target effects of the Injectrode system by comparing the activation thresholds of target A β -axons in the vagus nerve to the activation thresholds of A β - and A δ -cutaneous axons (Fig. 3.7 (c)). Generally, A β -cutaneous axons had the lowest activation thresholds, likely because of their large diameter and proximity to the surface stimulation electrodes. However, there is noticeable overlap in the distributions of Aβcutaneous and vagus thresholds. The cutaneous $A\delta$ -axon threshold distribution was more variable than the other two distributions, and the median $A\delta$ -axon threshold was considerably higher than the A β -vagus and cutaneous median thresholds. These results suggest that the Injectrode system may produce innocuous paresthesias as a side effect while activating deep nerve targets, without producing painful cutaneous sensations mediated by $A\delta$ - fibers. In contrast, TES without the aid of the Injectrode had a median Aβ-vagus threshold that was much higher than the median threshold of cutaneous A β - and A δ -axons. This result suggests that attempts to activate Aβ-vagus fibers using only surface stimulation electrodes may result in widespread activation of painful cutaneous A δ -axons.

Lastly, we analyzed how design parameters, such as the TES patch size, affected the relative activation of cutaneous and vagus axons via the Injectrode system (Fig. 3.7 (d)). In general, increasing TES patch size increased the activation thresholds of both cutaneous and vagus axons. However, the increase in cutaneous activation thresholds was larger than the increase in target vagus activation thresholds, and this effect became more pronounced as the patch side length increased. Therefore, using larger TES surface patches may reduce the off-target activation of cutaneous afferents relative to on-target activation of deep nerve structures.

General limitations of study

While the FEM model used in this study represented the skin, fat, and muscle as distinct domains, they were seen to be fused together in the swine cadaver studies. In particular, the skin and subcutaneous fat layers were inseparable and a source of error when measuring the thickness of skin, which is also the distance between the surface electrode and collector. Sensitivity analysis presented in Fig. 3.6 (d) shows that the current delivered to the nerve under voltage-controlled stimulation is sensitive to skin thickness. Ultrasound imaging may be used in future studies to more accurately quantify skin and fat thicknesses.

As explained in the Methods section, a 2.1 cm diameter stainless-steel disc was used as a consistent representation of the Injectrode collector. While the stainless-steel showed similar performance in the acute cadaver experimentation, it is possible that the porosity of the Injectrode will allow revascularization during chronic use, changing its electrical properties and

corresponding performance compared to a stainless-steel disc. Chronic performance of the transcutaneous charge coupling mechanisms needs to be further investigated.

We did not consider off-target neural recruitment by electric current from the Injectrode leads connecting the Injectrode collectors to the nerve interface (Fig. 3.7 (a)). In the implementation of the Injectrode where the lead wires are insulated, this source of off-target neural recruitment is unlikely. However, if uninsulated leads are used to connect the collector to the neural interface, off-target recruitment of neurons by the leads must be considered.

A simplified FEM model was used in the transcutaneous charge coupling investigation to isolate the effects of system parameters on transcutaneous coupling between the surface electrodes and collectors. As part of the simplification, a 1 k Ω resistor was used to model the Injectrode path between the two collectors, based on EIS measurements from Trevathan et al. (2019). In reality, the impedance of the path between the two collectors varies as a function of frequency, voltage, and tissue properties. However, at the same time, the alternate conduction path through tissue (leakage through tissue between the two collectors) would also vary similarly and the general trends presented here are expected to hold.

An instrumentation limitation explains why the spikes in surface electrode current predicted by the FEM model are higher than the cadaver measurements. The Keithley DAQ 6510 used to collect surface electrode current measurements is bandwidth limited, recording -3 dB at 25 kHz (Keithley). This frequency response means that higher frequency components were attenuated in their measured amplitude. However, the voltage measurements, made using an oscilloscope, were not bandwidth limited for the frequency range under investigation.

We used a field-cable model to investigate how the Injectrode system activates on- and off-target axons. Though the FEM and multi-compartment axon models were both constructed using experimental data and previously validated models, there are several limitations to this approach. For example, we used a previously published, but simplified, morphology to represent cutaneous A β - and A δ -axons (Tigerholm et al., 2019). The cutaneous A β -axon terminated in a passive node of Ranvier, while the cutaneous A δ -axon terminated in a branching structure designed to mimic the nerve fiber density in human skin. The extent to which terminal branching morphologies affect the neural response to TES is currently unknown. Future studies should examine how the complexity of branching structures, as well as electrophysiological differences across different types of sensory terminals, affect the neural response to TES.

Finally, we distributed cutaneous afferent terminals beneath the TES patch on a grid that extended 5 mm beyond the edges of the TES patch. This implies that using larger TES edge lengths would sample from more cutaneous axons. Therefore, when comparing cutaneous activation across different TES patch sizes, we were not making a one-to-one comparison between modeling conditions and may be over- or under-estimating the extent of neural activation across patch sizes. For this reason, when examining the effect of patch size on cutaneous activation, we compared the median thresholds of the 10 cutaneous axons with the lowest thresholds to understand how increased patch size affects the most excitable axons. It is also unclear how many cutaneous axons need to be activated to produce a painful or non-painful percept. Some argue that multiple afferents must be activated to produce a perceptible sensation (Wall and McMahon, 1985), while others argue activation of a single axon can

produce a percept (Torebjörk, 1987). Future modeling studies should be paired with psychophysical experiments to determine how many axons are needed to induce an innocuous or painful percept.

Conclusions

The Injectrode system, a minimally invasive technology, may provide the capabilities to recruit deep on-target fibers while minimizing side effects from off-target neural activation. This modeling study provides a framework on which to optimize the design and deployment of the Injectrode system. We investigated the transcutaneous charge coupling efficiency and neural fiber selectivity of the Injectrode system using validated computational models. Our results suggest that the Injectrode system lowers the activation thresholds of deep on-target vagal fibers by more than an order of magnitude compared to using only surface stimulation electrodes. This reduction in activation thresholds makes it possible to activate vagal fibers with only innocuous recruitment of paresthesia inducing Aβ-cutaneous fibers. Meanwhile, surface stimulation applied without the Injectrode system, will likely recruit painful A δ -cutaneous fibers before recruiting target deep vagal fibers. Exploration of the parameter space of the Injectrode system suggests that surface electrode and collector size can be selected to increase the current delivered to the deep target nerve while reducing surface electrode current density, a proxy for off-target cutaneous fiber activation. Voltage- and current-controlled waveforms were considered to assess how variability in anatomical parameters, such as tissue electrical properties and thicknesses, affects the performance of the Injectrode system. Currentcontrolled waveforms were found to be more stable to variations in the skin layer. Highfrequency waveforms were also investigated but were unsuccessful in preferentially increasing on-target vs. off-target neural activation. Our work highlights the need to consider the activation of superficial off-target neural structures when targeting deep neural fibers with non-invasive electrical stimulation modalities.

Acknowledgements

EJ for sourcing and delivering swine cadavers used in this study. Carly Frieders, Maria
LaLuzerne, Rex Chin-Hao Chen, Ashlesha Deshmukh, and Danny Lam for reviewing drafts of this
manuscript. Members of the Wisconsin Institute for Translational Neuroengineering (WITNe)
for feedback during group meetings.

Conflicts of Interest

JW and KAL are scientific board members and have stock interests in NeuroOne Medical Inc., a company developing next generation epilepsy monitoring devices. JW also has an equity interest in NeuroNexus technology Inc., a company that supplies electrophysiology equipment and multichannel probes to the neuroscience research community. SFL has equity in Hologram Consultants, LLC, is a member of the scientific advisory board for Abbott Neuromodulation, and receives research support from Medtronic, Inc. SFL also holds stock options, received research support, and serves on the scientific advisory board of Presidio Medical, Inc. KAL is also a paid member of the scientific advisory board of Cala Health, Blackfynn, Abbott and Battelle. KAL also is a paid consultant for Galvani and Boston Scientific. KAL, MF, and AJS are co-founder of NeuronOff Inc, which is commercializing the Injectrode.

The remaining authors declare that the research was conducted in the absence of any commercial or financial relationships that could be construed as a potential conflict of interest.

References

- Abdo, H., Calvo-Enrique, L., Lopez, J. M., Song, J., Zhang, M.-D., Usoskin, D., et al. (2019). Specialized cutaneous Schwann cells initiate pain sensation. *Science* 365, 695–699. doi:10.1126/science.aax6452.
- Ansory, A., Prajitno, P., and Wijaya, S. K. (2018). Design and development of electrical impedance tomography system with 32 electrodes and microcontroller. *AIP Conference Proceedings* 1933, 040023. doi:10.1063/1.5023993.
- Avci, P., Sadasivam, M., Gupta, A., De Melo, W. C., Huang, Y.-Y., Yin, R., et al. (2013). Animal models of skin disease for drug discovery. *Expert Opinion on Drug Discovery* 8, 331–355. doi:10.1517/17460441.2013.761202.
- Bossetti, C. A., Birdno, M. J., and Grill, W. M. (2008). Analysis of the quasi-static approximation for calculating potentials generated by neural stimulation. *J. Neural Eng.* 5, 44–53. doi:10.1088/1741-2560/5/1/005.
- Bucksot, J. E., Morales Castelan, K., Skipton, S. K., and Hays, S. A. (2020). Parametric characterization of the rat Hering-Breuer reflex evoked with implanted and non-invasive vagus nerve stimulation. *Experimental Neurology* 327, 113220. doi:10.1016/j.expneurol.2020.113220.
- Butson, C. R., and McIntyre, C. C. (2005). Tissue and electrode capacitance reduce neural activation volumes during deep brain stimulation. *Clinical Neurophysiology* 116, 2490–2500. doi:10.1016/j.clinph.2005.06.023.
- Chizmadzhev, Y. A., Indenbom, A. V., Kuzmin, P. I., Galichenko, S. V., Weaver, J. C., and Potts, R. O. (1998). Electrical Properties of Skin at Moderate Voltages: Contribution of Appendageal Macropores. *Biophysical Journal* 74, 14.
- Cooper, G., Barker, A. T., Heller, B. W., Good, T., Kenney, L. P. J., and Howard, D. (2011). The use of hydrogel as an electrode–skin interface for electrode array FES applications. *Medical Engineering & Physics* 33, 967–972. doi:10.1016/j.medengphy.2011.03.008.
- Crawford, L. K., and Caterina, M. J. (2020). Functional Anatomy of the Sensory Nervous System: Updates From the Neuroscience Bench. *Toxicol Pathol* 48, 174–189. doi:10.1177/0192623319869011.

- Dalrymple, A. N., Ting, J. E., Bose, R., Trevathan, J. K., Nieuwoudt, S., Lempka, S. F., et al. (2021). Stimulation of the Dorsal Root Ganglion Using an Injectrode®. *bioRxiv*. doi:10.1101/2021.08.16.456553.
- Foster, K. R., and Schwan, H. P. (1989). Dielectric Properties of Tissue and Biological Materials: A Critical Review. *Critical Reviews in Biomedical Engineering*. 17, 25-104.
- Gabriel, S., Lau, R. W., and Gabriel, C. (1996a). The dielectric properties of biological tissues: II. Measurements in the frequency range 10 Hz to 20 GHz. *Phys. Med. Biol.* 41, 2251–2269. doi:10.1088/0031-9155/41/11/002.
- Gabriel, S., Lau, R. W., and Gabriel, C. (1996b). The dielectric properties of biological tissues: III. Parametric models for the dielectric spectrum of tissues. *Phys. Med. Biol.* 41, 2271–2293. doi:10.1088/0031-9155/41/11/003.
- Gan, L. S., Prochazka, A., Bornes, T. D., Denington, A. A., and Chan, K. M. (2007). A New Means of Transcutaneous Coupling for Neural Prostheses. *IEEE Trans. Biomed. Eng.* 54, 509–517. doi:10.1109/TBME.2006.886664.
- Gan, L. S., and Prochazka, A. (2010). Properties of the Stimulus Router System, a Novel Neural Prosthesis. *IEEE Trans. Biomed. Eng.* 57, 450–459. doi:10.1109/TBME.2009.2031427.
- Gaunt, R. A., and Prochazka, A. (2009). Transcutaneously Coupled, High-Frequency Electrical Stimulation of the Pudendal Nerve Blocks External Urethral Sphincter Contractions. *Neurorehabil Neural Repair* 23, 615–626. doi:10.1177/1545968308328723.
- Graham, R. D., Bruns, T. M., Duan, B., and Lempka, S. F. (2019). Dorsal root ganglion stimulation for chronic pain modulates Aβ-fiber activity but not C-fiber activity: A computational modeling study. *Clinical Neurophysiology* 130, 941–951. doi:10.1016/j.clinph.2019.02.016.
- Graham, R. D., Bruns, T. M., Duan, B., and Lempka, S. F. (2020). The Effect of Clinically Controllable Factors on Neural Activation During Dorsal Root Ganglion Stimulation. *Neuromodulation: Technology at the Neural Interface*, ner.13211. doi:10.1111/ner.13211.
- Hammer, N., Löffler, S., Cakmak, Y. O., Ondruschka, B., Planitzer, U., Schultz, M., et al. (2018). Cervical vagus nerve morphometry and vascularity in the context of nerve stimulation A cadaveric study. *Sci Rep* 8, 7997. doi:10.1038/s41598-018-26135-8.
- Hines, M. (2009). NEURON and Python. Front. Neuroinform. 3. doi: 10.3389/neuro.11.001.2009.
- Hines, M. L., and Carnevale, N. T. (1997). The NEURON Simulation Environment. *Neural Computation* 9, 1179–1209. doi:10.1162/neco.1997.9.6.1179.
- Hoffmann, K., Stuucker, M., Dirschka, T., Goortz, S., El-Gammal, S., Dirting, K., et al. (1994). Twenty MHz B-scan sonography for visualization and skin thickness measurement of human skin. *J Eur Acad Dermatol Venerol* 3, 302–313. doi:10.1111/j.1468-3083.1994.tb00367.x.

- Keithley. DAQ6510 Data Acquisition and Logging, Multimeter System Datasheet. Rev 090617.
- Khadka, N., and Bikson, M. (2020). Role of skin tissue layers and ultra-structure in transcutaneous electrical stimulation including tDCS. *Phys. Med. Biol.* doi:10.1088/1361-6560/abb7c1.
- Kim, C. H. (2013). Importance of Axial Migration of Spinal CordStimulation Trial Leads with Position. *Pain Phys* 6;16, E763–E768. doi:10.36076/ppj.2013/16/E763.
- Krahl, S. (2012). Vagus nerve stimulation for epilepsy: A review of the peripheral mechanisms. *Surg Neurol Int* 3, 47. doi:10.4103/2152-7806.91610.
- Kuhn, A., Keller, T., Lawrence, M., and Morari, M. (2009). A model for transcutaneous current stimulation: simulations and experiments. *Med Biol Eng Comput* 47, 279–289. doi:10.1007/s11517-008-0422-z.
- Macefield et al. 1990 Perceptual responses to microstimulation of single.pdf.
- Macefield, G., Gandevia, S. C., and Burke, D. (1990). Perceptual responses to microstimulation of single afferents innervating joints, muscles and skin of the human hand. *The Journal of Physiology* 429, 113–129. doi:10.1113/jphysiol.1990.sp018247.
- Macefield, V. G. (2021). Recording and quantifying sympathetic outflow to muscle and skin in humans: methods, caveats and challenges. *Clin Auton Res* 31, 59–75. doi:10.1007/s10286-020-00700-6.
- McIntyre, C. C., Richardson, A. G., and Grill, W. M. (2002). Modeling the Excitability of Mammalian Nerve Fibers: Influence of Afterpotentials on the Recovery Cycle. *Journal of Neurophysiology* 87, 995–1006. doi:10.1152/jn.00353.2001.
- McIntyre, C. C., Grill, W. M., Sherman, D. L., and Thakor, N. V. (2004). Cellular Effects of Deep Brain Stimulation: Model-Based Analysis of Activation and Inhibition. *Journal of Neurophysiology* 91, 1457–1469. doi:10.1152/jn.00989.2003.
- Medina, L. E., and Grill, W. M. (2014). Volume conductor model of transcutaneous electrical stimulation with kilohertz signals. *J. Neural Eng.* 11, 066012. doi:10.1088/1741-2560/11/6/066012.
- Medina, L. E., and Grill, W. M. (2016). Nerve excitation using an amplitude-modulated signal with kilohertz-frequency carrier and non-zero offset. *J NeuroEngineering Rehabil* 13, 63. doi:10.1186/s12984-016-0171-4.
- Mirzakhalili, E., Barra, B., Capogrosso, M., and Lempka, S. F. (2020). Biophysics of Temporal Interference Stimulation. *Cell Systems* 11, 557-572.e5. doi:10.1016/j.cels.2020.10.004.
- Mørch, C. D., Hennings, K., and Andersen, O. K. (2011). Estimating nerve excitation thresholds to cutaneous electrical stimulation by finite element modeling combined with a stochastic

- branching nerve fiber model. *Med Biol Eng Comput* 49, 385–395. doi:10.1007/s11517-010-0725-8.
- Mourdoukoutas, A. P., Truong, D. Q., Adair, D. K., Simon, B. J., and Bikson, M. (2018). High-Resolution Multi-Scale Computational Model for Non-Invasive Cervical Vagus Nerve Stimulation. *Neuromodulation* 21, 261–268. doi:10.1111/ner.12706.
- Neerken, S., Lucassen, G. W., Bisschop, M. A., Lenderink, E., and Nuijs, T. (A. M.). (2004). Characterization of age-related effects in human skin: A comparative study that applies confocal laser scanning microscopy and optical coherence tomography. *J. Biomed. Opt.* 9, 274. doi:10.1117/1.1645795.
- Nicolai, E. N., Settell, M. L., Knudsen, B. E., McConico, A. L., Gosink, B. A., Trevathan, J. K., et al. (2020). Sources of off-target effects of vagus nerve stimulation using the helical clinical lead in domestic pigs. *J. Neural Eng.* 17, 046017. doi:10.1088/1741-2552/ab9db8.
- Nonis, R., D'Ostilio, K., Schoenen, J., and Magis, D. (2017). Evidence of activation of vagal afferents by non-invasive vagus nerve stimulation: An electrophysiological study in healthy volunteers. *Cephalalgia* 37, 1285–1293. doi:10.1177/0333102417717470.
- Ponnamma, D., Ninan, N., and Thomas, S. (2018). "Carbon Nanotube Tube Filled Polymer Nanocomposites and Their Applications in Tissue Engineering," in *Applications of Nanomaterials* (Elsevier), 391–414. doi:10.1016/B978-0-08-101971-9.00014-4.
- Poulsen, A. H., Tigerholm, J., Meijs, S., Andersen, O. K., and Mørch, C. D. (2020). Comparison of existing electrode designs for preferential activation of cutaneous nociceptors. *J. Neural Eng.* doi:10.1088/1741-2552/ab85b1.
- Pelot, N. A., Behrend, C. E., and Grill, W. M. (2019). On the parameters used in finite element modeling of compound peripheral nerves. *J. Neural Eng.* 16, 016007. doi:10.1088/1741-2552/aaeb0c.
- Roointan, S., Tovbis, D., Elder, C., and Yoo, P. B. (2020). Enhanced transcutaneous electrical nerve stimulation achieved by a localized virtual bipole: a computational study of human tibial nerve stimulation. *J. Neural Eng.* 17, 026041. doi:10.1088/1741-2552/ab85d3.
- Sandby-Møller, J., Poulsen, T., and Wulf, H. C. (2003). Epidermal Thickness at Different Body Sites: Relationship to Age, Gender, Pigmentation, Blood Content, Skin Type and Smoking Habits. *Acta Dermato-Venereologica* 83, 410–413. doi:10.1080/00015550310015419.
- Slopsema, J. P., Boss, J. M., Heyboer, L. A., Tobias, C. M., Draggoo, B. P., Finn, K. E., et al. (2018). Natural Sensations Evoked in Distal Extremities Using Surface Electrical Stimulation. *TOBEJ* 12, 1–15. doi:10.2174/1874120701812010001.

- Stakenborg, N., Gomez-Pinilla, P. J., Verlinden, T. J. M., Wolthuis, A. M., D'Hoore, A., Farré, R., et al. (2020). Comparison between the cervical and abdominal vagus nerves in mice, pigs, and humans. *Neurogastroenterology & Motility* 32. doi:10.1111/nmo.13889.
- Störchle, P., Müller, W., Sengeis, M., Lackner, S., Holasek, S., and Fürhapter-Rieger, A. (2018). Measurement of mean subcutaneous fat thickness: eight standardised ultrasound sites compared to 216 randomly selected sites. *Sci Rep* 8, 16268. doi:10.1038/s41598-018-34213-0.
- Tigerholm, J., Poulsen, A. H., Andersen, O. K., and Mørch, C. D. (2019). From Perception Threshold to Ion Channels—A Computational Study. *Biophysical Journal* 117, 281–295. doi:10.1016/j.bpj.2019.04.041.
- Torebjörk, H. E., Vallbo, Å. B., and Ochoa, J. L. (1987). Intraneural Microstimulation in Man: Its Relation to Specificity of Tactile Sensations. *Brain* 110, 1509–1529. doi:10.1093/brain/110.6.1509.
- Trevathan, J. K., Baumgart, I. W., Nicolai, E. N., Gosink, B. A., Asp, A. J., Settell, M. L., et al. (2019). An Injectable Neural Stimulation Electrode Made from an In-Body Curing Polymer/Metal Composite. *Adv. Healthcare Mater.* 8, 1900892. doi:10.1002/adhm.201900892.
- Tronstad, C., Johnsen, G. K., Grimnes, S., and Martinsen, Ø. G. (2010). A study on electrode gels for skin conductance measurements. *Physiol. Meas.* 31, 1395–1410. doi:10.1088/0967-3334/31/10/008.
- Uppal, P., Wright, T. B., Dahbour, L., Watterworth, B., Lee, S. J., Gattu, K., et al. Difficult removal of exposed peripheral nerve stimulator leads: a report of 2 cases. *PR9* 6, e946. doi:10.1097/PR9.0000000000000946.
- Vargas Luna, J. L., Krenn, M., Cortés Ramírez, J. A., and Mayr, W. (2015). Dynamic Impedance Model of the Skin-Electrode Interface for Transcutaneous Electrical Stimulation. *PLoS ONE* 10, e0125609. doi:10.1371/journal.pone.0125609.
- Wall, P. D., and McMahon, S. B. (1985). Microneuronography and its Relation to Perceived Sensation. A Critical Review. *Pain* 21, 209–229. doi:10.1016/0304-3959(85)90086-7.
- Wei, X. F., and Grill, W. M. (2009). Impedance characteristics of deep brain stimulation electrodes *in vitro* and *in vivo*. *J. Neural Eng.* 6, 046008. doi:10.1088/1741-2560/6/4/046008.
- Zakhar, J. (2020). Un-LINQed: Spontaneous extrusion of newer generation implantable loop recorders. *Indian Pacing and Electrophysiology Journal* 20, 189-192. doi:10.1016/j.ipej.2020.04.005.
- Zander, H. J., Graham, R. D., Anaya, C. J., and Lempka, S. F. (2020). Anatomical and technical factors affecting the neural response to epidural spinal cord stimulation. *J. Neural Eng.* 17, 036019. doi:10.1088/1741-2552/ab8fc4.

Zhu, K., Li, L., Wei, X., and Sui, X. (2017). A 3D Computational Model of Transcutaneous Electrical Nerve Stimulation for Estimating A β Tactile Nerve Fiber Excitability. *Front. Neurosci.* 11, 250. doi:10.3389/fnins.2017.00250.

Supplementary Material

Supplementary Material 1 – Market overview of minimally invasive neuromodulation devices

Supplementary Material 2 – Electrochemical interfaces measurement and modeling

Supplementary Material 3 – Current-controlled waveform in swine cadaver

Supplementary Material 4 – Cadaver validation overlayed with values representative of swine skin

Supplementary Material 5 – Mechanism of transcutaneous charge transfer

Supplementary Material 1 – Market overview of minimally invasive neuromodulation devices

Table 3.2: Energy transfer methods used in minimally invasive neuromodulation devices

Fundamental technology	Company
Thin percutaneous wire	SPR therapeutics
Ultrasound	Iota Biosciences (acquired)
Low frequency magnetic field (near-field, non-radiative)	SetPoint Medical
High frequency electromagnetic field (far/mid-field,	Neuspera, Nalu Medical,
radiative)	Stimwave
Low frequency electric field (non-radiative)	StimRouter, NeuronOff (this
	work)

Examples of minimally invasive neuromodulation technologies cleared or approved by the FDA include the SPRINT PNS System, using percutaneous energy transfer on a thin wire, by SPR Therapeutics (Minneapolis, MN) for the treatment of acute pain. In addition, Freedom SCS System and Nalu Neurostimulation System, using radio frequency energy transfer, by Stimwave (Pampano Beach, FL) and Nalu Medical (Carlsbad, CA), respectively, for the treatment of chronic pain.

Several other minimally invasive therapies are in the development pipeline. SetPoint Medical (Valencia, CA) is developing a device, using near-field energy transfer, for inflammatory diseases such as Crohn's and Rheumatoid Arthritis. Neuspera (San Jose, CA) is working on a mid-field powered device for urinary urgency incontinence. Near-field, mid-field, and far-field energy transfer are classified based on the distance of energy transfer relative to the

wavelength of the electromagnetic wave used. In near-field, the distance of energy transfer is short relative to the wavelength; electric and magnetic fields can exist independently of one another, and the waves are non-radiative. In far-field, the distance of energy transfer is long relative to the wavelength; electric and magnetic fields exist together, and the waves are radiative. Iota Biosciences (Berkeley, CA) is working on an ultrasound-powered neuromodulation technology platform.

Supplementary Material 2 - Electrochemical interfaces measurement and modeling

Electrochemical interfaces in the computational model were represented by surfaces that have both resistance and capacitance. The resistive and capacitive values used in the equivalent circuit were based on the empirically measured results described below.

Hydrogel

20 mA of current was sent through two hydrogel TES electrodes adhered to each other. Voltage required to deliver the 20 mA 300 μ s pulse is shown in the red trace below. The faradaic component represents a resistance of ~50 Ohms. The non-faradaic portion is approximately 0.4 V in amplitude. These measurements were used to calculate the conductivity of hydrogel as 1.6 x 10^-2 S/m and relative permittivity of 1.4 x 10^6.

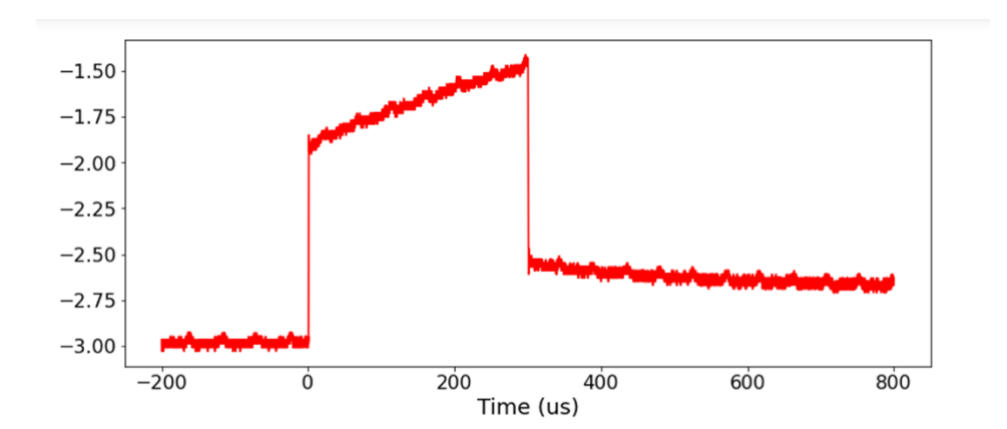


Figure 3.8: Plot of voltage against time when a 20 mA current pulse was delivered to two TES hydrogel electrodes adhered to each other.

Injectrode-tissue Interfaces

Voltage was applied across two collectors immersed in saline solution and current drawn was measured. The applied voltage reflected what was expected at the collector based on

preliminary cadaver measurements. Based on these measurements, the resistivity of the stainless-steel disc collector was calculated to be 6.9 x 10^-2 Ω .m².

Supplementary Material 3 – Current-controlled waveform in swine cadaver

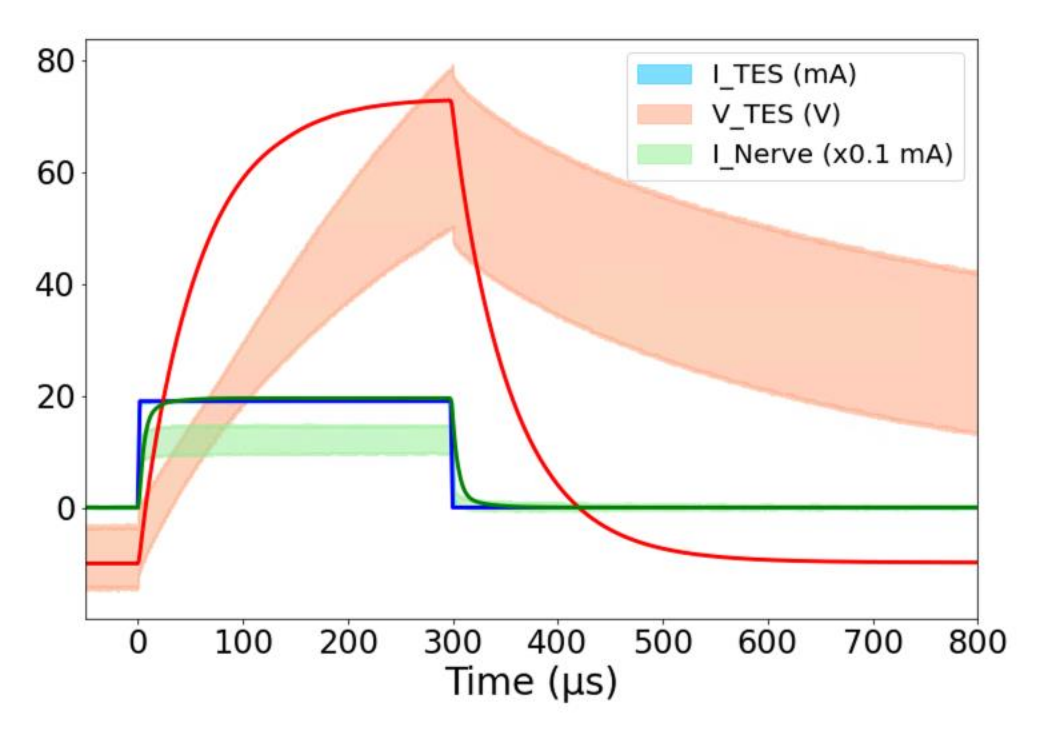


Figure 3.9: Current-controlled waveform in swine cadaver.

Current-controlled 300 μ s monophasic pulses. Three solid lines are simulation results, and three shaded areas are cadaver measurements \pm 1 SD (n=8 measurements from both sides of n=4 cadavers). Red solid line (simulation) and shaded area (cadaver validation measurements) represent voltage of applied stimulation waveform, blue represents current through surface electrodes, and green represents nerve current (scaled by x0.1 mA for visualization). The approximately -10 V offset in cadaver TES voltage is due to a direct current (DC) offset from the stimulation system in current-controlled mode. Computational model results for TES voltage were offset by a similar -10 V here for visualization purposes. Voltage-controlled measurements did not face this offset issue.

Supplementary Material 4 – Cadaver validation overlayed with values representative of swine

skin

Here, compared to Fig. 3.4 in the main manuscript and supplementary material 3, skin

conductivity and permittivity values were manually adjusted from the original Gabriel et al.

(1996b) human literature values to visually match the cadaver measured waveforms. Skin

conductivity was decreased, and permittivity was increased, matching the swine values more

accurately. Pig skin at the abdomen lacks hair follicles and therefore sweat glands – lowering

the conductivity when compared to human skin – which has sweat glands even in regions

without hair follicles (Avci et al., 2013). With the altered skin conductivity and permittivity

values for swine skin, we saw a better fit between the finite element method (FEM) model and

swine cadaver measurements.

Human skin conductivity = 1.80 x 10^-4 S/m

Human skin permittivity = 1.17 x 10³

Fitted swine skin conductivity = $0.9 \times 10^{-4} \text{ S/m}$

Fitted swine skin permittivity = 4.68 x 10³

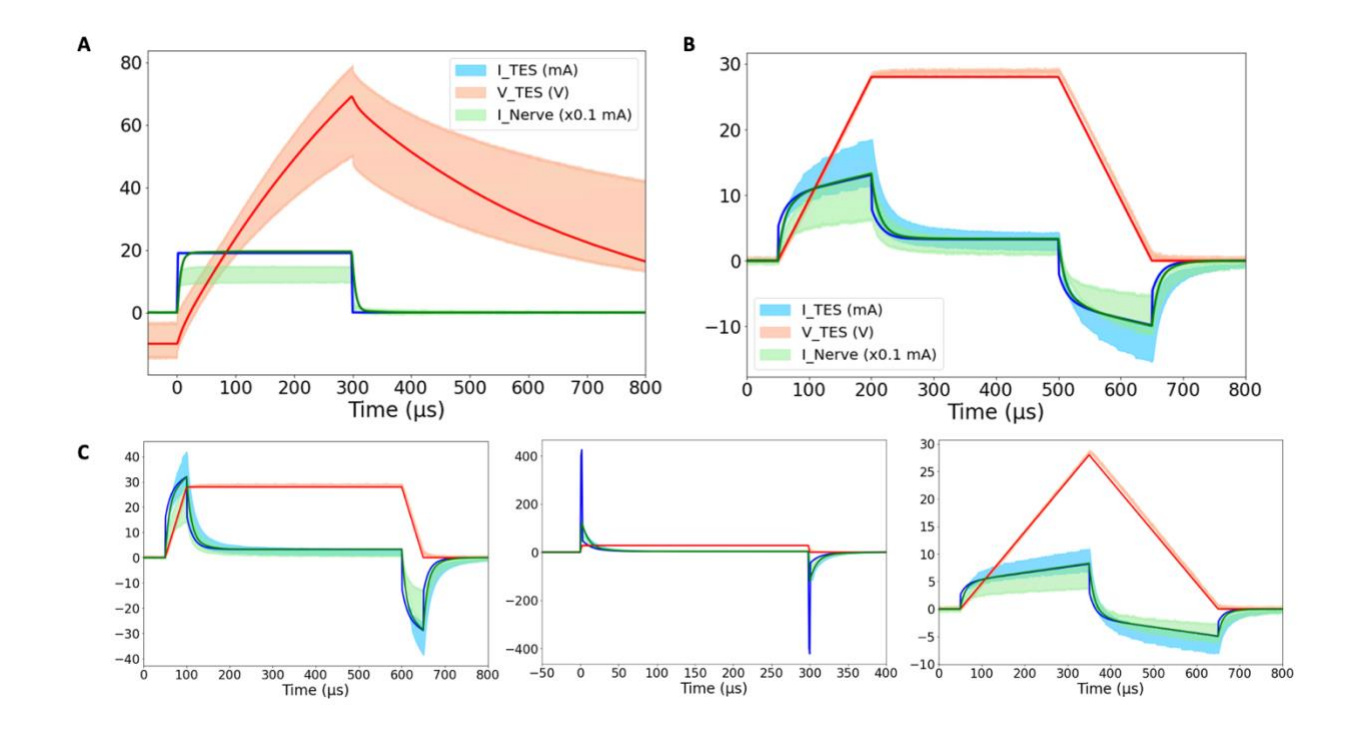


Figure 3.10: Domestic swine cadaver verification of FEM model with fitted skin properties.

Three solid lines are simulation results, and three shaded areas are cadaver measurements \pm 1 SD (n=8 measurements from both sides of n=4 cadavers). Red solid line (simulation) and shaded area (cadaver validation measurements) represent voltage of applied stimulation waveform, blue represents current through surface electrodes, and green represents nerve current (scaled by x0.1 mA for visualization). (a) Current-controlled 300 μ s monophasic pulses. The approximately -10 V offset in cadaver TES voltage is due to a DC offset from the stimulation system in current-controlled mode. Computational model results for TES voltage were offset by a similar -10 V for visualization purposes. Voltage-controlled measurements did not face this offset issue. (b) 28 V voltage-controlled 600 μ s pulses with 150 μ s rise and fall times. (c) (Left) 28 V voltage-controlled pulses of 600 μ s duration with 50 μ s rise and fall times. (Center) 300 μ s duration with fastest (~2 μ s) rise and fall time. (Right) 600 μ s duration with 300 μ s rise and fall times. Note: 50 μ s rise time (left) is n=7 measurements due to the incorrect application of waveform amplitude in one sample.

Supplementary Material 5 – Mechanism of transcutaneous charge transfer

Despite the exponential capacitive waveforms in Fig. 3.4 (b-c), the main mechanism of charge transfer to the nerve is ohmic. The TES-tissue interface is highly capacitive, but once charge enters tissue, ohmic charge transfer dominates. This trend was investigated by setting the skin conductivity to 0 S/m while leaving the permittivity unchanged in the transcutaneous coupling FEM model. A transient simulation was run, and charge transferred to the nerve was calculated as area under the rectified I_{Nerve} curve. In the Fig. 3.4 (c) waveform with the fastest rise time, 29% of the charge transferred to the nerve was maintained when the conductivity of skin was set to 0 S/m and the only way for charge to cross the skin layer was as displacement current.

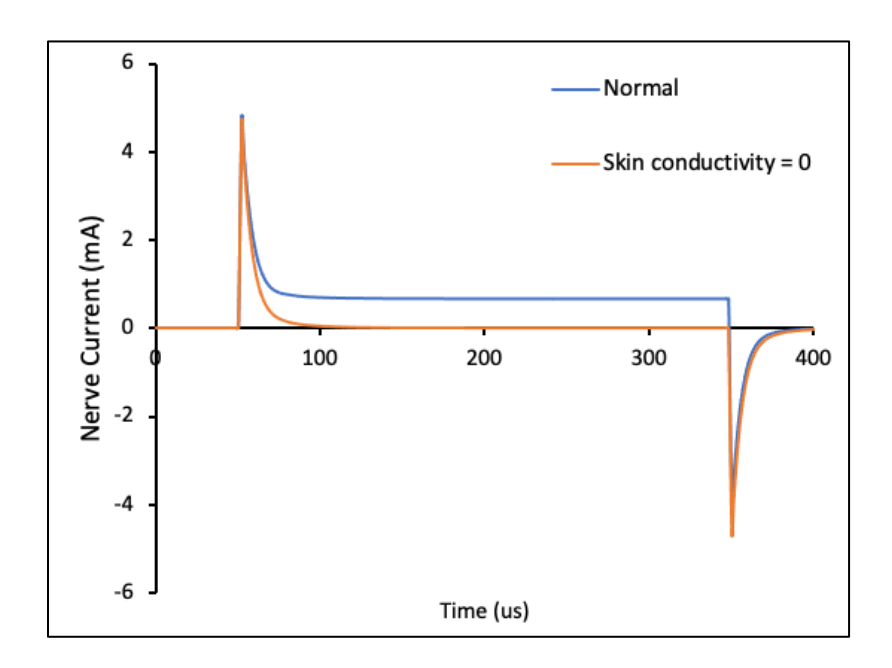


Figure 3.11: Main mechanism of transcutaneous charge transfer is ohmic.

Nerve current against time during application of a 300 μ s duration voltage-controlled pulse. Blue trace represents normal conductivity and permittivity values of skin. Orange trace represents skin conductivity set to 0 S/m (insulator) and the only mechanism for charge to enter tissue was as displacement current. This allowed us to quantify displacement charge transfer versus ohmic charge transfer into the tissue.

Chapter 4 Efficacy of Bone Stimulators in Large-Animal Models and Humans may be Limited by Weak Electric Fields Reaching Fracture This chapter was adapted from the following article accepted for publication in a peer-reviewed journal:

Verma, N., Le, T., Mudge, J., Nicksic, P. J., Xistris, L., Kasole, M., et al. (2022). Efficacy of Bone Stimulators in Large-Animal Models and Humans may be Limited by Weak Electric Fields

Reaching Fracture. *Accepted at Scientific Reports*. Pre-print doi: 10.21203/rs.3.rs-1805225/v1.

Abstract

Noninvasive electronic bone growth stimulators (EBGS) have been in clinical use for decades. However, systematic reviews show inconsistent and limited clinical efficacy. Further, noninvasive EBGS studies in small animals, where the stimulation electrode is closer to the fracture site, have shown promising efficacy, which has not translated to large animals or humans. We propose that this is due to the weaker electric fields reaching the fracture site when scaling from small animals to large animals and humans. To address this gap, we measured the electric field strength reaching the bone during noninvasive EBGS therapy in human and sheep cadaver legs and in validated finite element method (FEM) models of human and sheep legs. During application of 1,100 V/m with an external EBGS, only 21 V/m reached the fracture site in humans. Substantially weaker electric fields reached the fracture site during the later stages of healing and at increased bone depths. To augment the electric field strength reaching the fracture site during noninvasive EBGS therapy, we introduced the Injectrode, an injectable electrode that spans the distance between the bone and subcutaneous tissue. Our study lays the groundwork to improve the efficacy of noninvasive EBGSs by increasing the electric field strength reaching the fracture site.

Introduction

Orthopedic trauma causes \$256.4 billion per year of economic loss in the form of healthcare costs and time lost from work in the United States [1]. These huge costs have driven efforts to augment the well-studied process of fracture healing. Electrical stimulation is one method that has been explored to improve fracture healing. Fukada and Yusada discovered the

piezoelectric property of bone – that bone generates endogenous electrical fields when put under mechanical stress – and its relationship to bone formation in 1953 [2]. Since then, there have been multiple studies in *in vitro*, small animal, and large-animal models, as well as clinical studies, to explore the effects of electrical stimulation on an array of osseous injuries [3]. These studies have led to the approval of nine electronic bone growth stimulators (EBGSs) by the FDA for use in the treatment of osseous nonunion [4].

A recent survey study reported that only 32% of orthopedic traumatologists have ever used an EBGS, and the main reasons given were high costs and inconsistent clinical efficacy [5]. Direct current electrical stimulation (DCES) and capacitive coupling (CC) electrical stimulation are two popular forms of EBGSs. The clinical data suggest that direct current electrical stimulation methods appear to work better to promote bone healing than noninvasive stimulation methods but increase risk of infection [6] and require a costly and complex invasive device that has a high rate of failure due to device-related complications. Capacitive coupling is typically a noninvasive method of electrical stimulation that involves electrodes placed on the skin on opposite sides of the osseous injury. Alternating current generates an electric field between the electrodes, but the penetration of this field into tissues is poor [7], making this modality applicable to only superficial bones like the distal radius or tarsal bones.

The FDA Bone Stimulation workshop report [8] reported that improvements in healing after fracture caused by the application of an electric field are believed to be due to the activation of voltage-gated calcium channels. The report summarized that the electric field causes voltage-gated Ca²⁺ channels in the cell walls of osteocytes to open, changing intercellular and cytosolic Ca²⁺ levels [8, 9]. The change in intercellular and cytosolic Ca²⁺ levels

triggers signaling molecules to promote osteoblastic differentiation and formation, thereby upregulating bone formation activity [8, 10]. The putative mechanism of action depends critically on getting sufficient electric field strengths at the fracture site to open voltage-gated calcium channels and trigger the biological cascade leading to bone healing. The proposed mechanism of action is supported by clinical data suggesting that direct current electrical stimulation methods, where strong electric fields are applied directly to the fracture, appear to work better to promote bone healing than noninvasive stimulation methods [6].

Furthermore, early data *in vitro* [11] and in rodents suggest that noninvasive stimulation from the surface of the skin can work nearly or as effectively as invasive stimulation to promote bone growth, yet the positive results from these models have yet to be born out in clinically translatable large-animal models or clinical studies. One underappreciated factor that may explain this disconnect is the difference in scale between noninvasive stimulation in a rodent versus a human. Electric potential falls off from a bipolar electrode pair proportional to ~1/r² [7], where r is the distance of the tissue from the electrode. In a rodent this distance is often 1 mm or less, whereas in a human the distance to the apex of the fracture can be 1 cm or more, meaning the same voltage applied externally may yield more than two orders of magnitude less electric potential at the site of fracture in humans than in rodents. However, there are no reports in the literature of measurements of electric field strength reaching the fracture site during noninvasive EBGS therapy. This is despite the criticality of the electric field strength at the fracture site to activating voltage-gated calcium channels – central to the proposed mechanism of action of EBGSs.

In this study, we – for the first time – use computational modeling and direct measurements from sheep cadaver metatarsus and tibia and human cadaver tibia cortex to create a validated framework for estimating the electric field strength reaching the fracture site during noninvasive EBGS therapy. We demonstrate that noninvasive stimulation at the skin in a large-animal model only generates a weak electric field at the deep bone fracture. We show that the electric field reaching the fracture site is highly dependent on the depth of the fracture and the electrode configuration. To address these limitations, we introduce a strategy using a novel electrode, the Injectrode, which can be simply injected into the bone fracture in a minimally invasive fashion, to increase the electric field strength reaching the deep fracture site during noninvasive EBGS therapy. Finally, we discuss the changing impedance of tissue at the fracture site during healing and its impact on the electric field reaching the fracture site during noninvasive EBGS therapy. This study lays the groundwork for a future *in vivo* large-animal sheep study planned by our group to test Injectrode-augmented EBGSs versus standard noninvasive EBGSs.

Methods

We made direct measurements of the electric field strength reaching the fracture site in human tibia cadavers to study the limitations of conventional noninvasive EBGSs. These cadaver measurements were used to validate a FEM computer model of a human leg with an EBGS. We then created another FEM model for a sheep leg in the metatarsus region based on dimensions from literature and measured in sheep cadavers and tissue conductivity values from literature (Supplementary Material 1). The sheep model outputs were validated using cadaver

measurements in sheep legs. We used the validated sheep model to study optimal stimulation electrode configurations and the effect of healing stage on the electric field at the fracture site. Lastly, we modeled the Injectrode concept in both human and sheep and tested Injectrode prototypes in human tibia and sheep metatarsus and tibia cadavers.

Cadaver measurements

A total of 5 adult human legs and 5 adult sheep legs were received frozen, kept at -20°C, and thawed 48 hours before the experiment. No experiments were performed on living humans or animals. The de-identified human cadaver legs were ethically obtained from the Anatomy Gifts Registry (Hanover, MD, USA) by donation. In accordance with the United States Federal Policy for the Protection of Human Subjects ('Common Rule'), research on the cadaver legs was not considered human subjects research and did not require institutional ethics approval. Human legs were excluded for known osteoporosis or bone cancers.

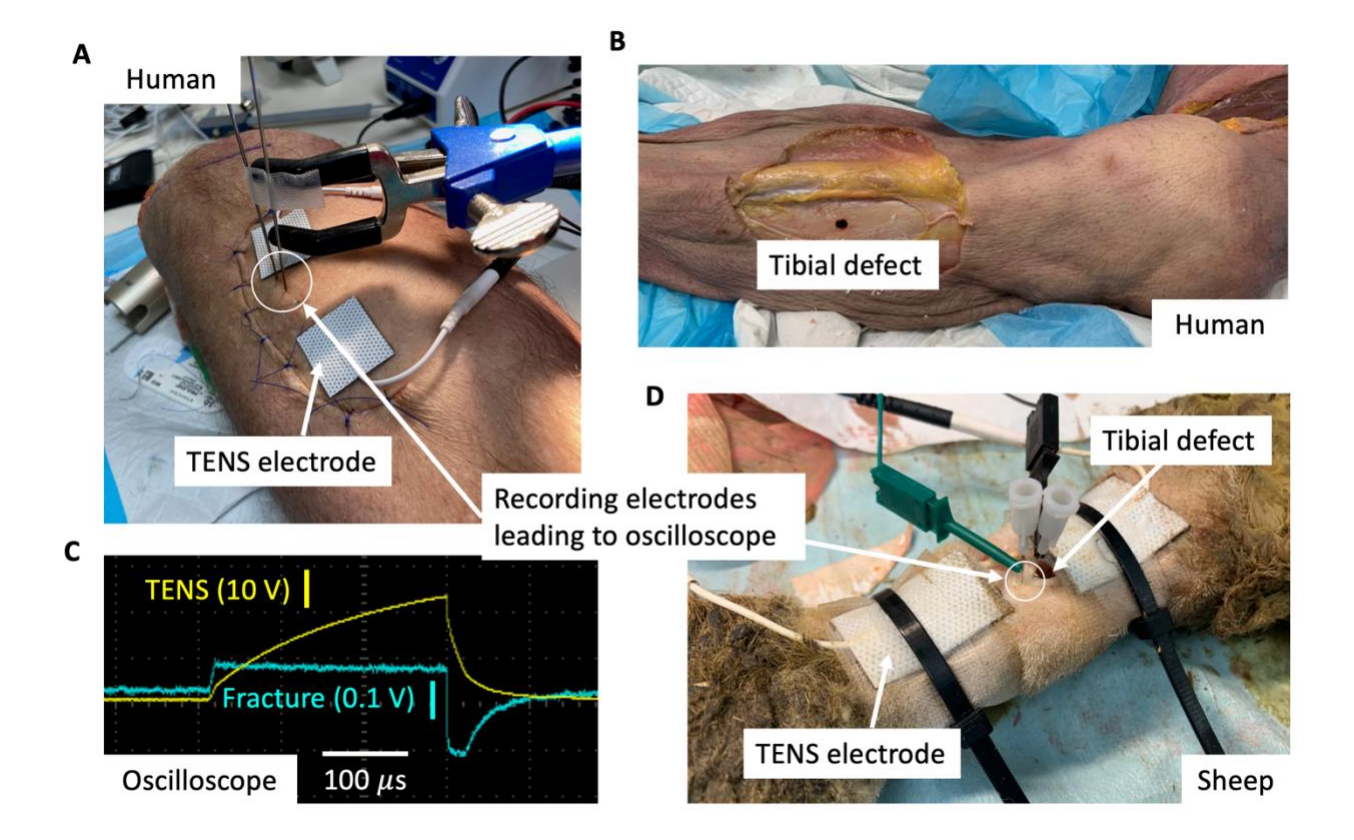


Figure 4.1: Direct electric field measurements at fracture site during noninvasive EBGS therapy.

- (a) Human cadaver leg instrumented with noninvasive stimulation electrodes akin to an EBGS. Surgical flap was created to access tibial bone to drill defect and two small holes for recording electrodes. Microneurography recording electrodes were inserted percutaneously into bipolar measurement holes in bone after the surgical flap was closed with sutures.
- **(b)** Tibial bone defect visible with surgical skin flap retracted.
- **(c)** Oscilloscope screenshot shows voltage delivered through EBGS TENS electrodes externally (yellow trace) and recording at tibial fracture defect internally (blue trace) in a human leg cadaver.
- (d) Recording setup similar to (a) in sheep leg cadaver with metatarsus fracture defect.

Surgical approach and fracture model

For human legs, the tibias were subdivided into three equal sections – proximal third, middle third, and distal third – with the tibial tuberosity as the most proximal landmark and the talocrural joint as the most distal landmark. After the limb was thoroughly shaved, within each section of the tibia, a crescenteric incision was made through the pretibial skin, subcutaneous

fat, and periosteum (Fig. 4.1A-B). The flap of soft tissue was then reflected laterally en-bloc to expose the underlying anterolateral tibial cortex. We measured the pretibial fat thickness of the soft tissue flap for human cadaver limbs, which is the distance between the fracture defect and the stimulation electrodes. A crescenteric incision was selected to minimize interference with soft tissue planes directly under the stimulation electrodes. In this manner, three separate measurement sites were created per human cadaver leg – proximal third, middle third, and distal third. Two human legs were too short to be divided into thirds, so these were divided into halves. One sample was determined to be an outlier based on statistical anomality and a distinct raw waveform shape, suggesting poor contact between the recording electrode and bone (all raw waveforms shown in Supplementary Material 2). Thus, (n=12) total measurements were available from human cadaver limbs. The sheep limbs (Fig. 4.1D) were not divided into thirds and one measurement was taken per limb (with the same approach and setup as described above for human limbs) for a total of (n=5) measurements. Further, Nair™ hair remover was applied to the sheep leg for an extended duration as shaving was insufficient to remove the dense, thick wool coat of the sheep.

To create the fracture model, we drilled a unicortical 5.5-mm diameter defect [12, 13] in the center of the exposed cortex through the anteromedial tibia until cancellous bone was encountered. The depth of the defect was dependent upon cortical thickness of the tibia, which varied from subject to subject, and anatomical location along the longitudinal axis of the tibia.

Drill holes (0.5-mm diameter) were made 2 mm and 5 mm from the defect along the longitudinal axis of the tibia for the recording electrode pair. The soft tissue flap was then closed in layers using 5-0 permanent suture to obliterate dead space. The recording electrodes

were inserted percutaneously through the flap into the 0.5-mm diameter holes made previously in the cortical bone. The noninvasive stimulation electrode pair, separated by 2 cm, was placed across the 5.5 mm osseous defect on the skin overlying the defect.

Electrical Stimulation

Electrical stimulation was delivered to the cadaver legs with a TDT electrical stimulator (Tucker-Davis Technologies, Alachua, FL, USA). Pulses at 5 mA with a pulse width of 300 μ s were administered at 25 Hz through two Transcutaneous Electrical Nerve Stimulation (TENS) electrodes (InTENSity, USA) cut into 1x1 inch squares. The two electrodes were positioned 2 cm apart on the skin overlying the defect. Delivery of the stimulation waveform was monitored on an oscilloscope through the duration of the experiment (Fig. 4.1C). The stimulation frequency and pulse width were selected to be representative of the wide range of parameters explored clinically and preclinically across EBGS modalities [3, 14]. Further work is needed to identify optimal stimulation parameters.

Electric potential measurement

Measurements of electric potentials at the fracture were performed using a pair of shank-insulated microneurography electrodes, with exposed recording tips, inserted into the two 0.5-mm diameter holes, separated by 3 mm, adjacent to the osseous defect. An electrically conductive gel (Physio Control, Redmond, WA, USA) was placed inside the two 0.5-mm recording electrode holes before recording electrode placement to ensure good electrical contact of the recording electrode with bone. 3 mm was selected as the minimum distance we

could reliably drill the second hole without concern of drill bit slippage and damage to the first hole. A smaller distance would give a better estimate of electric field at a point but could also introduce excessive electric field distortion, which occurs from the placement of the conductive measurement probe into less conductive tissue. We used an oscilloscope with differential probes to record the voltage (electric potential) waveform across the two recording electrodes inserted in the bone (Fig. 4.1C) to allow for good electrical isolation from ground.

Electric potential values between the measurement electrode pair were reported throughout this manuscript. To convert to electric field magnitude values (V/m), the electric potential (V) was divided by the distance between the measurement electrode pair (3 mm).

Results were reported in electric potential to allow for more intuitive contextualization by EBGS therapy practitioners who typically program EBGSs in the units of 'Volts' or 'mA'.

Finite element method (FEM) model

FEM models were set up in COMSOL Multiphysics (Burlington, MA, USA) representing simplified adult human legs (tibia region as shown in Fig. 4.2A) and sheep legs (metatarsus region), based on anatomical measurements, with a cortical defect in the anterolateral surface of the bone (Fig. 4.2B and 4.2D). The stimulation electrodes were modeled on the skin's surface overlying the defect. For both humans and sheep, tissue conductivity values were derived from the literature or measured and are summarized in Supplementary Material 1.

FEM Model geometry

We built a 5-layer human lower leg model comprising of skin, fat, muscle, cortical bone, and bone marrow. Cortical bone thickness was set to 12.9 mm with external cortical bone diameter set to 28.8 mm [15] in the human tibia model (Fig. 4.2B). For the sheep metatarsus model (Fig. 4.2D), based on an anatomical study in adult cross-bred ewes [16], cortical bone thickness was set to 14 mm with external cortical bone diameter set to 22 mm. In both models, fat thickness and skin thickness measurements were not available in the literature. Instead, we measured these to be ~2 mm each (Fig. 4.2C). No muscle layer was included in the sheep model to reflect the anatomy of metatarsus. In both the human and sheep models, the bone defect was modeled as a cylindrical cutout of the cortical bone with a diameter of 5.5 mm with full thickness down to the medullary canal. The stimulating electrodes were modeled based on commercially available hydrogel TENS electrodes cut to 1x1 inch squares.

Stage of healing

We defined a high conductivity and a low conductivity material to fill the bone defect to represent early-stage and late-stage fracture healing, respectively [17]. The high conductivity group resulted from averaging the conductivities of dominant bone defect constituents during early bone healing – extracellular fluid, hematoma, and cartilage (Supplementary Material 1). The low conductivity group resulted from averaging collagen and cortical bone conductivities (Supplementary Material 1). These computations generated values of 1.18 S/m and 0.005 S/m, respectively.

FEM solution specifications

The COMSOL stationary study was used to calculate the electric field at the fracture site during noninvasive electrical stimulation. The COMSOL stationary study is a direct current (DC) analysis of the steady-state electric potentials in the modeled volume when a constant electrical stimulation is delivered. A 'fine' mesh was used in both models with 312438 tetrahedral elements in the human model, and 67100 tetrahedral elements in the sheep model. Use of the 'fine' mesh setting was determined through a mesh convergence analysis [18]. For the monopolar configuration of the surface stimulation electrodes, all sides of the model were set as ground to mimic a distant return electrode. For bipolar configurations of the surface electrodes, a current-controlled stimulation was delivered between the two electrodes using a Dirichlet boundary condition [19]. All FEM model simulations were solved with electrical stimulation delivered at 1 mA. Electric potential results were scaled by a factor of five to match the cadaver-delivered stimulation current of 5 mA.

Ohm's law in vector form was used to calculate the spread of current from the surface stimulation electrodes and the corresponding electrical potentials (voltages) throughout the modeled volume. Electric potential at the drill hole fracture site was reported between five paired points (3 mm pair length) around the fracture hole in the model (Fig. 4.2E) because the critical direction relevant to bone healing is currently unknown. The five measurement pairs were selected to provide a representation of the electric field strength at and around the defect in the longitudinal and transverse directions.

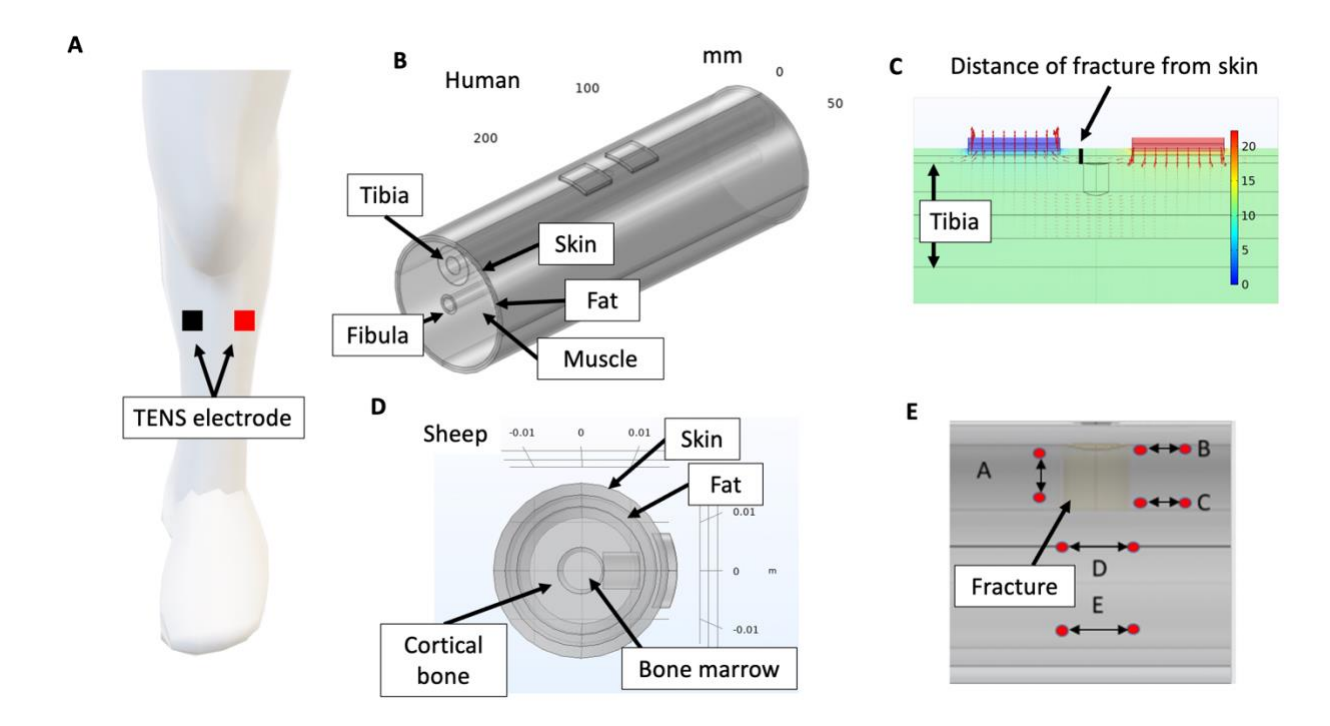


Figure 4.2: EBGS computational FEM modeling in humans and sheep.

- (a) EBGS electrodes deployed noninvasively (capacitive coupling) for tibial fracture.
- **(b)** 5-layer computational FEM model of human tibial defect with noninvasive EBGS electrodes patches as shown in **(a)**. FEM model includes tibia and fibula bone.
- **(c)** Electric potential solution of FEM model in **(b)** showing rapid drop off in electric potential from stimulation electrodes to bone defect, even at a short distance without excess adipose tissue.
- (d) FEM model of sheep metatarsus defect with noninvasive EBGS electrodes patches.
- **(e)** Electric potential measurement points around bone fracture defect. Measurements of electric potentials were taken at five representative points (A-E) as the critical field direction required for bone healing has not been established in literature to date.

Stimulation electrode configuration exploration in silico

Several combinations of different monopolar and bipolar stimulation electrode configurations were tested in the FEM model (Fig. 4.3B-F). Each configuration's resulting electric potential at the defect was measured at five different pairs of points in the model, shown in Fig. 4.2E. These paired points represented the magnitude of the electric field generated by the surface stimulation electrodes at the fracture site.

In the cadaver work, we used a bipolar stimulation electrode configuration with both electrodes over the defect (Fig. 4.3F) and recording electrode point B. Both these choices were motivated by computational modeling results and practical limitations on the set-up.

Practically, there were limitations on where the recording electrode could be inserted with minimal disruption to the anatomy and where the stimulation electrodes could be placed without creating a confound of a direct conductive path through skin by way of the edges of the surgical skin flap.

Injectrode Concept

We utilized an in-body curing injectable electrode, the Injectrode, to address the goal of increasing the electric field strength at the fracture site to promote calcium channel activation [8] and aid bone healing. Injectrode begins as an uncured, free-flowing prepolymer [20]. This prepolymer sets into a solid in the body and forms a conductive interface with the target tissue. In principle, the benefit of this minimally invasive electrode is that it offers increased stimulation strength by targeting the fracture site directly, similar to direct current electrical stimulation (DCES), by routing current from the EBGS TENS electrodes to the fracture site [18]. An Injectrode 'collector' can be added subcutaneously and routed to the bone defect in cases of a deeper fracture (Fig. 4.4C). The Injectrode is a minimally invasive method for delivering electrical stimulation that can be injected sterilely under imaging guidance and remains entirely subcutaneous. Energy is wirelessly delivered to the Injectrode using transcutaneous coupling from external surface electrodes [18]. In this manner, there is no open wound, and the

technique is hypothesized to be less susceptible to infections while increasing the electric current reaching the fracture site.

A silver-particle-based Injectrode prototype, formulated for preclinical studies, was used in this study to demonstrate proof of concept. Injectrode material used in this study was manufactured by NeuronOff, Inc. (Cleveland, OH, USA) using a polymer-conductor variant of the Injectrode as described previously [20]. Two parts of Pt-curing silicone elastomers (World Precision Instruments, FL, USA) with metallic silver particles (Sigma-Aldrich, MO, USA) were mixed and loaded into a 5 mL syringe.

After data collection was performed without the Injectrode, the sutures were released, and the flap was re-elevated. The Injectrode was administered in its elastomer state into the 5.5 mm osseous defect until the surface of the elastomer was flush with the surrounding cortical bone (Fig. 4.4A-B). The flap was then closed, and the recording and stimulation electrodes were placed. Data collection was repeated as it was performed without the Injectrode material in place. This way, each cadaver limb acted as its own control (within-subject design), and the electric potentials measured with the recording electrodes were compared in the non-Injectrode versus the Injectrode configurations to calculate a 'gain' value.

We directly compared measurements of the electric potential at the fracture site between the Injectrode and non-Injectrode states measured in cadavers to the values predicted by the computational FEM models. The Injectrode material was modeled to completely fill the bone defect and have the conductivity of a conductive metal (4e7 S/m) (Fig. 4.4D).

Statistical Analysis

One-sample one-tail t-tests were used to test the null hypothesis (H_0 : gain = 1) against the alternate hypothesis (H_1 : gain > 1) for human and sheep cadavers. One-sample t-tests were selected over paired t-tests as the hypothesis was that Injectrode would augment the electric potential reaching the fracture. The one-sample one-tail t-test offered the simplest method to test this hypothesis, while the calculation of the gain value (ratio of electric potential at fracture without Injectrode to electric potential with Injectrode) further collapsed the variability in electric potential values between cadaver legs. One-sample t-tests and correlation analysis were run in Microsoft Excel 2018. The Shapiro-Wilk test was used to verify the normality assumption of the student t-tests. Type II error tolerance was set at 5% ($\alpha = 0.05$). The study was not pre-registered, and findings should be considered exploratory and not confirmatory.

Results

In the following results section, we first report on measurements of the electric field strength at the fracture site of a human cadaver leg during noninvasive EBGS therapy. These measurements support our hypothesis that the efficacy of noninvasive EBGS therapy may be critically limited by the electric field reaching the fracture site. We then present a computational FEM model of the human leg, validated by the reported cadaver measurements, to study the effect of stage of healing on the electric field strength reaching the fracture site during EBGS therapy. Subsequently, we created a model for sheep, a preclinical large-animal model for fractures, and validated the model with measurements from sheep cadavers. We

used the sheep FEM model to explore stimulation electrode configurations and electric field measurement points around the fracture site.

Observing the limited electric field strengths reaching voltage-gated calcium channels within the bone during EBGS therapy, we evaluated the Injectrode as a minimally invasive method to augment these weak electric fields. We provide modeling results and cadaver measurements in sheep and humans to support the use of the Injectrode in an upcoming *in vivo* preclinical study. Lastly, we present results on the effect of stage of healing and fracture depth on electric field reaching the fracture site during Injectrode-augmented EBGS therapy.

First measurements of electric field at the fracture site during EBGS therapy

In a rodent the distance between the fracture site and the noninvasive EBGS electrodes is often 1 mm or less, whereas in a human the distance to the apex of the fracture can be 1 cm or more (mean of 1.1 cm in this study). The electric potential falls off from a bipolar electrode proportional to $\sim 1/r^2$ [7], where r is the distance between the electrode pair and the bone. This suggests that the same voltage applied externally may yield more than two orders of magnitude less electric potential at the fracture site in humans than in rodents. We hypothesize that the weak electric fields reaching the fracture site in humans explains the loss of efficacy in EBGS therapy from preclinical rodent testing to human clinical results.

To investigate our hypothesis, we made direct measurements of the electric potential at the fracture site during EBGS therapy in human cadavers. During 5 mA of externally applied stimulation through 1x1 inch square TENS electrodes, generating a voltage of ~15-30 V, only 64 mV (45 mV standard deviation (SD)) reached the fracture site on average (Table 4.1). Fig. 4.1C

shows representative traces of the voltage at the external TENS electrodes and internal fracture site during measurements in a human cadaver tibia. Converting electric potential values to electric field strength, only 21 V/m reached the fracture site when ~1,100 V/m was applied externally.

The small ratio, ~1.9%, of the externally applied electric field to the electric field at the fracture site in humans highlights why EBGS therapy may be critically limited in its clinical efficacy, while still performing well in small animal models, where there is a shorter distance between the noninvasive stimulation electrodes and the fracture site. In sheep cadavers, where the distance from the surface of the skin to the apex of the fracture is ~2-5 mm (intermediate to rodents and humans), we measured an average voltage of 680 mV (SD 550 mV) at the fracture site (Table 4.2). Further supporting our hypothesis that the distance between the fracture site and external stimulation electrodes is critical, we observed that with increased pretibial fat thickness in humans (distance between the fracture site and surface EBGS electrodes), the voltage measured at the fracture site decreased (R = - 0.75), shown in Fig. 4.3A.

Table 4.1: Summary of electric potentials reaching fracture site in humans

Human	Measurement pair B (mV)
Model: Early-stage healing	29.7
Model: Late-stage healing	22.0
Cadaver (n=12)	64 SD 45

Computational model of noninvasive EBGS therapy in humans

We constructed a computational FEM model of a human leg with representation of skin, muscle, fat, and the tibia and fibula bone. The computational model calculated 29.7 mV (earlystage healing) and 22.0 mV (late-stage healing) reaching the fracture site during 5 mA of stimulation delivered noninvasively (Table 4.1). The cadaver measurements, expected to be reflective of a stage of healing between early- and late-stage due to tissue preparation, resulted in a voltage of 64 mV (SD 45 mV) at the fracture site. The model prediction was within 1 SD of the cadaver measurements, which is a good fit considering the known variations in tissue conductivity at low frequencies [18]. The model underpredicted the average measured voltage at the fracture site by 54-66%. The error may be coming from the difference in skin impedance, a sensitive parameter, between the model and the cadaver. The cadaver skin impedance was likely higher due to the dehydration of the tissue and therefore required a greater voltage to deliver 5 mA of noninvasive stimulation. We calculated the voltage across the TENS electrode in the FEM model to be 3.8 V at 5 mA of stimulation compared to the 15-30 V in the cadavers (See Supplementary Material 2). The higher voltage across the TENS electrodes in the cadaver would result in a correspondingly higher voltage at the fracture site, compared to the FEM model.

We computed the ratio of electric field applied externally to the electric field at the fracture site to compare to the average 1.9% ratio measured in the human leg cadaver. The human FEM model predicted a ratio of 1.9% for late-stage healing and 2.6% for early-stage healing compared to the 1.9% measured in the cadaver. This excellent agreement of electric field ratios between model and cadaver suggested that the model predicted the spread of

electric field accurately. Therefore, trends in the FEM model may be accurate even when absolute values were not.

Stage of healing and electric field at fracture site with conventional EBGSs

The evolving biological process at the fracture site [17] during healing leads to different tissue electrical conductivities at the fracture site over the course of the healing process. In general, the conductivity at the fracture site decreases during healing, starting with a conductivity similar to extracellular fluid or hematoma and ending with the conductivity of cortical bone. This influences the electric field reaching the fracture site during use of an EBGS. More electric current reaches the fracture site in the acute stage of healing as the fracture is filled with higher conductivity material and represents a preferential, lower resistance, path for current to travel. For this reason, we computed model values for both early-stage and late-stage healing (Table 4.1).

Electric field at fracture site during EBGS therapy in sheep

We used a computational FEM model of a sheep leg to explore several different stimulation electrode configurations and identify optimal configurations for an upcoming sheep EBGS study planned by our group. We also used the model to explore electric field measurements at different points around the fracture site (Fig. 4.2E) because the critical direction relevant to bone healing is currently unknown.

We created a model for a sheep leg in the metatarsus region based on dimensions from literature and measured in sheep cadavers. We then attempted to validate the model with

measurements in sheep cadavers (n = 5). The model calculated 5385 mV reached the fracture site during 5 mA of noninvasive stimulation, while cadaver measurements averaged 680 mV (SD 550 mV) at the fracture site (Table 4.2). The model overpredicted the average measured voltage at the cadaver fracture site by 690%. The error may again be due to the difference in skin impedance between the model and the cadaver, a sensitive parameter [18]. The cadaver skin impedance could be substantially lower due to the application of Nair™ for an extended duration to remove the thick hair of the sheep. The Nair™ could have damaged the high impedance outer layer of skin (stratum corneum in the epidermis). With a lowered skin impedance, we would have required a lesser voltage to deliver 5 mA of noninvasive stimulation into the skin. The lesser voltage across the TENS electrodes in the cadaver would result in a lesser voltage at the fracture site compared to the FEM model. To test this hypothesis, we adjusted the skin layer conductivity in the model from 8.0e-4 S/m (dry skin [21]) to 4.34e-1 S/m (dermis [22]) to model skin with the outermost epidermis layer compromised by the extended application of Nair™. The updated FEM model calculated 536 mV reached the fracture site during 5 mA of noninvasive stimulation – in excellent agreement with the cadaver measurements of 680 mV (SD 550 mV). However, for the remaining study, we used the original conductance of skin (8.0e-4 S/m) in the sheep model. We did this to retain the relevance of the sheep model findings to the planned in vivo Injectrode-augmented EBGS sheep study, where the skin preparation will be more conservative and should not damage the epidermis.

Several electrode configurations were explored in the FEM model to identify suitable configurations for an upcoming sheep EBGS study planned by our group. Stimulation electrode configuration (Fig. 4.3B-F) and measurement point (Fig. 4.2E) had a profound impact on the

electric field value. The stimulation electrode configuration 'bipolar (both over defect)' produced the highest electric field at the fracture site at measurement point B (5385 mV). This motivated use of point B and stimulation electrode configuration 'bipolar (both over defect)' to maximize the signal to noise ratio for cadaver electric potential measurements.

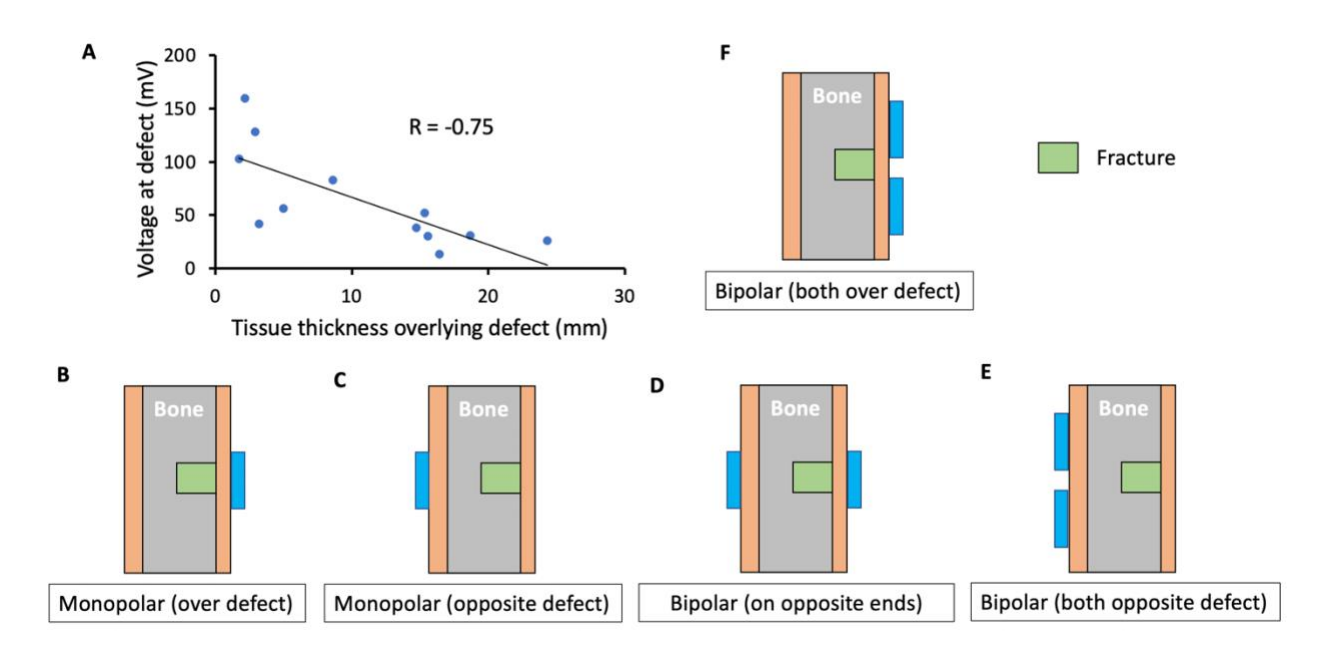


Figure 4.3: Results of noninvasive EBGS FEM models in sheep investigating stimulation electrode configurations.

- (a) Increased distance between the fracture defect and the stimulation electrodes is correlated to decreased voltage at the defect site during noninvasive EBGS therapy. This supports our hypothesis that EBGSs are critically limited in humans and large-animal models due to the weak electric fields reaching the fracture site.
- **(b)** Electric potential solution with stimulation electrode over defect site in monopolar configuration with distant return.
- **(c)** Electric potential solution with stimulation electrode opposite defect site in monopolar configuration with distant return.
- (d) Electric potential solution with stimulation electrodes in bipolar configuration: one over defect site and one opposite defect site.
- **(e)** Electric potential solution with stimulation electrodes in bipolar configuration: both opposite defect site.
- **(f)** Electric potential solution with stimulation electrodes in bipolar configuration: both over defect site. This configuration was used in all reported cadaver measurements.

Table 4.2: Summary of electric potential at fracture site in sheep

Sheep model: early-stage					
healing	Measurement pair (mV)				
Stimulation electrode configuration	Α	В	С	D	E
Monopolar (over defect)	751	1773	2677	0	0
Monopolar (opposite defect)	54	152	34	0	1
Bipolar (on opposite ends)	940	1305	2430	0	0
Bipolar (both opposite defect)	35	475	555	435	1235
Bipolar (both over defect)	840	5385	3725	1295	1125
Cadaver: Bipolar (both over defect) (n=5)	NA	680 SD 550	NA	NA	NA

Computational models and cadaver experiments support use of Injectrode to augment EBGS therapy

The Injectrode, a minimally invasive conductive electrode, may be injected under image guidance to the fracture site to guide current delivered noninvasively towards the fracture site. We hypothesize that utilizing Injectrode at the fracture site will augment the electric field reaching the bone during noninvasive EBGS therapy. To investigate the efficacy of the Injectrode to augment the electric field reaching the fracture site, we modified the previous sheep and human computation models to include the Injectrode. We also made measurements in the same cadaver models with the addition of Injectrode in the fracture. We report on the

'gain' in electric field at the fracture site (point B in Fig. 4.2E) with Injectrode compared to without Injectrode. A value greater than one indicates efficacy of the Injectrode.

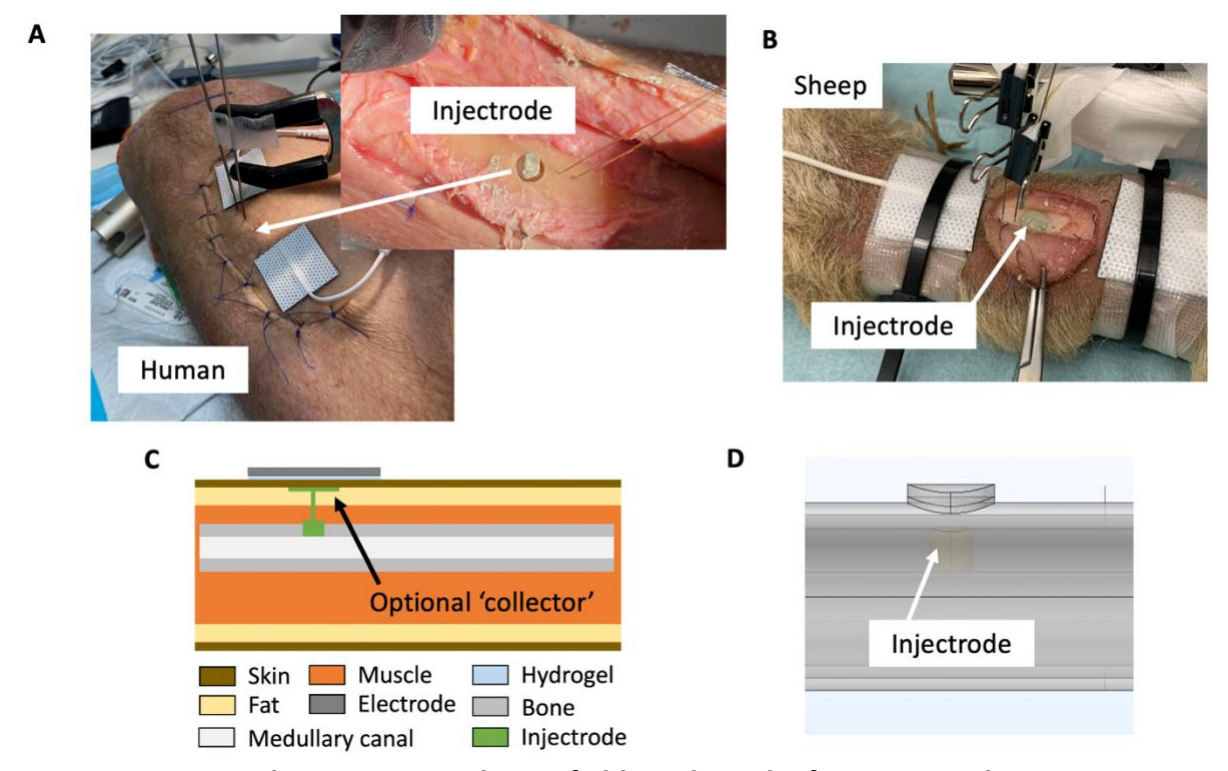


Figure 4.4: Injectrode to augment electric field reaching the fracture site during noninvasive EBGS therapy.

- (a) Addition of Injectrode to fracture defect under surgical flap in human cadaver.
- **(b)** Addition of Injectrode to fracture defect in sheep cadaver.
- **(c)** Illustration of Injectrode 'collector' placed subcutaneously with injected Injectrode wire leading to more Injectrode at the fracture site (monopolar configuration). Thereby, routing current from the surface of the body to the deep bone and increasing electric field strength reaching the fracture site. Note that the Injectrode 'collector' is optional for superficial fractures but will be beneficial for deep fractures.
- **(d)** Injectrode in the FEM model. 3D representation of schematic in **(c)** without optional Injectrode 'collector'.

Computational modeling for the human tibia in the late-stage healing state (low conductivity tissue at fracture site) resulted in a 37% gain in electric field at the fracture site with the addition of the Injectrode (Table 4.3). For the early-stage healing state (high conductivity tissue at fracture site), the gain was a lesser 2% with the addition of the Injectrode.

Human cadaver measurements (n=12), which are likely reflective of a state between early- and late-stage healing, showed an average gain of 23% (SD 22%, p=0.002, H_0 : gain = 1, H_1 : gain > 1, one-tail). The human cadaver measurements were in good agreement with the FEM model predictions with an error of 11-17% between model early- and late-stage healing and the cadaver setup. Note that we consider these findings exploratory and not confirmatory because the measurement and statistical analysis methods were not pre-registered but determined post-hoc instead.

Table 4.3: Human results of Injectrode-augmented EBGS

Human	Measurement pair B (gain)
Model: Early-stage healing	1.02
Model: Late-stage healing	1.37
Cadaver (n=12)	1.23 SD 0.22

FEM modeling for the sheep metatarsus predicted a 69% gain in electric field at the fracture site with the addition of the Injectrode in the late-stage healing state (low conductivity tissue at fracture site) (Table 4.4). In the early-stage healing state (high conductivity tissue at fracture site due to initial edema buildup), there was a lesser 1% gain predicted by the model with the addition of the Injectrode to the metatarsus fracture. Cadaver measurements at the superficial metatarsus bone (mimicking the model) showed a gain of 22% (SD 59%, p=0.23, H₀: gain = 1, H₁: gain > 1, one-tail), shown in Fig. 4.5A. The sheep metatarsus cadaver measurements were in good agreement with the FEM model predictions with an error of 17-39% between model early- and late-stage healing and the cadaver setup – despite larger errors

in the absolute voltage values at the fracture site (as discussed earlier in this paper). The sheep FEM model is therefore still useful for studying relative trends including the 'gain' ratio between the electric field at the fracture site with and without Injectrode. The sheep cadaver 'gain' increase was not statistically significant, in large part due to the higher variability (standard deviation) in the data. The methods for recording voltages at the bone defect in cadavers were initially developed during these sheep cadaver experiments, before the human cadaver measurements, and could explain the larger standard deviation of the sheep cadaver measurements compared to the human cadaver measurements.

Table 4.4: Sheep results of Injectrode-augmented EBGS

Sheep metatarsus model: early-stage					
healing (unless specified)	Measurement pair (gain)				
Stimulation electrode configuration	Α	В	С	D	E
Monopolar (over defect)	0.94	1.00	1.02	NA	NA
Monopolar (opposite defect)	0.94	1.02	0.85	NA	NA
Bipolar (two electrodes on opposite end)	0.94	0.99	1.02	NA	NA
Bipolar (both opposite defect)	1.00	1.01	1.02	0.99	1.00
Bipolar (both over defect)	0.97	1.01	1.01	-0.98	-1.00
Bipolar (both over defect), late-stage					
healing	0.59	1.69	1.66	-0.65	-0.88
		1.22 SD			
Cadaver: Bipolar (both over defect) (n=5)	NA	0.59	NA	NA	NA

Depth of fracture increased utility of Injectrode-augmented EBGS therapy

We found that the Injectrode provided more benefit over conventional EBGSs at greater depths of the fractured bone from the surface of the skin. With increased pretibial fat thickness in humans (distance between fracture site and surface EBGS electrodes), the 'gain' in electric field at the fracture site with the Injectrode compared to without increased (R = 0.54), shown in Fig. 4.5C. Furthermore, cadaver measurements at the deeper sheep tibia showed a gain of 39% (SD 70%, p=0.14, H_0 : gain = 1, H_1 : gain > 1, one-tail) compared with the superficial metatarsus bone, which showed a gain of only 22% (SD 59%, p=0.23, H_0 : gain = 1, H_1 : gain > 1, one-tail), shown in Fig. 4.5B.

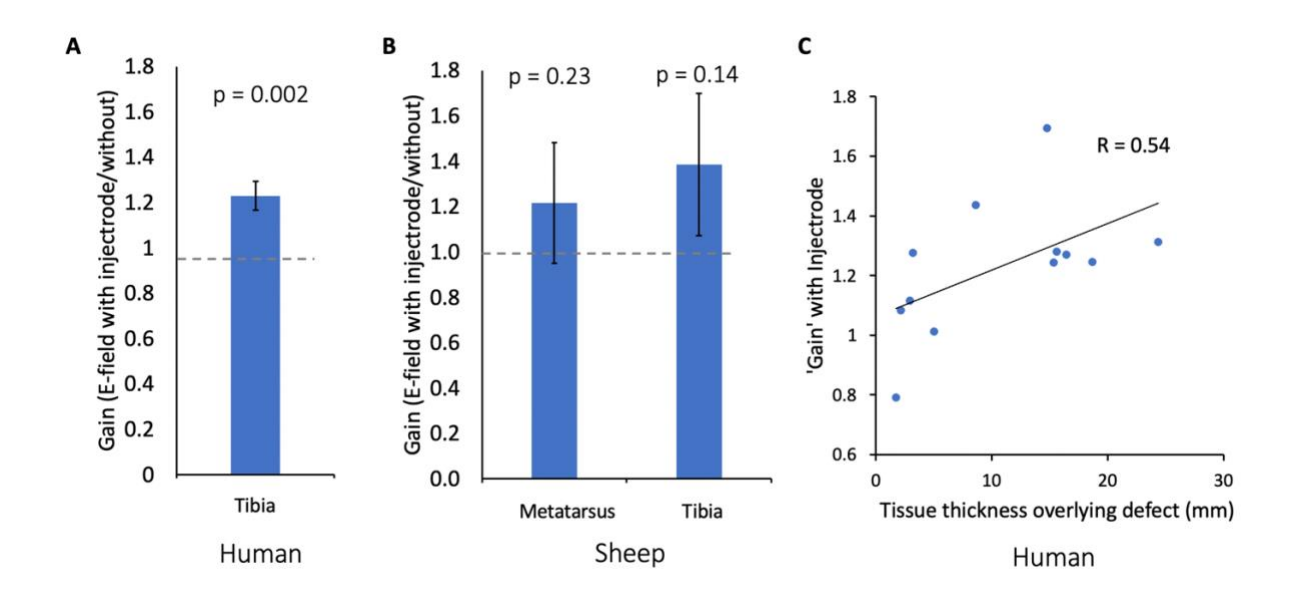


Figure 4.5: Injectrode increases electric field at fracture site when used with noninvasive EBGS therapy.

- (a) 'Gain' in electric field at tibial fracture defect with Injectrode-augmented EBGS therapy in human leg cadavers. Error bars indicate standard error of the mean (SEM). T-test H_0 : gain = 1, H_1 : gain > 1, one-tail.
- (b) 'Gain' in electric field at independent tibial and metatarsus fracture defects with Injectrode-augmented EBGS therapy in sheep leg cadavers. T-test H_0 : gain = 1, H_1 : gain > 1, one-tail.
- (c) Scatter plot showing increased utility of Injectrode to augment electric field at fracture site at increased bone depths.

Stage of healing and electric field at fracture site with Injectrode-augmented EBGS

Data in Tables 4.3 and 4.4 showed that, as with conventional noninvasive EBGSs, electric potential at the fracture site during Injectrode-augmented EBGS therapy was also affected by the tissue electrical conductivity in the fracture site as it changed with the stage of healing.

Opposite to conventional EBGSs, Injectrode was most advantageous after early stages of healing instead of during. This is because conductive edema acts, to some extent, similarly to the Injectrode, especially for more superficial defects. Computational modeling with the Injectrode showed a 34% and 67% greater electric field, in humans and sheep respectively, at the fracture site during later stages of healing compared to earlier stages of healing.

Discussion

In this study, we reported on electric fields measured at the fracture site during noninvasive EBGS therapy. Strength of the electric field at the fracture site is believed to be critical to the proposed mechanism of action of EBGSs – the activation of voltage-gated calcium ion channels [8]. We investigated the electric field strengths reaching the fracture site during noninvasive EBGS therapy in sheep and human cadavers and computational models. We observed minute electric fields reaching the fracture site. On average, only ~1.9% of the externally applied electric field reached the fracture site in human cadavers. We reported on the effects of fracture depth and healing stage on the electric field strength reaching the fracture site. We then proposed and investigated the use of a minimally invasive injectable electrode, the Injectrode, to augment the electric field reaching the deep fracture site. The computational and cadaver models in this study lay the groundwork for a preclinical sheep

study planned by our group to investigate the use of the Injectrode *in vivo* to augment electric field strength reaching the fracture site – and consequently improving time to fracture healing – during EBGS therapy.

To our knowledge, this is the first study to characterize electric field strengths at the fracture site during noninvasive EBGS therapy. This marks a critical step towards building consistent efficacy of EBGSs in human patients. We measured only ~1.9% of the externally applied electric field reaching the fracture site in human cadavers. This translates to an electric field strength of 21 V/m at the fracture site during 5 mA of noninvasive stimulation. The 21 V/m electric field strength is low compared to neural activation thresholds, which are reported to be >100 V/m [23]. Neural activation is predicated on voltage-gated sodium channel activation while bone healing is putatively based on voltage-gated calcium channel activation, so differences in activation threshold are expected between sodium and calcium channels. However, the known neural activation thresholds contextualize the weak electric field strengths reaching the fracture site during noninvasive EBGS therapy in humans — even on the most superficial of bones. There are notable parallels between bone stimulation and neurostimulation and both fields may benefit from adopting techniques used in the other [11].

Though there are many promising preclinical studies examining the effects of electrical stimulation for a wide array of osseous insults, many use custom stimulators and provide incomplete device specifications, making it difficult to repeat the experiment or translate the findings [3]. Moreover, many of these studies do not measure the electric field strength reaching the fracture site [3]. Directly measuring electric field in the cortex of the bone is critical to understand the field strengths required for a therapeutic effect and is also critical to scale

from culture and small animal studies to large animal and humans [24]. The authors recommend future studies in the bone stimulation field employ direct measurement strategies.

Both computational and cadaver models in our study showed that 1) conventional EBGSs deliver lower electric fields to deeper fracture sites (Fig 3A) and that 2) Injectrode-augmented EBGSs provides more of a benefit ('gain') over conventional EBGSs at deeper fracture sites. These findings explain why, in a previous study on the Injectrode for noninvasive neural stimulation [18], the Injectrode was shown to improve neural activation by more than an order of magnitude over conventional noninvasive stimulation, while in the current study, the Injectrode is showing a more limited benefit of a 37% increase in electric field at the fracture site. The current work is studying the tibial bone, where the fracture is at a depth of only a few mm from the stimulation electrodes, while in the previous neural study, the nerve of interest was at a depth of ~2 cm from the stimulation electrodes. Overall, this makes deeper bones, such as the femur, more ideal to show the benefit of Injectrode-augmented EBGSs over conventional EBGSs. For fractures at the depth of the femur, the optional Injectrode 'collector' (Fig. 4.4C) may be required to realize the full potential of the Injectrode.

The two findings highlighted in the previous paragraph also explain why the Injectrode was shown to have a statistically significant benefit in augmenting electric field at the fracture site in human but not sheep cadavers. The depth of the fracture was deeper on average in humans, due to pretibial fat, compared to sheep. This resulted in weaker electric fields at the fracture site with conventional EBGS therapy and more of a 'gain' with the Injectrode. The larger effect size contributes greatly to establishing statistical significance at small sample sizes.

Our findings also characterize the effect of the stage of bone healing on efficacy of conventional noninvasive EBGSs. With a conventional EBGS, the electric field reaching the fracture is higher during the acute stages of healing, when high conductivity tissue fills the fracture – acting to route current to the deep fracture site. However, with an Injectrode-augmented EBGS, the 'gain' in electric field at the fracture is higher during the later stages of healing – when low conductivity tissue fills the fracture. The higher 'gain' of the Injectrode at later stages of healing has positive implications towards the delivery of Injectrode after a fracture. The Injectrode does not need to be administered immediately in the acute stages of healing, but rather can be administered even in the later stages of healing – widening the therapeutic time window available for its application.

Inductive coupling is another noninvasive EBGS modality that exists in the form of pulsed electromagnetic field (PEMF) therapy, which uses pulsed currents through solenoids arranged parallel to the skin to generate an alternating magnetic field. The alternating magnetic field induces an alternating electric field in tissue. PEMF therapy suffers reliability issues with electric field strength variation due to variation in the placement of the device and the thickness of enveloping soft tissue layers [24]. PEMF devices would benefit from a similar study as reported in this paper with direct measures of the electric field reaching the bone.

There were discrepancies between the computational model and cadaver measurements in absolute electric field value, especially in the sheep model. This was explained by the differences in tissue conductivity − especially the skin layer, after freezing and thawing in the cadaver and the application of Nair™ for hair removal − compared to tissue conductivity values from literature performed in living subjects or fresh tissue samples used in the FEM

model. Although these differences in tissue conductivity make absolute electric field results from the model less predictive, relative results and trends still hold. An example of a relative result is the 'gain' value calculated for the model, which was the ratio of electric field at the fracture site with Injectrode compared to without. A better agreement was seen between cadaver and computational models in these gain values for both the human and sheep model.

Also due to differences in tissue conductivities, the cadaver measurements are likely reflective of values between early-stage and late-stage healing. The cadavers were frozen and then thawed, which created accumulation of high conductivity fluid in the leg. At the same time, due to the lengthy duration since the death of the subject, some tissue had congealed, forming lower conductivity spaces. Overall, the cadaver is likely more reflective of early-stage healing due to the accumulated fluid in the fracture drill hole from thawing of the cadaver limbs. For these reasons, we compared cadaver measurements to both early-stage and late-stage results from the FEM model. Opening and then suturing of the soft tissue flap in the cadaver legs could also have changed the conductivity of the thin fascial tissue layers compared to the intact state. Performing a similar protocol in a live anesthetized animal, or in a chronic experiment where scar formation occurs, would provide a more accurate picture of the electric fields reaching the fracture site during noninvasive EBGS therapy.

Further limitations of the experimental and modeling set-up may also explain the differences between the computational model and cadaver results. Firstly, the computational model assumed uniform thickness of fat and skin across the tibia. The human cadaver model in comparison is not a uniform cylinder and was subjected to wider variations. Secondly, the depth of the defect from the stimulation electrode has a profound effect on the electric

potential reaching the fracture ($^{\sim}1/r^2$ relationship, where 'r' is distance) [7]. To this end, in the FEM model, we had a single distance between the defect and the stimulation electrodes, representing the average distance in cadavers. In each cadaver, this distance varied and may have contributed greatly to the subject-to-subject variation observed in the cadaver results.

The unicortical fracture model we used in this study is established to study bone healing and novel therapeutics [12, 13]. While it does not fully capture the clinically relevant nonunion application of EBGS, for which an osteotomy 'gap' model may be more relevant, it does provide the capacity for high throughput testing with reduced risk to the animal. The unicortical fracture model was ultimately selected here to maximize the relevance of this study to the future chronic *in vivo* sheep study planned by our group to study Injectrode-augmented EBGSs versus standard noninvasive EBGSs.

The ideal EBGS would be relatively low cost and easy to administer, produce reliable stimulation, regardless of patient position or body habitus, and pose a minimal infection risk. Direct current electrical stimulation (DCES), as previously described, poses a significant infection risk and requires surgeries to implant and remove the device. Noninvasive stimulation (capacitive coupling) is an attractive option as it is noninvasive, thereby minimizing infection risk, and easy to use. However, the penetration of the electrical field into tissue is proportional to $\sim 1/r^2$ with 'r' being the distance from the electrode [7], making it useful only for superficial fractures. Finally, PEMF is noninvasive, and the magnetic field penetrates tissue well, but the devices are expensive and the electric fields at the fracture site are weak and heavily contingent upon device positioning and the thickness of tissue layers specific to each patient [24]. The

sensitivity to position also makes PEMF heavily operator dependent and potentially inconsistent from application to application.

The Injectrode has the potential to provide reliable stimulation strength similar to DCES without the need of open surgeries for implantation and removal, which lead to increased risk of infection. To this end, the Injectrode has already been validated to produce neural effects at similar levels as conventional electrodes for dorsal root ganglion stimulation in a cat model [25]. While there are significant differences between the conductivity of bone and nerve tissue, Injectrode-augmented noninvasive EBGS therapy may offer a promising solution for the treatment of osseous nonunion and acute fractures prone to nonunion.

The Injectrode formulation used in this study was an early silver-particle-based prototype – only for use in cadaver and acute preclinical studies due to the toxicity of silver. It was used in this study to demonstrate proof of concept of electric field increase at the fracture site with Injectrode-augmented noninvasive EBGS. Other electrically conductive materials would have a similar effect of increasing electric field at the fracture site. Future versions of the Injectrode under development are based on gold or platinum microwires. Future work will need to investigate biocompatibility of the Injectrode, degradation kinetics, and its suitability to be injected at the fracture site. Past work includes testing the biocompatibility of the Injectrode in humans [26].

This computational study lays the groundwork for a future preclinical study planned by our group to investigate augmenting conventional EBGSs with Injectrode to increase the electric field strength reaching the fracture site. While the Injectrode prototypes used in this study were used for proof-of-concept testing, newer generations of the microwire-based

devices have higher translational potential. In the later stages of healing, we showed in sheep computational models and cadavers that the Injectrode-augmented EBGS therapy increased electric field strength at the fracture site by ~70% and 60% respectively compared to conventional EBGS therapy. Rats [27, 28], rabbit [29, 30], and sheep [31] have been used as animal models in published fracture healing studies investigating electrical stimulation to improve osteogenesis. We intend to use the large-animal sheep model in our study and so focused on studying sheep alongside humans in this study.

Conclusions

In a large-animal fracture model, sheep, and human, both modeling and cadaver measurements demonstrate that noninvasive EBGS therapy applied transcutaneously generates weak electric fields at the fracture site. These data suggest it is critical to consider how the electric fields applied by stimulation electrodes change at a distant portion of tissue when scaling from culture or small animals to large animals or humans. Our findings 1) help explain the inconsistency in translating promising EBGS results showing improved fracture healing in small animal studies to clinical use and 2) lay the groundwork for a future large-animal study to test the use of Injectrode-augmented EBGSs to further aid bone healing by increasing electric field strengths reaching the deep fracture site.

Acknowledgements

Carly Frieders, Harrell Huff, and Jyoti Sahi for reviewing drafts of this manuscript.

Members of the Wisconsin Institute for Translational Neuroengineering (WITNe) for feedback during group meetings.

This work was funded by the University of Wisconsin – Madison Department of Surgery startup funds.

Author Contributions

NV, AJS, SOP, KAL, and AMD conceptualized and/or designed the study. NV, TL, JM, LX, and MK conducted the experiments. NV, TL, JM, PJN, and LX analyzed the data. NV, TL, JM, and PJN drafted the manuscript. All authors revised the manuscript and approved the final version for submission.

Competing Interests

NV is an employee of Abbott Neuromodulation and BioCircuit Technologies. KAL is a scientific board member and has stock interests in NeuroOne Medical Inc. KAL is also a paid member of the scientific advisory boards of Cala Health, Blackfynn, Abbott Neuromodulation, and Battelle. KAL also is a paid consultant for Galvani, Boston Scientific, CVRx, Presidio Medical, and the Alfred Mann Foundation. KAL and AJS are co-founders of NeuronOff Inc., which is commercializing the Injectrode.

The remaining authors declare that the research was conducted in the absence of any commercial or financial relationships that could be construed as a potential conflict of interest.

Data Availability

All data generated or analyzed during this study are included in this published article (and its Supplementary Information files).

References

- 1. Yelin, E., Weinstein, S. & King, T. The burden of musculoskeletal diseases in the United States. *Seminars in Arthritis and Rheumatism* **46**, 259–260 (2016).
- 2. Fukada, E., & Yasuda, I. On the Piezoelectric Effect of Bone. *Journal of the Physical Society of Japan* **12**, 1158–1162 (1957).
- 3. Nicksic, P. J. *et al.* Electronic Bone Growth Stimulators for Augmentation of Osteogenesis in In Vitro and In Vivo Models: A Narrative Review of Electrical Stimulation Mechanisms and Device Specifications. *Front. Bioeng. Biotechnol.* **10**, 793945 (2022).
- 4. Aleem, I. S. *et al.* Efficacy of Electrical Stimulators for Bone Healing: A Meta-Analysis of Randomized Sham-Controlled Trials. *Sci Rep* **6**, 31724 (2016).
- 5. Bhavsar, M. B. *et al.* Electrical stimulation-based bone fracture treatment, if it works so well why do not more surgeons use it? *Eur J Trauma Emerg Surg* **46**, 245–264 (2020).
- 6. Jorgensen, T. E. Electrical stimulation of human fracture healing by means of a slow pulsating, asymmetrical direct current. *Clinical orthopaedics and related research* **124** 124-127 (1977).
- 7. Plonsey, R. & Barr, R. C. Electric field stimulation of excitable tissue. *IEEE Trans. Biomed. Eng.* **42**, 329–336 (1995).
- 8. FDA. FDA Executive Summary Prepared for the September 8-9, 2020 Meeting of the Orthopaedic and Rehabilitation Devices Panel Reclassification of Non-Invasive Bone Growth Stimulators. (2020).
- 9. Pall, M. L. Electromagnetic fields act *via* activation of voltage-gated calcium channels to produce beneficial or adverse effects. *J. Cell. Mol. Med.* **17**, 958–965 (2013).
- 10. Tonelli, F. M. P. *et al.* Stem Cells and Calcium Signaling. in *Calcium Signaling* (ed. Islam, Md. S.) vol. 740 891–916 (Springer Netherlands, 2012).
- 11. Pettersen, E., Shah, F.A. & Ortiz-Catalan, M. Enhancing osteoblast survival through pulsed electrical stimulation and implications for osseointegration. *Sci Rep* **11**, 22416 (2021). https://doi.org/10.1038/s41598-021-01901-3
- 12. Vertenten, G. *et al.* Evaluation of an Injectable, Photopolymerizable, and Three-Dimensional Scaffold Based on Methacrylate-Endcapped Poly(D,L-Lactide-co-ε-Caprolactone) Combined with Autologous Mesenchymal Stem Cells in a Goat Tibial Unicortical Defect Model. *Tissue Engineering Part A* **15**, 1501–1511 (2009).

- 13. Lippens, E. *et al.* Evaluation of Bone Regeneration with an Injectable, *In Situ* Polymerizable Pluronic *F127 Hydrogel Derivative Combined with Autologous Mesenchymal Stem Cells in a Goat Tibia Defect Model. *Tissue Engineering Part A* **16**, 617–627 (2010).
- 14. Nicksic, P. J. *et al.* Electrical Stimulation of Acute Fractures: A Narrative Review of Stimulation Protocols and Device Specifications. *Frontiers in Bioengineering and Biotechnology* **10**, 11 (2022).
- 15. Hrdlicka, A. Study of the normal tibia. American Anthropologist. 11, 307-312 (1898).
- 16. Christou, C., Oliver, R. A., Pelletier, M. H. & Walsh, W. R. Ovine Model for Critical-Size Tibial Segmental Defects. *Comparative Medicine* **64**, 9 (2014).
- 17. Bahney, C. S. et al. Cellular biology of fracture healing. J. Orthop. Res. 37, 35–50 (2019).
- 18. Verma, N. *et al.* Augmented Transcutaneous Stimulation Using an Injectable Electrode: A Computational Study. *Front. Bioeng. Biotechnol.* **9**, 796042 (2021).
- 19. Wolfram Mathworld. Boundary Conditions. Accessed at https://mathworld.wolfram.com/BoundaryConditions.html (2022).
- 20. Trevathan, J. K. *et al.* An Injectable Neural Stimulation Electrode Made from an In-Body Curing Polymer/Metal Composite. *Adv. Healthcare Mater.* **8**, 1900892 (2019).
- 21. Raicu, V., Kitagawa, N. & Irimajiri, A. A quantitative approach to the dielectric properties of the skin. *Phys. Med. Biol.* **45**, L1–L4 (2000).
- 22. Wake, K., Sasaki, K. & Watanabe, S. Conductivities of epidermis, dermis, and subcutaneous tissue at intermediate frequencies. *Phys. Med. Biol.* **61**, 4376–4389 (2016).
- 23. Rotem, A. & Moses, E. Magnetic Stimulation of One-Dimensional Neuronal Cultures. *Biophysical Journal* **94**, 5065–5078 (2008).
- 24. Lunt, M. J. Theoretical model for investigating the magnetic and electric fields produced during pulsed magnetic field therapy for nonunion of the tibia. *Med. Biol. Eng. Comput.* 23, 293–300 (1985).
- 25. Dalrymple, A. N. *et al.* Stimulation of the dorsal root ganglion using an Injectrode *. *J. Neural Eng.* **18**, 056068 (2021).
- 26. Soin A., Basic Assessment of Safety and Minimally Invasive Stimulation Via Injectrode (BASMATI) accessed at https://clinicaltrials.gov/ct2/show/NCT04672096 (2021).
- 27. Androjna, C. *et al.* A comparison of alendronate to varying magnitude PEMF in mitigating bone loss and altering bone remodeling in skeletally mature osteoporotic rats. *Bone* **143**, 115761 (2021).

- 28. Leppik, L. *et al.* Combining electrical stimulation and tissue engineering to treat large bone defects in a rat model. *Sci Rep* **8**, 6307 (2018).
- 29. Brighton, C. T. & Hunt, R. M. Ultrastructure of electrically induced osteogenesis in the rabbit medullary canal. *J. Orthop. Res.* **4**, 27–36 (1986).
- 30. Fredericks, D. C., Piehl, D. J., Baker, J. T., Abbott, J. & Nepola, J. V. Effects of Pulsed Electromagnetic Field Stimulation on Distraction Osteogenesis in the Rabbit Tibial Leg Lengthening Model: *Journal of Pediatric Orthopaedics* **23**, 478–483 (2003).
- 31. Law, H. *et al*. The effect of induced electric currents on bone after experimental osteotomy in sheep. *The Journal of bone and joint surgery*. **67** 463–469 (1985).

Supplementary Material

Supplementary Material 1 – Electrical conductivity of materials in FEM model

Supplementary Material 2 – Raw waveform from all human cadaver measurements

Supplementary Material 1 – Electrical conductivity of materials in FEM model

Table 4.5: Conductivity of materials in human finite element method (FEM) model

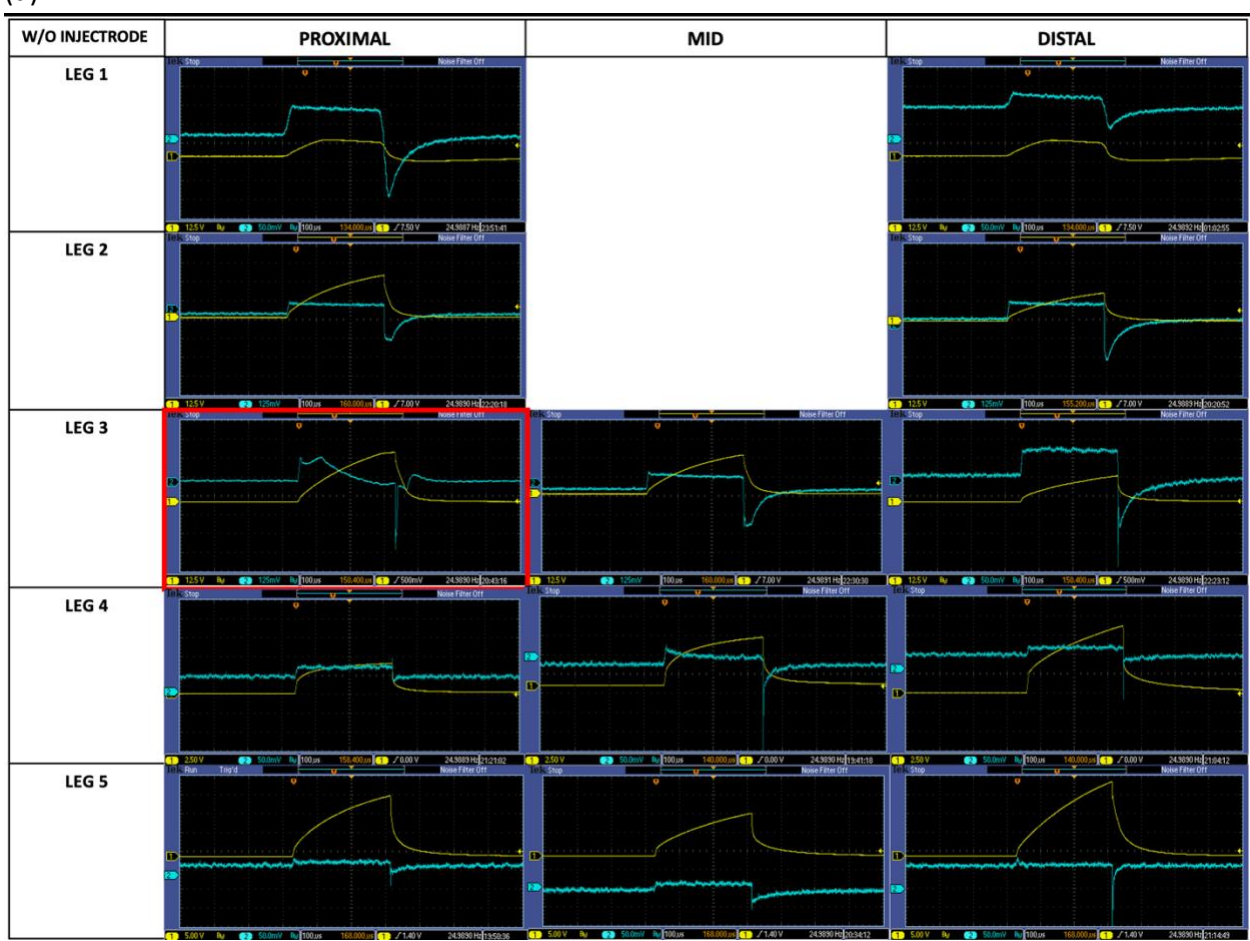
Material	Origin	Conductivity (S/m)
Cortical Bone	Human ¹	1.0e-2
Bone Marrow (infiltrated)	Bovine ²	2.1e-1
Adipose	Human ²	2.09e-2
Skin	Human ³	8.0e-4
Muscle	Bovine (parallel) ²	2.6e-1
Gel	Hydrogel ⁴	1.6e-2

Table 4.6: Conductivity of materials in sheep FEM model

Material	Origin	Conductivity (S/m)
Cortical Bone	Bovine ⁵	8.0e-3
Bone Marrow	Bovine ²	2.95e-3
Fat	Bovine ²	2.62e-2
Skin	Human ³	8.0e-4
Gel	Hydrogel ⁴	1.6e-2
Extracellular fluid	Human (heart) ⁶	6.67e-1
Hematoma	Human (brain) ⁷	2.0
Articular cartilage	Bovine ⁸	8.8e-1
Collagen	Bovine (achilles tendon) ⁹	2e-3

Supplementary Material 2 – Raw waveform from all human cadaver measurements

(a)



(b)

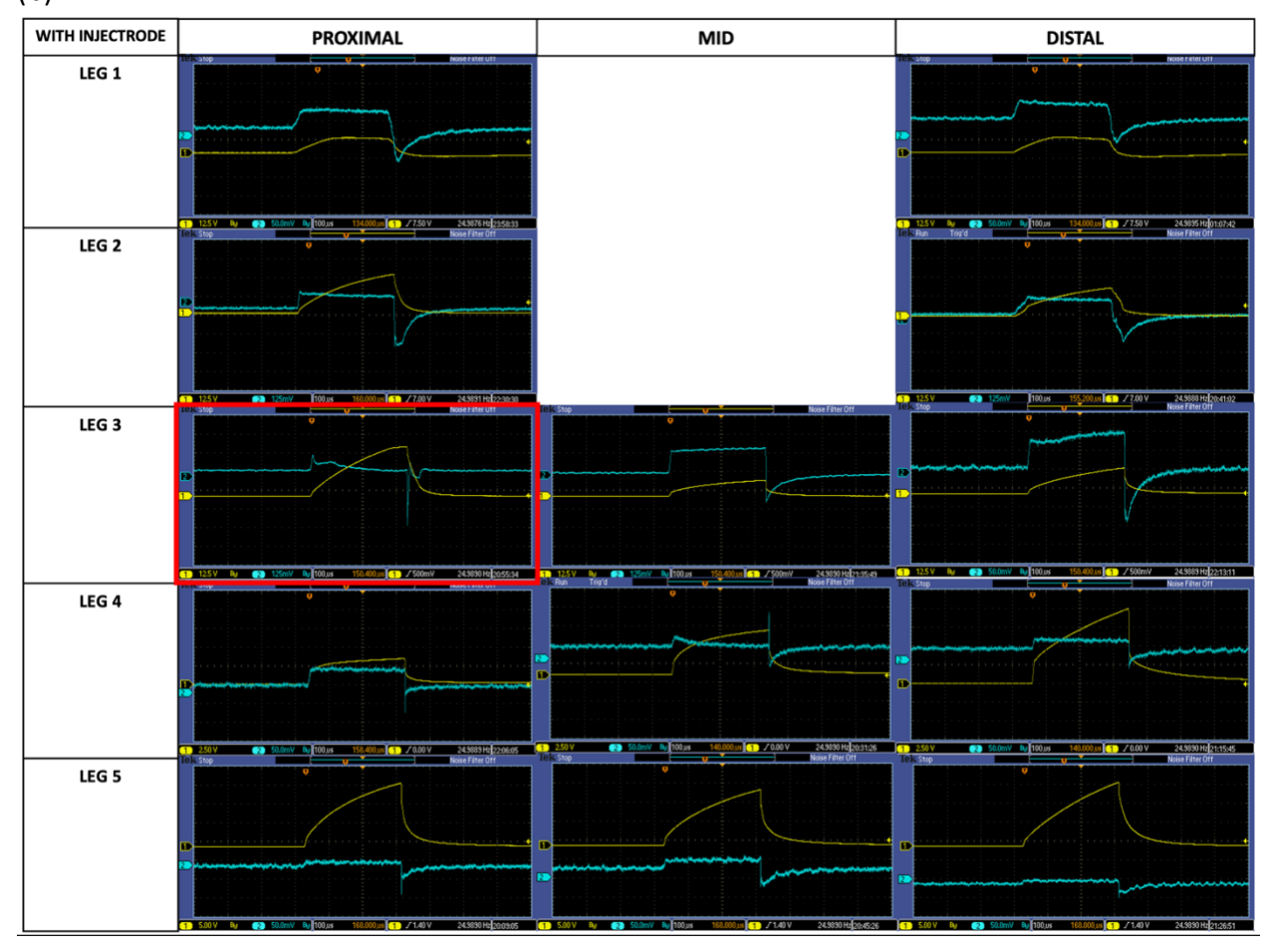


Figure 4.6: Raw waveform from all human cadaver measurements.

For human cadaveric modeling, oscilloscope readings were taken for all samples without Injectrode (a) and after Injectrode (b) administration. The average gain was calculated using a total of 12 measurements: 2 from leg 1 (proximal and distal), 2 from Leg 2 (proximal and distal), 2 from Leg 3 (mid and distal), 3 from Leg 4 (proximal, mid, and distal), and 3 from leg 5 (proximal, mid, and distal). Leg 1 and Leg 2 were limited by anatomical distance, making three experimental set-ups on the leg infeasible. The condition outlined in red (proximal cut of Leg 3) was a statistical outlier when comparing gain values. Furthermore, qualitatively, the blue curve (voltage at fracture site) shows an anomaly in the initial slope upward that has a curvilinear descend after. Any other curve that has a descend is either more gradual or more linear. The sharp peak with curved decline indicates a potential anomaly in the bone space that was not visualized or accounted for in the initial cadaveric acquisition. It could also indicate poor electrical contact between the recording electrodes and the bone.

Supplementary Material References

- 1. Kosterich, J. D., Foster, K. R. & Pollack, S. R. Dielectric Permittivity and Electrical Conductivity of Fluid Saturated Bone. *IEEE Trans. Biomed. Eng.* **BME-30**, 81–86 (1983).
- 2. Gabriel, C. Compilation of the Dielectric Properties of Body Tissues at RF and Microwave Frequencies.: http://www.dtic.mil/docs/citations/ADA303903 (1996) doi:10.21236/ADA303903.
- 3. Raicu, V., Kitagawa, N. & Irimajiri, A. A quantitative approach to the dielectric properties of the skin. *Phys. Med. Biol.* **45**, L1–L4 (2000).
- 4. Verma, N. *et al.* Augmented Transcutaneous Stimulation Using an Injectable Electrode: A Computational Study. *Front. Bioeng. Biotechnol.* **9**, 796042 (2021).
- 5. Balmer, T. W., Vesztergom, S., Broekmann, P., Stahel, A. & Büchler, P. Characterization of the electrical conductivity of bone and its correlation to osseous structure. *Sci. Rep.* **8**, 8601 (2018).
- 6. Spach, M. S., Miller, W. T., Miller-Jones, E., Warren, R. B. & Barr, R. C. Extracellular potentials related to intracellular action potentials during impulse conduction in anisotropic canine cardiac muscle. *Circ. Res.* **45**, 188–204 (1979).
- 7. Ke, L., Zu, W., Du, Q., Chen, J. & Ding, X. A bio-impedance quantitative method based on magnetic induction tomography for intracranial hematoma. *Med. Biol. Eng. Comput.* **58**, 857–869 (2020).
- 8. Binette, J. S., Garon, M., Savard, P., McKee, M. D. & Buschmann, M. D. Tetrapolar Measurement of Electrical Conductivity and Thickness of Articular Cartilage. *J. Biomech. Eng.* **126**, 475–484 (2004).
- 9. Bardelmeyer, G. H. Electrical conduction in hydrated collagen. I. Conductivity mechanisms. *Biopolymers* **12**, 2289–2302 (1973).

Chapter 5 Pilot Data for Future Directions: Trigeminal Nerve Stimulation to Restore Glymphatic Function This chapter presents work that has not yet been published in a peer-reviewed journal. The following will be authors on an eventual publication:

Nishant Verma^{1,2}, Mu-Lan Jen³, Robert Moskwa³, Kevin Cheng^{1,2}, Bruce Knudsen^{1,2}, Maria Laluzerne^{1,2}, Jennifer Frank^{1,2}, Jack Wells⁴, Samuel Hurley³, Justin Williams^{1,2}, Alan McMillan³, Ali Pirasteh³, Bradley Christian³, Walter Block³, Kevin Johnson³, Kip Ludwig^{1,2,5}

¹Department of Biomedical Engineering, University of Wisconsin – Madison, Madison, WI, USA

²Wisconsin Institute for Translational Neuroengineering (WITNe) – Madison, Madison, WI, USA

³Department of Medical Physics, University of Wisconsin – Madison, Madison, WI, USA

⁴Department of Medical Physics, University College London, London, UK

⁵Department of Neurosurgery, University of Wisconsin – Madison, Madison, WI, USA

Abstract

Decreases in cerebral blood flow are one of the earliest biomarkers of Alzheimer's disease. The recent discovery of the glymphatic waste clearance system lends mechanistic insight as to why cerebral hemodynamics is critical to healthy brain function. The glymphatic hypothesis proposes that cerebral vessel pulsation drives the exchange of cerebrospinal fluid (CSF) and interstitial fluid with waste in the brain. Meanwhile, numerous studies have shown that trigeminal nerve electrical stimulation can increase cerebral blood flow. We build on this extensive body of literature to investigate if noninvasive trigeminal stimulation can increase CSF movement, and therefore waste clearance, in the brain. We developed clinically viable readouts based on MRI to assess changes in cerebral hemodynamics, CSF movement, and CSF clearance. We used these readouts to measure the effects of electrical stimulation and a positive control, dobutamine, in fully mature minipigs. Our preliminary findings suggest that electrical stimulation increased cerebral blood flow and decreased flow pulsatility. The positive control, dobutamine, increased CSF movement in the large paravascular spaces. This is the first time dobutamine has been shown in a large animal model to enhance CSF movement in the paravascular spaces. We also present a surgical technique enabling direct neural recordings from the V3 trigeminal nerve as it enters the jaw to confirm neural target engagement during electrical stimulation. We envision trigeminal stimulation therapy could be delivered overnight, when brain waste clearance is most facile, through a mouthguard stimulator.

Introduction

The root cause(s) of Alzheimer's disease have not been established – although there are many hypotheses (Liu et al., 2019). One of the earliest changes in patients who eventually develop Alzheimer's disease is decrease in cerebral blood flow (Korte et al., 2020). This early biomarker of the disease relates to the recent discovery of the glymphatic and meningeal waste clearance systems from the brain, which has opened new potential targets to treat Alzheimer's disease (Illiff et al., 2012). Cerebrospinal fluid (CSF) – interstitial fluid (ISF) exchange in the glymphatic system is hypothesized to be powered by the cardiac pulsatile motion of cerebral vessels (Illiff et al., 2013). Paravascular and subarachnoid spaces (PVS) around the larger cerebral vessels are filled with CSF and the pumping of the vessels is hypothesized to be the pump of the glymphatic system, moving CSF along the PVS (Illiff et al., 2013). The pumping generates pressure to move CSF into the interstitial space and remove ISF with waste into the PVS surrounding cerebral veins. The decrease in cerebral blood flow preceding Alzheimer's may be decreasing the pumping efficiency of CSF in the PVS and CSF-ISF waste clearance.

There is an extensive body of literature showing that trigeminal nerve electrical stimulation can increase cerebral blood flow (White et al., 2021). Although cerebral vessel pulsatility is hypothesized to drive CSF movement in the surround PVS and CSF-ISF exchange, there has not been a systematic investigation on the effects of trigeminal nerve stimulation on CSF movement. We hypothesize that noninvasive trigeminal nerve stimulation can restore the decrease in glymphatic function observed with age and disease progression by favorably altering vascular dynamics (Li et al., 2022). If we find instead that trigeminal nerve stimulation has a negative effect on CSF dynamics, that is still a worthwhile finding as there are several FDA

cleared noninvasive stimulators on the market that stimulate the trigeminal nerve. Any cautionary effect of trigeminal nerve stimulation on CSF dynamics would be important to consider for the long term safety of these devices.

An acute study by our group in mice showed that electrical stimulation of the vagus nerve, another cranial nerve related in its autonomic function to the trigeminal, improved the penetrance of a dye into the brain parenchyma (Cheng et al., 2020). Several chronic mice studies, conducted independently of our group, showed that electrical stimulation in the region of the V1 branch of the trigeminal decreased soluble $A\beta$ in the brain and improved cognitive function (Luo et al., 2020; Liang et al., 2021; Choi et al., 2022). A recent study in mice showed that stimulation of the auricle, which is also innervated by the V1 branch of the trigeminal nerve, increased CSF flow velocity in the paravascular spaces of the large cerebral vessels (Choi et al., 2022).

Here, we build on these works in acute large-animal model experiments with mature mini pigs and use clinically viable readouts, based on magnetic resonance imaging (MRI) and positron emission tomography (PET), to investigate modulation of cerebral hemodynamics and CSF flow due to trigeminal nerve stimulation. We assessed neurofluid dynamics with multiple readouts to show various features, namely 1) 4D-Flow, a phase contrast MRI method, measured macrovasculature hemodynamics, 2) diffusion weighted imaging (DWI) measured movement of CSF in the PVS surrounding the largest cerebral arteries, and 3) PET measured movement of an intravenously administered radioactive tracer in CSF. Our preliminary results show that electrical stimulation of the trigeminal nerve favorably alters cerebral hemodynamics, does not have a measurable effect on CSF movement in the paravascular

spaces of the large pial arteries, and does not have a measurable effect on clearance rate of CSF from the brain parenchyma. The main goal of this study was to develop noninvasive measures of therapeutic effect and mechanisms of action. These noninvasive measures, paired with the noninvasive stimulation, allows a quick path to human studies. The many failed late-stage clinical trials (Korte et al., 2020) based on successful animal model results calls into question the relevance of these animal models and motivates pursuing strategies that can be tested and developed in human studies in the early stages.

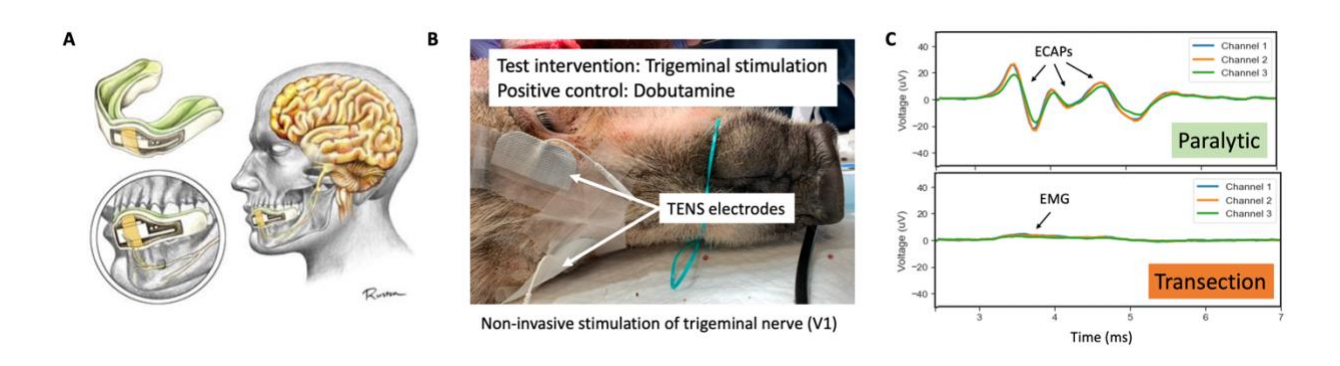


Figure 5.1: Mouthguard stimulator concept and measurement of neural target engagement during stimulation.

(A) Mouthguard stimulator concept to deliver electrical stimulation therapy during sleep. (B) Large animal pig model used in this study instrumented with noninvasive transcutaneous electrical nerve stimulation (TENS) electrodes on the V1 and V3 trigeminal. (C) Evoked compound action potentials (ECAPs) recorded during percutaneous stimulation to verify target engagement and measure fiber types activated during stimulation. (top) is under vecuronium, a muscle paralytic, to control for evoked myogenic bleed through into the recording. (bottom) is after a transection of the trigeminal nerve between the stimulation and recording electrode to verify the authenticity of the ECAPs.

This work is intended to facilitate new treatments for Alzheimer's disease that can be delivered overnight when waste clearance in the brain is most facile (Lohela et al., 2022). The therapy will be delivered by a mouthguard stimulator (Figure 5.1A) targeting the intraoral

innervation of the V1 trigeminal nerve. The mouth presents firstly, an isolated superficial sensory nerve amenable to activation by noninvasive stimulation, and secondly, a 'wet' interface', which enables more consistent electrical contact and stimulation delivery. Together, these present advantages that may lead to a larger therapeutic window between on- and off-target nerve activation. This work may also find applications in the treatment of hydrocephalus and aid in drug delivery to the central nervous system.

Results

The Methods section is found towards the end of this chapter and is briefly summarized here. We used clinically viable MRI and PET techniques to evaluate blood and CSF dynamics in the brain. We used this setup to investigate the effects of noninvasive trigeminal nerve electrical stimulation to increase cerebral blood flow and CSF movement for potential therapeutic applications. We investigated both electrical stimulation of the V1 trigeminal (Estim V1) and V3 trigeminal (Estim V3) motivated by results from literature (White et al., 2021) and our vision of a mouthguard stimulator, respectively. Electrical stimulation was delivered through noninvasive hydrogel transcutaneous electrical stimulation (TENS) electrodes cut to 1x2 cm applied to the region of the face innervated by the V1 and V3 branch of the trigeminal nerve. Figure 5.1B shows the bipolar pair of TENS electrodes applied bilaterally targeting the V1 branch of the trigeminal nerve. The stimulation waveform was delivered at 30 Hz, 240 μ s biphasic pulses, cycling for 10s ON and 10s OFF. The cycling follows the minimum duration for neurovascular coupling mediated blood flow changes. Stimulation amplitude was titrated to motor threshold for each subject.

Mature UW minipigs were used as the large animal model in the study. Intravenous dobutamine administered as a continuous rate infusion (CRI) was used as the positive control. Dobutamine is an agonist that binds specifically to β_1 . It increases ventricular contractility, which increases the diameter cardiac pulsatility of blood vessels. This increased vessel diameter pulsatility is believed to increase the pumping action on CSF in the PVS surrounding the major blood vessels in the brain. Dobutamine has been used as a positive control in past rodent studies investigating CSF movement in the large PVS spaces of the brain (Iliff et al., 2013; Harrison et al., 2018). In our study, dobutamine was titrated conservatively to increase systolic blood pressure by 20-30 mmHg without changing heart rate.

In the results section, we first present a surgical technique, which enables direct measurement of local neural target engagement to assess successfully delivered trigeminal nerve stimulation. We then present on cerebral blood flow dynamics during electrical stimulation and administration of the positive control evaluated using 4D-Flow MRI. Then, we present results measuring CSF dynamics in the paravascular spaces of the great arteries in the brain evaluated using a DWI MRI technique. Lastly, we present an attempt to measure clearance from the parenchyma using a PET based technique. We consider these results preliminary as we were refining the imaging techniques, stimulation protocol, and anesthesia (Table 5.1) through these pilot experiments. Further, the pig images were of lower signal-to-noise ratio (SNR) compared to typical human images due to the smaller brain size of the pig animal model and its thick skull, which increases the distance between the MRI coil and the tissue to be imaged.

Table 5.1: Subject anesthesia summary

Pig	Anesthesia
1	Isoflurane only (~3%)
2	Fentanyl and 1% Isoflurane
3	Propofol only
4	Propofol only

Neural target engagement during stimulation

It is critical to measure local neural target engagement to guide stimulation electrode development and improve translation between animal models and humans (Verma et al., 2022). For this purpose, we developed a surgical technique in the swine model, which allowed us to directly access the V3 branch of the trigeminal nerve a short distance after it split from the main trigeminal ganglion and before it entered the jawbone to eventually become the intraoral mental and lingual branches. Our envisioned therapy will target the mental and lingual branches of the V3 trigeminal nerve with a mouthguard stimulator. We instrumented the nerve with a recording cuff at the surgically accessed cranial point from where we could record stimulation evoked compound action potentials (ECAPSs) and verify target engagement of the V3 trigeminal nerve.

Figure 5.1C, above, shows successful and verified recordings of ECAPs from the V3 trigeminal during stimulation. Note a percutaneous bipolar stimulation electrode targeting the mental branch of the V1 trigeminal as it exited the mental foramen was used here as a proof of concept for the surgery and measurement technique of neural signals conducting on the V3

at the endpoint of swine studies to verify neural target engagement of the stimulation.

Administration of a muscle paralytic, vecuronium, was used to confirm that the signals were neural in origin and not due to evoked myogenic activity. Transection of the V3 trigeminal nerve between the stimulation and recording site was used to further verify the authenticity of the neural signal.

Macrovasculature blood flow increases and flow pulsatility decreases during stimulation Changes in cerebral hemodynamics is an early biomarker of Alzheimer's disease (Korte et al., 2020) and is being investigated as a clinically applicable biomarker of disease progression. We assessed cerebral hemodynamics using 4D-Flow, a phase contrast MRI method. This technique has been used in humans, including clinical dementia and Alzheimer's patients (Rivera-Rivera et al., 2016). Therefore, the interpretation of the biomarkers derived from this dataset is grounded in clinical results. The single-institution clinical study reported by Rivera-Rivera and colleagues (2016) showed that cerebral blood flow decreased and pulsatility index (*PI*) increased with age and disease severity. *PI* is based on Gosling's *PI* and calculated over the cardiac cycle as defined in the following equation:

$$PI = \frac{Flow_{max} - Flow_{min}}{Flow_{mean}}$$

In this paper, PI is referred to as 'flow pulsatility' to indicate it is calculated over the cardiac cycle and based on flow rate measurements. It is contrasted with 'diameter pulsatility', which quantifies the rhythmic change in a vessel's diameter over the cardiac or electrical stimulation cycle and is more closely tied to the glymphatic hypothesis and studies (Illif et al., 2013). We

still reported on flow pulsatility in this study due to its relevance as a clinical biomarker (Rivera-Rivera et al., 2016). Here, we present preliminary results in the pig model showing that electrical stimulation increases cerebral blood flow and decreases flow pulsatility – possibly reversing the effects of aging and disease.

We imaged each pig during several interventions. Table 5.2 summarizes the data notes for 4D-Flow. Each intervention was applied for a duration of 10-15 mins following the sequence acquisition time. Due to the SNR limitations in the pig images, noted earlier, we were only able to segment the largest vessels in the brain: the circle of Willis, anterior cerebral artery (ACA) and superior sagittal sinus (SSS). Figure 5.2A shows the vessels segmented in Pig 2. Table 5.2 notes which vessels were segmented per subject. Where available, we analyzed data from the ACA due to the relevance of arterial hemodynamics in propelling CSF movement in the glymphatic hypothesis. In clinical human imaging, the 4D-Flow technique is routinely able to capture the ACA, posterior cerebral artery (PCA), and middle cerebral artery (MCA) at both there P1 and P2 levels (Rivera-Rivera et al., 2016).

Table 5.2: 4D-Flow data summary

Pig	4D-Flow imaging notes	Vessel segmented
1	Stimulation induced motion artifact in Estim image	NA
2	Baseline, Estim V1, dobutamine, baseline, Estim V3	ACA, SSS
3	Baseline, Estim V1, dobutamine, baseline, Estim V3	SSS
4	Baseline, Estim V1, baseline, Estim V3, dobutamine	Pending

Stimulation increases cerebral blood flow in ACA and SSS

The single-site human study reported by Rivera-Rivera and colleagues (2016) showed that cerebral blood flow decreased with disease severity. We investigated the effects of trigeminal electrical stimulation on cerebral blood flow in the ACA and SSS. In Pig 2, where the ACA could be segmented, EStim V1 increased cerebral blood flow by 9.3% and velocity by 20% in the ACA (Figure 5.2B). In Pig 3, where only the SSS could be segmented, Estim V1 increased cerebral blood flow by 16% and velocity by 14% in the SSS (Figure 5.2D). The positive control also increased cerebral blood flow in the ACA and SSS relative to baseline. The error bars in Figure 5.2B-G are derived from the 95% confidence interval (CI) calculated based on five pixels along the vessel of interest. Note the images were acquired in the sequence in which the results are presented in the bar graph (left to right) in Figure 5.2 and summarized in Table 5.2. Five minutes were given after dobutamine administration was stopped in Pig 2 and 10 minutes in Pig 3 to allow the effects to wash out. In Pig 4, the study design was adjusted to administer the positive control, dobutamine, at the end of the 4D-Flow experiment block, to eliminate the concern of dobutamine wash out period. The increases in cerebral blood flow observed during electrical stimulation counteracts the decrease in cerebral blood flow with age and Alzheimer's disease measured using the same 4D-Flow technique in humans by Rivera-Rivera and colleagues (2016).

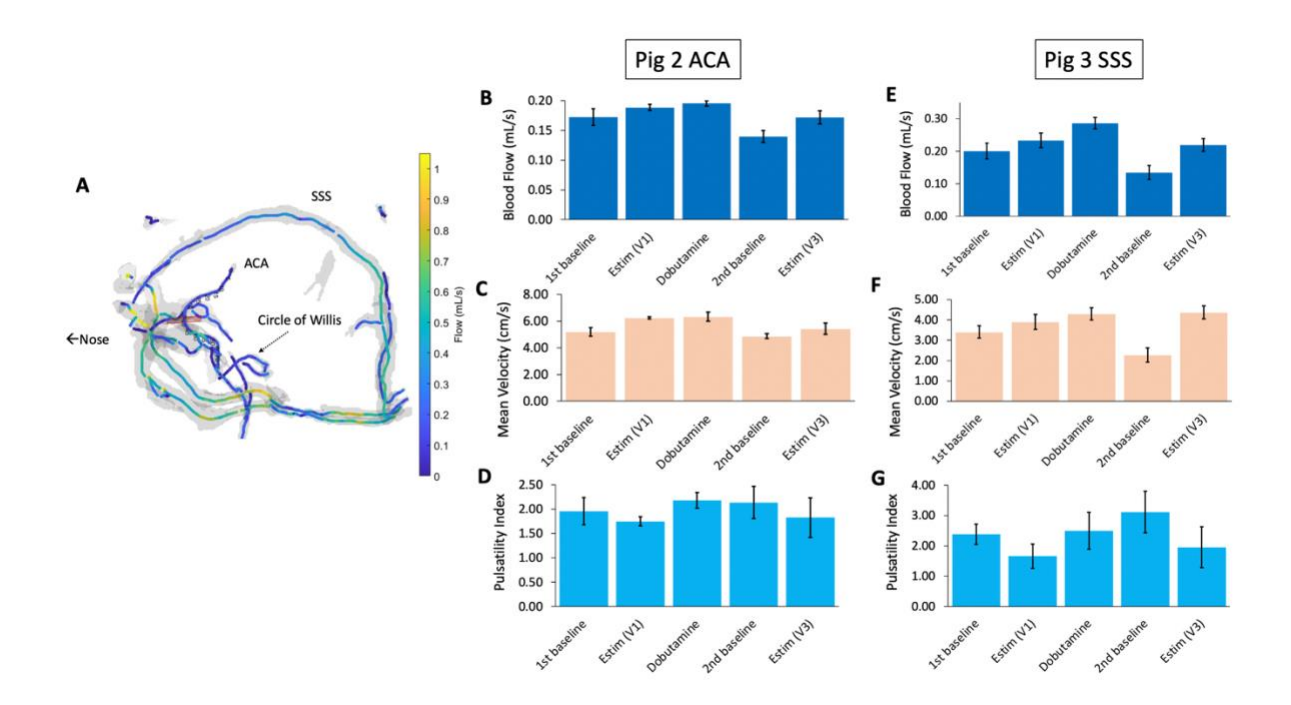


Figure 5.2: Blood flow, velocity, and flow pulsatility measured in the cerebral vessels using 4D-Flow MRI.

(A) Segmentation of Pig 2 4D-Flow image. (B) Blood flow in Pig 2 anterior cerebral artery (ACA). (C) Blood flow velocity in Pig 2 ACA. (D) Flow pulsatility in Pig 2 ACA. (E) Blood flow in Pig 3 superior sagittal sinus (SSS). (F) Blood flow velocity in Pig 3 SSS. (G) Flow pulsatility in Pig 3 SSS.

Stimulation decreases flow pulsatility in ACA and SSS

Diameter pulsatility of the cerebral vessels is key in the glymphatic hypothesis as a driver of CSF movement in the PVS (Illif et al., 2013). We were unable to measure diameter pulsatility due to the limited resolutions of MRI. Instead, we measure flow pulsatility (PI). While PI and diameter pulsatility are not well related, PI has been shown to increase with disease progression, likely due to vessel stiffening (Rivera-Rivera et al., 2016; Rivera-Rivera et al., 2017). Note that while increase in PI of arteries with age and disease has been established and is interpreted to be due to arterial wall stiffening in older adults (Fico et al., 2022), the changes in PI of the SSS are not well studied and understood. Early data suggests that SSS PI also increases with age and disease progression (Rivera-Rivera et al., 2017). The glymphatic hypothesis proposes that

similar to the arterial PVS, venous pulsatility drives CSF in the PVS of veins – but does not extend that proposal to the SSS. We report on SSS data in subjects where the ACA was unable to be segmented. In Pig 2, the flow pulsatility index in the ACA decreased by 11% during Estim V1. In Pig 3, the flow pulsatility index in the SSS decreased by 30% during Estim V1. On the other hand, the positive control, dobutamine, increased PI in the ACA by 12% in Pig 2 and by 4.8% in the SSS in Pig 3. The decrease in PI caused by electrical stimulation counteracts the increase in PI with age and Alzheimer's disease measured using the same 4D-Flow technique in humans by Rivera-Rivera and colleagues (2016).

Evaluating CSF movement during stimulation

While changes in cerebral blood dynamics are an established biomarker of age and disease and an important marker of target engagement, measures of CSF dynamics are more central to waste clearance from the brain. To study CSF dynamics, we adapted a technique developed in rats by Harrison and colleagues (2018) and translated to humans by Hirschler and colleagues (2019 and 2020). The technique is based on diffusion weighted imaging (DWI) and exploits a long echo time (T2 weighting) to retain primarily signal from the CSF including CSF in the PVS of pial arteries (Harrison et al., 2018) (Figure 5.3A). Motion probing gradients were then applied to sensitize to the flow of CSF in the PVS of pial arteries. From these data, D* values were calculated as a measure of intravoxel motion, combining diffusion in the voxel and the perfusion of CSF into the voxel (Le Bihan, 2019). The technique is not quantitative as the relation of D* to flow rate is not known. The technique also does not allow us to differentiate between pulsatile movement of CSF and unidirectional flow.

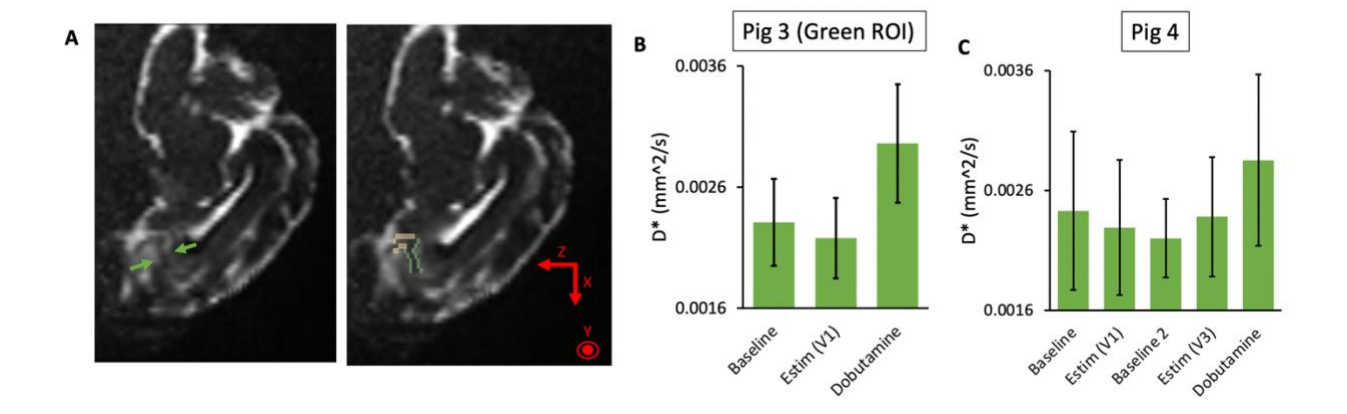


Figure 5.3: Diffusion weighted imaging (DWI) to measure cerebrospinal fluid (CSF) movement in the paravascular and subarachnoid spaces (PVS) of the anterior cerebral artery (ACA). (A) (left) Sagittal slice of Pig 3 showing characteristic 'train tracks' indicating ACA in black and PVS of the ACA in white. (right) Same slice with region of interests (ROIs) marked out. (B) D* for Pig 3. (C) D* for Pig 4.

We implemented the technique in a 3T scanner using a DWI sequence with echo planar imaging (EPI) acquisition and $b=150\ s/mm^2$ (Wen et al., 2022). Note that we attempted a PROPELLER acquisition scheme in the first pig, which failed due to extreme distortion and noise. The EPI sequence created distortion but still produced useable images. Table 5.3 summarizes the DWI sequence notes for all subjects.

Table 5.3: DWI data summary

Pig	DWI imaging notes	Vessel PVS analyzed
1	PROPELLER acquisition	NA
2	EPI acquisition: baseline, Estim V1, dobutamine (noisy image)	ACA
3	EPI acquisition: baseline, Estim V1, dobutamine	ACA
4	EPI acquisition: baseline, Estim V1, baseline 2, Estim V3,	ACA
	dobutamine	

We measured a 28% and 29% increase in D* during the administration of dobutamine in Pig 3 and Pig 4, respectively (Figure 5.3B). These results suggest that the DWI technique is sensitive to changes in CSF movement in the PVS of the ACA (Harrison et al., 2018). This is also the first report of dobutamine used as a positive control in a large animal model with a putatively positive effect on glymphatic clearance. In Pig 3, Estim V1 decreased D* by 5.7%, while in Pig 4, Estim V1 decreased D* by 5.7% and Estim V3 increased D* by 8.1%. See Discussion for future direction on image reconstruction based on stimulation cycle ON/OFF to dissect the effects of Estim on D* in both the ON and OFF stages. The error bars in Figure 5.3B-C are derived from the 95% CI calculated based on all the pixels consisting of the region of interest (ROI) (Figure 5.3A). There was large variation in D* across pixels. An ROI analysis (averaging across multiple pixels) may reduce the D* variation when making comparison across subjects. However, there were insufficient subjects to estimate across subject variability.

The images are noisy, affecting the D* values calculated using the equation:

$$D^* = -\frac{1}{b} \ln \left(\frac{s}{s_0} \right)$$

For example, addition of equal noise to the signal at $b=0\ mm^2/s\ (s_0)$ and the signal at $b=150\ s/mm^2\ (s)$ would have the overall effect of reducing the measured value of D*. This may explain why the D* reported here are lower than the D* of the self-diffusion water (Mills, 1973). Since we are measuring the combined effects of diffusion and perfusion, the D* we measure should be larger than the D* of just the self-diffusion of water. The additional noise in the image could be coming from radio frequency (RF) excitation of tissue outside of the imaging region of interest. In particular, due to the nonexistent 'neck' in pigs, it was challenging to keep its head in a separate plane from its body. RF excitation could have excited both tissue in the

head and along its body, contributing to additional signal noise into the image. Despite this systematic error, relative changes in D* measured in the same subject are still reflective of changes in intravoxel motion in the PVS of the major cerebral arteries.

Evaluating CSF clearance from the brain using PET

The gold standard to evaluate glymphatic function would be to track the movement of waste particles and CSF through the parenchyma. de Leon and colleagues (2017) and Li and colleagues (2021), also from the de Leon group, employed a PET based technique to measure the movement of radioactive tracer in the brain as a proxy for the movement of CSF. They used this measure to report on clearance rates of CSF from the brain. We adopted their technique using the C-11 PiB tracer delivered intravenously in a pilot experiment (4.92 mCi of activity). We collected PET data for 60 minutes following the injection during which we conducted 9 experimental blocks: starting with 3 repeats of baseline (no intervention) followed by electrical stimulation and followed by a baseline, a block of dobutamine positive control, and a final baseline.

In a preliminary analysis of the data, with the entire brain marked as the ROI, we observed no changes in CSF clearance rates during interventions compared to baseline. We had to control for unexpected CRI delivery of the tracer through an incorrectly placed IV extension line. To control for this unintended delivery, we monitored the additional radiation from the IV line, also visible in the PET image field of view (FOV), and adjusted the time activity curves (TACs) for this additional radiation. Future work could include further exploration of this

dataset considering specific brain ROIs where an effect may be more robust (e.g., gray matter) and by separating the electrical stimulation and dobutamine intervention analysis.

Effect of electrical stimulation and dobutamine on heart rate and blood pressure

Heart rate and blood pressure were measured throughout the experiment to identify if

systematic changes were driving the cerebral hemodynamic or CSF movement effects seen with

stimulation and dobutamine. In all subjects, no substantial changes were measured in heart

rate or blood pressure during electrical stimulation. Blood pressure increased by 20-30 mmHg

(systolic) during the administration of the positive control dobutamine with no substantial

change in heart rate.

Discussion

Neural target engagement

In this study, we used an invasive method to verify target engagement of the target V3 trigeminal nerve. Similar techniques could be performed in humans in a minimally invasive manner to directly measure ECAPs (Verma et al., 2022). Other measures of local neural target engagement, such as report of sensory perception, observation of muscle activity, and measurement of somatosensory evoked potentials (SSEPs) could also be used to guide electrode design and placement in humans.

Mechanisms of action of trigeminal stimulation

If the direct mechanism of action was dilation of the larger pial vessels, which are innervated by the trigeminal nerve, then blood flow velocity would be expected to decrease in the ACA. Visocchi and colleagues (1997) showed this expected decrease in MCA blood flow velocity, measured by transcranial doppler, when they invasively stimulated the trigeminal ganglion in humans, which has direct parasympathetic innervation to the cerebral pial arteries. The supraorbital trigeminal V1 and mental branch trigeminal V3 do not have direct neural innervation to the pial arteries. The 4D-Flow data suggests that the mechanisms of action of trigeminal electrical stimulation on hemodynamics is primarily mediated by neurovascular coupling and dilation of the downstream microvasculature. This could explain the increase in both blood flow and velocity in the ACA (Schulz et al., 2018).

The neurovascular coupling hypothesis also explains the decrease in flow pulsatility, which can occur with decrease in downstream vascular bed resistance. A lower downstream resistance would translate to less flow changes over the cardiac cycle due to the lack of resistance against the flow and hence a lower *PI*.

Neurovascular coupling can also be entrained by visual and sensory stimulation and motor tasks. In an EPI-based MRI human study, Kim and colleagues (2022) showed that during 23-46 seconds of visual stimulation or motor task, CSF pulsation at the level of the 4th ventricle decreased during the ON period and increased during the OFF period. In a computational study, based on empirical findings, Kedarasetti and colleagues (2022) showed that sensory-evoked and sleep related arteriolar dilations could drive convective flow of CSF in the paravascular spaces. Similarly, van Veluw and colleagues (2020) showed that they could increase the

amplitude of low frequency vasomotion by means of visually evoked vascular responses at 0.05 Hz in awake mice. They went on to show that this visual stimulation increased the clearance rate of parenchymal dextran measured using *in vivo* two-photon microscopy. Further, neurovascular coupling has been shown to be stronger during sleep, particularly in the NREM stage, than when awake (Turner et al., 2020).

Considering this body of evidence, electrical stimulation presents a clinically viable manner to entrain neurovascular responses in the brain during sleep, restore CSF flow in the paravascular spaces, and restore waste clearance from the brain. Electrical stimulation can be delivered in a compact and rugged form factor. Electrical stimulation could be delivered with a closed-loop control system, based on biomarkers (e.g., EEG), to finely adjust stimulation to induce entrainment without disturbing sleep.

Flow pulsatility versus diameter pulsatility

The glymphatic hypothesis proposes that diameter pulsatility of the cerebral vessels drives CSF movement in the PVS (Illif et al., 2013). The hypothesis suggests that increased diameter pulsatility would lead to increased CSF movement in the PVS of cerebral arteries. In our study, we were unable to measure diameter pulsatility due to the limited resolutions of MRI. Instead, we measure flow pulsatility. The elastic properties of the large pial arteries are not static and so flow pulsatility cannot be interpreted as cardiac diameter pulsatility. However, flow pulsatility (*PI*) is a useful measure as it is utilized widely in other studies and is well known to increase with age and disease (Mitchell et al., 2011; Rivera-Rivera, 2016).

We measured a decrease in flow pulsatility with trigeminal stimulation counteracting the known increase with age and disease. This is in line with neurovascular coupling as the main

mechanism of action of stimulation. Activation of somatosensory areas in the brain by electrical stimulation leads to microvasculature dilation and a decrease in downstream vessel resistance. A lower downstream resistance translates to less flow changes over the cardiac cycle due to the lack of resistance against the flow and hence a lower *PI*.

Future studies need to explore the effects of trigeminal nerve stimulation on diameter pulsatility in the cerebral vessels. The 10s ON/10s OFF cycling of stimulation could positively contribute to diameter pulsatility in the cerebral vessels and hence improved clearance (van Veluw et al., 2020). Further, binning the image reconstruction by stimulation cycle instead of cardiac cycle could lead to understanding of the lower frequency oscillation (LFO) effects induced by stimulation (Rivera-Rivera et al., 2020).

Binning of D* into stimulation cycle to study stimulation induced CSF dynamics

The D* values presented here from the DWI are averaged over the scan time of 5-10 minutes. The positive control resulted in an increased D* while electrical stimulation resulted in a D* similar to the baseline D*. Past work showed that CSF movement at the 4th ventricle is task dependent with periods of activity (motor or visual) leading to decreased CSF pulsatility and periods of inactivity between leading to increased CSF pulsatility (Kim et al., 2022). It is therefore possible that the D* value varied over the course of the scan as electrical stimulation was turned ON and OFF every 10 seconds. The D* values reported here were averaged over the entire scan time and multiple periods of ON and OFF, which could have averaged out stimulation related effects. Future work can explore reconstruction of the scan by retrospectively binning the data into periods of ON stimulation and OFF stimulation. The

binning into stimulation cycle may uncover stimulation event related changes in D*. The method and utility of retrospective binning, leading to discrimination of additional event related information, was previously demonstrated in application to the cardiac cycle (Hirschler et al., 2020).

Limitations of DWI technique and alternative methods

A major limitation of the DWI implementation in our study was the EPI image acquisition method, which acquires k-space in a scanning fashion and introduces severe distortions to the image in the process. Future work will include development of the sequence with a fast spin echo (FSE) image acquisition method with a T2-prep as implemented by Hirschler and colleagues (2019 and 2020).

A further confound of the DWI method is that it measures intravoxel motion, which arises from several sources including 1) diffusion, 2) CSF movement, where the technique is unable to differentiate between pulsatile movement and unidirectional flow, and 3) motion of the entire paravascular space. Motion of the paravascular space could be due to heartbeat and respiration. However, severe movement of the vessels is likely limited to the spinal cord, brainstem, and mid brain, while the ACA PVS region we analyzed should be relatively stationary.

Another diffusion-based MRI method that is gaining popularity as a measurement of 'glymphatic function' is the DTI-ALPS method (Taoka et al., 2017). We did not implement this technique in our work as while it may be indicative of underlying pathophysiology, it is not a specific measure of movement in the PVS (Barisano et al., 2022; Piantino et al., 2022).

General limitations

A general limitation of this study is that the rebound effects of dobutamine may have lasted for a longer duration than the 5-10 minutes allowed in Pig 1-3 and could have driven the decrease in cerebral blood flow in the 2nd baseline in Pig 2 and Pig 3 and the subsequent recovery of Estim V3, enlarging the apparent effect of Estim V3. We addressed this concern in Pig 4 by moving the dobutamine control to the end of the 4D-Flow experimental block.

A fundamental limitation of this work is that it is based on the glymphatic hypothesis, which has multiple components to it, not all of which have been supported by evidence. CSF movement along the pial artery PVS is well supported and was therefore the focus of this study. CSF/ISF exchange is less well supported and there is very little work showing ISF egress into the paravascular spaces of the veins. For this reason, we used multiple measures to quantify the effects of trigeminal nerve stimulation on neurofluidic flow so that the methods and findings of this work may be relevant even as the glymphatic hypothesis is refined.

Conclusions

We were motivated by the extensive literature showing the effects of trigeminal nerve stimulation on cerebral hemodynamics to investigate the effects of trigeminal nerve stimulation on CSF movement in the brain. We used multiple clinically viable measures of neurofluidic flow in the brain based on MRI and PET imaging. We showed preliminary results suggesting that trigeminal nerve stimulation increased cerebral blood flow and velocity in the ACA and SSS and decreased flow pulsatility. These changes, measured using 4D-Flow MRI, counteract changes that have been shown with the progression of dementia. We then used a DWI based technique

to evaluate CSF flow in the PVS of the ACA. We measured an effect of dobutamine, the positive control, on D* but no difference of trigeminal nerve stimulation on D* compared to the baseline D*. Lastly, we piloted a PET technique to measure clearance from the parenchyma. This pilot study has developed measurement techniques that lay the groundwork for further large animal and human experiments to explore trigeminal nerve stimulation device design and stimulation waveform.

Methods

Animal care. We used n=4 UW-mini pigs, 70-90 kg, fully mature (12-18 months old) in the experiments. All animal care and procedures were approved by the University of Wisconsin-Madison Institutional Animal Care and Use Committee (IACUC). Pig 1 was inducted and maintained with inhaled isoflurane (\sim 3%). Pig 2-4 were inducted with an intramuscular injection of Telazol (6 mg/kg) and xylazine (2 mg/kg). In Pig 2 the anesthetic plane was maintained with inhaled isoflurane (1%) and intravenous fentanyl (12-30 μ g/kg/hr), administered with lactated Ringer's solution (LRS), for analgesia. Pig 3 and 4 were maintained with propofol CRIs. All animals were intubated and mechanically ventilated. The variance in anesthesia across subjects was to explore the anesthesia options and due to the limited availability of fentanyl arising from supply chain shortages. Note that isoflurane is known to cause substantial cerebral vessel dilation (Turner et al., 2020). Dobutamine, administered as a CRI, was used as the positive control. We titrated dobutamine conservatively to increase systolic blood pressure by 20-30 mmHg without changing heart rate. Ferumoxytol was used as a CRI over 15 minutes

followed by a saline flush. A muscle paralytic, vecuronium, was administered intravenously during ECAP recordings to avoid myogenic artifacts in the neural recordings from electrically evoked muscle movement (Yoo et al., 2013; Nicolai et al., 2020; Blanz et al., 2022). We delivered vecuronium as a 0.1 mg/kg bolus over 1 minute followed by 1-1.5 mg/kg/hr constant rate infusion.

Surgical procedure for ECAP recordings. Skin flap was incised over the zygomatic process caudal to the margin of ramus, around the posterior margin of the temporomandibular articulation following the margin of the ramus around the bend in the jaw along the ventral margin of the ramus. The skin flap was retracted rostrally to expose the masseter muscle on the lateral margin of the ramus. The masseter muscle was then bluntly dissected from the ramus to expose bone. The superficial musculoaponeurotic layer and platysma were incised along the posterior margin of the ramus to allow access to the medial margin of the ramus and medial pterygoid muscle. This allowed for palpation of the mandibular foramen and provided a reference for the approximate location/route of the alveolar branch and lingual branch of the maxillary nerve (V3 trigeminal). A bone saw was used to cut a line through the ramus from the posterior edge of the ramus just inferior to the condylar process, approximately ¾ width of the ramus inferior to the coronoid process (~5 cm.). A second cut was made starting at the rostral edge of the first cut and following a straight line passing approximately 1.5 cm superior to the mandibular foramen and to the posterior margin of the ramus (~6 cm). This cut formed a wedge-shaped deficit in the ramus exposing connective/adipose tissue on the medial margin of

the ramus. The lingual and alveolar branches of the maxillary nerve were found coursing on the lateral surface of the pterygoid muscle in proximity with the alveolar artery and vein.

At this point the lingual and the alveolar nerves were cuffed with recording electrodes at approximately 2 cm superior to the mandibular foramen.

4D-Flow MRI. Images were acquired on a 3.0 T PET/MRI system (Signa PET/MR, GE Healthcare, Waukesha, WI) with a 16-channel phase array coil (GEM Flex LG Full, GE Healthcare, Waukesha, WI). Followed by Ferumoxytol administration, a volumetric, time-resolved phase contrast (PC) MRI was acquired using a 3D radially undersampled readout along with three-directional velocity encodings (PC-VIPR) (Johnson et al., 2008). Relevant imaging parameters included TR/TE = 7.38/3.0 ms, flip angle = 15°, bandwidth = 125 kHz, 4-point referenced flow encoding scheme at V_{enc} = 60 cm/s, field-of-view (FOV) = 240 x 240 x 240 cm³, number of projections = 16,000, total scan time = 9:51 minutes. Time-resolved data was obtained by retrospectively gating into 20 cardiac phases. Both time-averaged and time-resolved data were decoded and reconstructed into magnitude and velocity images (matrix size = 480 x 480 x 480, isotropic resolution of 0.5-mm) using partially parallel imaging with localized sensitivities (PILS) (Griswold et al., 2000) incorporated with 3D phase unwrapping for velocity aliasing correction (Loecher et al., 2016). Image analysis was performed in a MATLAB-based program (Schrauben et al., 2015). Background phase correction was implemented for each reconstructed image using a thirdorder polynomial fit (Roberts et al., 2022; Walker, et al., 1993). Vessel segments were delineated from the time-averaged complex difference images by segmenting each crosssection with k-means clustering along the vasculature centerline (Rivera-Rivera et al., 2020).

DWI MRI. Images were acquired on a 3.0 T PET/MRI system (Signa PET/MR, GE Healthcare, Waukesha, WI) with a 16-channel phase array coil (GEM Flex LG Full, GE Healthcare, Waukesha, WI) using an echo planar sequence (EPI). The frequency encoding gradient was aligned with the angular orientation of the vessel (we tried different areas of brain) so that motion probing gradients could be applied along and perpendicular to the fluid movement within the vessel. EPI sequences were acquired with (autoTR 16160 ms), TE = 145 ms, 1.4 mm slice thickness, 0.9 echo spacing, matrix size = 128 x 128, FOV = 18 x 18 mm, NEX = 2, b-value = 150 s/mm². Seven images were acquired per DWI sequence (5:30 minutes total): a b = 0 s/mm² image, separate acquisitions with motion probing gradients in three principal directions (x, y, z), and their opposite (-x, -y, -z). A long TE was implemented to attenuate signal from blood and parenchyma while preserving some signal from paravascular spaces (Harrison et al., 2018). Additionally, a long TE helped with minimizing partial volume effects.

Acknowledgements

Dr. Bradley Christian and Maxim Slesarev for PET tracer procurement and study design.

PET/MR staff for study support. Dr. Oliver Wieben for introduction to the 4D-Flow technique.

Dr. Ali Pirasteh for preforming PI duties on the PET study. Dr. Paul Min for advising on use of

MRI techniques in swine. Dr. Marissa Suchyta for input on anatomy of facial nerve. Members of
the Wisconsin Institute for Translational Neuroengineering (WITNe) for feedback during group
meetings.

This work was funded by a supplement on National Institutes of Health (NIH) National Institute of Biomedical Imaging and Bioengineering (NIBIB) grant No. 1-U18-EB029251-01 as part of the NIH HEAL Program.

Conflicts of Interest

NV was an employee of Abbott Neuromodulation and BioCircuit Technologies during the course of this study. KAL is a scientific board member and has stock interests in NeuroOne Medical Inc. KAL is also a paid member of the scientific advisory boards of Cala Health, Blackfynn, Abbott Neuromodulation, and Battelle. KAL also is a paid consultant for Galvani, Boston Scientific, CVRx, Presidio Medical, and the Alfred Mann Foundation. KAL and AJS are cofounders of NeuronOff Inc., which is commercializing the Injectrode. KAL and JW are cofounders and shareholders of NeuraWorx Inc., which has licensed patents to commercialize this technology.

The remaining authors declare that the research was conducted in the absence of any commercial or financial relationships that could be construed as a potential conflict of interest.

References

- Barisano, G., Lynch, K. M., Sibilia, F., Lan, H., Shih, N.-C., Sepehrband, F., et al. (2022). Imaging perivascular space structure and function using brain MRI. *NeuroImage*, 119329. doi: 10.1016/j.neuroimage.2022.119329.
- Blanz, S. L., Musselman, E. D., Settell, M. L., Knudsen, B. E., Nicolai, E. N., Trevathan, J. K., et al. (2022). Spatially selective stimulation of the pig vagus nerve to modulate target effect versus side effect. Bioengineering doi: 10.1101/2022.05.19.492726.
- Choi, S., Jang, D. C., Chung, G., and Kim, S. K. (2022). Transcutaneous Auricular Vagus Nerve Stimulation Enhances Cerebrospinal Fluid Circulation and Restores Cognitive Function in the Rodent Model of Vascular Cognitive Impairment. *Cells* 11, 3019. doi: 10.3390/cells11193019.

- de Leon, M. J., Li, Y., Okamura, N., Tsui, W. H., Saint-Louis, L. A., Glodzik, L., et al. (2017). Cerebrospinal Fluid Clearance in Alzheimer Disease Measured with Dynamic PET. *J Nucl Med* 58, 1471–1476. doi: 10.2967/jnumed.116.187211.
- Fico, B. G., Miller, K. B., Rivera-Rivera, L. A., Corkery, A. T., Pearson, A. G., Eisenmann, N. A., et al. (2022). The Impact of Aging on the Association between Aortic Stiffness and Cerebral Pulsatility Index. *The FASEB Journal* 36, fasebj.2022.36.S1.R4925.
- Griswold, M. A., Jakob, P. M., Nittka, M., Goldfarb, J. W., and Haase, A. (2000). Partially parallel imaging with localized sensitivities (PILS). *Magn. Reson. Med.* 44, 602–609. doi: 10.1002/1522-2594(200010)44:4<602::AID-MRM14>3.0.CO;2-5.
- Harrison, I. F., Siow, B., Akilo, A. B., Evans, P. G., Ismail, O., Ohene, Y., et al. (2018). Non-invasive imaging of CSF-mediated brain clearance pathways via assessment of perivascular fluid movement with diffusion tensor MRI. *eLife* 7, e34028. doi: 10.7554/eLife.34028.
- Hirschler, L. (2018). High resolution T2-prepared MRI enables non-invasive assessment of CSF flow in perivascular spaces of the human brain. *eLife* 7, e34028. doi: 10.7554/eLife.34028.
- Hirschler, L. The driving force of glymphatics: influence of the cardiac cycle on CSF-mobility in perivascular spaces in humans. 3.
- Iliff, J. J., Wang, M., Liao, Y., Plogg, B. A., Peng, W., Gundersen, G. A., et al. (2012). A Paravascular Pathway Facilitates CSF Flow Through the Brain Parenchyma and the Clearance of Interstitial Solutes, Including Amyloid β. *Sci. Transl. Med.* 4. doi: 10.1126/scitranslmed.3003748.
- Iliff, J. J., Wang, M., Zeppenfeld, D. M., Venkataraman, A., Plog, B. A., Liao, Y., et al. (2013). Cerebral Arterial Pulsation Drives Paravascular CSF-Interstitial Fluid Exchange in the Murine Brain. *Journal of Neuroscience* 33, 18190–18199. doi: 10.1523/JNEUROSCI.1592-13.2013.
- Johnson, K. M., Lum, D. P., Turski, P. A., Block, W. F., Mistretta, C. A., and Wieben, O. (2008).
 Improved 3D phase contrast MRI with off-resonance corrected dual echo VIPR: Improved 3D PC MRI With Corrected Dual Echo VIPR. *Magn. Reson. Med.* 60, 1329–1336. doi: 10.1002/mrm.21763.
- Kedarasetti, R. T., Drew, P. J., and Costanzo, F. (2022). Arterial vasodilation drives convective fluid flow in the brain: a poroelastic model. *Fluids Barriers CNS* 19, 34. doi: 10.1186/s12987-022-00326-y.
- Kim, J.-H., Im, J.-G., and Park, S.-H. (2022). Measurement of CSF pulsation from EPI-based human fMRI. *NeuroImage* 257, 119293. doi: 10.1016/j.neuroimage.2022.119293.
- Korte, N., Nortley, R., and Attwell, D. (2020). Cerebral blood flow decrease as an early pathological mechanism in Alzheimer's disease. *Acta Neuropathol* 140, 793–810. doi: 10.1007/s00401-020-02215-w.

- Le Bihan, D. (2019). What can we see with IVIM MRI? *NeuroImage* 187, 56–67. doi: 10.1016/j.neuroimage.2017.12.062.
- Li, L., Ding, G., Zhang, L., Davoodi-Bojd, E., Chopp, M., Li, Q., et al. (2022). Aging-Related Alterations of Glymphatic Transport in Rat: In vivo Magnetic Resonance Imaging and Kinetic Study. *Front. Aging Neurosci.* 14, 841798. doi: 10.3389/fnagi.2022.841798.
- Li, Y., Rusinek, H., Butler, T., Glodzik, L., Pirraglia, E., Babich, J., et al. (2021). Decreased CSF clearance and increased brain amyloid in Alzheimer's disease. In Review doi: 10.21203/rs.3.rs-900478/v1.
- Liang, P., Li, L., Zhang, Y., Shen, Y., Zhang, L., Zhou, J., et al. (2021). Electroacupuncture Improves Clearance of Amyloid-β through the Glymphatic System in the SAMP8 Mouse Model of Alzheimer's Disease. *Neural Plasticity* 2021, 1–11. doi: 10.1155/2021/9960304.
- Liu, P.-P., Xie, Y., Meng, X.-Y., and Kang, J.-S. (2019). History and progress of hypotheses and clinical trials for Alzheimer's disease. *Sig Transduct Target Ther* 4, 29. doi: 10.1038/s41392-019-0063-8.
- Loecher, M., Schrauben, E., Johnson, K. M., and Wieben, O. (2016). Phase unwrapping in 4D MR flow with a 4D single-step laplacian algorithm: 4D Laplacian Unwrapping for 4D Flow MRI. *J. Magn. Reson. Imaging* 43, 833–842. doi: 10.1002/jmri.25045.
- Lohela, T. J., Lilius, T. O., and Nedergaard, M. (2022). The glymphatic system: implications for drugs for central nervous system diseases. *Nat Rev Drug Discov*. doi: 10.1038/s41573-022-00500-9.
- Luo, Y., Yang, W., Li, N., Yang, X., Zhu, B., Wang, C., et al. (2020). Anodal Transcranial Direct Current Stimulation Can Improve Spatial Learning and Memory and Attenuate Aβ42 Burden at the Early Stage of Alzheimer's Disease in APP/PS1 Transgenic Mice. *Front. Aging Neurosci.* 12, 134. doi: 10.3389/fnagi.2020.00134.
- Mills, R. (1973). Self-diffusion in normal and heavy water in the range 1-45.deg. *J. Phys. Chem.* 77, 685–688. doi: 10.1021/j100624a025.
- Mitchell, G. F., van Buchem, M. A., Sigurdsson, S., Gotal, J. D., Jonsdottir, M. K., Kjartansson, Ó., et al. (2011). Arterial stiffness, pressure and flow pulsatility and brain structure and function: the Age, Gene/Environment Susceptibility Reykjavik Study. *Brain* 134, 3398–3407. doi: 10.1093/brain/awr253.
- Nicolai, E. N., Settell, M. L., Knudsen, B. E., McConico, A. L., Gosink, B. A., Trevathan, J. K., et al. (2020). Sources of off-target effects of vagus nerve stimulation using the helical clinical lead in domestic pigs. *J. Neural Eng.* 17, 046017. doi: 10.1088/1741-2552/ab9db8.
- Rivera-Rivera, L. A., Turski, P., Johnson, K. M., Hoffman, C., Berman, S. E., Kilgas, P., et al. (2016). 4D flow MRI for intracranial hemodynamics assessment in Alzheimer's disease. *J Cereb Blood Flow Metab* 36, 1718–1730. doi: 10.1177/0271678X15617171.

- Rivera-Rivera, L. A., Schubert, T., Turski, P., Johnson, K. M., Berman, S. E., Rowley, H. A., et al. (2017). Changes in intracranial venous blood flow and pulsatility in Alzheimer's disease: A 4D flow MRI study. *J Cereb Blood Flow Metab* 37, 2149–2158. doi: 10.1177/0271678X16661340.
- Rivera-Rivera, L. A., Cody, K. A., Rutkowski, D., Cary, P., Eisenmenger, L., Rowley, H. A., et al. (2020). Intracranial vascular flow oscillations in Alzheimer's disease from 4D flow MRI. *NeuroImage: Clinical* 28, 102379. doi: 10.1016/j.nicl.2020.102379.
- Roberts, G. S., Loecher, M. W., Spahic, A., Johnson, K. M., Turski, P. A., Eisenmenger, L. B., et al. (2022). Virtual injections using 4D flow MRI with displacement corrections and constrained probabilistic streamlines. *Magnetic Resonance in Med* 87, 2495–2511. doi: 10.1002/mrm.29134.
- Schulz, J. M., Al-Khazraji, B. K., and Shoemaker, J. K. (2018). Sodium nitroglycerin induces middle cerebral artery vasodilatation in young, healthy adults. *Exp Physiol* 103, 1047–1055. doi: 10.1113/EP087022.
- Piantino, J. A., Illif, J. J., Lim, M. M., and Levendovszky, S. R. (2022). Reader Response: Association of Sleep, Neuropsychological Performance, and Gray Matter Volume with Glymphatic Function in Community-Dwelling Older Adults. Accessed at https://n.neurology.org/content/reader-response-association-sleep-neuropsychological-performance-and-gray-matter-volume-0">https://n.neurology.org/content/reader-response-association-sleep-neuropsychological-performance-and-gray-matter-volume-0>
- Schrauben, E., Wåhlin, A., Ambarki, K., Spaak, E., Malm, J., Wieben, O., et al. (2015). Fast 4D flow MRI intracranial segmentation and quantification in tortuous arteries: Fast 4D Flow Processing Tool. *J. Magn. Reson. Imaging* 42, 1458–1464. doi: 10.1002/jmri.24900.
- Taoka, T. (2021). Neurofluid as Assessed by Diffusion-Weighted Imaging. *Magnetic Resonance Imaging Clinics of North America* 29, 243–251. doi: 10.1016/j.mric.2021.01.002.
- Turner, K. L., Gheres, K. W., Proctor, E. A., and Drew, P. J. (2020). Neurovascular coupling and bilateral connectivity during NREM and REM sleep. *eLife* 9, e62071. doi: <u>10.7554/eLife.62071</u>.
- van Veluw, S. J., Hou, S. S., Calvo-Rodriguez, M., Arbel-Ornath, M., Snyder, A. C., Frosch, M. P., et al. (2020). Vasomotion as a Driving Force for Paravascular Clearance in the Awake Mouse Brain. *Neuron* 105, 549-561.e5. doi: 10.1016/j.neuron.2019.10.033.
- Visocchi, M., Chiappini, F., Cioni, B., and Meglio, M. (1996). Cerebral blood flow velocities and trigeminal ganglion stimulation. *Stereotact. Funct. Neurosurg.*
- Walker, P. G., Cranney, G. B., Scheidegger, M. B., Waseleski, G., Pohost, G. M., and Yoganathan, A. P. (1993). Semiautomated method for noise reduction and background phase error correction in MR phase velocity data. *J. Magn. Reson. Imaging* 3, 521–530. doi: 10.1002/jmri.1880030315.
- Wen, Q. (2022). Assessing pulsatile waveforms of paravascular cerebrospinal fluid dynamics using dynamic diffusion-weighted imaging (dDWI). 16.

- White, T. G., Powell, K., Shah, K. A., Woo, H. H., Narayan, R. K., and Li, C. (2021). Trigeminal Nerve Control of Cerebral Blood Flow: A Brief Review. *Front. Neurosci.* 15, 649910. doi: 10.3389/fnins.2021.649910.
- Yoo, P. B., Lubock, N. B., Hincapie, J. G., Ruble, S. B., Hamann, J. J., and Grill, W. M. (2013). High-resolution measurement of electrically-evoked vagus nerve activity in the anesthetized dog. *J. Neural Eng.* 10, 026003. doi: 10.1088/1741-2560/10/2/026003.

Chapter 6 Thesis Chapter for the Public

Precise Targeting of Bioelectronic Medicine

Purpose of this chapter

I wrote this chapter to share the joy I find in science. Science is a journey of discovery to learn more about ourselves and the world we live in. Science is a shared journey – with experts also in our field, with future experts (who may be in middle school right now), and with those outside the field (including the public). The Ludwig lab is committed to research that furthers humanity and I am thankful for this opportunity to share our work. I would like to thank the Wisconsin Initiative for Science Literacy (WISL) for their support in putting together this chapter. In particular, I thank Elizabeth Reynolds for her feedback on drafts of this chapter.

Portions of this chapter were presented at the UW-Madison 3-minute thesis (3MT) competition 2022:

https://www.youtube.com/watch?v=xFAa44zQmAI

6.1 Analogy of the nervous system

We are a little bit like computers! A computer has wires connecting its mother board to its speakers and microphones, which is how it 'speaks' and 'listens'. Similarly, we have nerves connecting our brains to organs throughout our body. Organs include our heart, lungs, and stomach. The difference between nerves and wires is that our nerves can regrow. They are alive! Like an electrical wire, our nerves carry electrical signals, which our brain uses to communicate with our organs and our organs use to send signals back to the brain. We know how to tap into wires to edit the signals travelling on them — we call this hacking. Similarly, we can use electrical stimulation to edit the signals travelling on our nerves. By 'hacking' the electrical signals on nerves, we can change organ function for therapeutic reasons. This is the premise of bioelectronic medicine.

6.2 Example of a bioelectronic medicine therapy

The carotid sinus nerve is a small nerve in our neck that connects blood pressure sensors in the carotid artery, a major blood vessel in our neck, to our brain. This nerve conveys critical information on blood pressure in the carotid artery to the brain, which then uses it to adjust blood pressure throughout the body.

In a clinically utilized therapy, a metal stimulation electrode is implanted next to the carotid sinus nerve during a surgical procedure. Electrical stimulation is then delivered through the metal electrode and additional electrical signals are introduced on the carotid sinus nerve.

The brain receives these additional signals via the carotid sinus nerve and, concerned blood

pressure is too high in the carotid artery, sends signals to lower blood pressure throughout the body.

The response can be miraculous! A patient with chronic high blood pressure can have this device turned on, and within minutes their blood pressure returns to a healthy normal level.

6.3 The problem of imprecise stimulation in bioelectronic medicine

Unfortunately, this miraculous response is only the case for the minority of patients. In the majority, the stimulation dose, or electrical current, that can be delivered is limited by off-target nerve activation. And there are many off-target nerves in the region of the neck. These off-target nerves can be activated by the electrical stimulation before the on-target carotid sinus nerve and lead to painful side effects, for example, unintended muscle contractions.

To move bioelectronic medicine forward, we need ways to stimulate nerves that are more precise. This has been the subject of my PhD thesis!

6.4 Improving target engagement in bioelectronic medicine

With the goal of improving the precision of electrical stimulation in bioelectronic medicine therapies, I have been running computer models to develop the Injectrode. The Injectrode is an injectable stimulation electrode that is delivered to the target nerve under ultrasound imaging guidance. The Injectrode is soft and fits snugly around the target nerve (Figure 6.1). This snug fit allows isolation of the target nerve and more precision stimulation. Further, the metal Injectrode 'attracts' electric current to it, routing current towards the target nerve. I have shown that when the Injectrode is used in addition to standard noninvasive electrical

stimulation, it lowers the stimulation dose required to activate the target nerve by more than 10 times!

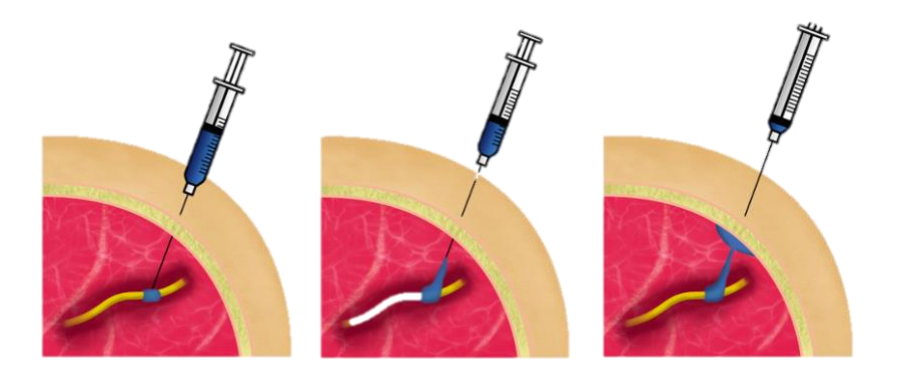


Figure 6.1: Injectrode delivery to the target nerve. Figure from Verma et al., 2021.

I then developed a way to directly measure nerve target engagement, which could be used in a human patient. I did this for two reasons. Firstly, we need to be able to measure target engagement to improve it. Secondly, I wanted to show that the Injectrode I developed using computer models would work in real human patients too.

When looking for methods to directly measure nerve target engagement, I was inspired by a paper from Ottaviani and his colleagues (2020). They introduced a very thin insulated metal wire with an exposed tip, called a microneurography electrode, into the target nerve and showed they could record neural activity from the nerve (Figure 6.2). Because the wire was so thin, it was barely felt as it entered flesh! I built on their work by investigating if the microneurography electrode could measure evoked electrical signals on the nerve following therapeutic electrical stimulation. I tested the microneurography electrode from Ottaviani's study alongside traditional recording electrodes used in the bioelectronic medicine fields. I did the experiments in living pigs. We needed to use pigs because they have similar size nerves to

humans. The pigs were under anesthesia during the experiment. My experiments showed that the microneurography electrode could accurately measure electrical signals on the nerve following therapeutic electrical stimulation. My work suggests that microneurography of the target nerve, as demonstrated by Ottaviani and his colleagues (2020) in humans, could be used in patients to measure and improve nerve target engagement during bioelectronic medicine therapies.

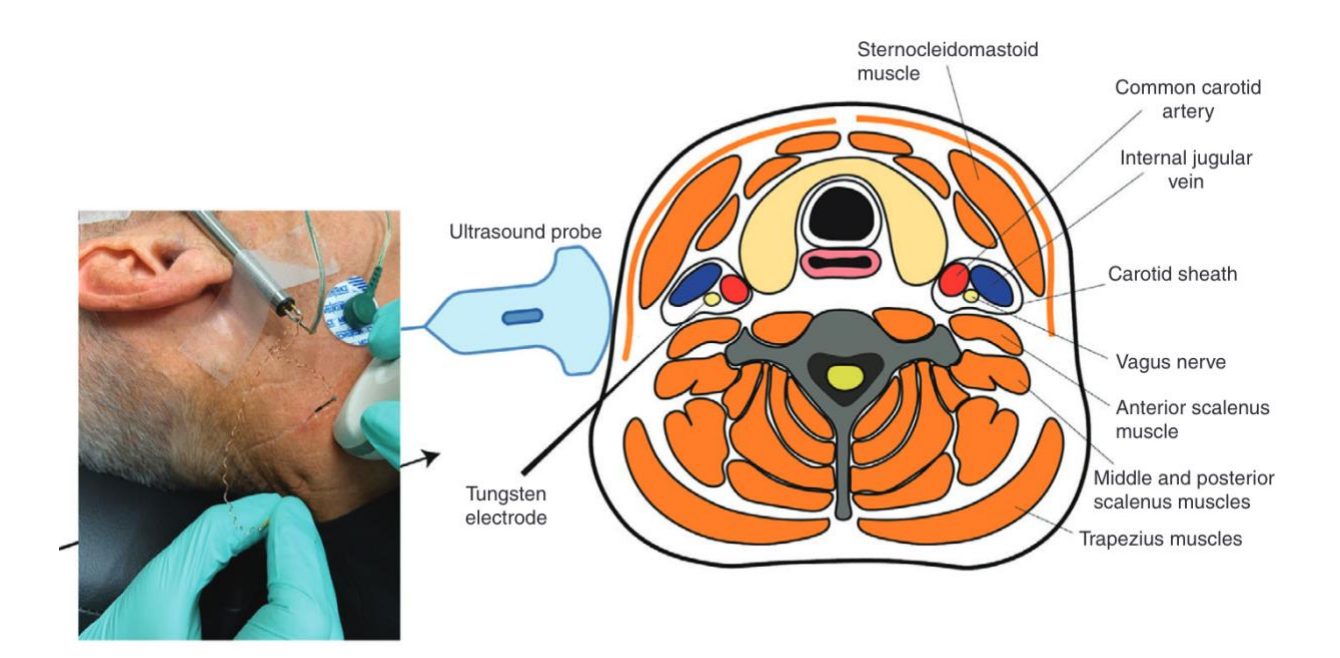


Figure 6.2: Ottaviani and his colleagues inserted a very thin metal wire through the skin and into the target nerve.

They were able to record electrical activity from the nerve. Figure from Ottaviani et al., 2020.

6.5 How I used the Injectrode and microneurography electrode to improve electronic bone growth stimulators

While working on my PhD, I came across noninvasive electronic bone growth stimulators. These devices are applied to the skin and deliver electric currents to the underlying bone, which helps

accelerate bone growth. Bone growth stimulators are prescribed by physicians for fractures that have not healed by themselves even after several weeks to months. I learnt several things about noninvasive electronic bone growth stimulators that led me to believe the therapy might be facing a target engagement problem. First, invasive electronic bone growth stimulators were shown to work better than noninvasive stimulators. Invasive stimulators are positioned closer to the bone and able to deliver a stronger electrical stimulation to the bone. Secondly, studies in small animals, where the fractured bone is closer to the noninvasive stimulation electrode and more electrical stimulation reaches the bone, showed that the therapy worked well. These excellent results were not always seen in humans. Thirdly, no one had yet measured the electrical current reaching the bone during noninvasive electronic bone growth stimulation. I decided to do just that!

I used the same microneurography electrodes from the previous study in pigs to measure the electrical stimulation reaching the bone during noninvasive electronic bone growth stimulation. I did these experiments in cadaver human legs that people had selflessly donated after their death. I found that very little of the applied noninvasive electrical stimulation was reaching the target bone! These results suggested that noninvasive electronic bone growth stimulation might have a target engagement problem.

In an effort to improve the electrical stimulation reaching the bone during noninvasive electronic bone growth stimulation, I believed the Injectrode could help – just as it had with noninvasive nerve stimulation. To test the idea, I compared the measurements taken in the human cadaver legs during noninvasive electronic bone growth stimulation to measurements taken with Injectrode-augmented (Injectrode filled into the bone fracture) electronic bone

growth stimulation. I measured an increase in electric stimulation reaching the bone with the Injectrode-augmented stimulation. I repeated the experiments in sheep, a large animal model commonly used to test fracture healing therapies, and came to the same conclusions.

This study in cadavers laid the groundwork for a future study where we will test Injectrode-augmented electronic bone growth stimulation versus traditional noninvasive electronic bone growth stimulation. We believe the Injectrode-augmented electronic bone growth stimulation will result in faster fracture healing.

6.6 What I am doing now

I am now using the target engagement framework and additional disease-relevant measurements to develop a new bioelectronic medicine therapy to tackle Alzheimer's disease. I look forward to sharing more about that work in the coming years!

6.7 My journey to bioelectronic medicine

It took me several years of describing my interests to discover the field of bioelectronic medicine. In middle school and high school, thanks to some particularly inspirational and supportive physics teachers, I loved physics! Thank you Ms Chee Hwai Mei, Mr Terrence Chiew, Mr Bernard Taylor, and Mr Jason Chan. In particular, I enjoyed the physics on electricity and magnetism. At the same time, biology was a subject I found fascinating but scored poorly in, particularly due to the need to memorize heavily to do well in the examinations. I wanted to use the conceptual lens of physics to study and understand biology. It took me several years of describing this, talking to people, and internships to land upon the field of 'bioelectronic medicine'. It was perfect — applying electricity to the body to excite neural activity and alter

physiology for therapeutic purposes. Since then, I have worked in several university labs and companies in the field and been guided by incredible mentors.

6.8 My future

In the long-term, my goal is to translate bioelectronic medicine advances from university labs to therapies that benefit patients. The last few years in graduate school have given me insights into the scientific methods, practices, and thought processes. Next, I plan to join a growing company in the field of bioelectronic medicine to contribute and understand what it takes to translate a proof of concept in animal studies to a clinically useful therapy.

Conclusions and Next Steps

Identifying the local neural substrates responsible for the on- and off-targets effects of a bioelectronic medicine therapy are critical to guide the development of the therapy. In this thesis, we developed a minimally invasive method that could be used clinically to directly measure neural target engagement. Next, we showed how stimulation electrode design can be exploited to improve local neural target engagement. We then applied these tools and target engagement framework to propose improvements to an existing bioelectronic therapy, electronic bone growth stimulators (EBGSs). Lastly, we applied these tools and target engagement framework along with other physiologically informative biomarkers towards developing a novel bioelectronic medicine therapy to restore glymphatic waste clearance from the brain with applications to Alzheimer's disease. In this last section, I briefly summarize the findings of each chapter and the next steps on each project.

In Chapter 2, we showed microneurography electrodes could be used to measured stimulation evoked compound action potentials (ECAPs) similar to traditional neural recording cuffs and intrafascicular electrodes. These microneurography electrodes are already used in human research and so have a fast path to clinical translation as tools to directly measure target engagement in bioelectronic therapies. To move this work forward, we could collaborate with a group that performs the microneurography technique in human research and is interested to extend its application to bioelectronic medicine. We would design a pilot clinical study to show the utility of measuring target engagement to inform stimulation paradigm and device design in bioelectronic medicine.

In Chapter 3, we showed that Injectrode-augmented TENS improved target engagement by over an order of magnitude compared to traditional TENS. Next in this work, we could identify a disease that is currently treated with bioelectronic medicine, which may be more accessible or have a more favorable side effect profile with the minimally invasive Injectrode-augmented TENS. We could then take the Injectrode to pilot clinical studies for this indication. A possible indication to pursue could be recovery of nonunion fractures, the subject of Chapter 4.

In Chapter 4, we showed in sheep and human cadavers and computational models that a weak electric field reaches the fracture site during traditional noninvasive electronic bone growth stimulator (EBGS) therapy. We then showed that application of the Injectrode to the fracture site increased the electric field reaching the fracture site during EBGS therapy. Future directions for this work would be to conduct a chronic *in vivo* large-animal sheep study to compare traditional noninvasive EBGSs to Injectrode-augmented EBGSs.

In Chapter 5, we showed trigeminal nerve stimulation increased cerebral blood flow and decreased flow pulsatility, opposing the changes that have been shown to occur with Alzheimer's disease progression. The glymphatic hypothesis proposes that cerebral hemodynamics is intimately linked to cerebrospinal (CSF) flow in paravascular spaces (PVS) and waste clearance from the brain. We implemented an MRI method to image CSF movement in the PVS of the great cerebral arteries. We showed for the first time in a large animal model that dobutamine, a positive control used in small animal glymphatic studies, increased CSF movement in the PVS. The MRI method to image CSF movement must be further refined to reduce measurement noise before stimulation temporal pattering and neural targets can be

systematically explored for an effect on CSF flow. Given the noninvasive nature of the stimulation intervention and the safety profile of existing trigeminal nerve stimulators, future studies could progress to human preclinical studies.

During the course of these studies, I learnt that target engagement is critically important and needs to be measured in clinical patients. Further, electrode design and placement need to be optimized for human patients. The bioelectronic medicine field is recognizing the need to measure and improve target engagement and target engagement measures are becoming more common in large animal studies. Next, I envision the field will develop to perform target engagement measures in human patients and on a patient specific level to inform therapy delivery. It is also possible that due to these measurements, we may discover that several existing efficacious therapies do not directly generate neural action potentials. Instead, they may alter neural membrane excitability or primarily act through non-neural cells. The field will research these non-neural cells to better understand the mechanism of action of bioelectronic medicine therapies. The better understanding of target engagement and/or non-neural mechanisms will provide a framework around which to optimize therapy device and stimulation waveforms.

This thesis has forwarded the tools and methods available to study and optimize target engagement in bioelectronic medicine. Future directions heavily involve clinical translation of the work. For this reason, I am positioning my career to gain more experience in clinical work. I will then be well setup to translate the development of bioelectronic medicine therapies with a focus on improving local neural target engagement.